Development of non-stimuli and stimuli-responsive ion carriers and their biological applications

विद्या वाचस्पति की
उपाधि की अपेक्षाओं की आंशिक पूर्ति में प्रस्तुत शोध प्रबंध

A thesis submitted in partial fulfillment of the requirements of the degree of Doctor of Philosophy

द्वारा / By

साळुंके स्वाती बन्सी / Salunke Swati Bansi

पंजीकरण सं. / Registration No.: 20173532

शोध प्रबंध पर्यवेक्षक / Thesis Supervisor: Prof. Pinaki Talukdar

भारतीय विज्ञान शिक्षा एवं अनुसंधान संस्थान पुणे
INDIAN INSTITUTE OF SCIENCE EDUCATION AND RESEARCH PUNE

2024

Development of non-stimuli and stimuli-responsive ion carriers and their biological applications

A Thesis
Submitted in Partial Fulfillment of the Requirements
for the Degree of

Doctor of Philosophy

by

Salunke Swati Bansi

ID: 20173532

Indian Institute of Science Education and Research, Pune

2024

Dedicated

To my parents…

भारतीय विज्ञान शिक्षा एवं अनुसंधान संस्थान पुणे
INDIAN INSTITUTE OF SCIENCE EDUCATION AND RESEARCH PUNE
डॉ. होमी भाभा मार्ग, पुणे 411008, महाराष्ट्र, भारत | Dr. Homi Bhabha Road, Pune 411008, Maharashtra, India
T +91 20 2590 8001 W www.iiserpune.ac.in
IISER PUNE

Dr. Pinaki Talukdar
Professor
Department of Chemistry,
IISER Pune

CERTIFICATE

Certified that the work incorporated in the thesis entitled *"**Development of non-stimuli and stimuli-responsive ion carriers and their biological applications**"* submitted by **Ms. Salunke Swati Bansi** was carried out by the candidate, under my supervision. The work presented here or any part of it has not been included in any other thesis submitted previously for the award of anydegree or diploma from any other university or institution.

Date: 16th July 2024

Dr. Pinaki Talukdar
(Research Supervisor)

भारतीय विज्ञान शिक्षा एवं अनुसंधान संस्थान पुणे
INDIAN INSTITUTE OF SCIENCE EDUCATION AND RESEARCH PUNE
डॉ. होमी भाभा मार्ग, पुणे 411008, महाराष्ट्र, भारत | Dr. Homi Bhabha Road, Pune 411008, Maharashtra, India
T +91 20 2590 8001 W www.iiserpune.ac.in
IISER PUNE

DECLARATION

I declare that this written submission represents my ideas in my own words and wherever other's ideas have been included; I have adequately cited and referenced the original sources. I also declare that I have adhered to all principles of academic honesty and integrity and have not misrepresented or fabricated or falsified any idea / data / fact / source in my submission. I understand that violation of the above will cause for disciplinary action by the Institute and can also evoke penal action from the sources which have thus not been properly cited or from whom proper permission has not been taken when needed.

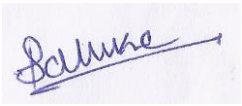

Date: 16th July 2024

Mr. Salunke Swati Bansi
I.D.: 20173532

Acknowledgments

This Ph.D. has been a long journey with its share of joy and pain, and through this journey, I have had the privilege of getting acquainted with many people who have given me support and encouragement. Thus, in this section, I would like to express my heartfelt gratitude to the people who made this journey memorable.

I would like to express my sincere thanks to my thesis supervisor, Prof. Pinaki Talukdar, for the opportunity he provided me to work in his lab. I am grateful for his guidance, encouragement, constructive criticism, and support throughout my Ph.D. tenure. I want to give my special thanks to sir because him I will be called as Dr. Swati.

I would like to thank my research advisory committee (RAC) members, Prof. Manickam Jayakannan (IISER Pune) and Dr. B L V Prasad (CSIR-NCL Pune), for their valuable suggestions, criticism, and inputs during review meetings that helped guide the course of my Ph.D.

My projects have included collaborative work and would not have been possible without support from Dr. Shilpy Sharma (SPPU) and her student Shreyada Save.

I express my gratitude to my lab mates, both past and present who have made a good environment in the lab. My sincier heartfelt thanks goes to Naveen Joseph Roy for always helping in research related difficulty and giving simple explanation of all queries which I had during my Ph.D life. I especially thank Dr. Sopan Shinde, Dr. Javid Ahmad Malla, Dr. Manzoor Ahmed, Ronedy Naorem and Dr. Rashmi Sharma for their assistance with various aspects of my work. I also acknowledge Dr. Debashis Mondal, Dr. Abhishek Mondal, Dr. Harshali Kathod, Dr. Avishikta Upadhyay, Ravindra, Parappa, Akram, Arjun, Arshad, Ahan, Anirban, Debarati, Umesh, Ranjeet, Debraj, Kavan, Kshitij, Neelam, Paras, Payel, Sandip, Shaharukh, Shreya, Soumyajit, Srijita and Tanvi Vyas.

I sincerely thank the staff at IISER Pune, Mayuresh Kulkarni (Chem office), Chinmay Lowalekar (NMR), Nitin Dalvi (NMR), Sandeep Mishra (NMR), Sandeep Kanade (HRMS), Ravinder Malothu (SCXRD), Parveen Nasa (SCXRD), Yathish T. S. (Chem office), Mahesh Jadav (Chem office),

Tushar Kurulkar (Academic office), Sayalee Damle (Academic office), Ganesh Dimbar (Chem office), and Sanjay Meena (Chem office) for their support

I acknowledge the Department of Science and Technology (DST), India for providing the INSPIRE fellowship that supported me in this journey.

I am very grateful to my friends and colleagues at IISER, and many more for all the help, fun times and encouragement.

I am thankful to my family for their unconditional love and support without whom I would not have been able to achieve this milestone. My parents, sister, and brother have constantly encouraged me and supported me in every way in both good times and bad. I would like to express my heartfelt gratitude to my husband without him I would not have completed my Ph.D. Finally, I want to thank my little angel Shravya (precious gift of my life) for always being reason of joy and happiness in my life.

Swati

Table of contents

Symbols and Abbreviations

δ	Chemical shift (NMR)
λ	Wavelength (lambda)
µL	Microliter
µM	Micromolar
µg	Microgram
ṽ	Wave number
Å	Angstrom
°C	Degrees Celsius

A

ACN	Acetonitrile
AcOH	Acetic acid
AO	Acridine orange
aq.	Aqueous medium
atm	Atmosphere
ATP	Adenosine triphosphate
ANTS	8-aminonaphthalene-1,3,6-trisulfonic acid, disodium salt

B

B3LYP	Becke, 3-parameter, Lee–Yang–Parr (exchange-correlation functional)

BSSE	Basis set superposition error
BODIPY	Fluorinated Boron-Dipyrromethene

C

c	Concentration
CD	Cyclodextrin
$(CD_3)_2CO$	Acetone-d_6
CD_3CN	Acetonitrile-d_3
$CDCl_3$	Chloroform-D
$CHCl_3$	Chloroform
CO_2	Carbon dioxide
cm	Centimeter
CsCl	Cesium chloride
CyPLOS	Cyclic phosphate-linked oligosaccharides
CH_2Cl_2	Dichloromethane
Calcd	Calculated
$CaCl_2$	Calcium chloride
Conf	Conformation
CF	Carboxyfluorescein
CFTR	Cystic Fibrosis Transmembrane Conductance Regulator
CLC	Chloride channel
CLCA	Calcium-activated chloride channel

CLIC	Chloride intracellular channel protein
CLNS1A	Chloride Nucleotide-Sensitive Channel 1A

D

d	Doublet
dt	Doublet of triplets
dd	Doublet of doublets
ddd	Doublet of doublets of doublets
D_2O	Deuterium oxide
DCM	Dichloromethane
DFT	Density functional theory
DMAP	4-Dimethylaminopyridine
DMEM	Dulbecco's Modified Eagle Medium
DMF	*N*,*N*-Dimethylformamide
DMSO	Dimethyl sulfoxide
DNA	Deoxyribonucleic acid
DPX	*p*-xylene-bis-pyridinium bromide

E

EC_{50}	Half maximal effective concentration
EDC·HCl	*N*-Ethyl-*N*′-(3-dimethylaminopropyl)carbodiimide hydrochloride
ESI	Electron spray ionization

em	Emission
ex	Excitation
Et_3N	Triethylamine
EtOAc	Ethyl acetate
EtOH	Ethanol
EYPC	Egg yolk phosphatidylcholine

F

FBS	Fetal bovine serum
FCCP	Carbonyl cyanide-p-trifluoromethoxyphenylhydrazone
FT-IR	Fourier transform infra-red spectroscopy

G

g	Gram

H

h	Hour
H_2	Hydrogen gas
H_2O	Water
H_2SO_4	Sulphuric acid
HCl	Hydrochloric acid
HEPES	4-(2-Hydroxyethyl)-1-piperazineethanesulfonic acid

HF	Hartree-Fock
HOBt	Hydroxybenzotriazole
HPTS	8-Hydroxypyrene-1,3,6-trisulfonic acid trisodium salt
HRMS	High resolution mass spectroscopy
Hz	Hertz
HBSS	Hanks' Balance Salt Solution

I

I_F	Normalized fluorescence intensity
IC_{50}	Half-maximal inhibitory concentration
IR	Infra-red (spectroscopy)

J

J	Joule
J	Coupling constant (NMR)

K

K	Kelvin
K_a	Association constant
kcal	Kilocalorie
KCl	Potassium chloride
KNO_3	Potassium nitrate

KOH	Potassium hydroxide
KH_2PO_4	Potassium dihydrogen phosphate

L

LED	Light emitting diode
LiCl	Lithium chloride
log*P*	Partition coefficient
LUVs	Large unilamellar vesicles

M

m	multiplet
M	Molar (molarity)
MCF-7	Michigan Cancer Foundation-7 (cell line)
Me	Methyl
MEF	Mouse embryonic fibroblast (cell line)
MeOH	Methanol
mg	Milligram
$MgCl_2$	Magnesium chloride
$MgSO_4$	Magnesium sulfate
MHz	Megahertz
mL	Milliliter
mM	Millimolar

mmol	Millimole
MMP	Mitochondrial membrane potential
Mol	Mole
MP	Melting point
MTT	3-(4,5-Dimethylthiazol-2-yl)-2,5-diphenyltetrazolium bromide
MW	Molecular weight
m/z	Mass to charge ratio

N

N	Normal (normality)
n	Hill coefficient
N_2	Nitrogen gas
Na_2CO_3	Sodium carbonate
Na_2SO_4	Sodium sulphate
$NaBH_4$	Sodium borohydride
NaBr	Sodium bromide
NaCl	Sodium chloride
NaI	Sodium iodide
$NaClO_4$	Sodium perchlorate
$NaHCO_3$	Sodium bicarbonate
$NaNO_2$	Sodium nitrite
$NaNO_3$	Sodium nitrate

NaOH	Sodium hydroxide
NaOAc	Sodium acetate
Na_2HPO_4	Disodium phosphate
NEt_3	Triethyl amine
nM	Nanomolar
nm	Nanometer
NMR	Nuclear magnetic resonance (spectroscopy)
ncm	6-nitro coumarin-7-ylmethyl

O

ONB	*o*-nitro benzyl

P

p	Pentet
Pd/C	Palladium on carbon
PBS	Phosphate buffered saline
PPG	Photocleavable protecting group
PPA	Polyphosphoric acid
PET ether	Petroleum ether
pH	Potential of hydrogen
PI	Propidium iodide
ppm	Parts per million

PEG	Polyethylene glycol
PG	Podigiosin

Q

q	Quartet

R

RbCl	Rubidium chloride
ROS	Reactive oxygen species
rt	room temperature

S

s	Singlet
s	Second(s)
sx	Sextet
SCXRD	Single crystal X-ray diffraction
$SnCl_2$	Stannous chloride
SDS	Sodium Dodecyl Sulfate

T

t	Time
t	Triplet

td	Triplet of doublets
*t*BuOK	Potassium tert-butoxide
TBA	Tetrabutyl ammonium
TBABr	Tetrabutyl ammonium bromide
TBACl	Tetrabutyl ammonium chloride
TBAI	Tetrabutyl ammonium iodide
THF	Tetrahydrofuran
TLC	Thin layer chromatography

U

UV	Ultraviolet

V

Val	Valinomycin
VARC	Voltage-Regulated Anion Channels

Z

ZPE	Zero-point energy

Synopsis

The fundamental aim of these thesis to introduce novel synthetic transmembrane anion carriers and their biomedical application in the cancer treatment. The thesis work included design and synthesis of anion carrier, investigation of anion transport across large unilamellar vesicles, to check ion selectivity and to look into operative ion transport mechanism across lipid membrane. Furthermore, apoptosis inducing activity due to disruption of chloride ion homeostasis caused by carrier in live cell was elucidated. The novelty of this thesis, the phototriggered strategy was established for the precise control on ion transport activity of carrier to achieve specificity in the cancer cells over healthy cells. This outcome could be the promising tool to achieve effective anticancer treatment compare to chemotherapy in future perspective of biomedical science.

Chapter 1: Introduction to membrane transport

The transmembrane transport of ions needs assistance from the membrane-embedded protein molecules to facilitate the transport over the hydrophobic barrier of the cell membrane. The transport process is the central movement of a natural system which is carried out by a carrier or channel, to maintain ion homeostasis, membrane potential, pH gradient, and osmotic pressure. The Cl^- is the most abundant anion in the physiological system. Dysfunction of the Cl^- channel due to mutation or malfunction causes life-threatening diseases such as cystic fibrosis, myotonia, etc. Recently Cl^- selective synthetic carriers or channels known to cause apoptotic cancer cell death. Although, the strategies of cancer chemotherapy have become increasingly sophisticated, yet there is no cancer treatment that is 100% effective in curing cancer is available due to the drug resistance that evolves during the treatment. The synthetic chloride carrier function in the lipid membrane and can overcome the resistance related to the mutations and over-expression of genes and proteins. Unfortunately, the apoptosis-inducing activity of reported synthetic chloride transporters is not selective only towards cancerous cells. The undesired damage of healthy cells by these systems necessitates the discovery of new synthetic chloride transporters which will work only under specific condition of stimuli and explore their therapeutic potential in targeting cancer.

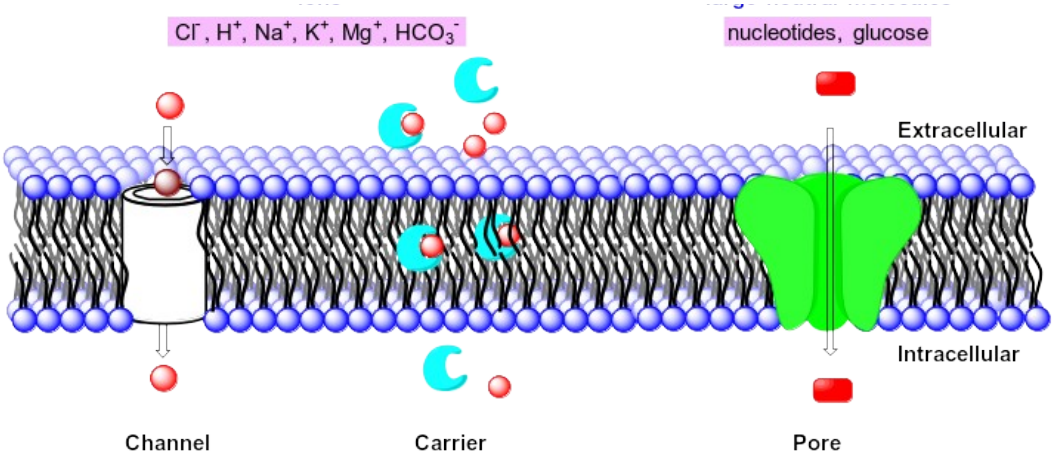

Figure 1. Schematic representation of ion transport across the membrane.

Chapter 2: Cyclic oligosaccharide-based anion carriers

Cyclic carbohydrate-based macrocycles were designed from tetrameric oligo-(1→6)-β-D-glucosamine unit of 3-amino-3-deoxyallose and 4-amino-4-deoxygalactose hexose sugar. The amide groups presented at axial position were decorated with different aromatic tails for the recognition of anion. Different aromatic tails also contributed different transport activity due to alteration of pKa and log P values. The synthesis of 12 3-amino-3-deoxyallose and 11 4-amino-4-deoxygalactose systems were done by Dr. Yuri Tsvetkov, N. D. Zelinsky Institute of Organic Chemistry, Moscow. Two systems with pyrrole and indole side chains in 3-amino-3-deoxyallose series were identified to exhibit good ion transport activity. On the other hand, in 4-amino-4-deoxygalactose series *p*-methyl, *p*-bromo, *p*-trifluoro methyl, pyrrole and indole tails possesses good transport activity. The ion selectivity provided significant difference in ion transport activity in the presence of different anions. However, cations not playing any role in the transport activity.

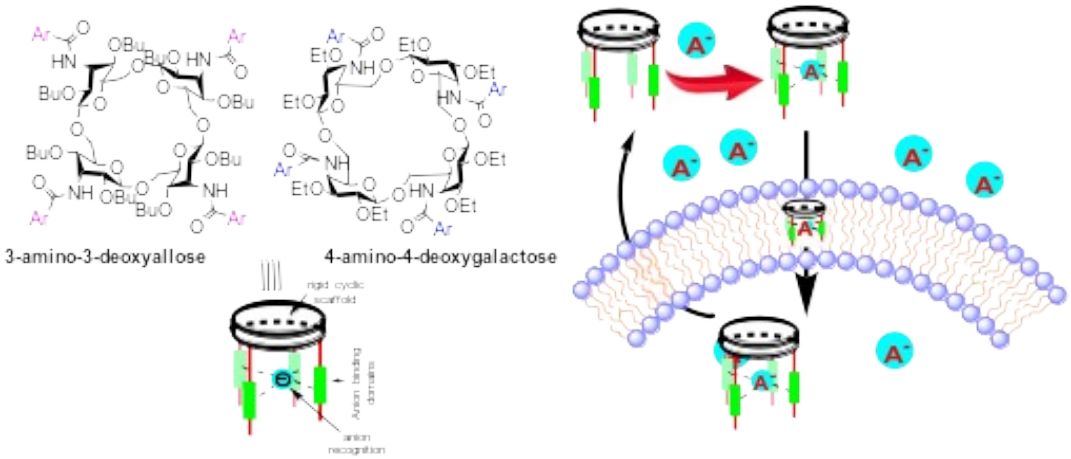

Figure 2. Structure and schematic representation of ion transport process by cyclic oligosaccharides-based carrier.

Chapter 3: Bisindole-based small molecules as transmembrane anion carriers and potential anticancer agents

The novel bisindole based anionophore were design and synthesised by the fusion of indole-2-carboxyllic acid and ester derivatives of 7-amino indole-2-carboxilic acid. The crystal structure of **1d** in DMSO elucidate the orientation of one of the indole N-H is opposite to that of amide N-H and another indole N-H. The comparative ion transport studies indicate **1b** as a most active carrier. The ion selectivity data validate transport activity is anion dependent. The lucigenin assay confirms Cl^- transport activity of all carriers. The cation selectivity and valinomycin assay result corroborates anion antiport as an operative ion transport mechanism. The MTT assay shows **1a** is inducing cytotoxicity in cancerous cell over non-cancerous cell via disruption of cellular chloride ion homeostasis. The occurrence of events such as depolarisation of mitochondrial membrane potential (MMP), enhanced level of ROS species and deacidification of lysosomes confirms apoptotic cancer cell death.

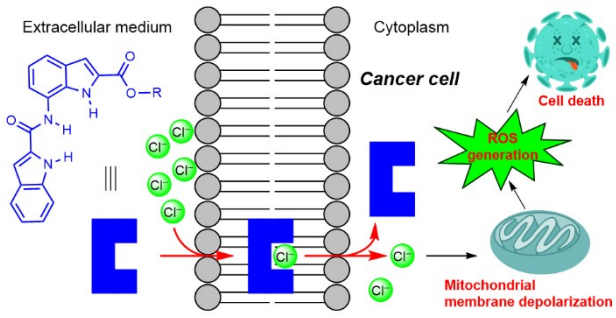

Figure 3. Structure and mechanism of apoptotic cancer cell death by bisindole carriers.

Chapter 4: Phototriggered release of transmembrane chloride carrier from an *o*-nitrobenzyl-linked procarrier

First time 1*H*-indole-2-carboxamide based chloride transporter was reported. Further we have developed light triggered procarrier **2** (inactive form of active carrier) for control on chloride transport activity of synthetic ion transporter. The ion transport activity across large lamellar vesicles (LUVs) elucidates active carrier possesses good transport activity, however procarrier is inactive at the same concentration. These results corroborate the presence of *o*-nitro benzyl (PPG) group block the binding site to make molecule inactive. The ^{1}H NMR studies confirmed the formation of active carrier **1d** upon photolysis of **2** after irradiation of 365 nm light. Photolysis of procarrier **2** across LUVs shows enhancement in chloride ion transport with time due to release of most active carrier **1d**. The cytotoxicity of procarrier **2** in cancer cells upon photoactivation were confirmed by MTT assay. This outcome is the proof of photoactivation in the field of synthetic ion transporter and can be extended for the direct biomedical application such as surface cancer treatment.

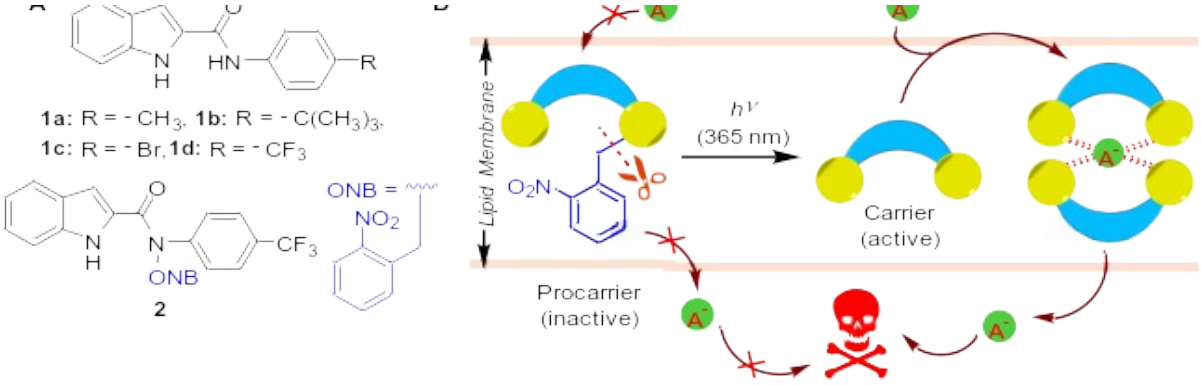

Figure 4. Structure of indole-based carrier and procarrier (**A**). Schematic representation of photoactivation of procarrier in the lipid membrane (**B**).

Chapter 1

Introduction to membrane transport

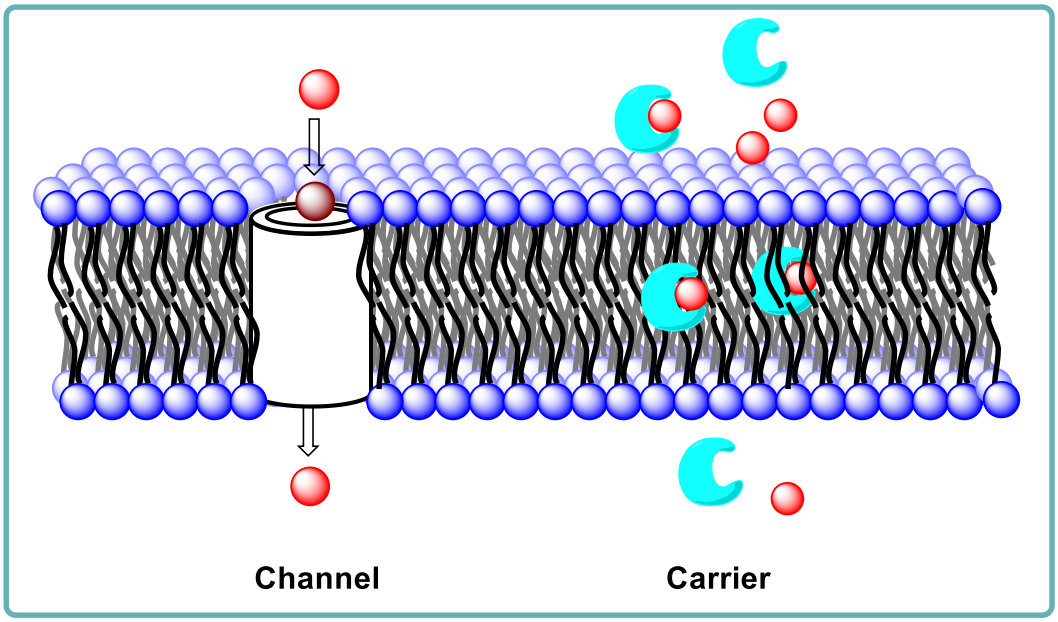

1.1 Introduction to the cell membrane

The cell is the smallest structural, functional, and biological unit of life on this earth and is composed of two parts: the cell membrane and the protoplasm. The protoplasm is made up of internal organelles like the nucleus, mitochondria, Golgi complex, endoplasmic reticulum, and cytoplasm. The cell membrane is the porous lipid bilayer that supports and protects cellular components from damage and leakage. The lipid bilayer is a self-assembled structure of a million amphiphilic molecules with one polar head group (hydrophilic part) and two nonpolar tail groups (hydrophobic part). In an aqueous medium, the hydrophobic parts (carbon chain) assemble, pointing towards the interior to form a bilayer, whereas polar head groups (phosphorous group) are exposed to the external aqueous media, forming the outer layer of the cell membrane. This lipid bilayer separates the external part of the cell from the protoplasm (nucleus and cytoplasm). For cellular communication, protein molecules are present on the cell membrane called membrane receptors, which play an important role in physiological and biological processes.

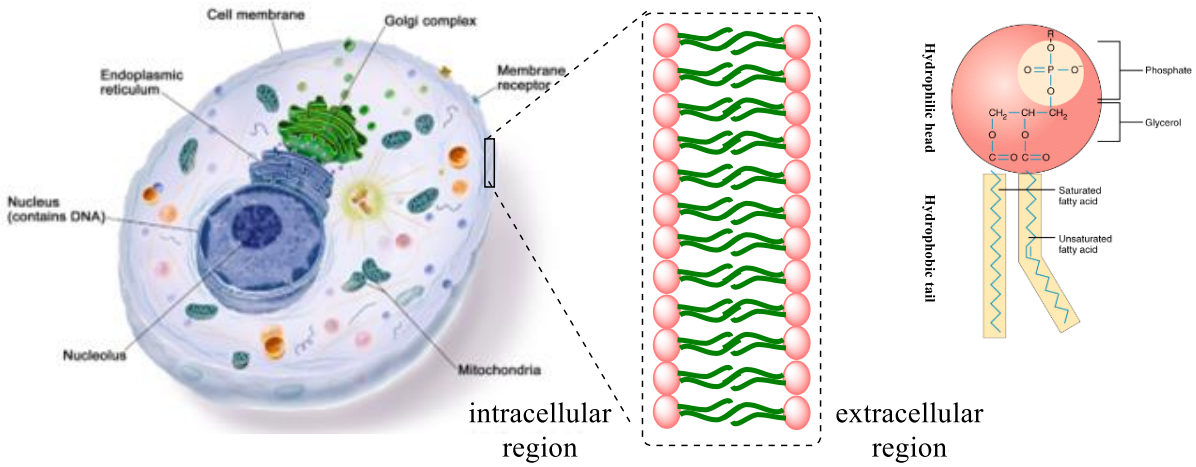

Figure 1.1 Schematic representation of eukaryotic cell and the structure of lipid bilayer. Adapted from https://www.cancer.gov/publications/dictionaries/cancer-terms/def/cell.

1.2 Membrane transport

Membrane transport is the mechanism that manages the passage of different solute molecules present in the cellular media across the lipid bilayer membrane. This membrane forms a

semipermeable barrier for molecules due to the nature of the arrangement of the hydrophilic and hydrophobic parts of the lipid membrane. The neutral molecules (like N_2, O_2, CO_2), small charged species, water, and ethanol move across the hydrophobic layer by simple diffusion. However, the hydrophobic core of the lipid bilayer creates a hydrophobic barrier for the transport of polar organic molecules (nucleotides, glucose, etc.), ions, and large biomolecules (DNA, proteins). Hence, nature has designed special proteins, carbohydrates, and their complexes embedded in the lipid bilayer that facilitate the transport of impermeable solute molecules across the cell membrane by overcoming the thermodynamic barrier imposed by the hydrophobic part of the plasma membrane.

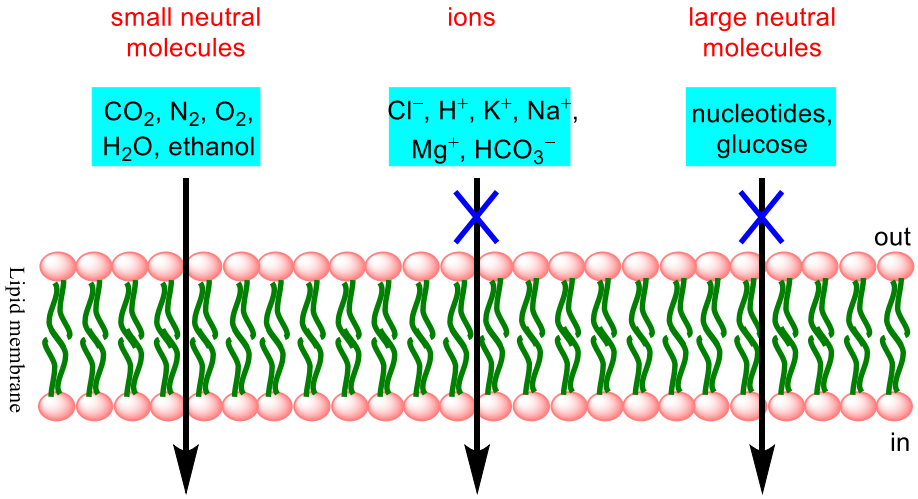

Figure 1.2 Representation of transport of different types of solutes across the lipid bilayer.

1.3 Ion transport

The transport of ions is an essential biological process that helps to maintain pH gradient, ion homeostasis, osmotic pressure and membrane potential. The uneven distribution of different solute molecules which are non-permeable across the lipid bilayer membrane creates a concentration gradient across the plasma membrane, which acts as a driving force for the transport process. The vital function of ion transport is carried out by two types of proteins intercalated in the lipid membrane: ion carriers and ion channels. Ion carriers diffuse ions from one side of the cell membrane to the other side of the cell membrane over an electrochemical gradient whereas ion channels form a continuous pathway for the passage of ions across a concentration gradient. Passive transport and active transport are the two main modes of ion transport across the lipid bilayer. Passive transport is the simple diffusion of ions across a

concentration gradient (from high concentration to low concentration of ions) from one side of the cell membrane to the other. Hence, it does not require energy for the transport process. Active carriers require energy for the movement of ions against the concentration gradient, which is obtained by the hydrolysis of the ATP molecule. The channel molecule transports ions through an active mode of transport referred to as an ion pump.

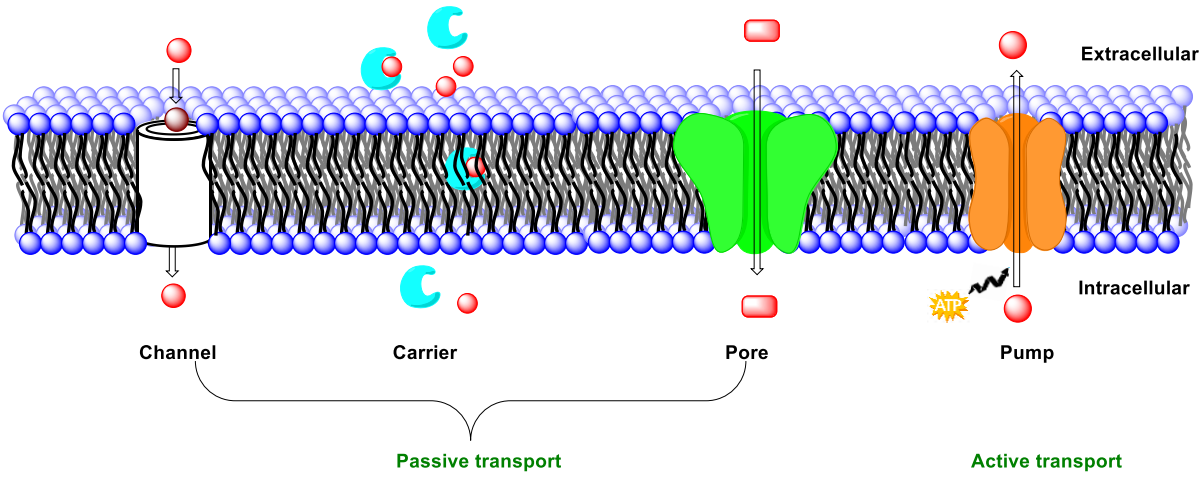

Figure 1.3 Schematic representation of different types of ion carriers and their mode of transport in natural systems.

Based on the direction of ion transport and the ratio of ions involved in the transport process, the carriers are classified as uniporters and cotransporters. Uniporters transport a single ion in one direction across the membrane whereas cotransporters transport two or more species across the cell membrane. Depending on the direction of ion transport cotransporters are further classified into symporters and antiporters. A symporter is a transport system that simultaneously diffuses two opposite-charged solute molecules in the same direction of the cell membrane. In contrast, antiporters transport two similar charged solute molecules in opposite directions across the cell membrane.

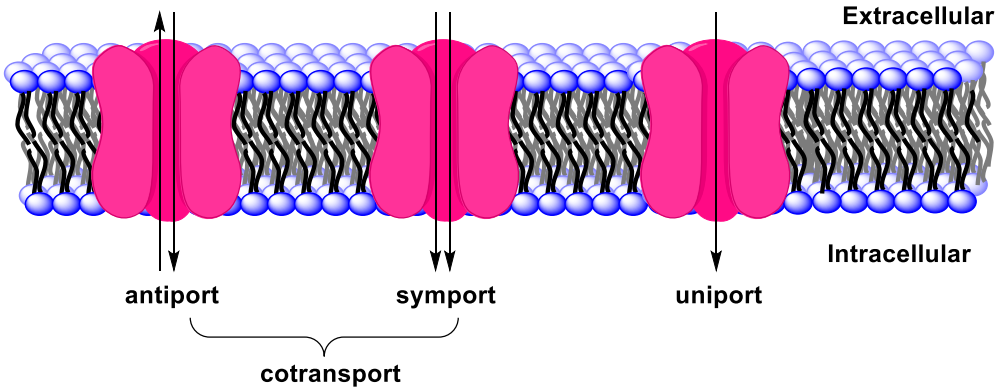

Figure 1.4 Schematic representation of the mechanism of ion transport based on transport direction and stoichiometry.

1.4 The biological role of ion transport

As stated above, ion transport plays a pivotal role in physiological functions such as the regulation of the flow of ions, muscle contraction, pH regulation, hormonal secretion, signal transduction, cell-to-cell communication, energy production and the body's salt and water homeostasis. Dysfunction of ion channels due to mutation of genes encoding ion transport protein or malfunction of ion channels leads to a variety of life-threatening inherited diseases called channelopathies such as cystic fibrosis, Dent disease, Barter syndrome etc. Among all anions, chloride is the most abundant ion present in the natural system. Chloride plays a pivotal role in the maintenance of membrane potential (30 mV – 60 mV), cell volume, cell proliferation transepithelial salt transport, acidification of intracellular and extracellular compartments and apoptosis. CLC, CFTR, CLCA, CLIC, and CLNS1A are a large family of proteins found in all phylae which are Cl^- conductors and Cl^-/H^+ exchangers. The impairment of CLC genes causes mortal genetic diseases like cystic fibrosis, kidney stones, myotonia, deafness, osteopetrosis and epilepsy. Voltage-regulated anion channels (VRAC), especially the chloride channel, play an important role in cell volume regulation due to which it is responsible for the apoptosis process, cell proliferation and drug resistance in a cancer cell.[1-3] CLC-3 is a voltage-gated chloride channel mainly expressed in the cancer cell. Overexpression of the CLC-3 channel influences the interphase of the cell cycle (G1 to S transition of the cell cycle) which is responsible for cell proliferation and hence stimulates the rate of tumours. On the other hand activation of the CLC-3 channel induces apoptosis by inhibiting cell signalling pathway PI3K/Akt/mTOR in nasopharyngealcarcina cells.[4] Knockout of CLC-3 decreases the effectiveness of basic anticancer drugs due to increasing acidification of the intracellular

compartment, hence increasing the drug resistance in a cancer cell. CLC-4, and CLC-5 cause acidification of the intracellular region of the cell.[5, 6]

CLCN1 genes produce protein molecules, and form channels responsible for the transport of chloride ions inside the cell which forbid muscle contraction by the stabilization of the electric charge of the cell. Mutation in the CLCN1 gene affects the flow rate of chloride ions due to alteration of the structure or function of a channel which causes muscle stiffness, this disorder is known as myotonia congenita. Mutation in cystic fibrosis transmembrane conductance regulator (CFTR) makes the CFTR channel dysfunctional, so it is unable to transport chloride ions, which affects the movement of water to the cell surface; hence, mucus becomes thicker and stickier; this condition is called cystic fibrosis. The malfunction of the chloride channel is the root of renal tubular disorders like Dent's syndrome, Barter syndrome, etc. Consequently, the concentration of chloride ions in the intracellular region of the cell plays a crucial role in the maintenance of physiological processes.

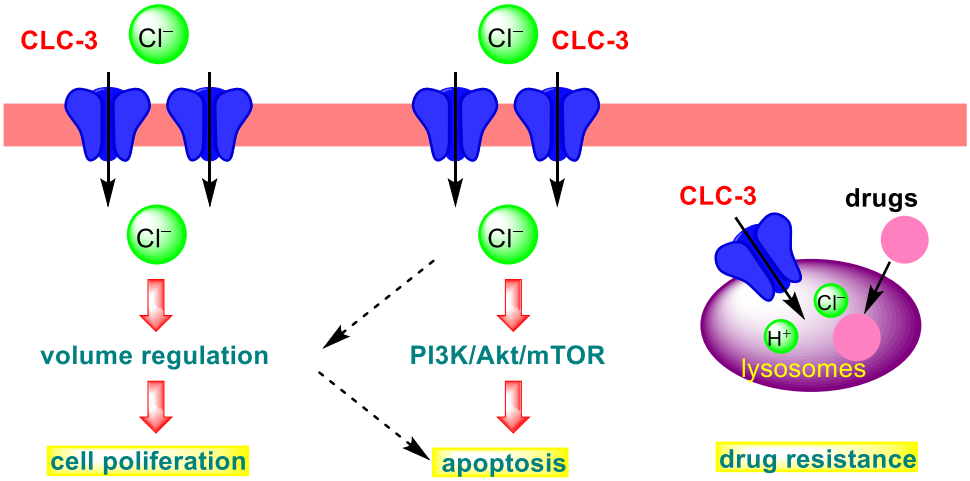

Figure 1.5 Schematic representation of the effect of CLC-3 channel dysfunction in cancer cells.

1.5 Natural ion transport systems

As stated above, for the maintenance of healthy biological processes ion carriers play a central role in the biological system. Natural ion carriers are molecules that transport ions either through the formation of a static hydrophilic pathway or shuttling between intracellular and extracellular regions of the cell membrane.

Prodigiosin (PG) is a naturally occurring tripyrrollic bioactive red pigment mainly produced by *Serratia marcescens* strains and other microorganisms, that transports Cl^- ions across cell

membranes and shows anticancer, antimicrobial, antiparasitic, immunomodulatory and insecticidal activities. It acts as an effective proapoptotic agent against multiple cancer cell lines causing low or no toxicity toward normal cell lines due to disruption of pH gradient through transmembrane transport of H^+ and Cl^- ions. Tambjamines are another group of naturally occurring ion carriers which resemble structurally prodigiosin having two pyrrole moieties instead of three pyrrole groups.[7] Valinomycin is a naturally occurring neutral macro-cyclic ionophore having twelve alternative esters and amino acid forms a binding pocket for potassium ions.[8] Gramicidin A is a hydrophobic linear peptide form beta-helix nanopore by the self-assembly of two identical helical peptides in biological membranes permeable to water and specific monovalent cations and acts as an antibiotic agent.[9, 10] Alpha hemolysin is a pore-forming heptamer complex secreted by *Staphylococcus aureus bacteria* which transport water, ions and small molecules. KcsA (K^+ channel of streptomyces A) is an inverted cone-shaped tetrameric potassium selective channel which opens at acidic pH and is inactivated by voltage gating.[11] Amphotericin B is a polyene class of antifungal agents which form channels after binding with ergosterol causing loss of monovalent cations (specially K^+) that results in fungal cell death due to depolarization.[12, 13]

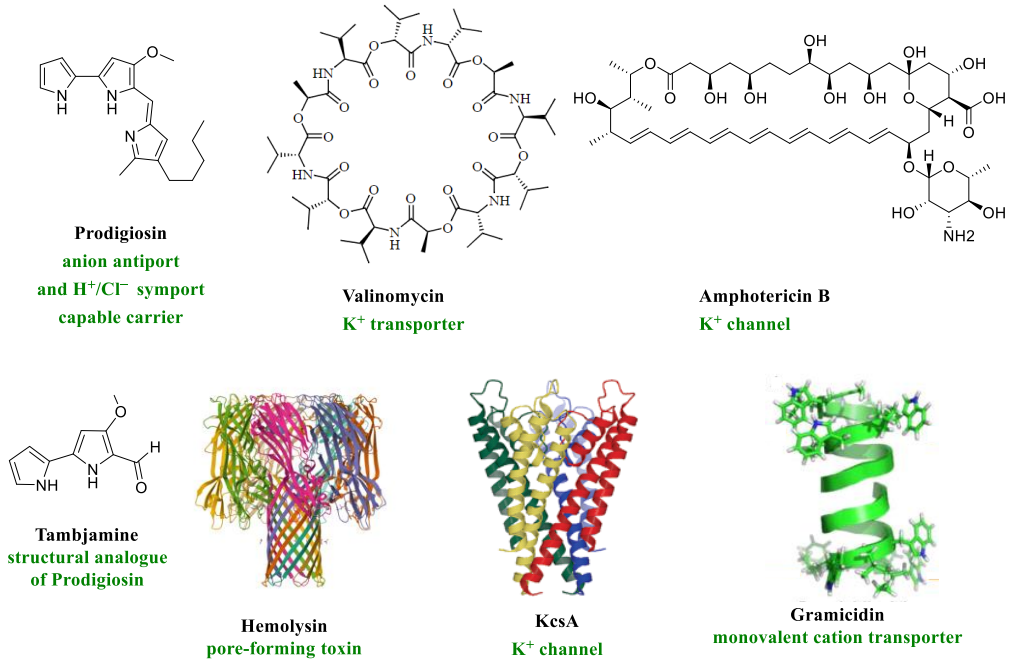

Figure 1.6 Structure of naturally occurring ion channels and ion carriers.

1.6 Artificial ion carriers

The importance of the diverse functions of natural ion carriers inspired scientists to mimic natural ion transport systems and achieve a better understanding of supramolecular chemistry. This motivation allows a supramolecular chemist to do interdisciplinary research in the science world. The natural motif of ion carriers is very complicated machinery so designing a system which can mimic the function of a natural organization is a very challenging job, excessive evolution has been made in the artificial ion transport field and the progress continues. The inspiration comes from valinomycin, a natural K^+ carrier and prodigiosin, a natural Cl^- carrier as well as H^+/Cl^- symporter. In recent years ion recognition and ion transport fields have been exploited by the development of several small molecules and various strategies established for the design of artificial ion carriers. The principles of design of an artificial ion carrier are:

1. It should have a hydrophobic part so that it can embedded in the lipophilic part of the cell membrane.
2. It should have a hydrophilic part with multiple ion binding sites for efficient ion binding.
3. It should have a rigid motif for better binding to ions.
4. It should be suitably soluble in water for better delivery.
5. According to Lipinski's rule, it should possess a log P value of ~ 5.

Using the above design principles several synthetic ion carriers have been reported in the literature. The examples include squaramides (**1**),[14-17] trans-decalin (**2**),[18, 19] thiourea (**3**),[19, 20] cholapod-based carriers (**4**),[21-23] tripodal anion carriers (**5**),[20, 24, 25] calix[4]pyrrole (**6**)[26-28] etc. In this examples hydrogen bonding is used as an ion recognition force for ion transport purposes. In literature anion-π interaction (**8**)[29, 30] and dipole anion interaction[30-32] also elaborated for the transmembrane ion transport. The derivatives of naturally occurring prodigiosin are also reported in the literature (**7**).[33, 34] Recently, Matile and co-workers extended the anion binding interaction with halogen bond (**9**),[30] chalcogen bond (**10**)[35] and pnictogen bond (**11**).[36]

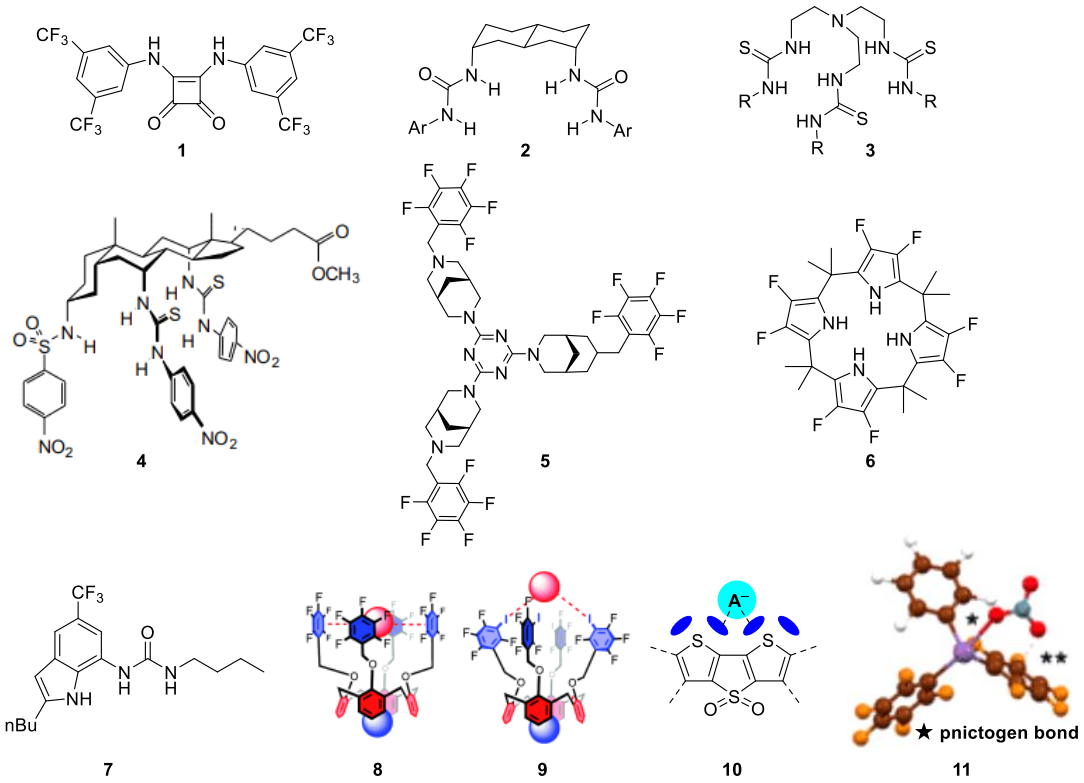

Figure 1.7 Examples of synthetic ion carriers based on various rigid scaffolds and ion binding motifs.

1.7 Artificial ion transport systems in view of next-generation therapeutics

1.7.1 Synthetic ion carriers and channelopathies

In the last few decades, tremendous progress has been made in supramolecular research for the application of natural ion carriers. They are widely used in biotechnology and nanotechnology for sensing, catalysis, fluidic diode and porous material.[37-39] The applicative study of synthetic ion carriers also extended to the life-threatening diseases i.e., channelopathies caused by defective natural ion channels. They have the potential as 'channel replacement therapy'. Davis and co-workers designed a simple, low-molecular-weight trimeric synthetic carrier Tris-(*N*-butyl-2-phenoxyacetamide), which maintains a transmembrane potential due to its ability to transport Cl^- and has prospective application as a therapeutic agent for channelopathies.[40] Tomich and co-workers reported channel channel-forming peptides, are responsible for the restoration of Cl^- transport in cystic fibrosis. These peptides interact with the apical surface of cystic fibrosis airway tissue and promote Cl^- secretion and surface hydration, acting as a treatment modality for the disease.[41] Recently, Broke and co-workers reported amphotericin B for the potential treatment of cystic fibrosis. Amphotericin B forms a non-selective ion channel

in the cystic fibrosis cells from a patient and with the help of an independent CFTR mechanism it restored host defences in cystic fibrosis airway epithelia and thus it acts as independent of genotype.[42] Gokel and co-workers reported crown ether-based unimolecular hydrophilic channel as an antibiotic agent.[43, 44] Few crown ether-based cationic channels reported by Voyer and Leevy causes cancer cell death via necrotic pathway.[45, 46] Therefore, based on results obtained in cell models, synthetic ion transporters hypothesised that these are the prospective agents for the channelopathies.

1.7.2 Synthetic ion carriers and cancer

The application of synthetic ion carriers is also elaborated as an anticancer agent. The naturally occurring prodigiosin[33] is the best Cl^- carrier which transports Cl^- either H^+/Cl^- symport mechanism or the Cl^-/anion antiport mechanism.[47] Prodigiosin and its analogues act as anticancer agents by either changing pH or disrupting ion homeostasis of cells.[48-50] Likewise, tambjamine derivatives also showed potential cytotoxicity in cancerous cells.[34, 51] Synthetic ion carriers such as urea/amide,[52, 53] thiourea[19] and bis-sulfonamides[54] also showed potential anticancer activities. Similarly, vicinal diol[55] destroys ion homeostasis by the formation of a chloride ion selective channel that also acts as an anticancer agent. However, the mechanism of apoptotic cancer cell death induced by transmembrane ion carriers was described by Shin and co-workers.[56] They have reported calix[4]pyrrole molecule as an anticancer agent, which shows activation of the caspase-dependent pathway was effective during apoptosis induction.

In classical anticancer chemotherapy, the drugs target specific genes or proteins/enzymes found in cancer cells to trigger apoptosis induction and related cell death networks to eliminate malignant cells.[57, 58] However, the activation of different anti-apoptotic pathways,[59] mutations in the drug targets that prevent the binding of the drug,[60, 61] and over-expression of proteins that compensate for the loss of the drug target[62] are known to cause tumour survival, therapeutic resistance, and recurrence of cancer. Synthetic ion carriers function in the lipid membrane, unlike binding to any specific genes or proteins/enzymes, and perturb the intracellular chloride ion concentration to kill the cells. Therefore, in principle, synthetic chloride carriers can overcome the resistance related to the mutations and over-expression of genes and proteins. Even though these synthetic molecules show anticancer activity, they cannot differentiate between healthy cells and cancerous cells. They kill cancerous cells as well as healthy cells, which is not good from a biological perceptive. Therefore, designing a system which only

works in the cancerous environment without touching healthy cells is a big challenge for supramolecular chemists. Hence, addressing the issue of selectivity for the cancer cell is an emerging topic in the realm of the biochemical field.

1.8 Future direction in view of cancer treatment by synthetic carriers systems

Herein, we have proposed the design of the stimuli-triggered procarrier molecules which on treatment with stimuli can be selectively converted into active carriers and thus the selective target of cancer cells can be achieved.

Therefore, we are interested in designing small-molecule ion carriers, which are initially connected to stimuli-responsive protecting groups so that the ion binding ability of the receptor is blocked (Figure 1.8). If the protecting group is removed by an external stimulus, the ion-binding ability can be retained. The generated receptor can function as a transmembrane ion carrier. Different external stimuli such as light (photocleavable protecting groups)[63], enzymes (for enzyme cleavable protecting groups)[64, 65], pH (for pH cleavable protecting groups)[66-69], etc. would be used for this purpose.

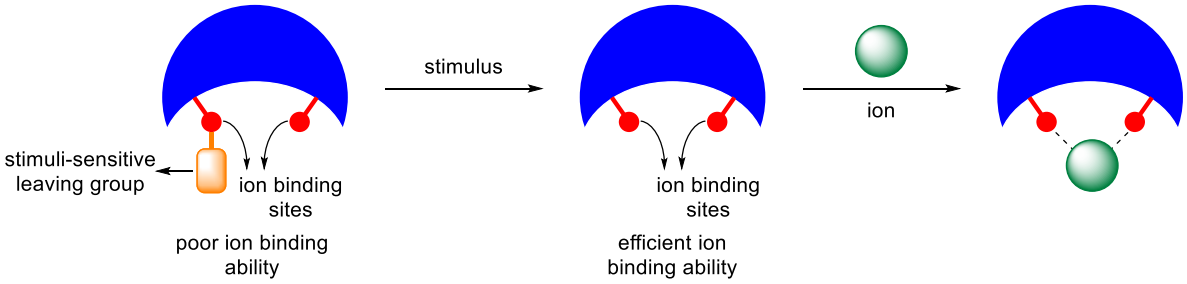

Figure 1.8 Representative activation of ion carrier by external stimulus.

1.9 Techniques Used in Ion Transport Studies

To study the ion transport properties of synthetic ion carriers, natural cell membrane mimics i.e., vesicles were prepared from commercially available egg yolk phosphatidylcholine (EYPC) as a solution of chloroform (25 mg/ mL). A brief description of various techniques used to check ion transport properties is discussed here.

Ion transport studies across spherical lipid bilayer:

The large unilamellar vesicles (LUVs) are prepared by standard freeze and thaw method after complete evaporation of chloroform of commercially available chloroform solution of egg yolk phosphatidylcholine (EYPC) under vacuum. The vesicles of desired size are formed when extruded through polycarbonate membrane filters. Finally, the vesicles are separated from an unentrapped dye by size exclusion chromatography over Sephadex-G50 using an adequate buffer. To study ion transport properties of prepared liposomal membrane various analytical techniques are used such as fluorescence, ion selective electrode and NMR study.

Fluorescence assay: To study ion transport property by fluorescence techniques large unilamellar vesicles (LUVs) are prepared by encapsulation of fluorescent dye 8-hydroxypyrene-1,3,6- trisulfonate (HPTS, λ_{ex} = 450 nm and λ_{em} = 510 nm), a pH sensitive dye.[70] A pH gradient (pH_{in} = 7.0, pH_{out} = 7.8) is applied by the addition of NaOH (0.5 M) in extravesicular media, and then a compound is added. The fluorescence of HPTS was monitored with time,[71, 72] if there is an influx of OH^- or efflux of H^+ through a synthetic ion carrier, an increase in fluorescence of HPTS will be observed due to an increase in intracellular pH. The more the enhancement of emission intensity at λ_{em} = 510 nm, the better will be the ion transport ability of the synthetic ion carrier. Similarly, the chloride transport property of an artificial ion agent is investigated by entrapping lucigenin (bis-*N*-methylacridinium nitrate) dye (λ_{ex} = 455 nm and λ_{em} = 535 nm) in the vesicles. Lucigenin is a halide-sensitive dye whose fluorescence quenches in the presence of chloride.[73] Likewise, using a known protocol other fluorescent dyes Carboxyfluorescein (CF), ANTS-DPX and calcein can be used to investigate ion transport properties. The formation of channel or pore (diameter more than 10 nm) by the synthetic carrier can be identified by Carboxyfluorescein (CF)[74] and ANTS (8-aminonaphthalene-1,3,6-trisulfonic acid, disodium salt)-DPX (*p*-xylene-bis-pyridinium bromide) dye.[75] These dyes are also useful to study the effect of the integrity of the vesicle upon the addition of a compound. Calcein dye can be used to detect membrane leakage of vesicles.[76]

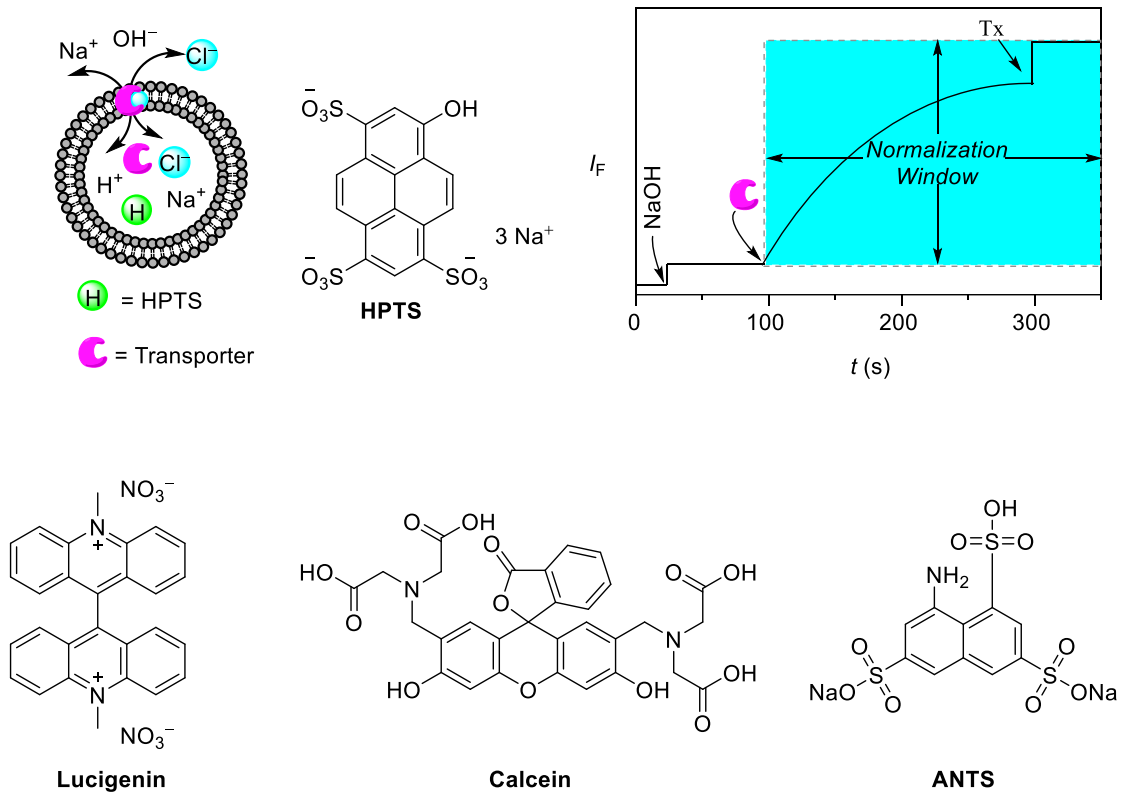

Figure 1.9 Representation of fluorescence-based ion transport assay using vesicles and the structure of fluorescent dyes used in ion transport assay.

Ion-selective electrode: The outflow of the respective ion encapsulated in the liposomal membrane is measured by recording the change in conductivity of the solution using ion ion-selective electrode. To record the Cl^- ion transport property of the carrier, a chloride selective electrode was suspended in $NaNO_3$ solution with a vesicle entrapped with NaCl. Upon addition of compound, the degree of the outside flow of Cl^- is observed via recording variation of conductivity of Cl^- selective electrode.

NMR studies: To check ion transport property by NMR spectroscopy the ions of interest should be NMR active (^{35}Cl, $H^{13}CO_3^-$, $^{33}SO_4^-$ etc.). The large unilamellar vesicles (LUVs) are prepared by entrapping NaA (where A is NMR active anion) with an extravesicular buffer of NMR inactive anion along with paramagnetic shift reagent Mn^{2+}. The peaks corresponding to intra and extravesicular anions show changes, either broadening of peaks or upfield-downfield changes in chemical shift value. Hence such enhancement of chemical shift value or broadening of corresponding peaks can be monitored in NMR studies to study ion transport properties of synthetic transport agents.

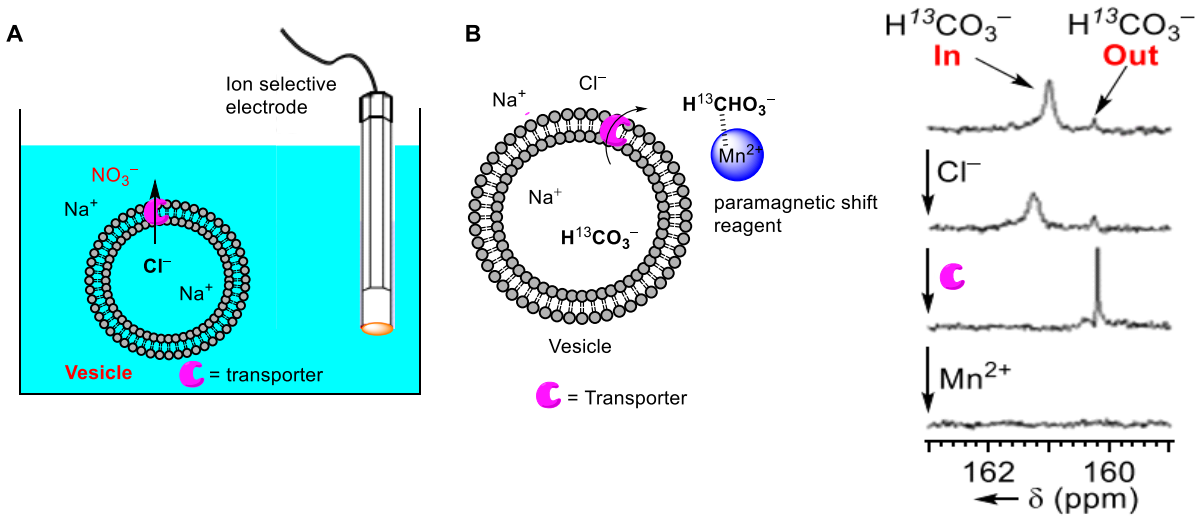

Figure 1.10 Schematic representation of ion transport study using ion selective electrode (**A**) and NMR spectroscopy (**B**).

1.10 References

1. V. Lehen'kyi, G. Shapovalov, R. Skryma and N. Prevarskaya, *Am. J. of physiol. Cell Physiol.*, 2011, **301**, C1281-1289.
2. J. Mao, L. Chen, B. Xu, L. Wang, W. Wang, M. Li, M. Zheng, H. Li, J. Guo, W. Li, T. J. C. Jacob and L. Wang, *Biochem. Pharmacol.*, 2009, **77**, 159-168.
3. B. Nilius, J. Eggermont, T. Voets and G. Droogmans, *Gen. Pharmacol.*, 1996, **27**, 1131-1140.
4. S. Hong, M. Bi, L. Wang, Z. Kang, L. Ling and C. Zhao, *Oncol. Rep.*, 2015, **33**, 507-514.
5. R. Mohammad-Panah, R. Harrison, S. Dhani, C. Ackerley, L. J. Huan, Y. Wang and C. E. Bear, *J. Biol. Chem.*, 2003, **278**, 29267-29277.
6. A. J. Smith and J. D. Lippiat, *J. Physiol.*, 2010, **588**, 2033-2045.
7. R. Herráez, R. Quesada, N. Dahdah, M. Viñas and T. Vinuesa, *Pharmaceutics*, 2021, **13**.
8. G. Stark, B. Ketterer, R. Benz and P. Läuger, *Biophys. J.*, 1971, **11**, 981-994.
9. J. M. David and A. K. Rajasekaran, *Journal of kidney cancer and VHL*, 2015, **2**, 15-24.
10. B. Roux and M. Karplus, *Biophys. J.*, 1991, **59**, 961-981.

11. D. A. Doyle, J. Morais Cabral, R. A. Pfuetzner, A. Kuo, J. M. Gulbis, S. L. Cohen, B. T. Chait and R. MacKinnon, *Science (New York, N.Y.)*, 1998, **280**, 69-77.
12. G. Fujii, J. E. Chang, T. Coley and B. Steere, *Biochem.*, 1997, **36**, 4959-4968.
13. N. Matsumori, N. Yamaji, S. Matsuoka, T. Oishi and M. Murata, *J. Am. Chem. Soc.*, 2002, **124**, 4180-4181.
14. S. J. Edwards, H. Valkenier, N. Busschaert, P. A. Gale and A. P. Davis, *Angew. Chem. Int. Ed.*, 2015, **54**, 4592-4596.
15. N. Busschaert, I. L. Kirby, S. Young, S. J. Coles, P. N. Horton, M. E. Light and P. A. Gale, *Angew. Chem. Int. Ed.*, 2012, **51**, 4426-4430.
16. X. Bao, X. Wu, S. N. Berry, E. N. W. Howe, Y.-T. Chang and P. A. Gale, *Chem. Commun.*, 2018, **54**, 1363-1366.
17. D. Mondal, A. Sathyan, S. V. Shinde, K. K. Mishra and P. Talukdar, *Org. Biomol. Chem.*, 2018, **16**, 8690-8694.
18. S. Hussain, P. R. Brotherhood, L. W. Judd and A. P. Davis, *J. Am. Chem. Soc.*, 2011, **133**, 1614-1617.
19. H. Valkenier, L. W. Judd, H. Li, S. Hussain, D. N. Sheppard and A. P. Davis, *J. Am. Chem. Soc.*, 2014, **136**, 12507-12512.
20. N. Busschaert, P. A. Gale, C. J. E. Haynes, M. E. Light, S. J. Moore, C. C. Tong, J. T. Davis and J. W. A. Harrell, *Chem. Commun.*, 2010, **46**, 6252-6254.
21. J. P. Clare, A. J. Ayling, J.-B. Joos, A. L. Sisson, G. Magro, M. N. Pérez-Payán, T. N. Lambert, R. Shukla, B. D. Smith and A. P. Davis, *J. Am. Chem. Soc.*, 2005, **127**, 10739-10746.
22. A. P. Davis, *Coord. Chem. Rev*, 2006, **250**, 2939-2951.
23. B. A. McNally, A. V. Koulov, T. N. Lambert, B. D. Smith, J.-B. Joos, A. L. Sisson, J. P. Clare, V. Sgarlata, L. W. Judd, G. Magro and A. P. Davis, *Chem. Eur. J.*, 2008, **14**, 9599-9606.
24. D. Mondal, A. Sathyan, S. V. Shinde, K. K. Mishra and P. Talukdar, *Org. Biomol. Chem*, 2018, **16**, 8690-8694.
25. A. Roy, D. Saha, P. S. Mandal, A. Mukherjee and P. Talukdar, *Chem. Eur. J*, 2017, **23**, 1241-1247.
26. C. C. Tong, R. Quesada, J. L. Sessler and P. A. Gale, *Chem. Commun.*, 2008, 6321-6323.
27. P. A. Gale, C. C. Tong, C. J. E. Haynes, O. Adeosun, D. E. Gross, E. Karnas, E. M. Sedenberg, R. Quesada and J. L. Sessler, *J. Am. Chem. Soc.*, 2010, **132**, 3240-3241.

28. M. G. Fisher, P. A. Gale, J. R. Hiscock, M. B. Hursthouse, M. E. Light, F. P. Schmidtchen and C. C. Tong, *Chem. Commun.*, 2009, 3017-3019.
29. N.-T. Lin, A. Vargas Jentzsch, L. Guénée, J.-M. Neudörfl, S. Aziz, A. Berkessel, E. Orentas, N. Sakai and S. Matile, *Chem. Sci.*, 2012, **3**, 1121-1127.
30. A. Vargas Jentzsch, D. Emery, J. Mareda, P. Metrangolo, G. Resnati and S. Matile, *Angew. Chem. Int. Ed.*, 2011, **50**, 11675-11678.
31. J. Shang, W. Si, W. Zhao, Y. Che, J.-L. Hou and H. Jiang, *Org. Lett.*, 2014, **16**, 4008-4011.
32. M. Lisbjerg, H. Valkenier, B. M. Jessen, H. Al-Kerdi, A. P. Davis and M. Pittelkow, *J. Am. Chem. Soc.*, 2015, **137**, 4948-4951.
33. A. Fürstner, *Angew. Chem. Int. Ed.*, 2003, **42**, 3582-3603.
34. V. Soto-Cerrato, P. Manuel-Manresa, E. Hernando, S. Calabuig-Fariñas, A. Martínez-Romero, V. Fernández-Dueñas, K. Sahlholm, T. Knöpfel, M. García-Valverde, A. M. Rodilla, E. Jantus-Lewintre, R. Farràs, F. Ciruela, R. Pérez-Tomás and R. Quesada, *J. Am. Chem. Soc.*, 2015, **137**, 15892-15898.
35. S. Benz, M. Macchione, Q. Verolet, J. Mareda, N. Sakai and S. Matile, *J. Am. Chem. Soc.*, 2016, **138**, 9093-9096.
36. L. M. Lee, M. Tsemperouli, A. I. Poblador-Bahamonde, S. Benz, N. Sakai, K. Sugihara and S. Matile, *J. Am. Chem. Soc.*, 2019, **141**, 810-814.
37. D. Wang, L. Guo, J. Zhang, L. R. Jones, Z. Chen, C. Pritchard and R. W. Roeske, *The journal of peptide research : official journal of the American Peptide Society*, 2001, **57**, 301-306.
38. L. Steller, M. Kreir and R. Salzer, *Anal. Bioanal. Chem.*, 2012, **402**, 209-230.
39. S. Blake, R. Capone, M. Mayer and J. Yang, *Bioconjug. Chem.* . 2008, **19**, 1614-1624.
40. V. Sidorov, F. W. Kotch, J. L. Kuebler, Y.-F. Lam and J. T. Davis, *J. Am. Chem. Soc.*, 2003, **125**, 2840-2841.
41. J. R. Broughman, L. P. Shank, W. Takeguchi, B. D. Schultz, T. Iwamoto, K. E. Mitchell and J. M. Tomich, *Biochemistry*, 2002, **41**, 7350-7358.
42. K. A. Muraglia, R. S. Chorghade, B. R. Kim, X. X. Tang, V. S. Shah, A. S. Grillo, P. N. Daniels, A. G. Cioffi, P. H. Karp, L. Zhu, M. J. Welsh and M. D. Burke, *Nature*, 2019, **567**, 405-408.
43. W. M. Leevy, G. M. Donato, R. Ferdani, W. E. Goldman, P. H. Schlesinger and G. W. Gokel, *J. Am. Chem. Soc.*, 2002, **124**, 9022-9023.

44. W. M. Leevy, M. R. Gokel, G. B. Hughes-Strange, P. H. Schlesinger and G. W. Gokel, *New J. Chem.*, 2005, **29**, 205-209.
45. P.-L. Boudreault, M. Arseneault, F. Otis and N. Voyer, *Chem. Commun.*, 2008, 2118-2120.
46. B. A. Smith, M. M. Daschbach, S. T. Gammon, S. Xiao, S. E. Chapman, C. Hudson, M. Suckow, D. Piwnica-Worms, G. W. Gokel and W. M. Leevy, *Chem. Commun.*, 2011, **47**, 7977-7979.
47. J. L. Seganish and J. T. Davis, *Chem. Commun.*, 2005, 5781-5783.
48. J. L. Sessler, L. R. Eller, W. S. Cho, S. Nicolaou, A. Aguilar, J. T. Lee, V. M. Lynch and D. J. Magda, *Angew. Chem. Int. Ed.*, 2005, **44**, 5989-5992.
49. E. Marchal, S. Rastogi, A. Thompson and J. T. Davis, *Org. Biomol. Chem*, 2014, **12**, 7515-7522.
50. S. Cheung, D. Wu, H. C. Daly, N. Busschaert, M. Morgunova, J. C. Simpson, D. Scholz, P. A. Gale and D. F. O'Shea, *Chem*, 2018, **4**, 879-895.
51. E. Hernando, V. Soto-Cerrato, S. Cortés-Arroyo, R. Pérez-Tomás and R. Quesada, *Org. Biomol. Chem.*, 2014, **12**, 1771-1778.
52. J. H. Lee, J. H. Lee, Y. R. Choi, P. Kang, M.-G. Choi and K.-S. Jeong, *Org. Biomol. Chem.*, 2014, **79**, 6403-6409.
53. S. K. Ko, S. K. Kim, A. Share, V. M. Lynch, J. Park, W. Namkung, W. Van Rossom, N. Busschaert, P. A. Gale, J. L. Sessler and I. Shin, *Nat. Chem.*, 2014, **6**, 885-892.
54. T. Saha, M. S. Hossain, D. Saha, M. Lahiri and P. Talukdar, *J. Am. Chem. Soc.*, 2016, **138**, 7558-7567.
55. T. Saha, A. Gautam, A. Mukherjee, M. Lahiri and P. Talukdar, *J. Am. Chem. Soc.*, 2016, **138**, 16443-16451.
56. S.-K. Ko, S. K. Kim, A. Share, V. M. Lynch, J. Park, W. Namkung, W. Van Rossom, N. Busschaert, P. A. Gale, J. L. Sessler and I. Shin, *Nat. Chem.*, 2014, **6**, 885-892.
57. L. H. Pinto, G. R. Dieckmann, C. S. Gandhi, C. G. Papworth, J. Braman, M. A. Shaughnessy, J. D. Lear, R. A. Lamb and W. F. DeGrado, *Proc. Natl. Acad. Sci.*, 1997, **94**, 11301-11306.
58. F. Lang, M. Föller, K. S. Lang, P. A. Lang, M. Ritter, E. Gulbins, A. Vereninov and S. M. Huber, *J. Membr. Biol.*, 2005, **205**, 147-157.
59. W. R. Sellers and D. E. Fisher, *J Clin Invest*, 1999, **104**, 1655-1661.
60. J. M. Brown and L. D. Attardi, *Nat. Rev. Cancer*, 2005, **5**, 231.

61. L. Portt, G. Norman, C. Clapp, M. Greenwood and M. T. Greenwood, *Biochim. Biophys. Acta*, 2011, **1813**, 238-259.
62. R. S. Y. Wong, *J. Exp. Clin. Cancer Res.*, 2011, **30**, 87.
63. Y. R. Choi, G. C. Kim, H.-G. Jeon, J. Park, W. Namkung and K.-S. Jeong, *Chem. Commun.*, 2014, **50**, 15305-15308.
64. Y. R. Choi, B. Lee, J. Park, W. Namkung and K.-S. Jeong, *J. Am. Chem. Soc.*, 2016, **138**, 15319-15322.
65. E. B. Park and K.-S. Jeong, *Chem. Commun.*, 2015, **51**, 9197-9200.
66. E. N. W. Howe, N. Busschaert, X. Wu, S. N. Berry, J. Ho, M. E. Light, D. D. Czech, H. A. Klein, J. A. Kitchen and P. A. Gale, *J. Am. Chem. Soc.*, 2016, **138**, 8301-8308.
67. N. Busschaert, R. B. P. Elmes, D. D. Czech, X. Wu, I. L. Kirby, E. M. Peck, K. D. Hendzel, S. K. Shaw, B. Chan, B. D. Smith, K. A. Jolliffe and P. A. Gale, *Chem. Sci.*, 2014, **5**, 3617-3626.
68. A. Roy, O. Biswas and P. Talukdar, *Chem. Commun.*, 2017, **53**, 3122-3125.
69. S. V. Shinde and P. Talukdar, *Angew. Chem. Int. Ed.*, 2017, **56**, 4238-4242.
70. K. Kano and J. H. Fendler, *Biochimica et biophysica acta*, 1978, **509**, 289-299.
71. S. Matile and N. Sakai, in *Analytical Methods in Supramolecular Chemistry*, 2006, pp. 391-418.
72. A. M. Gilchrist, P. Wang, I. Carreira-Barral, D. Alonso-Carrillo, X. Wu, R. Quesada and P. A. Gale, *Supramol. Chem.*, 2021, **33**, 325-344.
73. K. D. Legg and D. M. Hercules, *J. Phys. Chem.*, 1970, **74**, 2114-2118.
74. H. Pan, J. N. Marsh, E. T. Christenson, N. R. Soman, O. Ivashyna, G. M. Lanza, P. H. Schlesinger and S. A. Wickline, in *Methods in Enzymology*, ed. N. Düzgüneş, Academic Press, 2012, vol. 508, pp. 17-39.
75. W. C. Wimley, *Methods in molecular biology (Clifton, N.J.)*, 2015, **1324**, 89-106.
76. H. Patel, C. Tscheka and H. Heerklotz, *J. Soft Matter*, 2009, **5**, 2849-2851.

Chapter 2

Cyclic oligosaccharide-based anion carriers

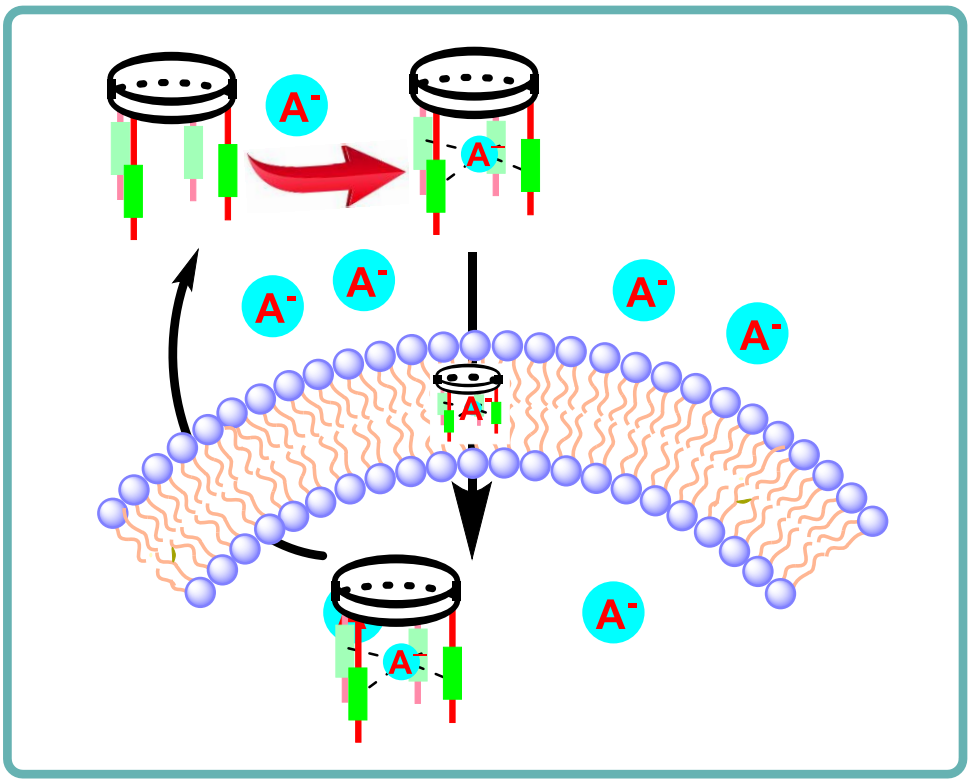

2.1 Introduction

Carbohydrates have been utilized extensively in the design of anion receptors. Fernández and coworkers have applied the bis(β-D-glucopyranosyl)thiourea for carboxylate anion recognition (Figure 2.1A)[1] and reported the use of trehalose-based cyclodextrin analogs (Cyclotrehalans), for benzoate, naphthalene sulfonate, and adamantane carboxylate anion binding in water.[2, 3] Xie and coworkers have reported carbohydrate-based BODIPY-functionalized fluorescent macrocycles for sensing F^- and CN^- (Figure 2.1B).[4] Tecilla and coworkers have reported cyclic phosphate-linked oligosaccharide (CyPLOS) macrocycles as the receptors for alkali metal cations and anions such as halides (except fluoride), nitrate, and perchlorate (Figure 2.1C).[5]

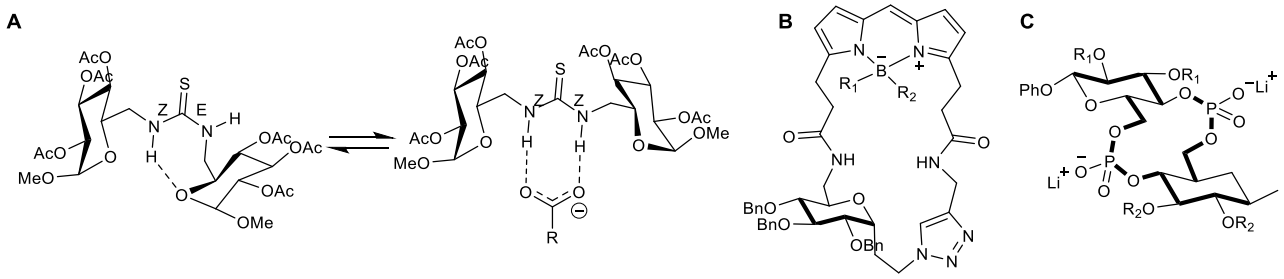

Figure 2.1 The conformational behaviour and binding properties of sugar thiourea receptors in chloroform solution (**A**). Carbohydrate-based BODIPY-functionalised fluorescent macrocycles (**B**). Cyclic phosphate-linked oligosaccharides (CyPLOS) macrocycles (**C**).

The application of sugar-derived systems in the ion transport field has been less explored. Dhavale and coworkers have studied the self-assembled ion channel formation by acyclic αγα-tripeptides with fluorinated-furanoid sugar (Figure 2.2A).[6] They have further studied the anion transport by fluorinated sugar amino acid derived α,γ-cyclic peptides.[7] The designs of sugar-based ion channels are mainly centred around cyclodextrins (CDs). The common design strategies employed include the connection of membrane-spanning linkers to the CDs to achieve either cation or anion selectivity of the channels. Tabushi and co-workers reported the A,C,D,F,-tetra-6-(6-n-butyrylamino-n-hexylsulfenyl)-β-CD as a half-channel dimer that displayed cation transport across lipid membranes.[8] Fyles and Chui reported triazole-linked β-CD derivatives as half-channel dimers for forming dimeric cation channels.[9, 10] The per-(2,3-di-O-heptyl)-6-methoxyPEG-6-(1,2,3-triazole)-β-CDs (PEG = polyethylene glycol) were also developed for their pH-dependent aggregation channel formation in the lipid membranes.[11] Gin and coworkers reported a β-cyclodextrin-based monomolecular ion channel that transports both

anions and cations.[12, 13] Moreover, the anion selectivity of the channel was mostly towards iodide.

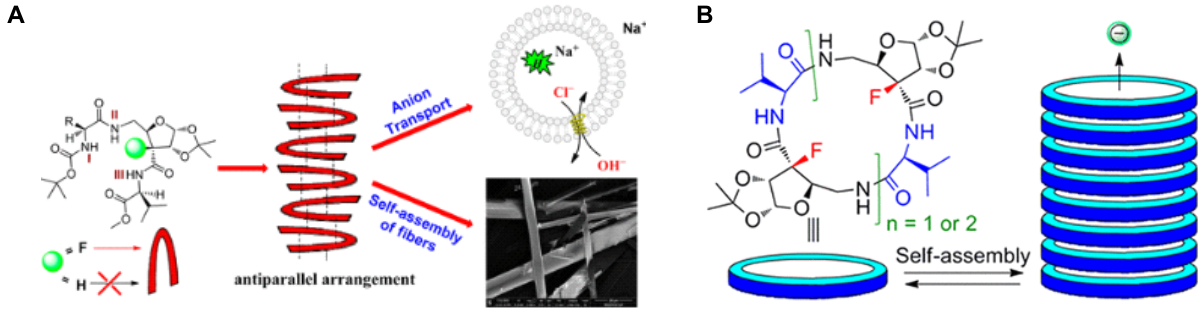

Figure 2.2 Acyclic fluorinated furanoid sugar-based self-assemble ion channel (**A**) Reprinted with permission from (*J. Org. Chem.*, 2017, **82**, 5826-5834) copyright 2017 American Chemical Society. Fluorinated sugar amino acid derived cyclic peptide form a supramolecular channel across lipid membrane (**B**) Reprinted with permission from (*Org. Lett.*, 2017, **19**, 5948-5951) copyright 2017 American Chemical Society.

The large hydrophobic cavity of β-cyclodextrin can be utilized for the recognition of hydrophobic anions. To address the challenge of selective chloride recognition by sugar-based macrocycles, we noted the importance of oligo-(1→6)-β-D-glucosamine-based derivatives which were reported to exhibit polar cavities.[14] This system is also amenable to the ring-size variation based on the intramolecular glycosylation of thioglycoside precursors. The rigidity of such macrocycles retained up to tetra-(1→6)-β-D-glucosamine and higher oligomers were flexible. Our group took advantage of such oligo-(1→6)-β-D-glucosamines, and reported cyclo-Oligo-(1→6)-β-D-glucosamine-based artificial ion transport systems to achieve trimodal control of anion transport activity tuneable pore diameter and varied tail length (Figure 2.3A).[15-17] The selectivity study with these systems confirmed better transport of chloride compared to bromide and iodide.

In collaboration with Dr. Yuri Tsvetkov of the N. D. Zelinsky Institute of Organic Chemistry, Moscow, we proposed new macrocycles with amino groups at axial positions on hexose sugars *e.g.* allose or galactose with axial $–NH_2$ at C-3 or C-4, respectively (Figure 2.3B – 2.3C). The chloride recognition within a cyclic oligosaccharide can be improved if the tails connected to the axial amino groups also contribute to the anion recognition. Therefore, we proposed the

design of cyclic oligosaccharides with anion binding axial tails. During the transport process, this class of molecules would act as mobile carriers of anions.

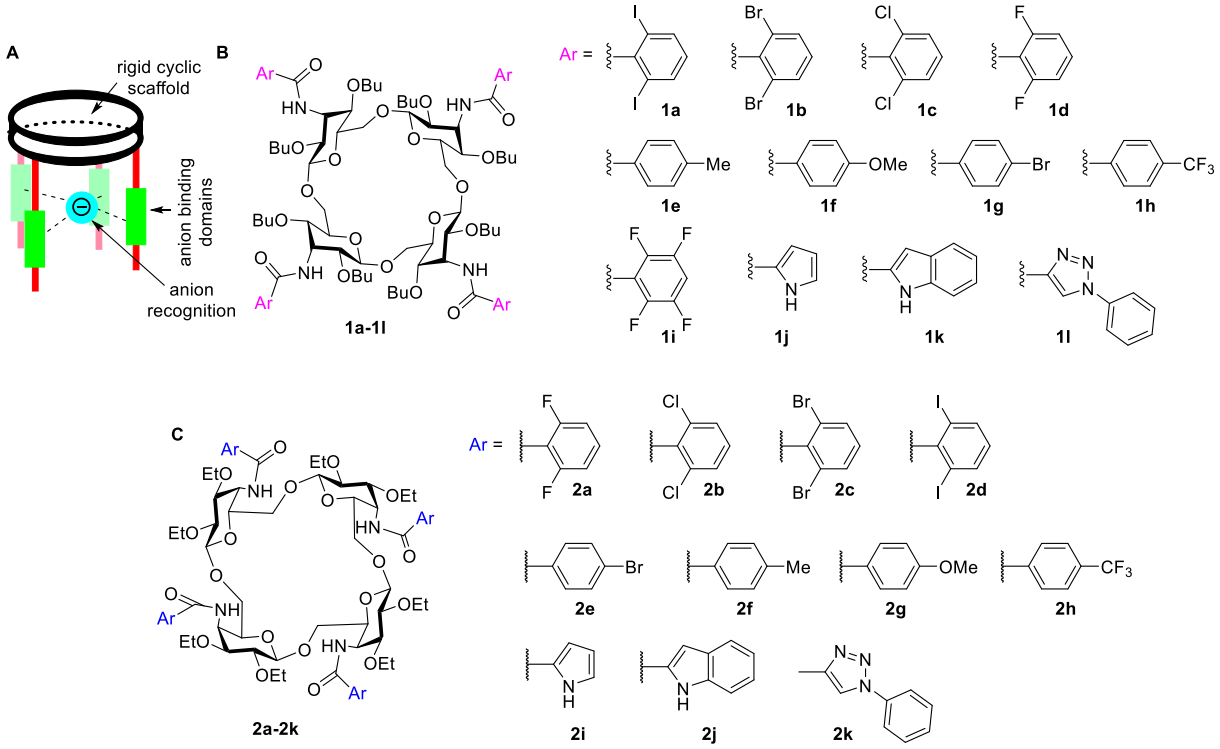

Figure 2.3 Proposed model of cyclic oligosaccharide-based artificial ion carriers (**A**). Structure of ion carriers based on the cyclic tetramer of 3-amino-3-deoxyallose (**B**) and 4-amino-4-deoxygalactose (**C**).

2.2 Results and Discussion

2.2.1 Synthesis

The 3-amino-3-deoxyallose and 4-amino-4-deoxygalactose-based cyclic carriers were provided by Dr. Yuri Tsvetkov, N. D. Zelinsky Institute of Organic Chemistry, Moscow.

2.2.2 Ion transport studies

The ion transport ability of compounds **1a** – **1l** and **2a** – **2k** were examined across large unilamellar vesicles (LUVs), of 100 nm diameter average size, prepared using EYPC (L-α-Phosphatidylcholine from egg yolk) lipid that acts as a model system of natural cell membrane for the ion transport studies. The pH-sensitive 8-hydroxypyrene-1,3,6- trisulfonate (HPTS) dye, whose fluorescence intensity λ_{em} = 510 nm (λ_{ex} = 450 nm) increases with an increase in

pH, was entrapped inside the LUVs (EYPC-LUVs⊃HPTS).[18] A pH gradient of 0.8 (pH_{in} = 7.0, pH_{out} = 7.8) was applied by the addition of 0.5 M NaOH, and upon addition of the carrier molecule, the ion transport process induced collapse of this gradient was measured by monitoring the fluorescence intensity of HPTS dye with time.[19-21] In the absence of a carrier, no change in fluorescence intensity was expected as there was no enhancement of intravesicular pH. Finally, the complete dissipation of the pH gradient was achieved by lysing the vesicle upon the addition of the surfactant Triton X-100.

The ion transport activity sequence for 3-amino-3-deoxyallose system compounds **1a** – **1l** was obtained as shown in Figure 2.4A. Among the derivatives, only **1j** and **1k** showed significant activity while all other compounds precipitated at higher concentrations (Figure 2.4A). For 4-amino-4-deoxygalactose systems, **2e**, **2f**, **2h**, **2i**, and **2j** exhibited good transport activity compared to others (Figure 2.4B). Hill coefficients (*n*, indicates the involvement of a number of molecules in active carrier formation) and EC_{50} values (effective concentration at 50% transport activity) were calculated using the Hill equation by performing dose-dependent ion transport activity. The dose-responsive studies were carried out only for most active carriers i.e., **1j**, **1k**, **2e**, **2f**, **2h**, **2i** and **2j**. Using Hill analysis, EC_{50} values were determined to be 1.55 μM and 9.14 μM for **1j** and **1k** respectively (Figure 2.5). The Hill coefficient value of $n \sim 1$ for compounds **1j** and **1k** indicates the involvement of one molecule in catalyzing the ion transport process (Figure 2.5). The EC_{50} values for galactose systems were found to be 2.6 μM, 4.2 μM, 3.64μM and 1.7 μM for **2e**, **2f**, **2i**, and **2j** respectively (Figure 2.6). The Hill coefficient value of $n \sim 1$ for all these compounds indicates the involvement of one molecule in the transport process (Figure 2.6). The EC_{50} and *n* values could not be determined for **2h** due to precipitation at higher concentration.

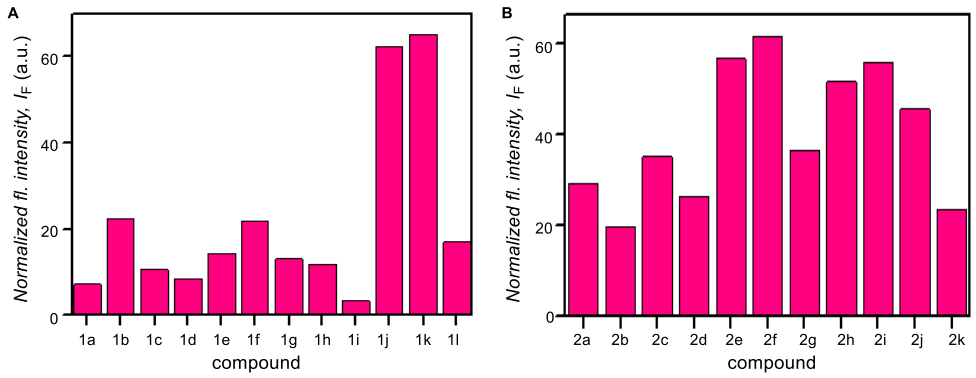

Figure 2.4 Comparative ion transport studies of **1a** – **1l** (10 μM) (**A**) and **2a** – **2k** (10 μM) (**B**) across EYPC–LUVs⊃HPTS.

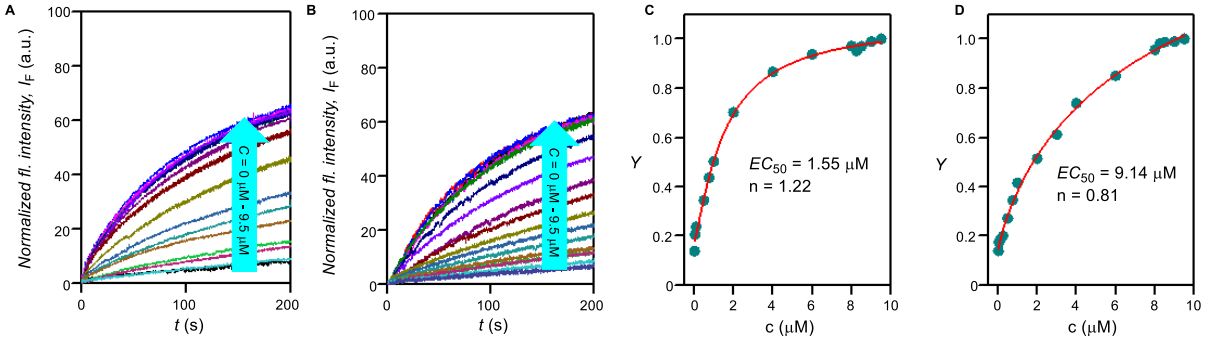

Figure 2.5 The concentration-dependent activity of 3-amino-3-deoxyallose derivatives **1j** (**A**)and **1k** (**B**) across EYPC–LUVs⊃HPTS. Hill analyses of compounds **1j** (**C**) and **1k** (**D**) at 190s after the addition of compound.

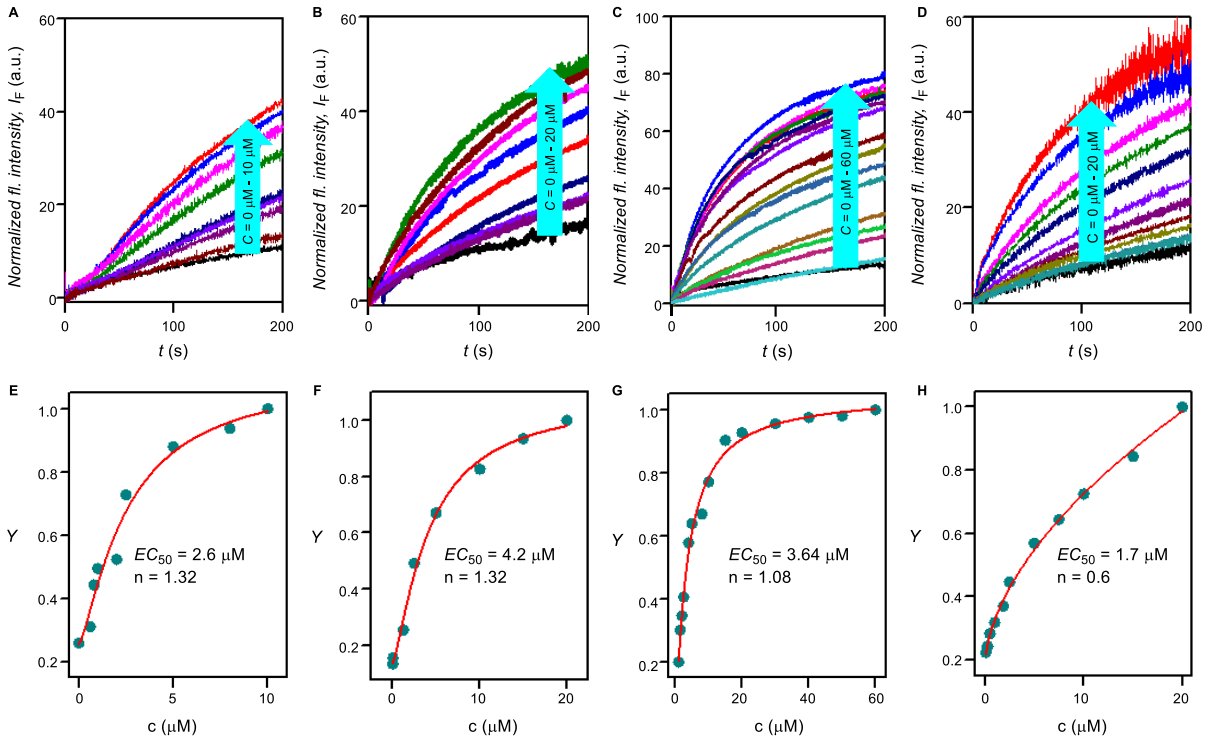

Figure 2.6 The concentration-dependent activity of 4-amino-4-deoxygalactose derivatives **2e** (**A**), **2f** (**B**), **2i** (**C**)and **2j** (**D**) across EYPC–LUVs⊃HPTS. Hill analyses of compounds **2e** (**E**), **2f** (**F**), **2i** (**G**) and **2j** (**H**) at 190s after the addition of compound.

Ion selectivity studies were performed across EYPC–LUVs⊃HPTS for all active carriers among 3-amino 3-deoxyallose and 4-amino 4-deoxygalactose series. Anion selectivity was initially investigated for **1j** and **1k** using EYPC-LUVs⊃HPTS assay, where external anions using anion salts of sodium (NaX, $X^- = Cl^-$, Br^-, I^-, SO_4^{2-}, NO_3^-) were varied. A significant difference in the transport rate confirmed the involvement of anions in an overall transport

process, and the activity sequence comes out to be $Br^- > Cl^- > NO_3^- > SO_4^{2-}$ (Figure 2.7A and 2.7B). Anion selectivity of **2e**, **2i** and **2k** also showed significant transport activity difference by the variation of external anions (NaX, X^- = Cl^-, Br^-, I^-, NO_3^- and ClO_4^-) (Figure 2.7C – 2.7E). The 4-amino-4-deoxygalactose system carriers were Cl^- selective however 3-amino-3-deoxyallose based carriers were selective towards Br^-. However, variation of the extravesicular cations by using different MCl salts (M^+ = Li^+, Na^+, K^+, Rb^+, Cs^+) for all carriers (**1j**, **1k**, **2e**, **2i** and **2k**) (Figure 2.8) did not yield any significant change in the activity, thus excluding the role of cations in the transport process. Ion selectivity studies of **2j** could not performed due to the decomposition of the compound stocks on storage. Further mechanistic studies and lucigenin assay[22] (chloride transport assay) could not be carried out due to precipitation problems and limitations of solubility of the compounds.

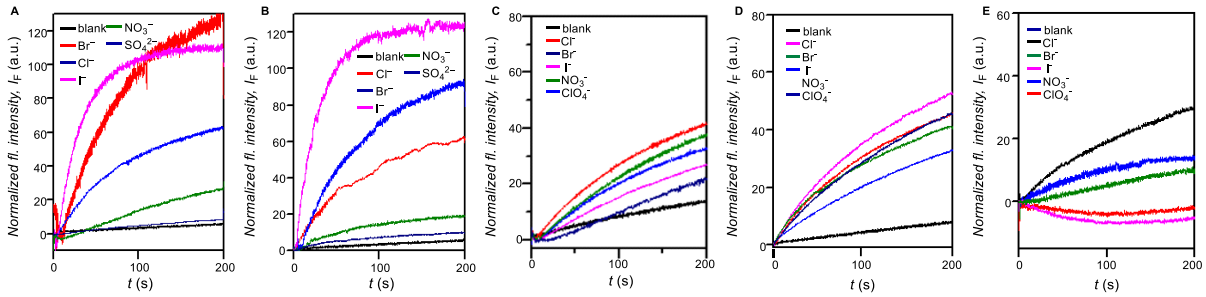

Figure 2.7 Anion selectivity of compounds **1j** (**A**), **1k** (**B**), **2e** (**C**), **2i** (**D**) and **2j** (**E**) was measured by the variation of extravesicular anions.

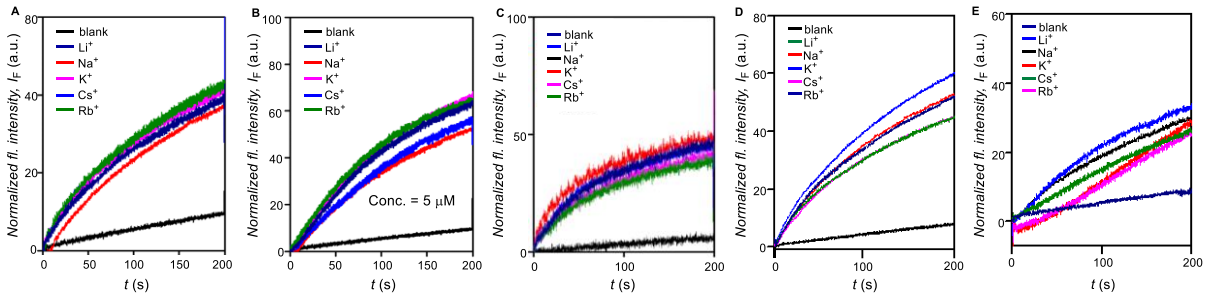

Figure 2.8 Cation selectivity of compounds **1j** (**A**), **1k** (**B**), **2e** (**C**), **2i** (**D**) and **2j** (**E**) was measured by the variation of extravesicular cations.

2.2.3 Biological studies

The assessment of anticancer activities of the reported active compounds was attempted in MCF-7 breast cancer cell line[23] but no conclusive data could be obtained due to the precipitation of the compounds in cell culture media following treatment.

2.3 Conclusion

In summary, we have designed novel cyclic carbohydrate (3-amino-3-deoxyallose and 4-amino-4-deoxygalactose) based ion carriers. The synthesis of the carriers was done by Dr. Yuri Tsvetkov, N. D. Zelinsky Institute of Organic Chemistry, Moscow. The ion transport properties of the molecules were assessed across EYPC-LUVs⊃HPTS. The comparative studies of 3-amino 3-deoxyallose system showed that derivatives with pyrrole and indole side chains exhibited good ion transport activity. However, the 4-amino-4-deoxyagalactose core series showed derivatives with *p*-bromo, *p*-methyl, *p*-trifluoro benzyl, pyrrole and indole possess significant transport activity compared to other carriers. The p-bromo and p-trifluoromethyl substituents, being electron-withdrawing groups, increased the acidity of the amide proton, which resulted in better activity. The pyrrole and indole-based systems were most active due to compound stability and the presence of an additional binding site furnished by the indole/pyrrole NH proton. The dose dependent studies provided EC_{50} values for **1j**, **1k**, **2e**, **2f**, **2i** and **2j**. The hill coefficient (*n*) was found to be ~1 for all carriers, indicating only one molecule of the carrier binds to an anion and carries it across the membrane. Due to precipitation in the buffer at higher concentrations, Hill analysis for **2h** could not be performed. Ion selectivity data confirmed that the ion transport activity of all most active carriers is anion-dependent and cation-independent. Ion selectivity studies of **2f** could not performed due to the decomposition of these molecules. The lucigenin (Cl^- selective dye) assay and further investigation of the ion transport mechanism could not be performed as all carriers were soluble only in DMSO. Biological studies also could not be performed due to the precipitation of the compounds in cell culture media.

As designed cyclic carbohydrate-based system is more hydrophobic which results in precipitation at higher concentrations. To solve this problem, the compounds can be made more hydrophilic by the attachment of polar groups like PEG, so that systems will be more water soluble and precipitation problems would be avoidable. Also reported sugar-based carriers are

more complex to synthesise, to compensate for this issue we can think of a simple system which is easier to handle practically.

2.4 Experimental section

2.4.1 General methods

Egg yolk phosphatidylcholine (EYPC) as a solution of chloroform (25 mg/ mL), mini extruder set and polycarbonate membrane of 100 nm pore size were purchased from Avanti Polar Lipids (Merck). HEPES, HPTS, NaOH, Triton X-100, Sephadex G-50 and all inorganic salts were of molecular biology grade from Sigma Aldrich. All stock solutions were prepared in HPLC grade DMSO (Rankem). All buffer solutions were prepared in autoclaved Milli-Q water.

2.4.2 Physical measurements

Fluorescence spectra were recorded on a HORIBA Jobin Yvon Fluoromax® 4 spectrofluorometer equipped with an injector port and magnetic stirrer. All buffer solutions were adjusted to the necessary pH using a Hanna Instruments pHep® (HI98107) pocket-sized pH tester. All data from fluorescence studies were processed using OriginPro 8.5 software. ChemDraw 21.0.0 was used for drawing structures and processing figures.

2.4.3 Ion transport studies[20, 24-26]

Ion transport studies across EYPC-LUVs⊃HPTS

Preparation of HEPES buffer and stock solutions: The HEPES buffer of pH = 7.0 was prepared by dissolving an appropriate amount of solid HEPES (10 mM) and NaCl (100 mM) in autoclaved water. The pH was adjusted to 7.0 by the addition of aliquots from 0.5 M NaOH solution. The stock solution of all carriers was prepared using HPLC grade DMSO.

Preparation of EYPC-LUVs⊃HPTS in NaCl (Vesicle preparation protocol 1): In a clean and dry 10 mL round bottom flask a thin transparent film of egg yolk phosphatidylcholine (EYPC) was formed from 1 mL EYPC lipid (25 mg/mL in $CHCl_3$) by providing continuous rotation and purging nitrogen gas. The transparent thin film was completely dried under high vacuum for 4-5 h. After that transparent thin film was hydrated with 1 mL HEPES buffer (1

mM HPTS, 10 mM HEPES, 100 mM NaCl, pH = 7.0) and the resulting suspension was vortexed at 10 min intervals during 1 h. This hydrated suspension was subjected to 15 cycles of freeze-thaw (N_2 gas, 55 °C) followed by extrusion through a 100 nm (pore size) polycarbonate membrane 21 times, to obtain the vesicles of an average 100 nm diameter. The unentrapped HPTS dyes were removed by size exclusion chromatography using Sephadex G-50 and eluting with HEPES buffer (10 mM HEPES, 100 mM NaCl, pH = 7.0). Finally, collected vesicles were diluted to 6 mL to get EYPC-LUVs⊃HPTS. *Final conditions:* ~ 5 mM EYPC, Inside: 1 mM HPTS, 10 mM HEPES, 100 mM NaCl, pH = 7.0, Outside: 10 mM HEPES, 100 mM NaCl, pH = 7.0.

Ion transport activity by HPTS assay (Assay protocol P1): In clean and dry fluorescence cuvette, 1975 μL of HEPES buffer (10 mM HEPES, 100 mM NaCl, pH =7.0) and 25 μL of EYPC–LUVs⊃HPTS vesicle was added. The cuvette was placed in a slowly stirring condition using a magnetic stirrer equipped in a fluorescence instrument (t = 0 s). The time-dependent HPTS emission intensity was monitored at λ_{em} = 510 nm (λ_{ex} = 450 nm) by creating a pH gradient between the intra- and extra-vesicular system by the addition of 0.5 M NaOH (20 μL) at t = 20 s. Then different concentrations of carrier molecules in DMSO were added at t = 100 s. Finally, the vesicles were lysed by the addition of 10% Triton X-100 (25 μL) at t = 300 s to disturb the pH gradient.

The time axis was normalized according to Equation 1:

$$t = t - 100 \quad \text{Equation 1}$$

The time-dependent data were normalized to percent change in fluorescence intensity using Equation 2:

$$I_F = [(I_t - I_0) / (I_\infty - I_0)] \times 100 \quad \text{Equation 2}$$

Where I_0 is the initial intensity, I_t is the intensity at time t, and I_∞ is the final intensity after the addition of Triton X-100.

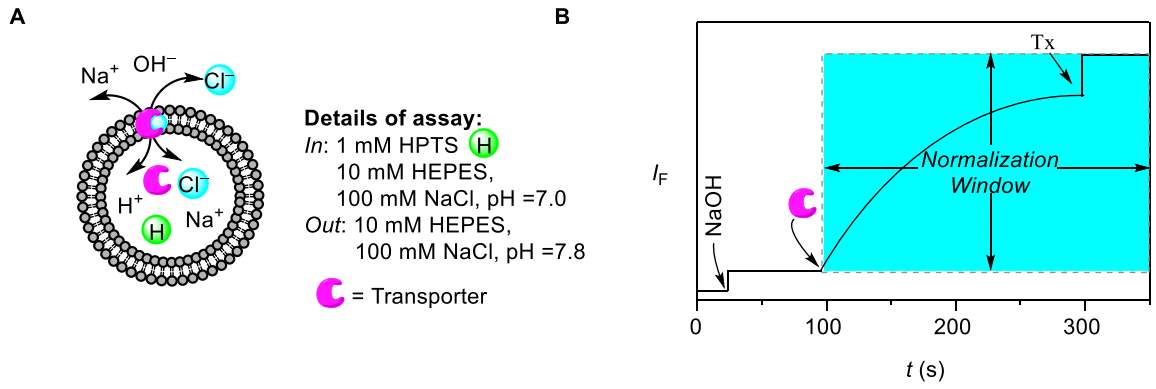

Figure 2.9 Representations of fluorescence-based ion transport activity assay using EYPC-LUVs⊃HPTS (**A**), and illustration of ion transport kinetics showing normalization window (**B**).

Dose-response activity: The fluorescence kinetics of each carrier at different concentrations was studied as a course of time. The concentration profile data were evaluated at t = 290 s to get effective concentration, EC_{50} (i.e. the concentration of carrier needed to achieve 50% chloride efflux)[27] using the Hill equation (Equation 3):

$$Y = Y_\infty + (Y_0 - Y_\infty) / [1 + (c/EC_{50})^n] \qquad \text{Equation 3}$$

Where, Y_0 = fluorescence intensity just before the carrier addition (at t = 0 s), Y_∞ = fluorescence intensity with excess carrier concentration, c = concentration of carrier compound, and n = Hill coefficient (i.e. indicative for the number of monomers needed to form an active supramolecule).[28]

Ion selectivity studies across EYPC-LUVs⊃HPTS

Preparation of EYPC-LUVs⊃HPTS: The vesicles were prepared as per the previous protocol **(Vesicle preparation protocol 1)**.

Preparation of buffer and stock solutions: The HEPES buffer solution of 10 mM HEPES and 100 mM salts were prepared by dissolving appropriate amounts of solid HEPES and salts (NaCl, NaBr, NaI, $NaNO_3$, $NaClO_4$, LiCl, KCl, RbCl, and CsCl) in autoclaved water, followed by adjustment of pH = 7.0 using 0.5 M NaOH. The stock solution of the most active carrier was prepared in HPLC grade DMSO.

Anion selectivity assay (Assay protocol P2): In clean and dry fluorescence cuvette, 1975 µL HEPES buffer (10 mM HEPES, 100 mM NaX, pH = 7.0; where X = F^-, Cl^-, Br^-, OAc^-, and

NO_3^-) was taken, followed by addition of 25 μL EYPC-LUVs⊃HPTS. The resulting solution was slowly stirred in a fluorescence instrument equipped with a magnetic stirrer (t = 0 s). The fluorescence intensity of HPTS was observed at λ_{em} = 510 nm (λ_{ex} = 450 nm) as a course of time t, with creating pH gradient by the addition of 20 μL 0.5 M NaOH at t = 20 s, followed by addition of carrier **1d** (as a DMSO solution) at t = 100 s to initiate ion transport, and finally vesicles were lysed for complete destruction of pH gradient by addition of 10% Triton X-100 (25 μL) at t = 300 s. The time axis was normalized according to Equation 1. The time-dependent data were normalized to percent change in intensity using Equation 2.

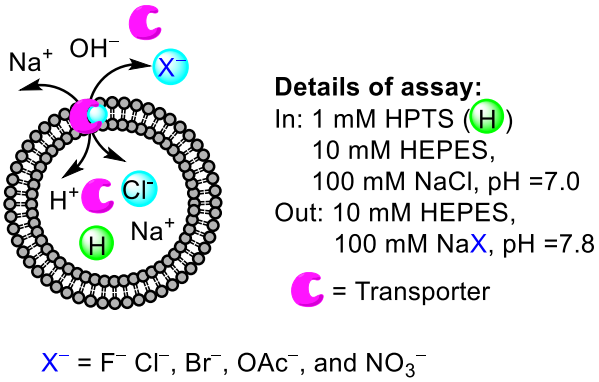

Figure 2.10 Schematic representations of fluorescence-based anion assay.

Cation selectivity assay (Assay protocol P3): Similarly, cation selectivity of carrier **1d** (as a DMSO solution) was explored by changing extravesicular HEPES buffer solution (10 mM HEPES, 100 mM MCl, pH = 7.0) of chloride salts (MCl) of different cation (M = Li^+, Na^+, K^+, Rb^+, and Cs^+). The time axis was normalized according to Equation 1. The fluorescence data were normalized to percent change in intensity as a course of time using Equation 2.

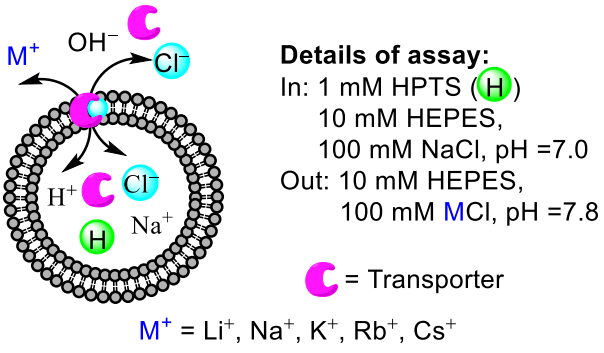

Figure 2.11 Schematic representations of fluorescence-based cation selectivity assay (**A**).

2.5 References

1. J. L. Jiménez Blanco, J. M. Benito, C. O. Mellet and J. M. García Fernández, *Org. Lett.*, 1999, **1**, 1217-1220.
2. J. M. Benito, J. L. Jiménez Blanco, C. Ortiz Mellet and J. M. García Fernández, *Angew. Chem., Int. Ed.*, 2002, **41**, 3674-3676.
3. D. Rodríguez-Lucena, J. M. Benito, E. Alvarez, C. Jaime, J. Perez-Miron, C. Ortiz Mellet and J. M. Garcia Fernandez, *J. Org. Chem.*, 2008, **73**, 2967-2979.
4. Y. Yu, N. Bogliotti, J. Tang and J. Xie, *Eur. J. Org. Chem.* , 2013, **2013**, 7749-7760.
5. S. Licen, C. Coppola, J. D'Onofrio, D. Montesarchio and P. Tecilla, *Org. Biomol. Chem.*, 2009, **7**, 1060-1063.
6. S. S. Burade, S. V. Shinde, N. Bhuma, N. Kumbhar, A. Kotmale, P. R. Rajamohanan, R. G. Gonnade, P. Talukdar and D. D. Dhavale, *J. Org. Chem.*, 2017, **82**, 5826-5834.
7. S. S. Burade, T. Saha, N. Bhuma, N. Kumbhar, A. Kotmale, P. R. Rajamohanan, R. G. Gonnade, P. Talukdar and D. D. Dhavale, *Org. Lett.*, 2017, **19**, 5948-5951.
8. I. Tabushi, Y. Kuroda and K. Yokota, *Tetrahedron Lett.*, 1982, **23**, 4601-4604.
9. J. K. Chui and T. Fyles, *Org. Biomol. Chem.*, 2014, **12**, 3622-3634.
10. J. K. Chui and T. M. Fyles, *Chem. Comm.*, 2010, **46**, 4169-4171.
11. Y. El Ghoul, R. Renia, I. Faye, S. Rassou, N. Badi, V. Bennevault-Celton, C. Huin and P. Guégan, *Chem. Comm.*, 2013, **49**, 11647-11649.
12. N. Madhavan, E. C. Robert and M. S. Gin, *Angew. Chem. Int. Ed.*, 2005, **44**, 7584-7587.
13. N. Madhavan and M. S. Gin, *ChemBioChem*, 2007, **8**, 1834-1840.
14. M. L. Gening, D. V. Titov, A. A. Grachev, A. G. Gerbst, O. N. Yudina, A. S. Shashkov, A. O. Chizhov, Y. E. Tsvetkov and N. E. Nifantiev, *Eur. J. Org. Chem.*, 2010, **2010**, 2465-2475.
15. M. L. Gening, Y. E. Tsvetkov, D. V. Titov, A. G. Gerbst, O. N. Yudina, A. A. Grachev, A. S. Shashkov, S. Vidal, A. Imberty, T. Saha, D. Kand, P. Talukdar, G. B. Pier and N. E. Nifantiev, *Pure Appl. Chem.*, 2013, **85**, 1879-1891.
16. T. Saha, A. Roy, M. L. Gening, D. V. Titov, A. G. Gerbst, Y. E. Tsvetkov, N. E. Nifantiev and P. Talukdar, *Chem. Commun.*, 2014, **50**, 5514-5516.
17. A. Roy, T. Saha, M. L. Gening, D. V. Titov, A. G. Gerbst, Y. E. Tsvetkov, N. E. Nifantiev and P. Talukdar, *Chem. Eur. J.*, 2015, **21**, 17445-17452.

18. A. M. Gilchrist, P. Wang, I. Carreira-Barral, D. Alonso-Carrillo, X. Wu, R. Quesada and P. A. Gale, *Supramol. Chem.*, 2021, **33**, 325-344.
19. N. Sakai and S. Matile, *J. Am. Chem. Soc.*, 2003, **125**, 14348-14356.
20. P. Talukdar, G. Bollot, J. Mareda, N. Sakai and S. Matile, *J. Am. Chem. Soc.*, 2005, **127**, 6528-6529.
21. T. Saha, M. S. Hossain, D. Saha, M. Lahiri and P. Talukdar, *J. Am. Chem. Soc.*, 2016, **138**, 7558-7567.
22. M. Chvojka, A. Singh, A. Cataldo, A. Torres-Huerta, M. Konopka, V. Šindelář and H. Valkenier, *Anal. Sens.*, 2024, **4**, e202300044.
23. T. Saha, M. S. Hossain, D. Saha, M. Lahiri and P. Talukdar, *J. Am. Chem. Soc.*, 2016, **138**, 7558-7567.
24. T. Saha, S. Dasari, D. Tewari, A. Prathap, K. M. Sureshan, A. K. Bera, A. Mukherjee and P. Talukdar, *J. Am. Chem. Soc.*, 2014, **136**, 14128-14135.
25. V. Gorteau, G. Bollot, J. Mareda, A. Perez-Velasco and S. Matile, *J. Am. Chem. Soc.*, 2006, **128**, 14788-14789.
26. T. Saha, A. Gautam, A. Mukherjee, M. Lahiri and P. Talukdar, *J. Am. Chem. Soc.*, 2016, **138**, 16443-16451.
27. A. Vargas Jentzsch, D. Emery, J. Mareda, P. Metrangolo, G. Resnati and S. Matile, *Angew. Chem. Int. Ed.*, 2011, **50**, 11675-11678.
28. S. Bhosale and S. Matile, *Chirality*, 2006, **18**, 849-856.

Chapter 3

Bisindole-based small molecules as transmembrane anion carriers and potential anticancer agents

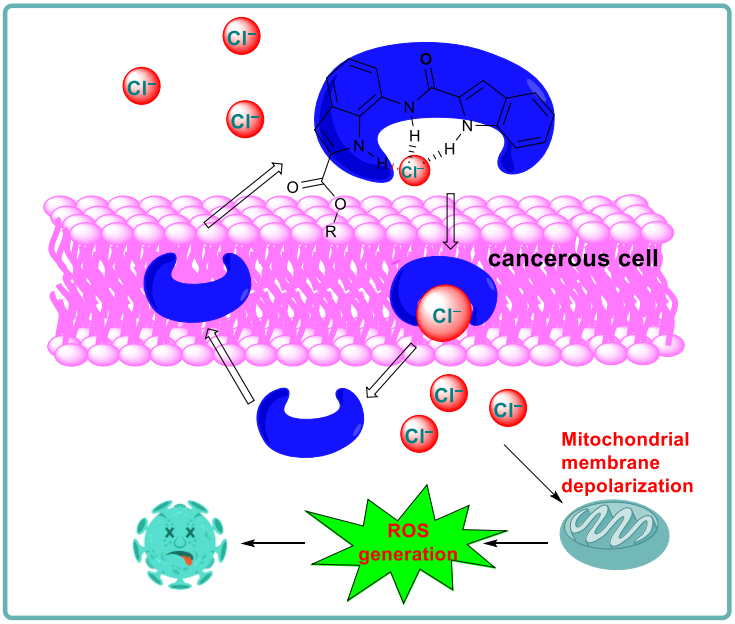

3.1 Introduction

As discussed in Chapter 2, the hydrophobicity of the cyclic carbohydrate-based carriers led to their precipitation in aqueous medium making them inefficient ion carriers lacking in biological activity. Due to the difficulty associated with the redesign and synthesis of these cyclic carbohydrate systems, owing to their complexity of structure, it was decided to make the test system structurally simpler. As carbohydrate carrier derivatives with indole tails yielded good transport activities, the utility of the indole moiety was assessed for the design of a more simple and efficient ion transport system.

Prodigiosins are a well-known family of naturally occurring tripyrrolic carriers capable of both transmembrane H^+/Cl^- symport and Cl^-/HCO_3^- antiport.[1-4] Prodigiosin shows therapeutic potential in anticancer, antimicrobial, and antifungal roles.[5,6] The anticancer properties of prodigiosins are linked to their ion transport ability.[7, 8] H^+/Cl^- transport by prodigiosin from acidic compartments within a cell, results in acidification of cytoplasm which is the early event of apoptotic cell death. Pyrrole is the core moiety of the ion binding site (N-H hydrogen bond donor) in these compounds, and thus inspired, many pyrrole carriers have been reported.[9, 10] Like pyrrole, indole also has a single N-H hydrogen bond donor, but surprisingly has been neglected in the anion receptor role, even though indole N-H is more acidic than pyrrole N-H (pK_a in DMSO: pyrrole 23.0 and indole 21.0).[11] Until 2004, indole anion complexation was only recognized in biological systems in the form of tryptophan as part of the binding core in nitrate,[12] sulfate[13] and bicarbonate [14] binding proteins. It also forms a complex with chloride in haloalkane dehalogenase confirmed by X-ray crystallography.[15]

In 2005, Kyu-Sung Jeong and co-workers reported the first indole-based macrocycle as an anion receptor.[16] They have shown the complexation of indole N-H with various anions via hydrogen bonds based on the change in NMR chemical shifts. Thenceforth, Philip Gale's group reported several indole anion receptors (Figure 3.1) e.g. simple indole/biindole,[17] acyclic indole,[18] 2-amidoindole,[19] 1,3-diindolylureas/thioureas,[20] and 2,7-functionalized indole (Figure 3.1).[21] The anion receptor properties of all mentioned indole receptors were demonstrated in the solution state (by NMR and UV study) and solid state (by crystallography). The same group has reported drug-like properties of indole-substituted urea and thiourea-based anion carriers (Figure 3.2A).[22] Inspired by the structure of prodigiosin Gale and coworkers fused the pyrrole and imine part of prodigiosin with indole, called perenosins[23] which showed to be highly potent H^+/Cl^- co-carriers (Figure 3.2B). However, unlike pyrrole, indole has not

been much explored in the supramolecular field for ion transport and its resultant biological activity.

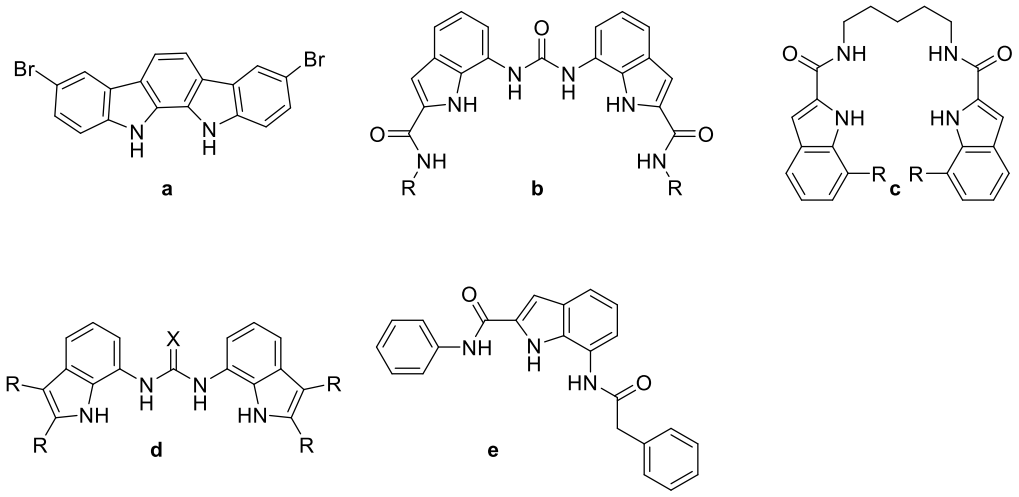

Figure 3.1 Structure of indole-based anion receptors.

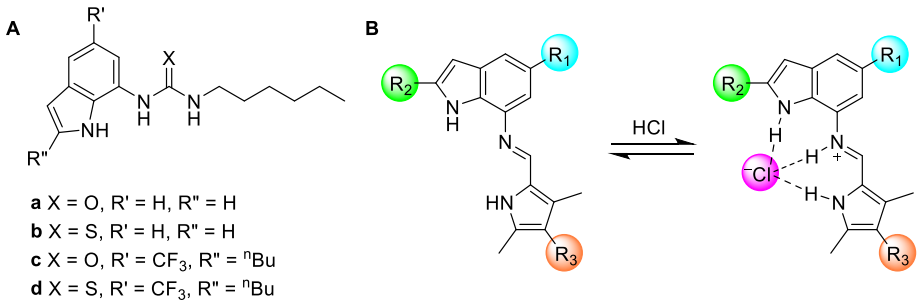

Figure 3.2 Structure of indole-based urea and thiourea carriers (**A**). Schematic representation of perenosin as an H^+/Cl^- co-transporter (**B**).

Therefore, a class of bisindole-based carriers (**1a – 1d**) were designed by the fusion of indole-2-carboxylic acid with ester derivatives of 7-amino indole-2-carboxylic acid (Figure 3.3A). This simple system has a semi-preorganised N-H group for anion binding. To achieve selectivity in biological applications (cancer treatment), a procarrier could be designed by the attachment of stimuli-responsive groups to the N-H_b proton. The variation of the R group can be utilized to tune the log*P* value close to 5 (Lipinski's rule), for better permeability across the lipid bilayer. The structures of carriers **1a**–**1d** and log*P* values are shown in Figure 3.3B. Based on the predicted (MarvinSketch 5.8.0)[24] pK_a values of the N-H groups, (indole) N-H_a - 11.92, (amide) N-H_b - 15.88, and (indole) N-H_c – 10.45. We hypothesized that the bisindole system

can effectively complex with the anion using its three N-H groups through hydrogen bonding and transport it across the membrane while the indole rings efficiently shielded the charge from the hydrophobic environment of the lipid bilayer (Figure 3.3C).

A

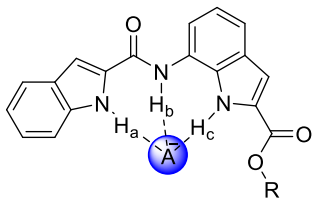

B

	R	log P
1a	Ethyl	3.46
1b	Butyl	4.43
1c	Hexyl	5.32
1d	Octyl	6.21

C

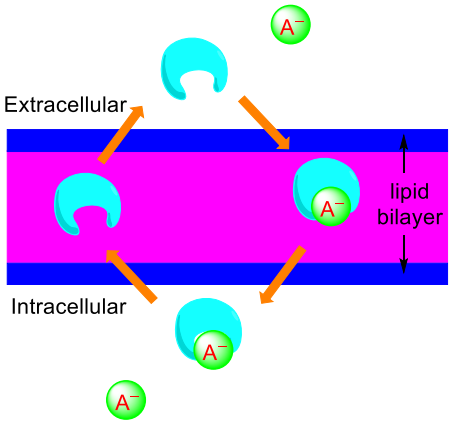

Figure 3.3 Structure of synthetic bisindole-based carriers **1a** – **1d** and its complexation with anion (**A**). The log *P* values of **1a** – **1d** were calculated using MarvinSketch 5.8.0 software (**B**). Schematic representation of anion transport process by bisindole-based ion carrier across the lipid bilayer membrane (**C**).

3.2 Results and Discussion

3.2.1 Synthesis

The synthesis strategy used for the bisindole carriers is outlined in Scheme 2.1. Carriers **1a** – **1d** were synthesised starting from *o*-nitroaniline (**2**). The *o*-nitroaniline (**2**) was subjected to diazotization followed by reduction using stannous chloride to get hydrazine derivative **3**. Compound **3** was treated with ethyl pyruvate (**4**) in the presence of sodium acetate and methanol to form imine **5**. The substituted indole **6** was synthesised by Fischer indole synthesis protocol using polyphosphoric acid (PPA). The ester group of indole **6** was hydrolysed by aq. KOH in ethanol to get acid **7**. The synthetic route till compound **7** was based on the reported literature protocol and characterization data compared to the literature report.[25] The ester derivatives **8a** – **8d** were synthesized by coupling aliphatic alcohols with acid **2** using EDC·HCl as the coupling agent. The reduction of the nitro group of **8a** – **8d** to corresponding amine **9a** – **9d** was done in the presence of H_2, Pd/C. Finally, the amine derivatives **9a** – **9d** were coupled with indole-2-carboxylic acid chloride to furnish carriers **1a** – **1d**. All compounds

were purified through column chromatography and characterised using ^{1}H and ^{13}C NMR, and HRMS.

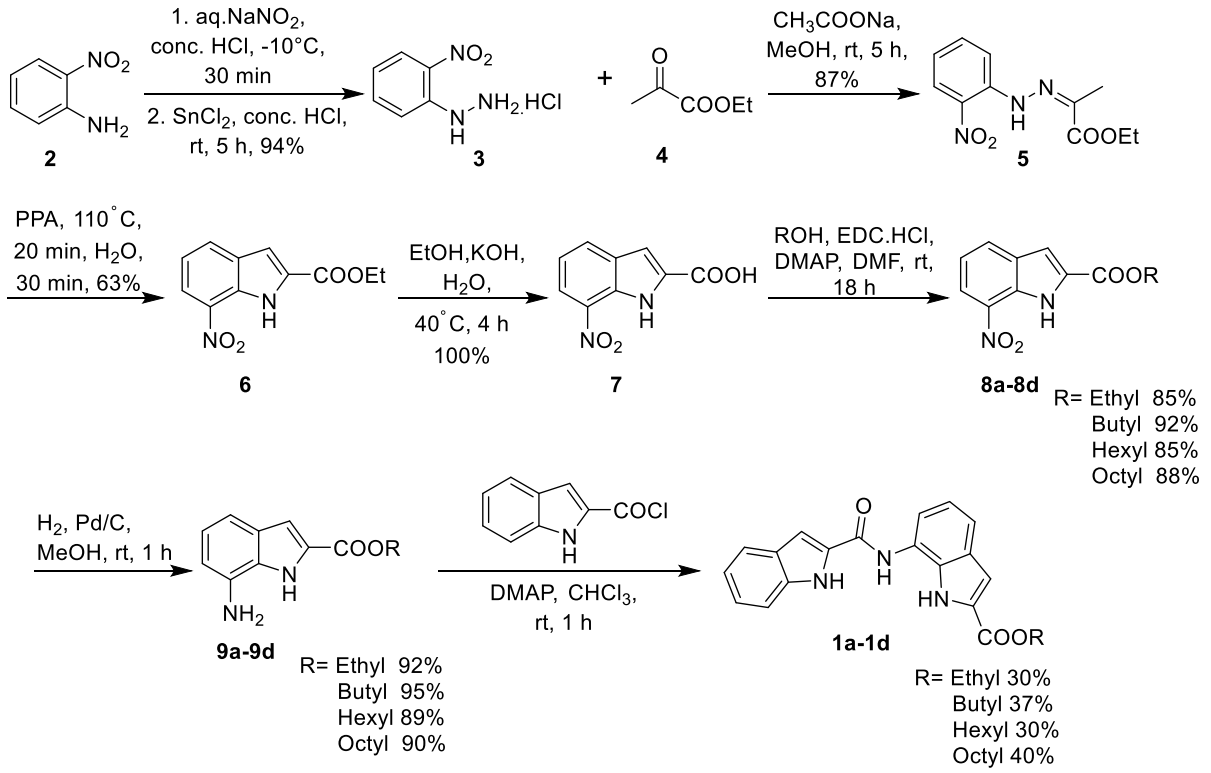

Scheme 3.1 Synthesis scheme of bisindole-based ion carrier **1a** – **1d**.

3.2.2 X-ray crystallography

Amid all synthesized compounds **1a–1d**, the crystal for **1d** was obtained by slow evaporation from its saturated solution in DMSO. The carrier was found to co-crystallize with DMSO where the amide N-H_b and indole N-H_c interacted with the solvent (S=O) while indole N-H_a contributed to the three-dimensional crystal packing (Figure 3.4B). The hydrogen bond distance between N-H_c···O=S and N-H_b···O=S is 2.011 Å and 2.435 Å respectively. Due to this strong interaction of the carrier with DMSO, we were unable to perform ion titration studies on the system as occupancy of the ion binding site by the solvent prevented anion binding at lower ion concentrations. Co-crystallization of carriers with Cl^{-} was attempted in various solvents but was unsuccessful.

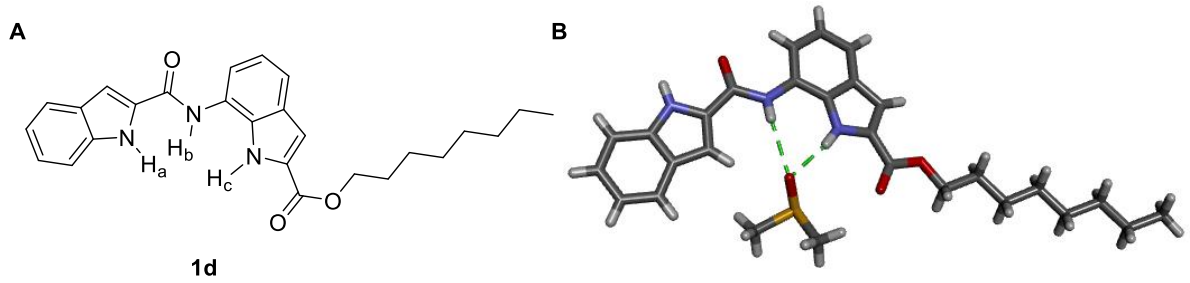

Figure 3.4 Structure of compound **1d** (**A**). The single crystal structure of **1d** with dimethyl sulfoxide indicates amide $NH_b\cdots O$ and indole $NH_c\cdots O$ hydrogen bond interaction (**B**).

3.2.3 Anion recognition studies by ^{1}H NMR titration

First, the Cl^- ion binding properties of bisindole-based carriers were verified by ^{1}H NMR titration experiments in a mixture of CD_3COCD_3 and CD_3CN (1:9). If Cl^- is interacting with a proton of carriers, then there would be downfield or upfield chemical shift of interacting protons in NMR spectrum. Upon addition of tetrabutylammonium chloride (TBACl) (0.2 M in 1:9 CD_3COCD_3 + CD_3CN) to a solution of 1:9 CD_3COCD_3 + CD_3CN **1a** and **1b** (2 mM), downfield shifts of H_a, H_b, and H_c protons were observed indicating the interactions of these protons with the Cl^- ion (Figure 3.5A–3.6A). Job's plot analysis was performed to check the stoichiometry of ion binding. The Job's plot analysis based on the change in N-H_a proton chemical shift of **1a** confirmed the 2:1 complexation of the receptor and Cl^- (Figure 3.5B.) The binding constant, K_a = 5862.74 ± 6.73 M^{-1} was also calculated for **1a** using Bindfit program(Figure 3.5B). The Cl^- ion binding stoichiometry of **1b** was found to be 1:1 based on a change in the chemical shift of H_a proton and the binding constants for **1b**, K_a = 2489.49 ± 3.67 M^{-1} (Figure 3.6B). Thus, ^{1}H NMR titration confirmed carriers interact with Cl^- ion through H bonding.

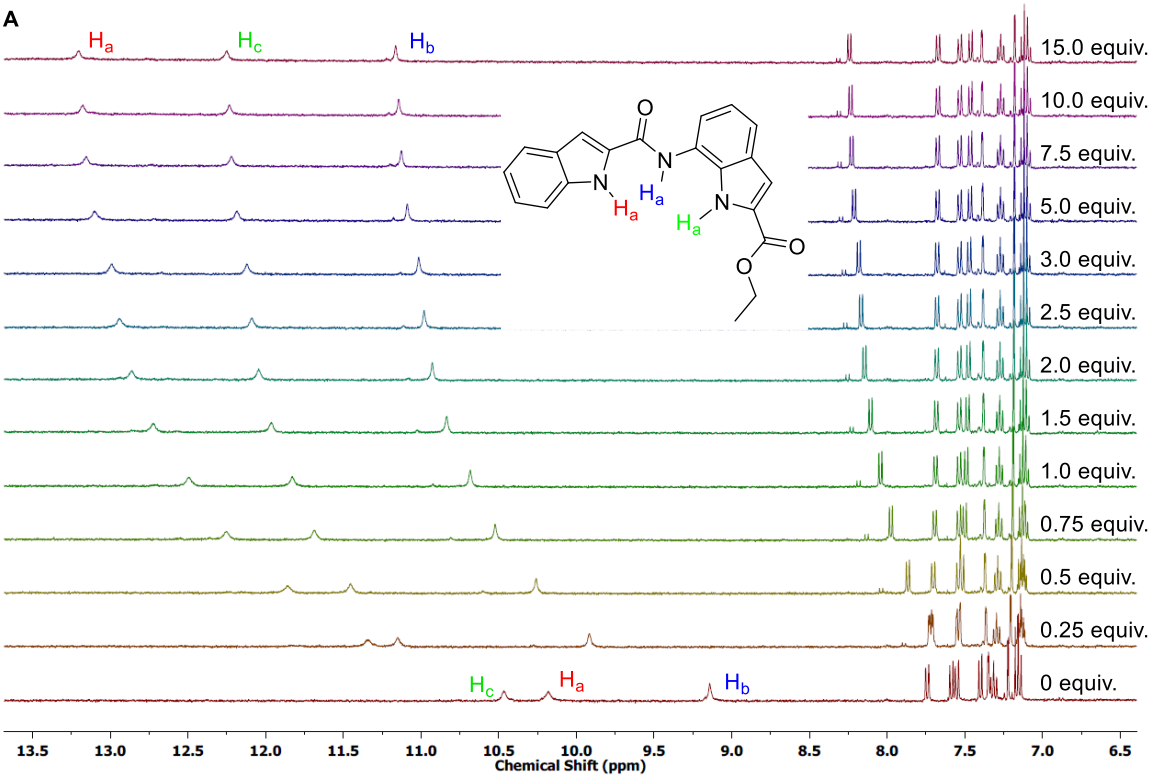

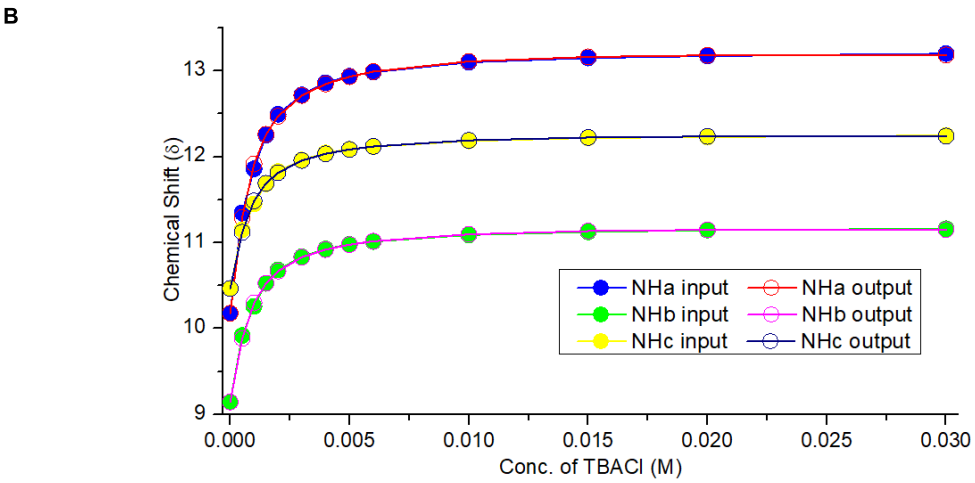

Parameter (bounds)	Optimised	Error	Initial
K_{11} (0 → 200)	137.66 M^{-1}	± 8.8156 %	150.00 M^{-1}
K_{21} (0 → 7000)	5862.74 M^{-1}	± 6.7320 %	5500.00 M^{-1}

Figure 3.5 ^{1}H NMR titration spectra of **1a** (2 mM) with stepwise addition of TBACl in 1:9 CD_3COCD_3 + CD_3CN. The number of TBACl equivalents added per reading is shown on the stacked spectra (**A**). The plot of chemical shifts (δ) of protons H_a, H_b, and H_c vs concentration of TBACl added, fitted to 2:1 binding model using BindFit v0.5 (**B**).

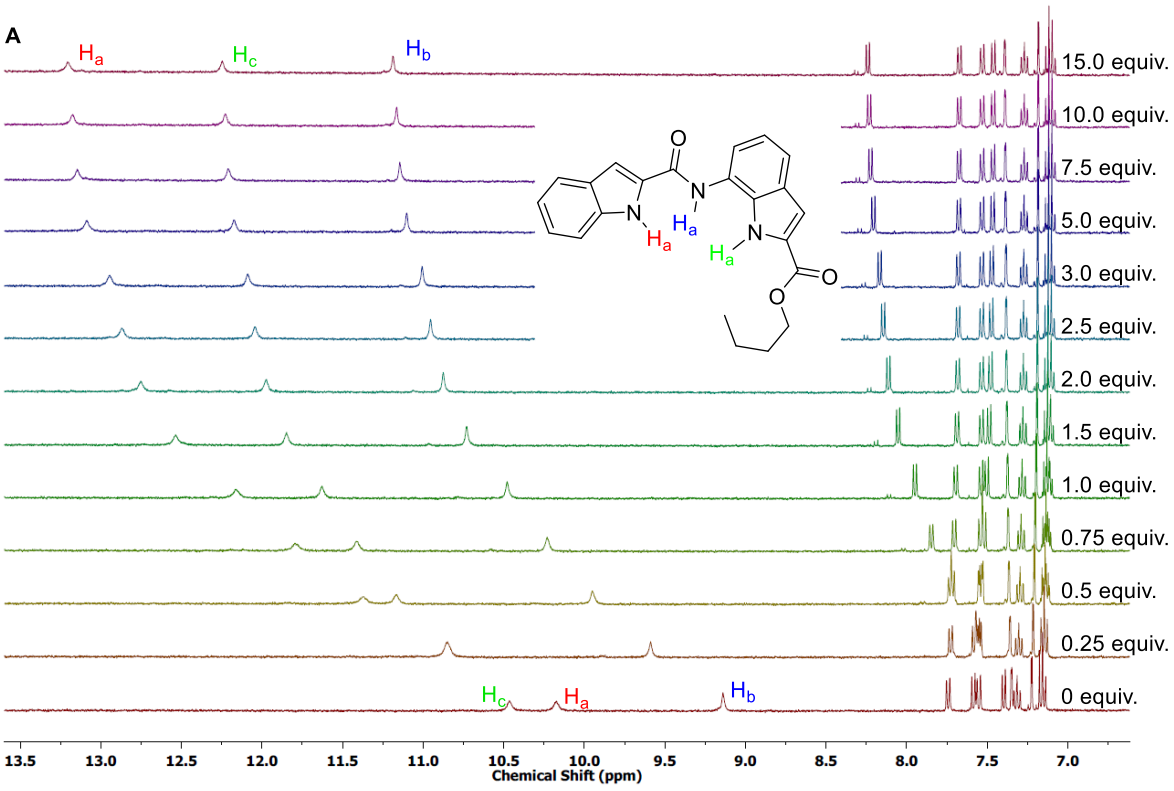

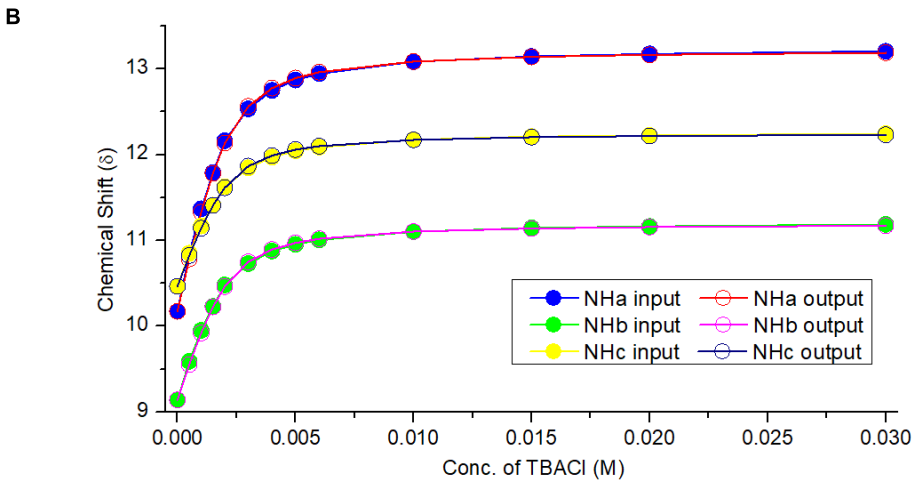

Parameter (bounds)	Optimised	Error	Initial
K (0 → 5000)	2489.49 M^{-1}	± 3.6658 %	2500.00 M^{-1}

Figure 3.6 ^{1}H NMR titration spectra of **1b** (2 mM) with stepwise addition of TBACl in 1:9 CD_3COCD_3 + CD_3CN. The number of TBACl equivalents added per reading is shown on the stacked spectra (**A**). The plot of chemical shifts (δ) of protons H_a, H_b, and H_c vs concentration of TBACl added, fitted to 1:1 binding model using BindFit v0.5 (**B**).

3.2.4 Ion transport studies

Initially, ion transport studies of all carriers **1a** – **1d** were performed across EYPC–LUVs⊃HPTS. The comparative studies of all carriers at 500 nM concentration yielded the transport activity sequence **1b** > **1c** ~ **1a** > **1d** which showed a correlation of transport activity with log*P* values (Figure 3.8A). Hill coefficient (*n*) and EC_{50} value (effective concentration at 50% transport activity) were calculated using the Hill equation (chapter 2, Equation 3) by performing dose-dependent ion transport studies. The Hill analysis of the dose-response studies of **1b** provided the EC_{50} = 347 nM. The calculated Hill coefficient, *n* = 1.3, indicates the involvement of one molecule of **1b** in the active carrier formation (Figure 3.7E). For **1a** and **1c** the EC_{50} values were 751 nM and 748 nM respectively and *n* values were 1.69 and 1.5 respectively (Figure 3.7D and 3.7F). Due to precipitation at higher concentrations in the buffer, the *n* and EC_{50} values of compound **1d** could not be calculated.

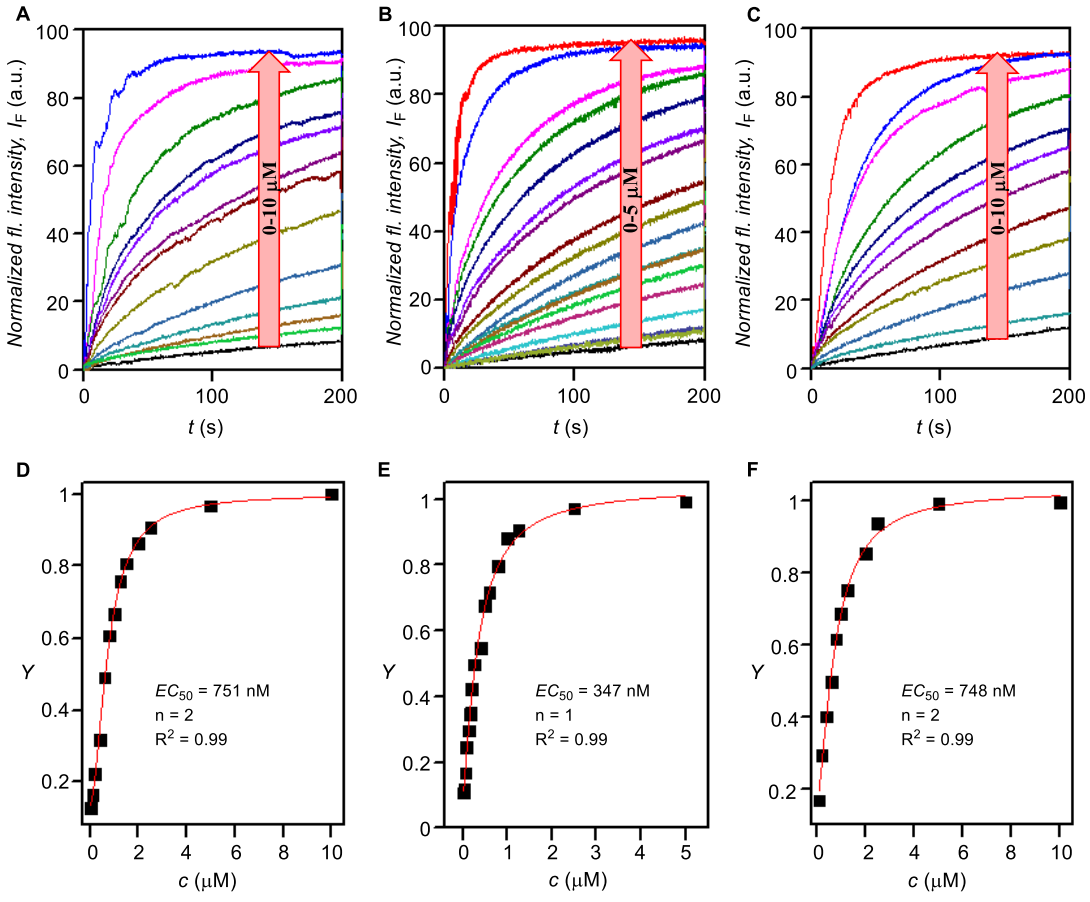

Figure 3.7 The concentration-dependent activity of compounds **1a** (**A**), **1b** (**B**), and **1c** (**C**) across EYPC–LUVs⊃HPTS. Hill plot analysis of compounds **1a** (**D**), **1b** (**E**), and **1c** (**F**) at 170s after the addition of compound.

Since carrier **1b** furnished the highest ion transport activity, it was used for further mechanistic studies. The cation selectivity of **1b** (500 nM) was assessed across EYPC–LUVs⊃HPTS vesicles by the variation of cations in the extravesicular buffer solution using different alkali metal chloride salts (MCl; M^+ = Li^+, Na^+, K^+, Rb^+, and Cs^+). Negligible change in ion transport activities was observed, suggesting cations did not play any role in the ion transport process (Figure 3.8B). However, variation of the extravesicular anions using various sodium salts (NaX, X^- = Cl^-, Br^-, I^-, OAc^-, NO_3^- and ClO_4^-) showed a significant change in the rates of ion transport of **1b** (600 nM), indicating the process to be anion dependent (Figure 3.8C). The order of ion transport activity was Cl^- > Br^- > OAc^- > I^- > NO_3^- > ClO_4^-. Anion selectivity data confirmed Cl^- selectivity of carrier **1b**. The ion selectivity studies show that the ion transport activity of **1b** depends on the nature of the anion.

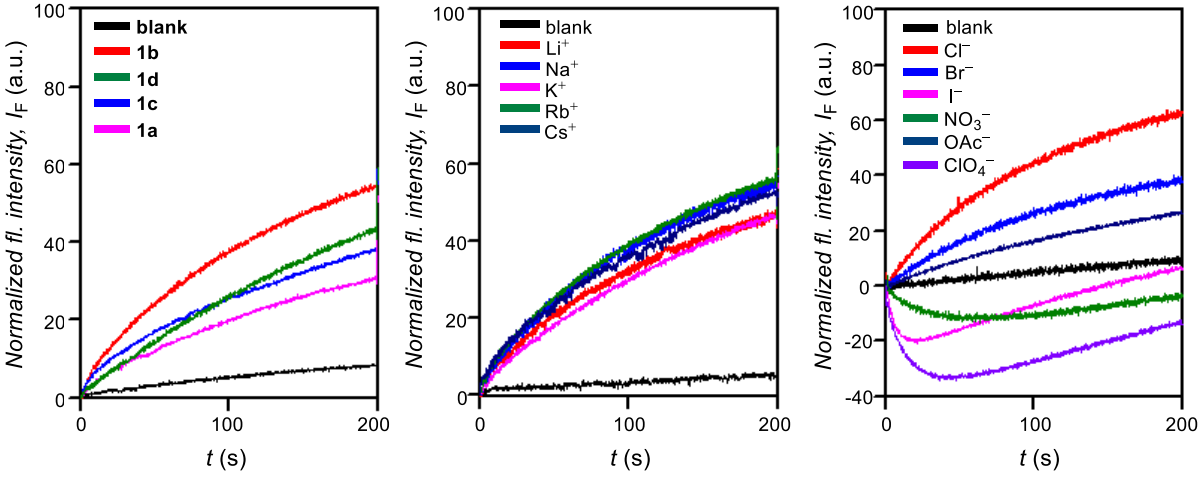

Figure 3.8 Comparative studies of **1a** – **1d** (500 nM) across EYPC–LUVs⊃HPTS (**A**). Ion selectivity of compound **1b** was measured by the variation of extravesicular cations (**B**) and anions (**C**) across EYPC–LUVs⊃HPTS.

The ion selectivity studies across EYPC–LUVs⊃HPTS confirmed that the change in fluorescence intensity of HPTS is due to anion transport. Chloride is the most abundant anion in physiological systems (extracellular concentration 110 mM, intracellular concentration 5 – 15 mM)) and it plays a crucial role in the maintenance of physiological function.[26, 27] Therefore, to confirm Cl^- transport by bisindoles **1a – 1d** studies were carried out across lucigenin-entrapped LUVs (EYPC–LUVs⊃lucigenin). Lucigenin is a chloride-sensitive dye, whose fluorescence intensity λ_{em} = 535 nm (λ_{ex} = 455 nm) quenches with increasing concentrations

of Cl^- ion.[28] The diffusion-mediated quenching in the fluorescence intensity of lucigenin dye in the presence of Cl^- ion would be studied in this assay. The influx of Cl^- ion by the anionophores **1a – 1d** were examined across EYPC–LUVs⊃lucigenin by creating a Cl^- gradient by the addition of 2 M NaCl to the extravesicular buffer. The comparative studies of **1a – 1d** (2.5 μM) yielded the same order of transport activity as observed across HPTS-entrapped vesicles. The chloride transport activity sequence was **1b** > **1c** ~ **1a** > **1d** (Figure 3.11A). The dose-dependent Cl^- influx study was performed for **1a** and **1b**. Based on the Hill plot analysis EC_{50} (effective concentration at 50% activity) and hill coefficient (*n;* number of molecules form complex with ion in transport process) were calculated. The Hill plot analysis provided EC_{50} values for **1a** 1.914 μM and for **1b** 1.245 μM (Figure 3.9-3.10). The hill coefficient for **1a** was found to be 2 means 2 molecules of carrier **1a** mediate the ion transport process. However, the hill coefficient for **1b** is 1 i.e., only one molecule of **1b** forms a complex with Cl^- for the transport process. Concentration-dependent study for **1c** and **1d** could not performed due precipitation of these compounds at high concentrations. Further, the cation selectivity of **1b** (2.5 μM) was investigated across EYPC–LUVs⊃lucigenin by the variation of extravesicular cation as alkali metal chloride salts (MCl; M = Li^+, Na^+, K^+, Rb^+ and Cs^+). Carrier **1b** showed no change in the rate of ion transport which confirms the cation not playing a role in the ion transport process (Figure 3.11B).

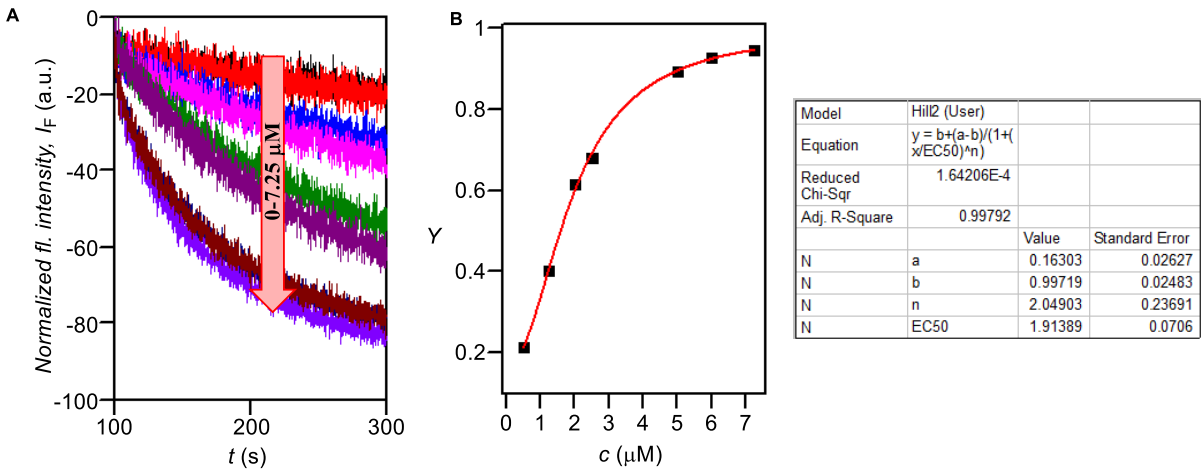

Figure 3.9 Dose-dependent activity of compound **1a** across EYPC-LUVs⊃lucigenin (**A**). Hill plot analysis of compound **1a** at t = 290 s (**B**).

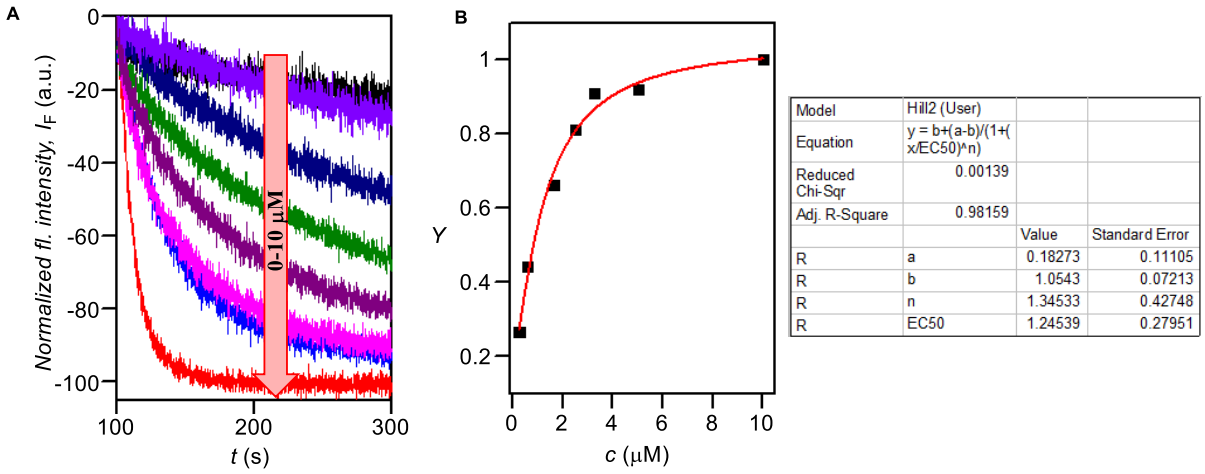

Model	Hill2 (User)		
Equation	y = b+(a-b)/(1+(x/EC50)^n)		
Reduced Chi-Sqr	0.00139		
Adj. R-Square	0.98159		
		Value	Standard Error
R	a	0.18273	0.11105
R	b	1.0543	0.07213
R	n	1.34533	0.42748
R	EC50	1.24539	0.27951

Figure 3.10 Dose-dependent activity of compound **1b** across EYPC-LUVs⊃lucigenin (**A**). Hill plot analysis of compound **1b** at t = 290 s (**B**).

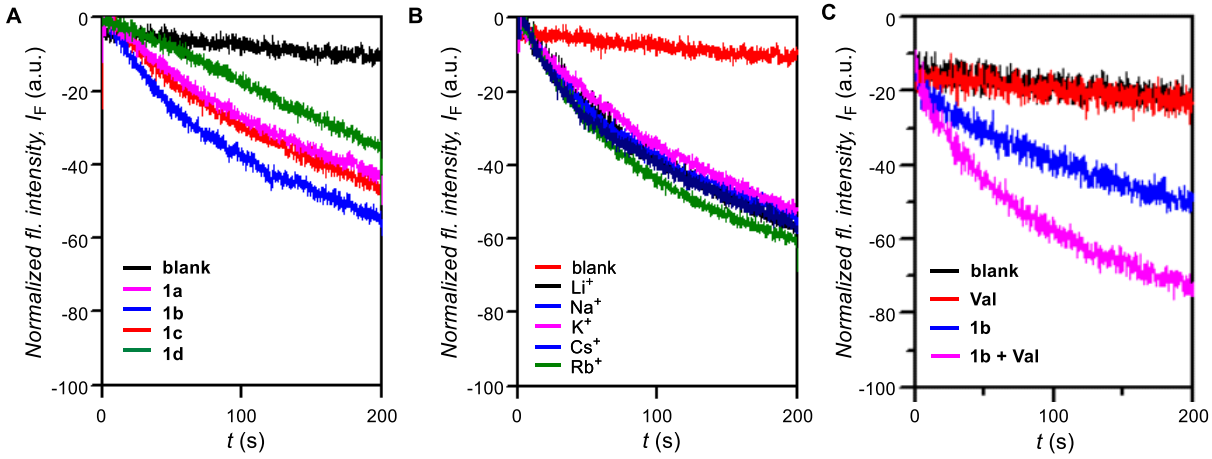

Figure 3.11 Comparative studies of **1a** – **1d** (2.5 µM) across EYPC–LUVs⊃lucigenin (**A**). The cation selectivity of compound **1b** (2.5 µM) was measured by varying the extravesicular cations across EYPC–LUVs⊃lucigenin (**B**). Valinomycin (0.2 µM) coupled assay of **1b** (1 µM) across EYPC-LUVs⊃lucigenin (**C**).

For the transport process to be detectable in lucigenin assay, the symport mechanism could be either M^+/A^- or H^+/A^- and the antiport mechanism could be X^-/A^- (X^-, A^- are two different anions) and M^+/H^+. Cation selectivity data in both HPTS and lucigenin assay confirms the transport process to be cation independent, therefore M^+/A^- symport and M^+/H^+ antiport could be ruled out. Hence, the Cl^- transport properties of **1b** were evaluated in the presence and absence of the K^+ selective carrier valinomycin. If the mechanism of ion transport is antiport (NO_3^-/Cl^-) then there would be a cooperative effect of valinomycin on transport activity of

1b.[29] A significant increase in the ion transport activity of **1b** across EYPC–LUVs⊃lucigenin was observed following treatment with valinomycin (Figure 3.11C), which confirmed anion antiport as the main mechanism of transport in bisindole.

Further, compounds **1a** and **1b** were tested for carrier mechanism of transmembrane ion transport through a variable temperature assay across 1,2-dipalmitoyl-*sn*-glycero-3-phosphocholine liposomes entrapping HPTS dye (DPPC−LUVs⊃HPTS).[30] DPPC undergoes gel to liquid-crystalline phase transition at T_c = 41.3°C.[31] The transport ability of both **1a** and **1b** (2.5 μM, 3.64 mol%) were inhibited at 25°C when the lipid was in the gel phase, which then recovered above T_c at 45°C (Figure 3.12). This confirmed the mobile carrier mechanism of ion transport, as carrier mobility is greatly inhibited in the gel phase.[30] Transport through ion channels is unaffected by the lipid phase due to their membrane-spanning nature and thus this mechanism of ion transport can be ruled out for the bisindole system.

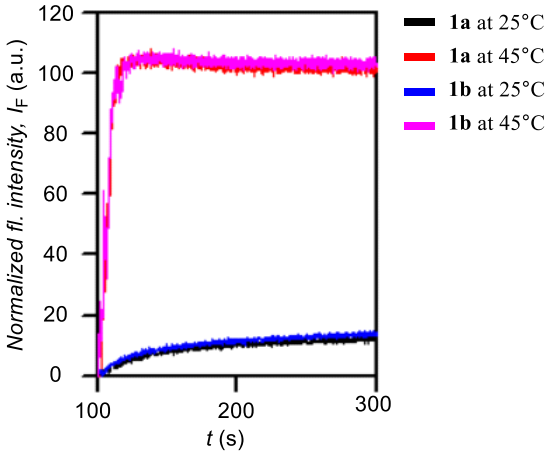

Figure 3.12 Assessment of compounds **1a** and **1b** (2.5 μM) across DPPC-LUVs⊃HPTS at 25 °C and 45 °C. Activity restoration at 45 °C confirms the mobile carrier mechanism.

3.2.5 Theoretical calculations

A Hill coefficient (*n*) of ~1 for carrier **1b** indicated the formation of a [**1b**+ Cl^-] complex during ion transport, while **1a** with *n* ≈2 forms a ([(**1a**)$_2$+ Cl^-] complex. For a better understanding of the structures of these complexes, theoretical predictions of the most probable geometries of carriers **1a** and **1b** and their respective ion transport complexes were attempted.

Geometry optimization of compound 1a

A list of possible geometries of carrier **1a** was generated using the CONFLEX 8 conformation search software package[32, 33] using the MMFF94S (2010-12-04HG) force field with a search limit of 10 kcal/mol. A total of 26 predicted conformers were obtained, of which conformers with predicted Boltzmann population <5% were rejected. Geometry optimization of the remaining four conformations **CE1-CE4** were conducted on Gaussian 09 program suite[34] using the B3LYP exchange-correlation functional[35, 36] and 6-31G (d, p) basis set.[37, 38] The conformations were observed to exhibit variation in their ethyl (ester) chains (Figure 3.13). The bis-indole core conformation remained constant, with adjacent NH bonds anti to each other. Hartree-Fock energies were observed to be very similar for the structures. The lowest energy structure, **CE1**, was selected for further calculations.

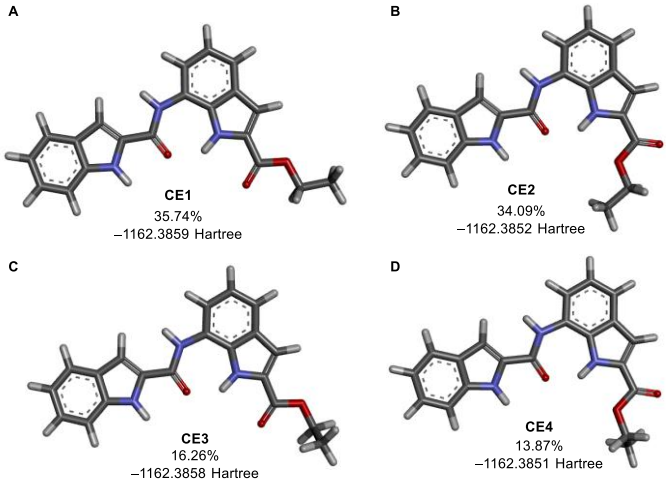

Figure 3.13 Geometry optimized structures of highest probability conformers of **1a** predicted using CONFLEX 8. The predicted Boltzmann populations (from CONFLEX 8 output) and calculated Hartree-Fock (HF) energies of the optimized structures are provided.

For **CE1**

- HF energy = –1162.3859526 Hartree
- Zero-point energy = 0.3386918 Hartree

Structure of [(1a)$_2$ + Cl$^-$] complex

The prediction of possible geometries of the [(**1a**)$_2$ + Cl$^-$] ion transport complex using CONFLEX 8 yielded a total of 10726 predicted conformers were obtained, of which conformers with predicted Boltzmann population <5% were rejected, which left 6 conformers.

Geometry optimization of these conformations were conducted on Gaussian 09 (B3LYP, 6-31G(d,p)). The resultant conformations were observed to be highly similar, with only slight conformational variations and had similar Hartree-Fock energies. The conformer with the lowest energy (**CEC**) (Figure 3.14A-B) was chosen for binding energy calculation. Geometry-optimized conformer **CEC** exhibited interactions of chloride ion with all three NH groups in [(**1a**)$_2$ + Cl$^-$] complex (Figure 3.14C-D). The two **1a** molecules were arranged in an orthogonal fashion to form a hydrophobic shell completely encapsulating the anion.

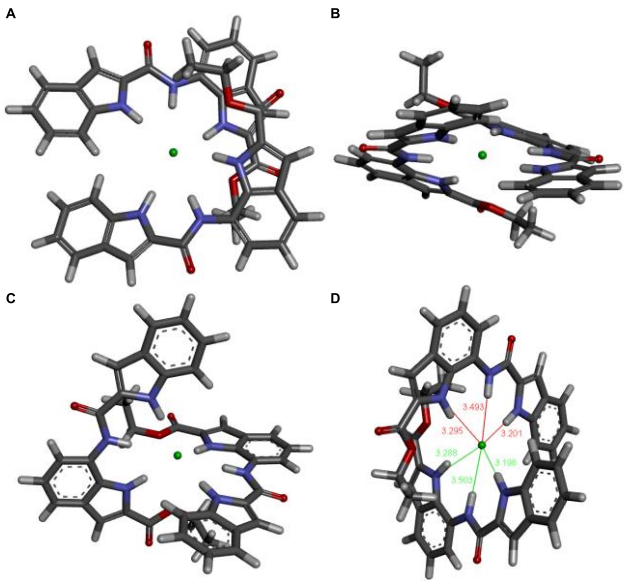

Figure 3.14 CONFLEX 8 predicted geometry of **CEC** conformer of [(**1a**)$_2$ + Cl$^-$] complex (predicted Boltzmann population- 9.38%) (**A**), (**B**). Geometry-optimized [(**1a**)$_2$ + Cl$^-$] complex (Gaussian 09, B3LYP/6-31G(d,p)) derived from **CEC** conformer (**C**). NH···Cl$^-$ H-bond distances in ion transport complex (**D**).

For [(**1a**)$_2$ + Cl$^-$]:

- HF energy = –2785.1237509 Hartree
- Zero-point energy = 0.6791279 Hartree
- BSSE = 0.019149779046 Hartree
- Binding energy = -0.078718321 Hartree = –49.39653358 kcal/mol

Geometry optimization of compound 1b

A total of 145 predicted conformers were obtained for carrier **1b** in CONFLEX 8 of which conformers with predicted Boltzmann population <5% were rejected. Geometry optimization of the remaining four conformations **CB1-CB8** were conducted on Gaussian 09 (B3LYP, 6-

31G(d,p)). The conformations were observed to exhibit variation in their ethyl (ester) chains (Figure 3.15). The bis-indole core conformation remained constant, with adjacent NH bonds anti to each other. Hartree-Fock energies were observed to be very similar for the structures. The lowest energy structure, **CB4**, was selected for further calculations.

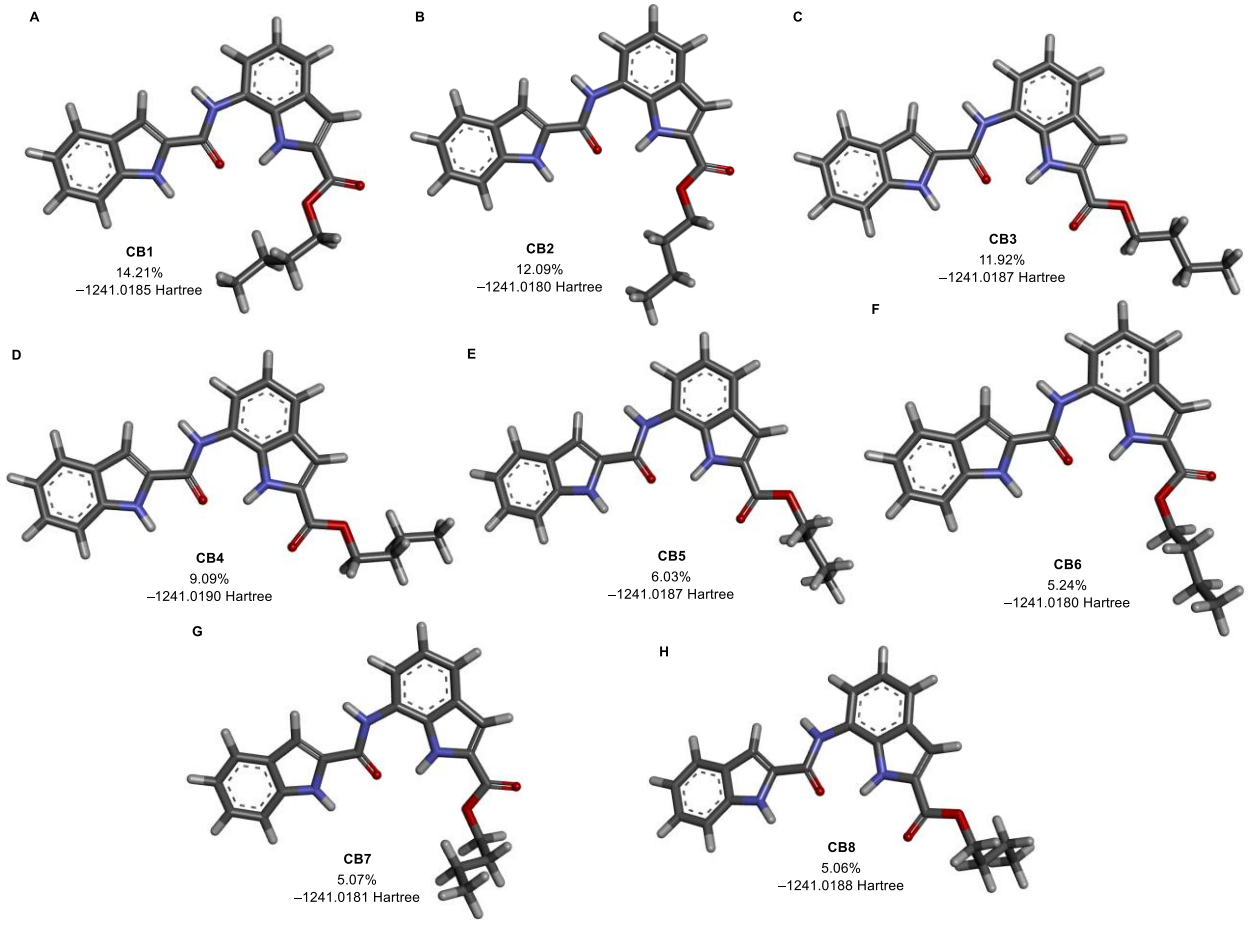

Figure 3.15 Geometry-optimized structures of highest probability conformers of **1b** predicted using CONFLEX 8. The predicted Boltzmann populations (from CONFLEX 8 output) and calculated Hartree-Fock (HF) energies of the optimized structures are provided.

For **CB4**

- HF energy = –1241.0190006 Hartree
- Zero-point energy = 0.3958468 Hartree

Structure of [1b + Cl^-] complex

A total of 101 predicted conformers were obtained from CONFLEX 8 for [**1b** + Cl^-] ion transport complex of which conformers with predicted Boltzmann population <5% were rejected, which left 7 conformers. Geometry optimization yielded conformers which were

highly similar, with only slight conformational variations and had similar Hartree-Fock energies. The conformer with the lowest energy (**CBC**) (Figure 3.16A) was chosen for binding energy calculation. Geometry-optimized conformer **CBC** exhibited interactions of chloride ion with all three NH groups in [**1b** + Cl^-] complex (Figure 3.16B).

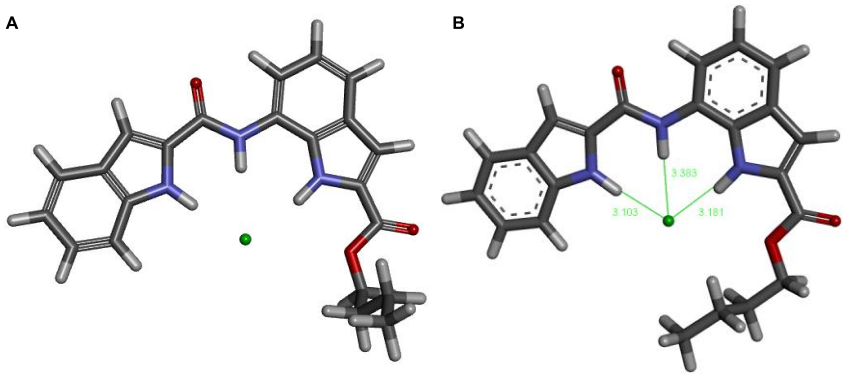

Figure 3.16 CONFLEX 8 predicted geometry of **CBC** conformer of [**1b** + Cl^-] complex (predicted Boltzmann population- 5.10%) (**A**). Geometry-optimized [**1b** + Cl^-] complex (Gaussian 09, B3LYP/6-31G(d,p)) derived from **CBC** conformer showing NH···Cl^- H-bond distances (**B**).

For [**1b** + Cl^-]

- HF energy = –1701.3436392 Hartree
- Zero-point energy = 0.3958335 Hartree
- BSSE = 0.010760023126 Hartree
- Binding energy = –0.061658577 Hartree = –38.69137357 kcal/mol

3.2.6 Biological studies

The promising results obtained from ion transport studies conducted for the bisindoles **1a-1d** encouraged the assessment of their biological activity. Recent studies have shown that the perturbation of ion homeostasis by small molecule-induced ion transport leads to apoptotic cell death of cancerous cells.[39-42] Initially, the cell viability in the presence of **1a** – **1d** were examined by colorimetric MTT (3-(4,5-dimethylthiazol-2-yl)-2,5-diphenyltetrazolium bromide) assay.[43] The dehydrogenase in active mitochondria of living cells reduces MTT (a tetrazolium derivative) to water-insoluble purple-coloured formazan. The intensity of the purple colour is directly proportional to the number of viable cells which is measured by spectrophotometer.[44] The viability of non-cancerous Mouse Embryonic Fibroblasts (MEFs) and cancerous cells i.e., human breast cancer cells (MCF–7) were monitored after incubation

of **1a** – **1d** for 24 h by MTT assay. The addition of compounds **1a** – **1d** showed significant cell death in cancerous cells (Figure 3.17B). However, these compounds were non-toxic up to 20 μM concentration in the non-cancerous MEFs cells (Figure 3.17C). Due to the good activity of anionophores in the cell line, MCF–7 was carried forward for further biological studies. Amongst the four derivatives, carrier **1a** was the most potent in terms of its anti-cancer activity, although highest ion transport activity was observed for **1b**. This discrepancy could likely be attributed to the difference in membrane composition between the mammalian cells and the artificial liposomes used in the study. An IC_{50} value of 15 μM was obtained for **1a** in MCF-7 cells.

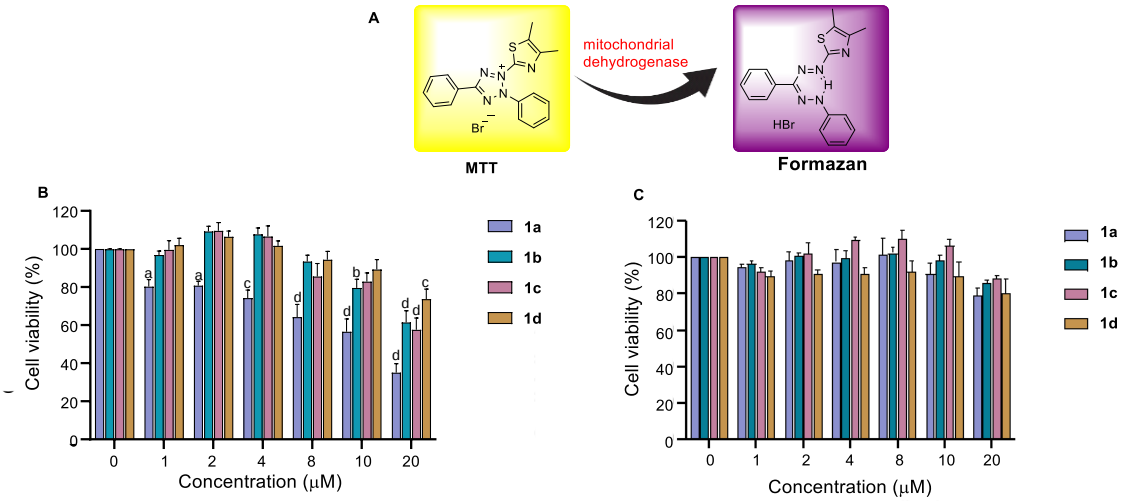

Figure 3.17 Schematic representation of mitochondrial reduction of yellow MMT dye to purple formazan (**A**). Dose-dependent cell viability of MCF–7 (**B**), and MEFs (**C**) cells using MTT assay incubated with **1a** – **1d** for 24 h. **a** represents < 0.05; **b** represents $p < 0.01$; **c** represents for $p < 0.001$; and **d** for $p < 0.0001$ when compared to untreated control using Tukey HSD tests.

To evaluate the dependence of Cl^- transport on the cytotoxicity of **1a**, a MTT assay was performed in the presence and absence of Cl^- ion in MCF-7 cells using two different HBSS solutions. For the preparation of cultural media two different HBSS (Hank balanced salt solution) solutions with Cl^- and without Cl^- ion were prepared and cells were grown separately in these buffers. Interestingly, the incubation of **1a** (0 – 20 μM) for 24 h shows almost negligible cytotoxicity in the extracellular media without Cl^- ion as compared to that of extracellular media with Cl^- ion (Figure 3.18). These results confirmed the necessity of extracellular Cl^- for bisindole toxicity towards MCF-7 cells, indicating carrier-mediated

chloride transport to be the initiator of cell death. Such chloride-mediated apoptotic cell death of cancer cells is well known in the literature.[39, 42, 45]

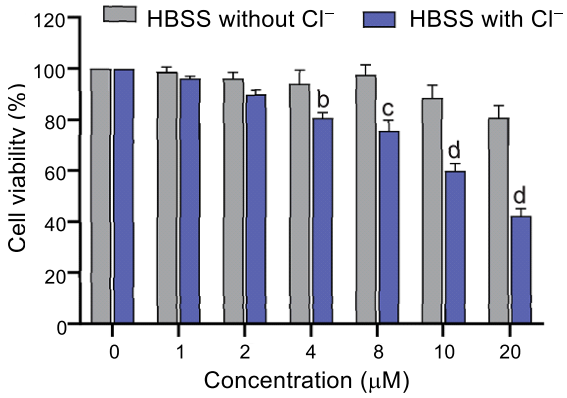

Figure 3.18 MTT assay comparing cell viability of MCF–7 cells in the presence and absence of Cl^- ion in extracellular media (HBSS buffer) upon dose-dependent treatment of **1a** (0 – 20 μM) for 24 h. **a** represents < 0.05; **b** represents $p < 0.01$; **c** represents for $p < 0.001$; and **d** for $p < 0.0001$ when compared to untreated control using Tukey HSD tests.

This perturbation of cellular chloride concentration was associated with altered cell cycle profiles with a reduced percentage of cells observed in the G_1 and S/G2M phases with a significant increase in the G0 population in **1a** treated MCF-7 cells (Figure 3.19).

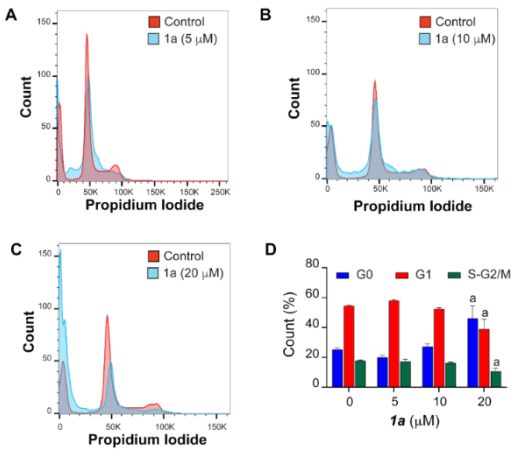

Figure 3.19 Representative cell cycle profile overlays of untreated MCF-7 cells with those treated for 24 h with (**A**) 5 μM; (**B**) 10 μM; and (**C**) 20 μM concentration of **1a**. (**D**) Quantitation of cells (in %) in different phases of the cell cycle. A represents $p < 0.05$ when compared to untreated control using Tukey HSD tests.

Experiments were performed to evaluate the mechanism of cell death i.e., whether cell death is being mediated by apoptosis or necrosis. To verify the apoptotic mechanism of cell death; the events involved in the apoptosis were evaluated experimentally with **1a**. In the intrinsic pathway of apoptotic cell death, one of the steps that triggers apoptosis is a disturbance of mitochondrial membrane potential (MMP)[46] which subsequently releases cytochrome *c* into the cytoplasm from the mitochondrial membrane. The released cytochrome c activates caspase 9 by the formation of the cytochrome *c*/apaf-1 complex. Activated caspase 9 further initiates multiple pathways to induce apoptotic cell death.[47-51] Initially, the depolarisation of MMP was investigated using MMP-sensitive JC-1 dye (Figure 3.20A). JC-1 is a cationic dye that forms complexes in the healthy mitochondria known as J-aggregates with intense red fluorescence.[52, 53] Due to the disruption of MMP J-aggregates collapses into a monomeric form of JC-1 which possess green fluorescence. Compound **1a** was incubated with MCF–7 cells for 24 h, followed by treatment with JC-1 (8 μM) dye as per the reported protocol. Cells were investigated under a microscope to monitor the fluorescence of JC-1 dye. Following treatment of MCF 7 cells with **1a** (0 − 20 μM) for 24 h, a decrease in red fluorescence of the JC-1 dye along with a subsequent increase in green fluorescence was observed (Figure 3.21), indicating mitochondrial membrane depolarization as a result of bisindole facilitated disruption of chloride ion homeostasis. The quantification of red/green fluorescence shows higher levels of MMP disruption with increasing concentration of **1a** (Figure 3.20B).

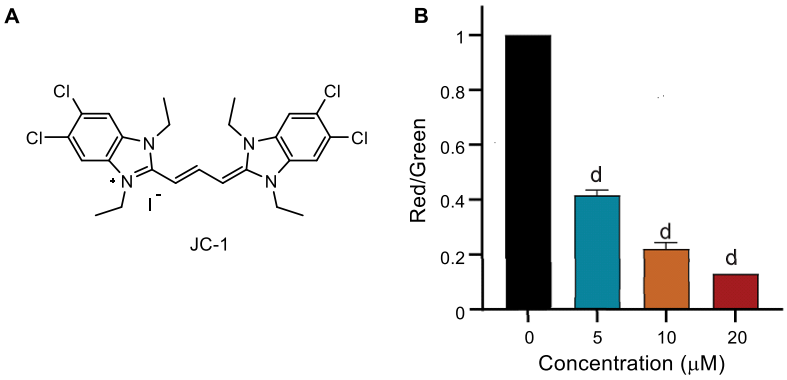

Figure 3.20 The structure of JC-1 Dye (**A**). The pixel ratio (red/green) for each set of concentrations was plotted in the bar graph (**B**). **d** for $p < 0.0001$ when compared to untreated control using Tukey HSD tests.

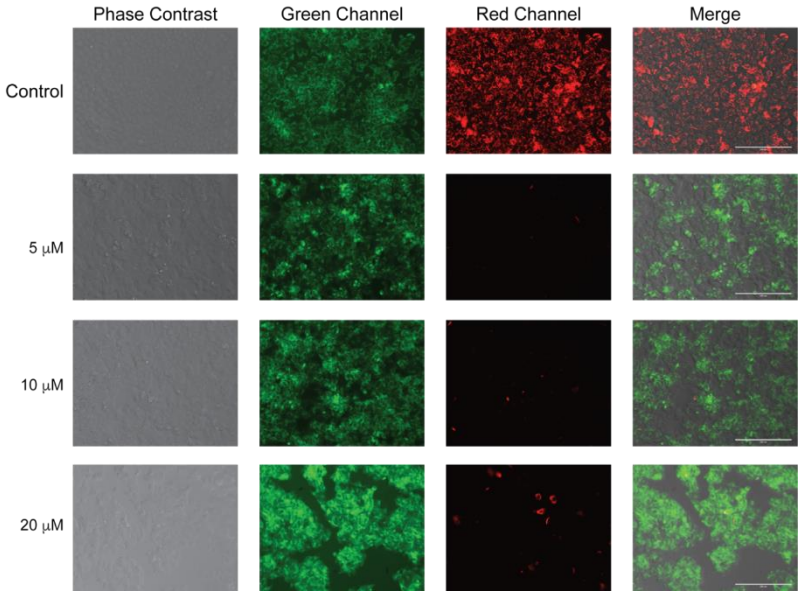

Figure 3.21 Representative merged images of JC-1 stained MCF-7 cells after treatment with different concentrations (0 (control), 5, 10 and 20 μM) of compound **1a** for 24 h. (Magnification 20X. Scale bar: 200 μm)

The depolarization of MMP causes an interruption in the electron transport chain of the mitochondrial respiratory cycle, leading to the generation of reactive oxygen species (ROS).[54-56] The ROS level in MCF–7 cells was detected using ROS probe MitoSOX which is cell membrane permeable where they specifically target mitochondria. In the presence of ROS species MitoSOX rapidly oxidizes to a highly fluorescent product (Figure 3.22A).[57] Increasing dosage of **1a** (0-20 μM) in MCF-7 yielded higher readout of MitoSOX fluorescence, confirming the generation of ROS species. (Figure 3.22B). Increased ROS levels lead to alteration of mitochondrial membrane potential (MMP), a hallmark of cells experiencing cell death through the intrinsic apoptotic pathway.

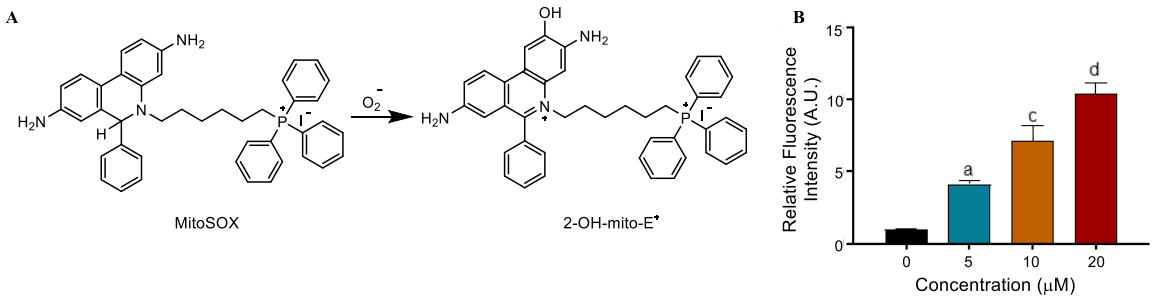

Figure 3.22 Chemical reaction of oxidation of MitoSOX dye in the presence of reactive active species (ROS) (**A**). Quantification of dose-dependent mitochondrial ROS generation in MCF−7 cells incubated with **1a** by MitoSOX dye (5 μM) (**B**).

Since compound **1a** was involved in perturbing chloride ion homeostasis, we attempted to measure the lysosomal pH using acridine orange dye – a membrane-permeable pH-sensitive dye, which upon accumulation in acidified organelles including acidic lysosomes emits orange fluorescence and green in deacidified, inactive lysosomes. A significant reduction in the red fluorescence with a concomitant increase in green fluorescence was observed in MCF−7 cells treated with increasing concentrations of **1a** (Figure 3.23). These observations clearly point out towards chloride transport in these cells which led to the deacidification of the lysosomes and induction of apoptosis in these cells.

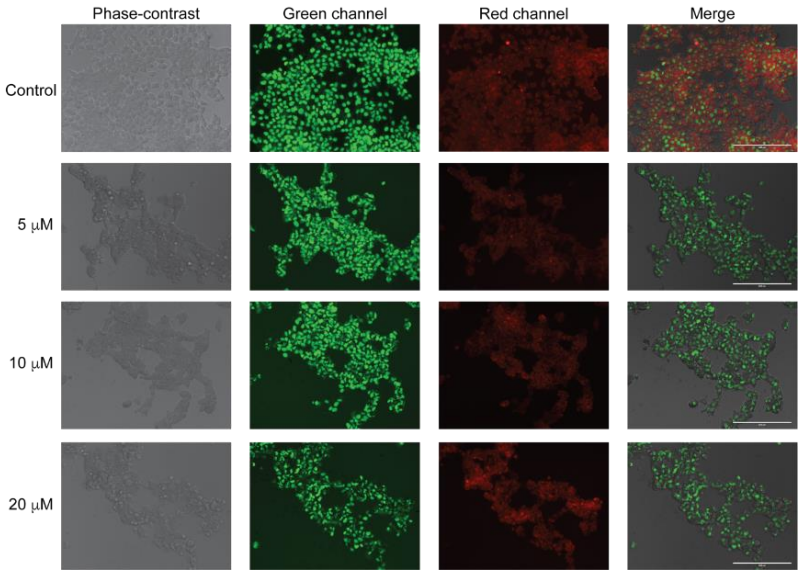

Figure 3.23 Live cell imaging of MCF−7 cells upon treating with increasing concentrations of **1a** after staining with acridine orange dye. (Magnification 20X. Scale bar: 200 μm).

3.3 Conclusion

In summary, four bisindole-based ion carriers were designed and synthesized by the fusion of indole-2-carboxylic acid and 7-aminoindole-2-carboxylate. ^{1}H NMR studies confirmed carrier binds with Cl^- through an H bonding. The ion transport activity of the anionophores **1a – 1d** were examined across HPTS-entrapped vesicles. The proper tuning of hydrophobicity and thus ion transport activity was achieved through variation of the ester moiety. The comparative studies across EYPC–LUVs⊃HPTS provided **1b** as the most active carrier. Ion selectivity of **1b** by the variation of external anions and cations showed transport activity to be cation-independent and anion-dependent. The Cl^- transport activity of carriers **1a – 1d** was confirmed across lucigenin-entrapped vesicles. Valinomycin coupled assay in lucigenin entrapped vesicles revealed antiport was the main operative ion transport mechanism. DPPC assay elucidated the molecule shuttle through a membrane by carrier mechanism. The carriers were capable of inducing cytotoxicity in MCF-7 breast cancer cells via destabilization of cellular chloride ion homeostasis. This perturbation of the cellular ion homeostasis by the bisindole carrier resulted in mitochondrial membrane depolarization, enhanced ROS generation and alteration in lysosomal pH in MCF-7 cells.

As mentioned in the introductory chapter, the primary limitation in the treatment of cancer using ion carriers is their lack of selectivity. To achieve a higher degree of selectivity, we planned the design of a procarrier (an inactive form of carrier) by the blockage of one of the ion binding sites with a photocleavable protecting group (PPG). Following irradiation with the appropriate wavelength of light, the carrier molecule will get activated by the cleavage of the PPG. Several photocleavable groups have found applications in biology and chemistry.[58] To make the procarrier, attachment of xanthene[59] and 6-nitrocoumarin-7-ylmethyl (ncm)[60] photocleavable groups to amide N-H have been attempted but unsuccessful.

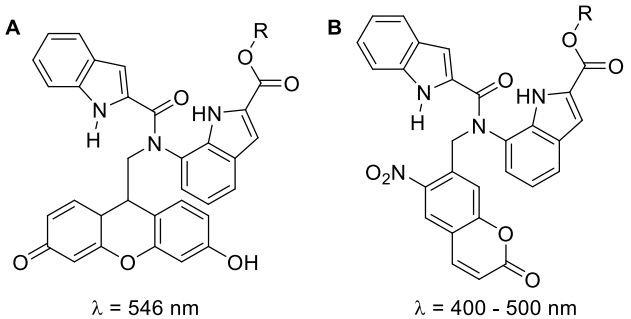

Figure 3.24 Structure of xanthene (**A**) and ncm (**B**) based procarrier.

Hence as proof of concept for photoactivated ion transport, the design of a simpler system was planned where attachment of the photocleavable group would be easier. Both the PPGs mentioned above and the bisindole carriers require multistep synthesis, hence a new simpler combination of carrier and the photocleavable group was planned.

3.4 Experimental section

3.4.1 General methods

All chemical reactions were performed under a nitrogen atmosphere. All reagents and solvents for synthesis were purchased from commercial sources (Sigma-Aldrich, Spectrochem, Avra) and used further without purification. The column chromatography was carried out using Merck silica (100–200/ 230–400 mesh size). The thin layer chromatography was performed on E. Merck silica gel 60-F254 plates. Egg yolk phosphatidylcholine (EYPC) as a solution of chloroform (25 mg/ mL), mini extruder, and polycarbonate membrane of 100 nm and 200 nm were purchased from Avanti Polar Lipid. HEPES, HPTS, lucigenin, NaOH, Triton X-100, FCCP, valinomycin, and all inorganic salts were obtained as molecular biology grade from Sigma Aldrich.

3.4.2 Physical measurements

The ^{1}H NMR spectra were recorded at 400 MHz whereas ^{13}C at 101 MHz. The residual solvent signals were considered as an internal reference (δ_H = 7.26 ppm for $CDCl_3$, δ_H = 2.50 for DMSO-*d*$_6$, δ_H = 2.05 for $(CD_3)_2CO$, and δ_H = 1.94 for CD_3CN) to calibrate spectra. The chemical shifts were reported in ppm. The following abbreviations were used to indicate multiplicity patterns m: multiplet, s: singlet, d: doublet, t: triplet, q: quartet, p: pentet, sx: sextet, dd: doublet of doublets, td: triplet of doublets. Coupling constants were measured in Hz. Infrared (IR) spectra were measured in cm^{-1} using an FT–IR spectrophotometer. Melting points were measured on a micro melting point apparatus. High-resolution mass spectra (HRMS) were recorded on electrospray ionization time-of-flight (ESI-TOF). Fluorescence experiments were recorded on Fluoromax-4 from Jobin Yvon Edison equipped with an injector port and magnetic stirrer in a microfluorescence cuvette. All buffer solutions were prepared from the autoclaved water. Adjustment of the pH of buffer solutions was made using a Helmer pH meter. The extravesicular dye was removed by performing gel chromatography using Sephadex-50. The

fluorescence studies proceeded using OriginPro 8.5.n Lipophilicity (log*P*-value) of the compound was calculated using Marvin Sketch software.

3.4.3 Synthesis

Synthesis of (2 nitrophenyl)hydrazine-1-ium chloride (3):

In 500 mL round bottom flask *o*-nitroaniline (**2**, 2.7 g, 20 mmol) in conc. HCl (40 mL) was taken and cooled at -10°C. The resulting solution was turned into suspension. To this suspension aqueous solution of $NaNO_2$ (1.39 g, 20.2 mmol 2 mL in water) was added dropwise. While addition reaction temperature was kept at 0°C. After 30 min solution of $SnCl_2.2H_2O$ in conc. HCl (15 mL) was slowly added to the reaction mixture. The reaction mixture was stirred at room temperature overnight. The precipitate was formed after the completion of the reaction. The product was filtered without the addition of HCl or water. The collected product was dried and used for the next step without purification. The crude product was obtained as a brown solid (75%).

Synthesis of ethyl (Z)-2-(2-(2-nitrophenyl)hydrazinylidene) propanoate (5):

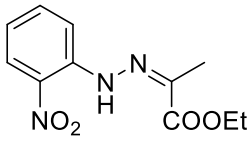

In a 25 mL round bottom flask (2 nitrophenyl) hydrazine-1-ium chloride (**3**, 200 mg, 1.06 mmol) was dissolved in methanol (6 mL). To this solution, NaOAc (104 mg, 1.27 mmol) and ethyl pyruvate (**4**, 129 µL, 1.16 mmol) was added. The resulting solution was stirred at room temperature for 5 hr. After the reaction was completed (monitored by TLC), the reaction mixture was concentrated and purified using column chromatography (Eluent: 5% ethyl acetate in petroleum ether). The product was obtained as a yellow solid (81%).

^{1}H NMR (400 MHz, $CDCl_3$): δ 10.95 (s, 1H), 8.24 – 8.18 (td, t = 8.4, 1.2 Hz, 1H), 8.04 (d, J = 8.6 Hz, 1H), 7.62 (ddd, J = 8.6, 1.4, 0.7 Hz, 1H), 6.99 (ddd, J = 8.1, 7.2, 1.0 Hz, 1H), 4.35 (q, J = 7.1 Hz, 2H), 2.24 (s, 3H), 1.40 (t, J = 7.1 Hz, 3H). **^{13}C NMR (101 MHz, $CDCl_3$):** δ 164.70 (s), 140.76 (s), 139.42 (s), 136.51 (s), 132.89 (s), 125.99 (s), 120.50 (s), 116.98 (s), 61.88 (s), 14.42 (s), 11.81 (s).

Synthesis of ethyl-7-nitro-1H-indole-2-carboxylate (6):

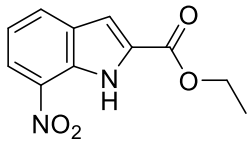

In a 100 mL round bottom flask, polyphosphoric acid (PPA, highly viscous liquid) (1 g) was heated to 110°C and stirred using a mechanical stirrer. When PPA became less viscous The ethyl (Z)-2-(2-(2-nitrophenyl)hydrazinylidene) propanoate (**5**, 360 mg, 1.42 mmol) was added to this solution and the mixture was stirred at 110°C for 20 min. Then reaction mixture was cooled to 45°C and 20 mL water was added to hydrolysed excess polyphosphoric acid, stirred for an additional 40 min. The product was extracted in ethyl acetate (3 × 10 mL), washed with brine (2 × 5 mL), dried over Na_2SO_4, filtered and concentrated under vacuum. The crude product was purified using flash chromatography. The product was obtained as a light yellow solid (60%).

^{1}H NMR (400 MHz, $CDCl_3$): δ 10.32 (s, 1H), 8.30 (d, J = 7.9 Hz, 1H), 8.03 (d, J = 7.9 Hz, 1H), 7.34 (d, J = 2.3 Hz, 1H), 7.25 (t, J = 7.6 Hz, H), 4.45 (q, J = 7.3 Hz, 2H), 1.43 (t, J = 7.3, 3H). **^{13}C NMR (101 MHz, $CDCl_3$)**: δ 160.87 (s), 131.06 (s), 131.06 (s), 130.87 (s), 129.81 (s), 122.34 (s), 120.22 (s), 109.42 (s), 61.72 (s), 14.46 (s).

Synthesis of 7-nitro-1H-indole-2-carboxylic acid (7):

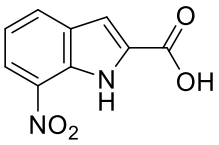

In a 50 mL round bottom flask, ethyl-7-nitro-1H-indole-2-carboxylate (**6**, 200 mg, 0.85 mmol), ethanol (5 mL) and a solution of KOH (1 mol/L, 2 mL) were mixed. The mixture was stirred and heated at 40°C. After 4 h, the reaction was completed according to the TLC detection, and then the mixture was poured into a 50 mL beaker with 10 mL water to get a clear red solution. The red solution was acidified with concentrated HCl to pH = 1-2, and a precipitate was formed. The precipitate was filtered and dried. The product was obtained as a yellow solid (91%). **^{1}H NMR (400 MHz, $CDCl_3$):** δ 13.80 (br, 1H), 11.16 (s, 1H), 8.28 (d, J = 7.6 Hz, 1H), 8.23 (d, J = 5.2 Hz, 1H), 7.42 (s, 1H), 7.36 (d, J = 5.2 Hz, 1H)

General procedure for synthesizing 7-nitro indole ester derivatives (8a – 8d):

In a 10 mL round bottom flask, 7-nitro-1H-indole-2-carboxylic acid (**7**, 100 mg, 0.486 mmol) was dissolved in dry DMF (4 mL). To this solution EDC.HCl (112 mg, 0.584 mmol), corresponding alcohol derivative (0.534 mmol), and DMAP (cat.) were added. The resulting

reaction mixture was stirred at room temperature for 18 h. After completion of product formation, DMF was evaporated. The crude mixture was dissolved in EtOAc (5 mL) and washed with Sat.$NaHCO_3$ solution (2 mL). The product was extracted with EtOAc (3 × 5 mL), and the organic phase was washed with brine (2 × 3 mL) and then dried over Na_2SO_4, filtered, and concentrated under reduced pressure. The crude product was purified by silica gel column chromatography to give pure compound **8a** – **8d**.

Ethyl 7-nitro-1H-indole-2-carboxylate (8a):

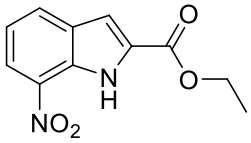

Eluent for column chromatography: 4% ethyl acetate in petroleum ether. **Physical appearance**: yellow solid. **Yield**: 85%. **^{1}H NMR (400 MHz, $CDCl_3$)**: δ 10.32 (s, 1H), 8.28 (d, *J* = 7.9 Hz, 1H), 8.03 (d, *J* = 7.9 Hz, 1H), 7.34 (d, *J* = 2.3 Hz, 1H), 7.26 (t, *J* = 7.9 Hz, 1H), 4.45 (q, *J* = 7.3 Hz, 2H), 1.43 (t, *J* = 7.9 Hz, 3H). **^{13}C NMR (101 MHz, $CDCl_3$):** δ 160.9 (s), 131.1 (s), 130.9 (s), 130.3 (s), 129.8 (s), 122.3 (s), 120.2 (s), 109.4 (s), 61.7 (s), 14.5 (s). **IR (ṽ cm^{-1}):** 3276.96, 2928.27, 1711.15, 1633.02, 1536.12, 1327.90, 1290.52, 1243.80, 1192.57, 1109.10, 1020.25, 730.88. **HRMS (ESI):** Calcd. for $C_{11}H_{11}N_2O_4$ $[M+H]^+$: 235.0719; Observed: 235.0716.

Butyl 7-nitro-1H-indole-2-carboxylate (8b):

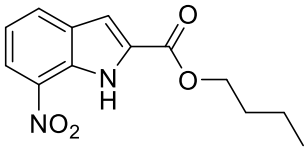

Eluent for column chromatography: 3% ethyl acetate in petroleum ether. **Physical appearance**: yellow solid. **Yield**: 92%. **^{1}H NMR (400 MHz, $CDCl_3$)**: δ 10.31 (s, 1H), 8.26 (d, *J* = 8.1 Hz, 1H), 8.01 (d, *J* = 7.8 Hz, 1H), 7.32 (d, *J* = 2.3 Hz, 1H), 7.23 (d, *J* = 6.9 Hz, 1H), 4.37 (t, *J* = 6.7 Hz, 2H), 1.80 (p, *J* = 6.8, 2H), 1.46 (sx, *J* = 7.4 Hz, 2H), 0.97 (t, *J* = 7.4 Hz, 3H). **^{13}C NMR (101 MHz, $CDCl_3$)**: δ 161.0 (s), 131.1 (s), 130.9 (s), 130.3 (s), 129.9 (s), 122.4 (s), 120.3 (s), 109.4 (s), 65.6 (s), 30.9 (s), 19.3 (s), 13.9 (s). **IR (ṽ cm^{-1}):** 3460.69, 3332.51, 2960.47, 2875.44, 1711.19, 1547.47, 1292.15, 1234.10, 832.11, 766.63, 733.95. **HRMS (ESI):** Calcd. for $C_{13}H_{15}N_2O_4$ $[M+H]^+$: 263.1032; Observed: 263.1032.

Hexyl 7-nitro-1H-indole-2-carboxylate (8c):

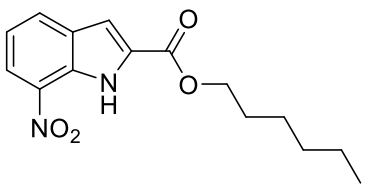

Eluent for column chromatography: 3% ethyl acetate in petroleum ether. **Physical appearance**: yellow solid. **Yield**: 85%.**^{1}H NMR (400 MHz, CDCl$_3$)**: δ 10.35 (s, 1H), 8.30 (d, *J* = 8.0 Hz, 1H), 8.05 (d, *J* = 7.9 Hz, 1H), 7.36 (d, *J* = 2.2 Hz, 1H), 7.29 (d, *J* = 8.0 Hz, 1H), 4.40 (t, *J* = 6.8 Hz, 2H), 1.80 (p, *J* = 7.0 Hz, 2H), 1.46 (p, *J* = 7.0 Hz, 2H), 1.36 (m, 4H), 0.92 (t, *J* = 7.0 Hz, 3H). **^{13}C NMR (101 MHz, CDCl$_3$)**: δ 161.0 (s), 133.7 (s), 131.2 (s), 130.9 (s), 130.4 (s), 129.9 (s), 122.4 (s), 120.3 (s), 109.4 (s), 65.9 (s), 31.6 (s), 28.8 (s), 25.8 (s), 22.7 (s), 14.1 (s). **IR (ṽ cm^{-1}):** 3455.15, 2924.69, 1713.34, 1546.92, 1337.54, 1318.65, 1291.69, 1232.58, 730.61. **HRMS (ESI):** Calcd. for $C_{15}H_{19}N_2O_4$ $[M+H]^+$: 291.1345; Observed: 291.1375.

Octyl 7-nitro-1H-indole-2-carboxylate (8d):

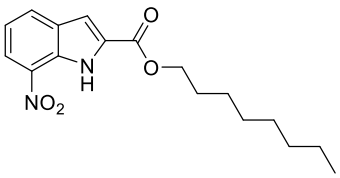

Eluent for column chromatography: 2% ethyl acetate in petroleum ether. **Physical appearance**: light yellow solid. **Yield**: 88%. **^{1}H NMR (400 MHz, CDCl$_3$)**: δ 10.33 (s, 1H), 8.28 (d, *J* = 8.0 Hz, 1H), 8.03 (d, *J* = 7.8 Hz, 1H), 7.34 (d, *J* = 2.1 Hz, 1H), 7.26 (t, *J* = 8.0 Hz, 1H), 4.38 (t, *J* = 6.8 Hz, 2H), 1.8 (p, *J* = 6.8 Hz, 2H), 1.44 (p, *J* = 6.8 Hz, 2H), 1.39 – 1.23 (m, 8H), 0.87 (t, *J* = 6.7 Hz, 3H). **^{13}C NMR (101 MHz, CDCl$_3$)**: δ 161.0 (s), 133.6 (s), 131.1 (s), 130.9 (s), 130.4 (s), 129.9 (s), 122.4 (s), 120.3 (s), 109.4 (s), 65.9 (s), 31.9 (s), 29.4 (s), 29.3 (s), 28.8 (s), 26.1 (s), 22.8 (s), 14.2 (s).

General procedure for synthesizing 7-amine indole ester derivatives (9a – 9d):

In stirring solution of compound **8a – 8d** (100 mg) in ethyl acetate (8 mL) was added Pd/C (15 mg). The solution was completely degassed three times under vacuum/N_2. The reaction mixture was reacted with H_2 (1 atm) for 2 h. After completion of the reduction process, the reaction mixture was filtered through a celite pad. The celite bed was washed with EtOAc (3 × 5 mL) and the filtrate was concentrated under reduced pressure to obtain a crude product. The crude product was purified by silica gel column chromatography to give pure compound **9a – 9d**.

Ethyl 7-amino-1H-indole-2-carboxylate (9a):

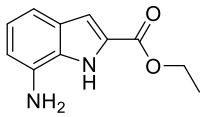

Eluent for column chromatography: 15% ethyl acetate in petroleum ether. **Physical appearance**: white solid. **Yield**: 92%. **^{1}H NMR (400 MHz, $CDCl_3$):** δ 10.02 (s, 1H), 7.23 (d, J = 2.1 Hz, 1H), 7.18 (d, J = 8.1 Hz, 1H), 6.99 (t, J = 8.0, 1H), 6.66 (dd, J = 7.4, 0.8 Hz, 1H), 4.43 (q, J = 7.1 Hz, 2H), 4.36 – 4.00 (br s, 2H), 1.44 (t, J = 7.1 Hz, 3H). **^{13}C NMR (101 MHz, $CDCl_3$):** δ 163.4 (s), 132.3 (s), 128.6 (s), 128.6 (s), 127.0 (s), 121.8 (s), 113.4 (s), 110.0 (s), 109.9 (s), 61.5 (s), 14.5 (s). **IR (ṽ cm^{-1}):** 3335.07, 1680.30, 1253.98, 1214.95, 1025.94, 828.94, 735.70, 645.5. **HRMS (ESI):** Calcd. for $C_{11}H_{13}N_2O_2$ $[M+H]^+$: 205.0977; Observed: 205.0979.

Butyl 7-amino-1H-indole-2-carboxylate (9b):

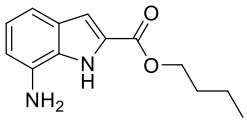

Eluent for column chromatography: 20% ethyl acetate in petroleum ether. **Physical appearance**: white solid. **Yield**: 95%. **^{1}H NMR (400 MHz, $CDCl_3$):** δ 9.63 (s, 1H), 7.22 (t, *J* = 2 Hz, 1H), 7.19 (d, *J* = 8 Hz, 1H), 6.99 (t, *J* = 8 Hz, 1H), 6.67 (d, *J* = 7.4 Hz, 1H), 4.37 (t, *J* = 6.8 Hz, 2H), 1.79 (q, *J* = 6.8 Hz, 2H), 1.50 (sx, *J* = 7.6 Hz, 2H), 1.0 (t, *J* = 7.6 Hz, 3H). **^{13}C NMR (101 MHz, $CDCl_3$)**: δ 163.0 (s), 132.0 (s), 128.7 (s), 128.6 (s), 127.2 (s), 121.8 (s), 113.8 (s), 110.4 (s), 109.7 (s), 65.2 (s), 30.9 (s), 19.4 (s), 13.9 (s). **IR (ṽ cm^{-1}):** 3366.77, 3336.15, 2959.33, 1678.44, 1285.89, 1248.37, 1209.98, 826.39, 781.61, 732.70. **HRMS (ESI):** Calcd. for $C_{13}H_{17}N_2O_2$ $[M+H]^+$: 233.1290; Observed: 233.1288.

Hexyl 7-amino-1H-indole-2-carboxylate (9c):

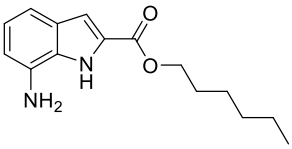

Eluent for column chromatography: 18% ethyl acetate in petroleum ether. **Physical appearance**: white solid. **Yield**: 89%. **^{1}H NMR (400 MHz, $CDCl_3$)**: δ 9.64 (s, 1H), 7.21 (d, *J* = 1.8 Hz, 1H), 7.18 (d, *J* = 8.1 Hz, 1H), 6.99 (t, *J* = 7.8 Hz, 1H), 6.66 (d, *J* = 7.4 Hz, 1H), 4.36 (t, *J* = 6.7 Hz, 2H), 4.02 (s, 2H), 1.79 (p, *J* = 6.7 Hz, 2H), 1.46 (p, *J* = 7.2 Hz, 2H), 1.36 (m, 4H), 0.91 (t, *J* = 7.0 Hz, 3H). **^{13}C NMR (101 MHz, $CDCl_3$)**: δ 163.1 (s), 132.1 (s), 128.7 (s), 128.6 (s), 127.2 (s), 121.8 (s), 113.7 (s), 110.3 (s), 109.7 (s), 65.5 (s), 31.6 (s), 28.8 (s), 25.8 (s), 22.7 (s), 14.2 (s). **IR (ṽ cm^{-1}):** 3364.06, 3328.22, 2956.93, 2927.31, 2858.55, 1682.35, 1248.18, 1215.06,

750.19, 731.53. **HRMS (ESI):** Calcd. for $C_{15}H_{21}N_2O_2$ $[M+H]^+$: 261.1603; Observed: 261.1605.

Octyl 7-amino-1H-indole-2-carboxylate (9d):

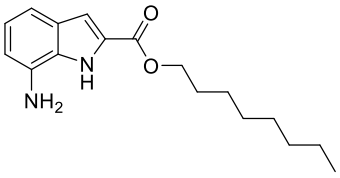

Eluent for column chromatography: 18% ethyl acetate in petroleum ether. **Physical appearance**: white solid. **Yield**: 90%. **^{1}H NMR (400 MHz, $CDCl_3$)**: δ 9.88 (s, 1H), 7.22 (d, *J* = 2.1 Hz, 1H), 7.18 (d, *J* = 8.1 Hz, 1H), 6.99 (t, *J* = 7.0 Hz, 1H), 6.66 (dd, *J* = 7.3, 0.7 Hz, 1H), 4.36 (t, *J* = 6.7 Hz, 2H), 4.11 (s, 2H), 1.8 (p, *J* = 6.9 Hz, 2H), 1.46 (p, *J* = 7.0 Hz, 2H), 1.41 – 1.24 (m, 8H), 0.89 (t, *J* = 6.9 Hz, 3H). **^{13}C NMR (101 MHz, $CDCl_3$)**: δ 163.4 (s), 132.2 (s), 128.6 (s), 127.1 (s), 121.8 (s), 113.5 (s), 110.1 (s), 110.0 (s), 109.8 (s), 65.6 (s), 31.9 (s), 29.4 (s), 29.3 (s), 28.8 (s), 26.2 (s), 22.8 (s), 14.3 (s). **IR ($\tilde{\nu}$ cm^{-1}):** 3442.57, 3330.35, 2922.56, 2855.10, 1687.35, 1289.18, 1245.74, 1215.99, 825.82, 780.14, 731.19. **HRMS (ESI):** Calcd. for $C_{17}H_{25}N_2O_2$ $[M+H,]^+$: 289.1916; Observed: 289.1918.

General procedure for synthesizing bisindole-based carrier (1a-1d):

To a solution of indole-2-carboxylic acid (200 mg, 1.24 mmol) in CH_2Cl_2 (2 mL), thionyl chloride (0.36 mL, 4.96 mmol) and 2 drops of DMF were added. The reaction mixture was stirred for 1 h at room temperature. Then the solvent was evaporated to dryness in *vacuo* to give indole-2-carbonyl chloride. The residue was dissolved in $CHCl_3$ (3 mL). This solution was added dropwise to the mixture of **4a – 4d** (0.6836 mmol) and DMAP (0.6836 mmol) in $CHCl_3$ (3 mL). The reaction mixture was stirred for 1 h and quenched with water. Following extraction with CH_2Cl_2 (3 × 5 mL), the organic phase was washed with brine (2 × 4 mL) and then dried over Na_2SO_4, filtered, and concentrated under reduced pressure. The crude product was purified by silica gel column chromatography to give pure compound **1a – 1d**.

Ethyl 7-(1H-indole-2-carboxamido)-1H-indole-2-carboxylate (1a):

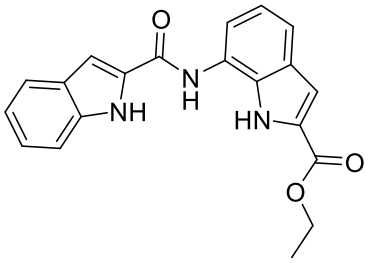

Eluent for column chromatography: 15% ethyl acetate in petroleum ether. **Physical appearance**: white solid. **Yield**: 30%. **^{1}H NMR (400 MHz, DMSO-*d*$_6$)**: δ 11.99 (s, 1H), 11.81 (s, 1H), 10.06 (s, 1H), 7.99 – 7.91 (m, 1H), 7.73 (d, J = 8.0 Hz, 1H), 7.52 – 7.48 (m, 3H), 7.28 – 7.21 (m, 2H), 7.18 – 7.06 (m, 2H), 4.38 (q, J = 7.1 Hz, 2H), 1.36 (t, J = 7.1 Hz, 3H). **^{13}C NMR (101 MHz, DMSO-*d*$_6$):** δ 161.3 (s), 160.1 (s), 136.9 (s), 131.4 (s), 129.6 (s), 128.4 (s), 127.4 (s), 127.0 (s), 124.1 (s), 123.8 (s), 121.7 (s), 120.5 (s), 120.0 (s), 118.3 (s), 116.9 (s), 112.4 (s), 108.4 (s), 104.4 (s), 60.6 (s), 14.3 (s).. **IR (ṽ cm^{-1}):** 3325.26, 3255.64, 2926.01, 1692.96, 1628.27, 1535.13, 1418.37, 1374.84, 1309.20, 1242.92, 1202.05, 1119.38, 1020.28, 738.01. **HRMS (ESI):** Calcd. for $C_{20}H_{18}N_3O_3$ $[M+H]^+$: 348.1348; Observed: 348.1352.

Butyl 7-(1H-indole-2-carboxamido)-1H-indole-2-carboxylate (1b):

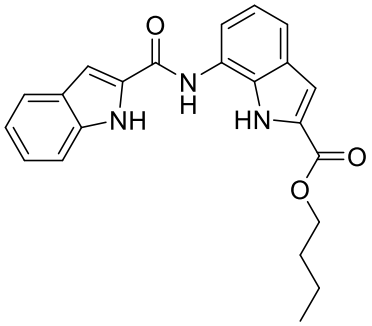

Eluent for column chromatography: 10% ethyl acetate in petroleum ether. **Physical appearance**: white solid. **Yield**: 37%. **^{1}H NMR (400 MHz, Acetone- *d*$_6$):** δ 11.00 (s, 2H), 9.80 (s, 1H), 7.70 (d, *J* = 8.0 Hz, 1H), 7.61 (d, *J* = 8.3 Hz, 1H), 7.57 (dd, *J* = 7.8, 3.5 Hz, 2H), 7.45 (s, 1H), 7.29 (t, *J* = 7.6 Hz, 1H), 7.24 (d, *J* = 1.9 Hz, 1H), 7.13 (td, *J* = 7.6, 4.8 Hz, 2H), 4.35 (t, *J* = 6.6 Hz, 2H), 1.76 (q, *J* = 6.8 Hz, 2H), 1.49 (sx, *J* = 7.6 Hz, 2H), 0.98 (t, *J* = 7.4 Hz, 3H). **^{13}C NMR (101 MHz, Acetone- *d*$_6$):** δ 162.4 (s), 161.1 (s), 138.3 (s), 132.1 (s), 131.1 (s), 130.6 (s), 129.0 (s), 128.8 (s), 125.3 (s), 125.0 (s), 122.9 (s), 121.5 (s), 121.3 (s), 120.2 (s), 118.4 (s), 113.3 (s), 109.2 (s), 105.2 (s), 65.3 (s), 31.7 (s), 19.9 (s), 14.1 (s). **IR (ṽ cm^{-1}):** 3305.42, 2959.83, 1693.99, 1643.28, 1537.13, 1417.39, 1309.48, 1243.79, 1202.49, 739.32. **HRMS (ESI):** Calcd. for $C_{22}H_{22}N_3O_3$ $[M+H]^+$: 376.1661; Observed: 376.1655.

Hexyl 7-(1H-indole-2-carboxamido)-1H-indole-2-carboxylate (1c):

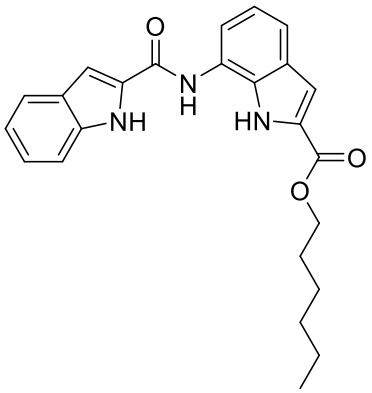

Eluent for column chromatography: 10% ethyl acetate in petroleum ether. **Physical appearance**: white solid. **Yield**: 30%. **^{1}H NMR (400 MHz, DMSO-*d*$_6$)**: δ 11.99 (s, 1H), 11.81 (s, 1H), 10.06 (s, 1H), 7.95 (d, *J* = 7.7 Hz, 1H), 7.72 (d, *J* = 8.0 Hz, 1H), 7.50 (t, *J* = 5.6 Hz, 3H), 7.25 (d, *J* = 7.3 Hz, 1H), 7.22 (s, 1H), 7.16 – 7.06 (m, 2H), 4.33 (t, *J* = 6.5 Hz, 2H), 1.73 (p, *J* = 6.4, 2H), 1.41 (p, *J* = 7.2 Hz, 2H), 1.32 (m, 4H), 0.88 (t, *J* = 6.3 Hz, 3H). **^{13}C NMR (101 MHz, DMSO-*d*$_6$)**: δ 161.4 (s), 160.1 (s), 136.9 (s), 131.4 (s), 129.7 (s), 128.4 (s), 127.3 (s), 127.0 (s), 124.1 (s), 124.0 (s), 121.7 (s), 120.5 (s), 120.0 (s), 118.4 (s), 116.9 (s), 112.4 (s), 108.3 (s), 104.5 (s), 64.6 (s), 30.9 (s), 28.3 (s), 25.1 (s), 22.0 (s), 13.9 (s). **IR (ṽ cm^{-1}):** 3333.85, 3301.67, 3248.29, 1690.49, 1627.04, 1535.74, 1265.53, 738.07. **HRMS (ESI):** Calcd. for $C_{24}H_{25}N_3NaO_3$ $[M+Na]^+$: 426.1794; Observed: 426.1794.

Octyl 7-(1H-indole-2-carboxamido)-1H-indole-2-carboxylate (1d):

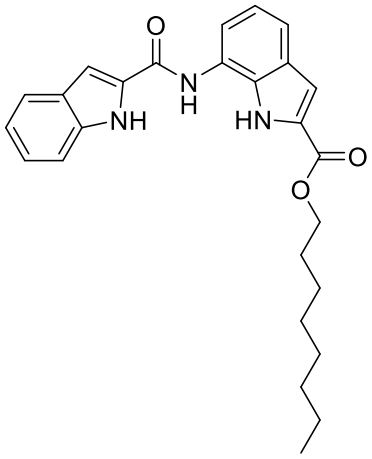

Eluent for column chromatography: 8% ethyl acetate in petroleum ether. **Physical appearance**: white solid. **Yield**: 40%. **^{1}H NMR (400 MHz, DMSO-*d*$_6$)**: δ 11.96 (s, 1H), 11.80 (s, 1H), 10.07 (s, 1H), 7.92 (d, *J* = 7.7 Hz, 1H), 7.71 (d, *J* = 7.8 Hz, 1H), 7.51 (d, *J* = 3.6 Hz, 1H), 7.49 – 7.47 (m, 2H), 7.25 (d, *J* = 7.3 Hz, 1H), 7.22 (d, *J* = 2.1 Hz, 1H), 7.12 (t, *J* = 8 Hz, 1H), 7.09 (t, *J* = 8 Hz, 1H), 4.31 (t, *J* = 6.6 Hz, 2H), 1.71 (p, *J* = 6.9 Hz, 2H), 1.38 (m, 2H), 1.27 (m, 8H), 0.83 (t, *J* = 5.9 Hz, 3H). **^{13}C NMR (101 MHz, DMSO-*d*$_6$)**: δ 161.5 (s), 160.2 (s), 136.9 (s), 131.4 (s), 129.7 (s), 128.5 (s), 127.4 (s), 127.0 (s), 124.2 (s), 124.0 (s), 121.8 (s), 120.6 (s), 120.0 (s), 118.4 (s), 117.0 (s), 112.5 (s), 108.4 (s), 104.5 (s), 64.6 (s), 31.3 (s), 28.7 (s), 28.6 (s), 28.3 (s), 25.5 (s), 22.1 (s), 14.0 (s). **IR (ṽ cm^{-1}):** 3333.76, 2921.59, 1693.78, 1625.21, 1532.96, 1260.42, 740.50. **HRMS (ESI):** Calcd. for $C_{26}H_{30}N_3O_3$ $[M+H]^+$: 432.2287; Observed: 432.2284.

3.4.4 Anion binding studies by ^{1}H NMR:

The ^{1}H NMR titration study was conducted at ambient temperature on a Bruker Avance III HD 400 MHz spectrometer. The titration with Cl^- ion was conducted by addition of aliquots of tetrabutylammonium chloride (TBACl) solution (0.2 M in 1:9 CD_3COCD_3 + CD_3CN) to a solution of the receptor in 1:9 CD_3COCD_3 + CD_3CN (0.002 M). The spectra were calibrated using the residual signal from CD_3CN (δH = 1.94 ppm) as an internal reference. TBACl was dried under vacuum in a desiccator prior to use.[61, 62]

3.4.5 Ion transport studies

Ion transport studies across EYPC–LUVs⊃HPTS

The ion transport studies across EYPC-LUVs⊃HPTS were performed by following the vesicle preparation protocol 1 and assay protocol 1 mentioned in Chapter 2.

Ion selectivity studies across EYPC–LUVs⊃HPTS

The ion selectivity of most active carrier **1b** across EYPC-LUVs⊃HPTS was investigated by following the vesicle preparation protocol 1 and assay protocols 2 and 3 mentioned in Chapter 2.

Ion transporting activity studies across EYPC–LUVs⊃lucigenin

Preparation of EYPC–LUVs⊃lucigenin (Vesicle preparation protocol 2): The thin transparent film of egg yolk phosphatidylcholine (EYPC) was prepared by the slow evaporation of 1 mL chloroform solution of EYPC (25 mg/mL in chloroform) under nitrogen gas. The thin transparent film was kept on a high vacuum to remove all traces of chloroform for 4–5 h. After that, a thin transparent film was hydrated with 1 mL aqueous $NaNO_3$ solution (200 mM, 1 mM lucigenin) by giving vertex at 10-minute intervals for 1 h. The resulting suspension was subjected to 15 cycles of freeze-thaw (liquid nitrogen, 55 °C) followed by extrusion through a 200 nm polycarbonate membrane 21 times, to access vesicles of average 200 nm diameter. The extravesicular HPTS dye was removed by size exclusion chromatography using Sephadex G50 (stationary phase) with eluting aqueous $NaNO_3$ (200 mM). Finally, vesicles were diluted to 4 mL to get EYPC–LUVs⊃lucigenin. *Final conditions*: ~ 5 mM EYPC, Inside: 1 mM lucigenin, 200 mM $NaNO_3$, Outside: 200 mM $NaNO_3$.

Ion transport activity by lucigenin assay (Assay protocol 4): In a clean and dry fluorescence cuvette, 1975 µL aqueous $NaNO_3$ (200 mM) and 25 µL EYPC-LUVs⊃lucigenin vesicles were taken. The cuvette was placed in fluorescence instrument furnishes with slow stirring conditions (t = 0). After 20 s, a NaCl pulse (2 M, 33.3 µL) was given to create a chloride gradient across the intra and extravesicular system. The time-dependent quenching of fluorescence intensity of lucigenin at λ_{em} = 535 nm (λ_{ex} = 455 nm) was monitored after the addition of carrier molecule at t = 100 s. Finally, vesicles were lysed upon the addition of 10% Triton X-100 (20 µL) at t = 300 s for the complete dissipation of the chloride gradient.

The time-dependent data were normalized to percent change in fluorescence intensity using Equation 4:

$$I_F = [(I_t - I_0) / (I_\infty - I_0)] \times (-100) \qquad \text{Equation 4}$$

Where I_0 is the initial intensity, I_t is the intensity at time t, I_∞ is the final intensity after the addition of triton X-100.

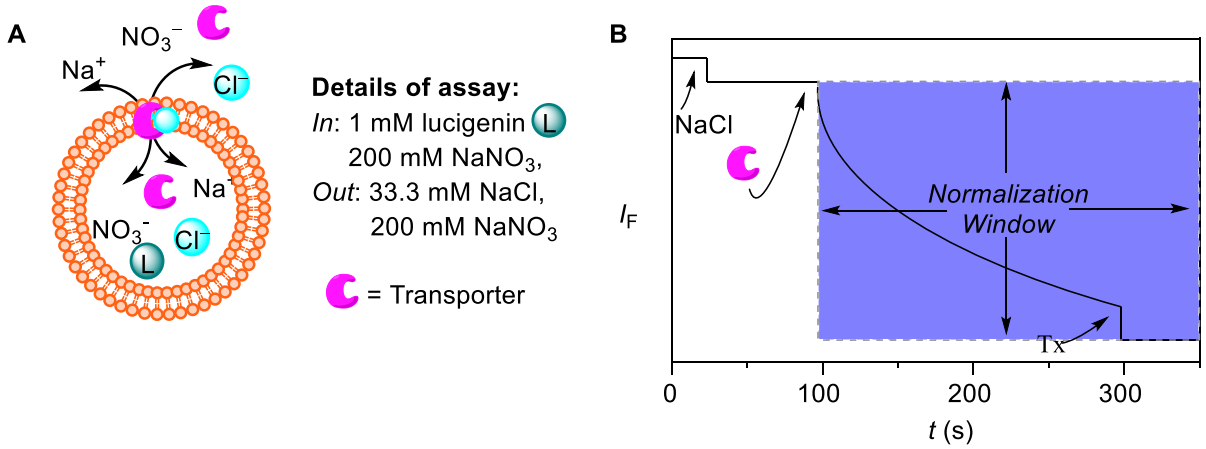

Figure 3.25 Schematic representation of fluorescence-based ion transport activity assay using EYPC–LUVs⊃lucigenin (**A**), and illustration of ion transport kinetics showing normalization window (**B**).

Cation selectivity assay across EYPC–LUVs⊃lucigenin vesicles (Assay protocol 5): The vesicles were prepared by following the same protocol (vesicle preparation protocol 2) as stated above. In a clean and dry fluorescence cuvette, 1975 µL aqueous $NaNO_3$ (200 mM) and 25 µL EYPC-LUVs⊃lucigenin vesicles were taken. The cuvette was placed in fluorescence

instrument furnishes with slow stirring conditions (t = 0). After 20 s, a chloride salt of different cations, MCl (where M^+ = Li^+, Na^+, K^+, Rb^+, and Cs^+) (2 M, 33.3 µL) was given to create a chloride gradient across the intra and extravesicular system. The time-dependent quenching of fluorescence intensity of lucigenin at λem = 535 nm (λex = 455 nm) was monitored after the addition of carrier molecule at t = 100 s. Finally, vesicles were lysed upon the addition of 10% Triton X-100 (20 µL) at t = 300 s for the complete dissipation of the chloride gradient. The time-dependent data were normalized to the percent change in fluorescence intensity using Equation 4.

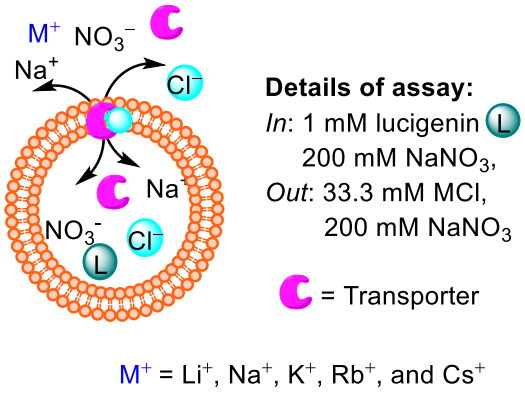

Figure 3.26 Schematic representation of fluorescent-based cation selectivity assay by the variation of extravesicular cations across EYPC–LUVs⊃lucigenin.

Ion transport activity across EYPC–LUVs⊃lucigenin in the presence of valinomycin: The antiport mechanism (i.e., simultaneous transport of two different ions, in opposite directions, across the membrane) of **1b** was experimentally confirmed by lucigenin assay in the presence and absence of valinomycin (selective natural K^+ carrier). The ion transport activity of **1b** was monitored in a vesicle entrapped with lucigenin (1 mM) and $NaNO_3$ (200 mM) suspended in KCl (2 M) solution with and without valinomycin.

Preparation of EYPC–LUVs⊃lucigenin: The vesicles were prepared by the following vesicle preparation protocol 2 as stated above.

Antiport mechanism (Assay protocol 6): In clean and dry fluorescence cuvette, 1975 µL aqueous $NaNO_3$ (200 mM) and 25 µL EYPC-LUVs⊃lucigenin vesicles were taken. The cuvette was placed in fluorescence instrument furnishes with slow stirring conditions (t = 0). After 20 s, a solution of KCl (2 M, 33.3 µL) was added to create a chloride gradient across

intra and extravesicular systems, followed by the addition of valinomycin (0.2 μM) at t = 50 s and carrier **1b** (1 μM) at t = 100 s. The time-dependent quenching of fluorescence intensity of lucigenin at λ_{em} = 535 nm (λ_{ex} = 455 nm) was monitored as the course of time. Finally, vesicles were lysed upon the addition of 10% Triton X-100 (20 μL) at t = 300 s for the complete dissipation of the chloride gradient. The time-dependent data were normalized to percent change in fluorescence intensity using Equation 4.

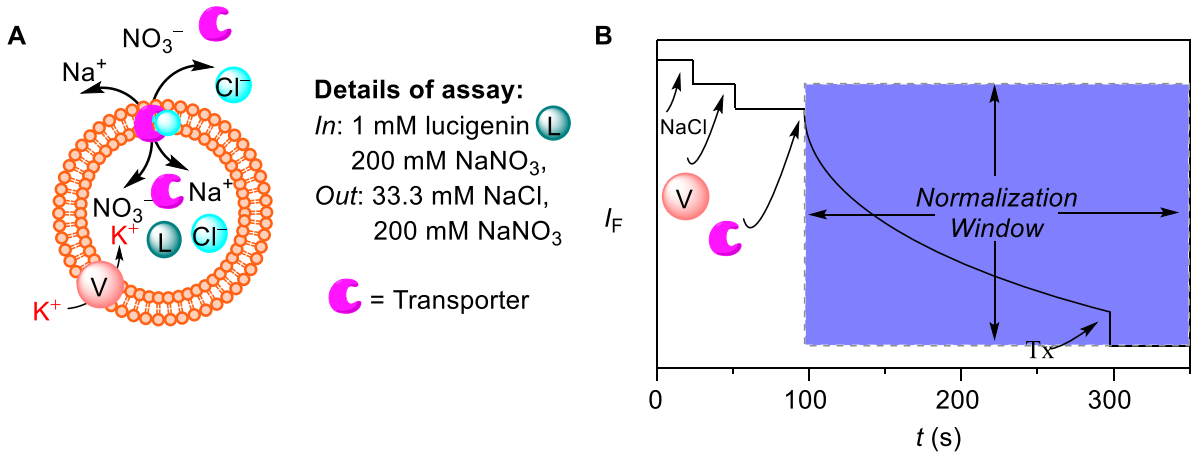

Figure 3.27 Representative fluorescence-based valinomycin assay using EYPC-LUVs⊃lucigenin (**A**) and representation of ion transport kinetics showing normalization window (**B**).

Ion transport activity studies across DPPC-LUVs⊃HPTS (Carrier vs channel mechanism):

Preparation of HEPES buffer and stock solutions: The buffers and stock solutions were prepared in the same as for EYPC-LUVs⊃HPTS.

Preparation of DPPC-LUVs⊃HPTS in NaCl: 12.5 mg of 1,2-dipalmitoyl-*sn*-glycero-3-phosphocholine (DPPC) was dissolved in 0.5 ml of HPLC grade chloroform and a thin film of the lipid was prepared by slow evaporation of chloroform under nitrogen gas. It was then kept on a high vacuum for 5 h to remove all traces of chloroform. After that, the thin transparent film was hydrated with 0.5 mL HEPES buffer (10 mM HEPES, 100 mM NaCl, 1 mM HPTS) by giving vertex at 10-minute intervals for 1 h. The resulting suspension was subjected to 15 cycles of freeze-thaw (liquid nitrogen, 55 °C) followed by extrusion through a 200 nm polycarbonate membrane 35 times, to access vesicles of average 200 nm diameter. The extravesicular HPTS dye was removed by the size exclusion chromatography using Sephadex-

G50 (stationary phase) with HEPES buffer (1 mM HPTS, 10 mM HEPES, 100 mM NaCl, pH = 7.0) as the mobile phase. Finally, vesicles were diluted to 3 mL to get DPPC-LUVs⊃HPTS. *Final conditions*: ~5.5 mM DPPC, Inside: 1 mM HPTS, 10 mM HEPES, 100 mM NaCl, pH = 7.0, Outside: 10 mM HEPES, 100 mM NaCl, pH = 7.0.

Ion transport assay across DPPC-LUVs⊃HPTS: The DPPC assay was conducted on a HORIBA Jobin Yvon Fluoromax+ spectrofluorometer equipped with an injector port, and a Quantum Northwest, Inc. (QNW) Luma 40 Peltier-based temperature-controlled cuvette holder, with temperature control achieved using a QNW TC-1 temperature controller. The experiments were conducted in the same way as in ion transport studies with EYPC-LUVs⊃HPTS. Temperatures of 25 °C and 45 °C for experiments were maintained using the temperature-controlled cuvette holder. The time-dependent data were normalized to percent change in fluorescence intensity using Equation 1 (Chapter 2).

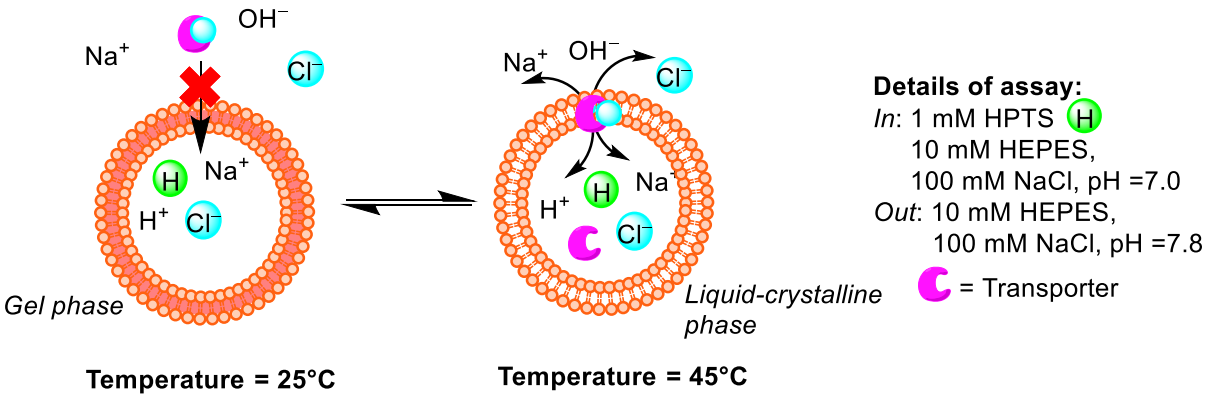

Figure 3.28 Schematic representation of DPPC assay.

3.4.6 Theoretical calculations

Initial prediction of the most probable geometry of molecules/complexes were first conducted with CONFLEX 8 conformation search software package[63, 64] using MMFF94S (2010-12-04HG) force field with a search limit of 10 kcal/mol. The DFT geometry optimization and energy calculation of the initial model obtained/constructed was conducted on Gaussian 09 program suite[34] the B3LYP exchange-correlation functional[65, 66] and the 6-31G(d,p) basis set.[67, 68] The zero-point energy (ZPE) and basis set superposition error (BSSE) of each complex were calculated and used in the following equation to obtain the binding energy (BE)-

$$BE = [HF_{HG} + ZPE_{HG} + BSSE_{HG}] - n_H*[HF_H + ZPE_H] - n_G*[HF_G] \quad \text{(Equation 5)}$$

where H = host (receptor), G = guest (Cl^-), HF_{HG} = electronic energy of host-guest complex, ZPE_{HG} = ZPE of host-guest complex, $BSSE_{HG}$ = BSSE of host-guest complex, HF_H = electronic energy of host, ZPE_H = ZPE of host, HF_G = electronic energy of guest, n_H = number of host (receptor) species, n_G = number of guest (Cl^-) species.

3.4.7 Biological studies

Cell culture

Biological studies were carried out in the human breast cancer cells, namely, MCF-7 and the non-cancerous MEFs (mouse embryonic fibroblasts). These cells were grown in high glucose containing Dulbecco's Modified Eagle Medium (DMEM; Lonza) containing 2 mM of L-glutamine supplemented with 10% fetal bovine serum (FBS; Invitrogen), and 100 units/mL penicillin and 100 µg/ml streptomycin (Invitrogen). Cells were maintained in tissue culture-treated T25 flasks at 37 °C in a humidified 5% CO_2 incubator (Thermo Scientific) until they achieved 80% confluence and were split in 1:3 ratios every alternate day.

Assessment of cellular viability by MTT assay

To check the anti-cancer activity of the bisindole compounds (**1a**-**1d**), **a** cellular viability assay was performed using MTT (3-[4,5-dimethylthiazol-2-yl]-2,5 diphenyl tetrazolium bromide). Briefly, cells were seeded in a tissue culture-treated 96-well plate (Corning) at a density of 8 x 10^3 cells/well/100 µl in DMEM and incubated at 37 °C in a humidified 5% CO_2 incubator for a period of 24 h. Post incubation, the cells were treated with increasing concentrations (range 1-20 µM) of the **1a**, **1b**, **1c**, and **1d** compounds for a period of 24 h. Subsequently, the media was removed, MTT solution (0.5 mg/ml MTT in PBS) was added and the plates were incubated in the dark at 37 °C for an additional 4 h. The formazan crystals, thus formed, were dissolved using solubilization buffer (10% SDS/0.1N HCl in PBS) by incubating the plates overnight at room temperature. Absorbance was measured at 570 nm using a multi-mode plate reader (Hidex). All experiments were performed in triplicate (N = 3). Cellular viability was expressed as the percentage of viable cells for each treatment when compared with the untreated cells (control, set as 100%).

Chloride-based cell death studies

HBSS buffer composition: Hank's balanced salt solution with chloride (HBSS with Cl^-) was prepared with the following components: 136.9 mM NaCl, 5.5 mM KCl, 0.34 mM Na_2HPO_4, 0.44 mM KH_2PO_4, 0.81 mM $MgSO_4$, 1.25 mM $CaCl_2$, 5.5 mM D-glucose, 4.2 mM $NaHCO_3$ and 10 mM HEPES (pH 7.4). Likewise, chloride-free HBSS (HBSS without Cl^-) was prepared using the following constituents: 136.9 mM Na-gluconate, 5.5 mM K-gluconate, 0.34 mM Na_2HPO_4, 0.44 mM KH_2PO_4, 0.81 mM $MgSO_4$, 1.25 mM Ca-gluconate, 5.5 mM D-glucose, 4.2 mM $NaHCO_3$ and 10 mM HEPES (pH 7.4).

MCF-7 cells were seeded in 96-well tissue culture-treated plates (Corning) at a density of 8 x 10^3 cells/well/100 µl in a complete DMEM medium and incubated at 37 °C in a humidified 5% CO_2 incubator for 24 h. Post incubation, the cellular media was replaced by 100 µl HBSS buffer (either with Cl^- or without Cl^-) containing 10% fetal bovine serum, and 100 units/mL penicillin and 100 µg/ml streptomycin and cells were treated with increasing concentrations (range 1-20 µM) of **1a** compound for 24h. After incubation, MTT solution (5 mg MTT/mL of PBS) was added to each well and incubated for an additional 4 h. After 4 h, formazan crystals were dissolved using solubilization buffer (10% SDS/0.1N HCl in PBS) by incubating the plates overnight at room temperature. The absorbance was measured at 570 nm using a multi-mode plate reader (Hidex).

Cell cycle analysis

MCF-7 cells were dispersed in 35 mm tissue culture-treated plates (Corning) at the density of 8 x 10^3 cells/well/100 µl in complete DMEM media and were incubated at 37 °C in a 5% CO2 incubator overnight for recovery. Post-recovery, the cells were treated with increasing concentration of **1a** (0-20 µM) for 24 h. After incubation, cells were harvested by trypsinization, washed with ice-cold 1X PBS and fixed with 70% methanol at -20 °C overnight. Subsequently, the cells were resuspended in PBS buffer containing 1 µL RNase A (stock 20 mg/ml; Himedia) and incubated for 20 min at room temperature. The cells were then stained with 50 µg/ml propidium iodide (Stock-1mg/ml; Himedia) for 30 min in the dark at room temperature. The cells were analyzed by acquiring 10,000 events using a BD FACS Celesta™ flow cytometer (BD Biosciences, San Jose, CA, USA) and analyzed using FloJo software (Ashland, OR). The representative overlay of histograms has been depicted in Figure 3.14 and

the percentage of cells in the different phases of the cell cycle has been quantitated in Figure 3.14D.

Measurement of reactive oxygen species (ROS)

MCF-7 cells were seeded in 96-well tissue culture-treated plates (Corning) at a density of 8 x 10^3 cells/well/100 µl in complete DMEM medium and incubated at 37 °C in a humidified 5% CO_2 incubator for 24 h. Post incubation, the cells were treated with increasing concentrations (0-20 µM) of **1a** for another 24h. After incubation, the cells were washed with ice-cold PBS and incubated with MitoSox red reagent (5 µM, Invitrogen) for ~20 minutes at 37 °C in the dark. Following this, the cells were washed thrice with ice-cold 1X PBS, and the fluorescence intensities were read using a multi-mode plate reader (Hidex) (λ_{ex} 510 nm/λ_{em} 580 nm). All the experiments were performed in triplicate (N = 3). The readings obtained were then normalized with MTT values.

Measurement of mitochondrial membrane potential (MMP)

MCF-7 cells were seeded in 96-well tissue culture-treated plates (Corning) at a density of 8 x 10^3 cells/well/100 µl in complete DMEM medium and incubated at 37 °C in a humidified 5% CO_2 incubator for 24 h. Post incubation, the cells were treated with increasing concentrations of **1a** (0- 20 µM) for 24 h. Following this, the cells were washed with ice-cold PBS and incubated with JC-1 reagent (2 µg/ml) for ~20 minutes at 37 °C in the dark. Subsequently, the cells were washed twice with ice-cold 1X PBS and the relative fluorescence intensities were read at 485/530 nm and 510/580 nm wavelengths for quantitation using a multi-mode plate reader (Hidex). All the experiments were performed in triplicate (N=3). The readings obtained were then normalized with MTT values. The ratios of red/green fluorescence intensities were quantified and plotted. For qualitative analysis, fluorescence imaging was performed in red and green channels using EVOS FL Auto Imaging System (Life Technologies).

Acridine Orange (AO) Staining

MCF-7 cells were seeded in 24-well tissue culture-treated plates (Corning) at a density of 8 x 10^3 cells/well/100 µl in complete DMEM medium and incubated at 37 °C in a humidified 5%

CO_2 incubator for 24 h. Post incubation, the cells were treated with increasing concentrations of **1a** (0-20 µM) for 24 h. After incubation, the cells were washed with ice-cold 1X PBS and incubated with acridine orange reagent (5 µg/ml, Sigma) for ~20 minutes at 37 °C in the dark. The cells were washed thrice with ice-cold 1X PBS and fluorescence images were acquired in both red and green channels using EVOS FL Auto Imaging System (Life Technologies).

Statistical analysis

All cellular experiments were performed in triplicate unless stated otherwise. Data has been represented as Mean ± SEM, where SEM represents the standard error of the mean and is expressed as the standard deviation divided by the square root of sample size. Statistical analysis was performed using one-way analysis of variance (ANOVA) followed by Tukey HSD post-hoc test. $p < 0.05$ was considered to be statistically different when comparing different groups.

3.4.8 NMR spectra

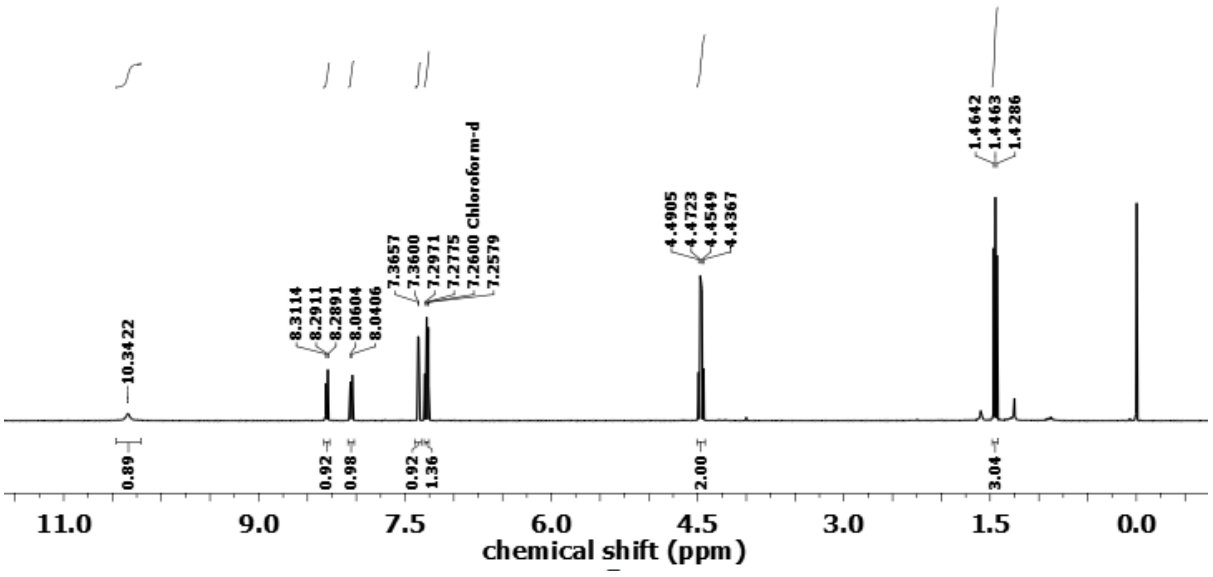

Figure 3.29 [1]H NMR spectrum of compound **3a**.

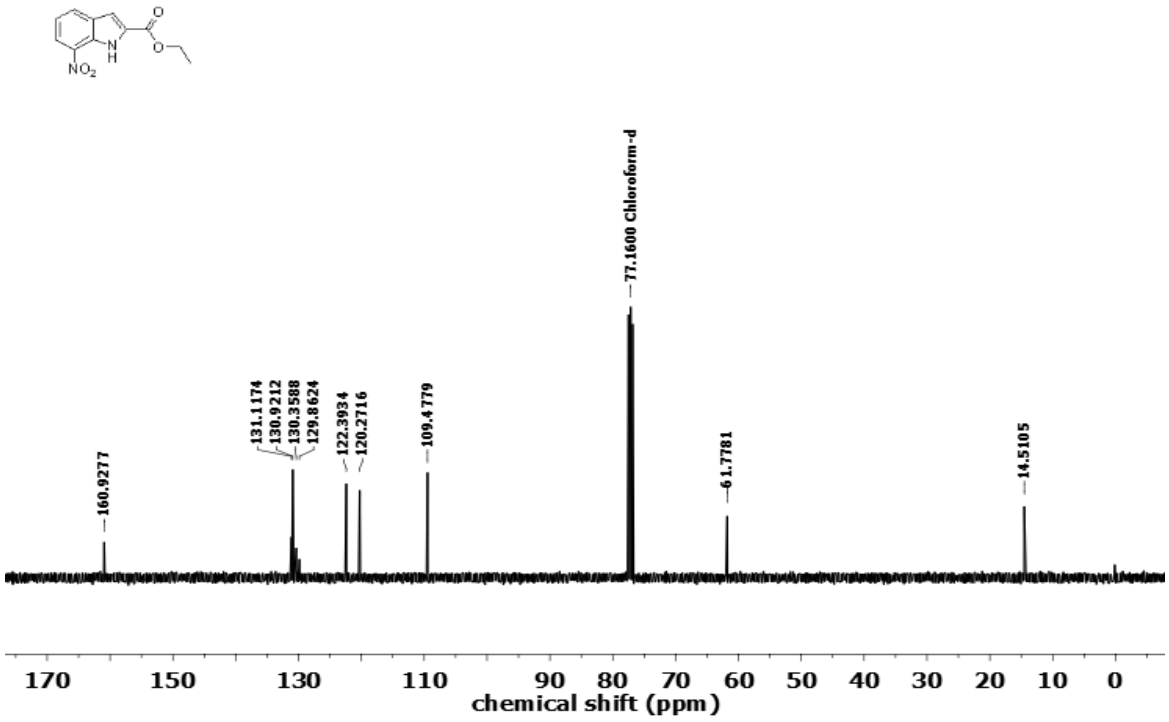

Figure 3.30 [13]C NMR spectrum of compound **3a**.

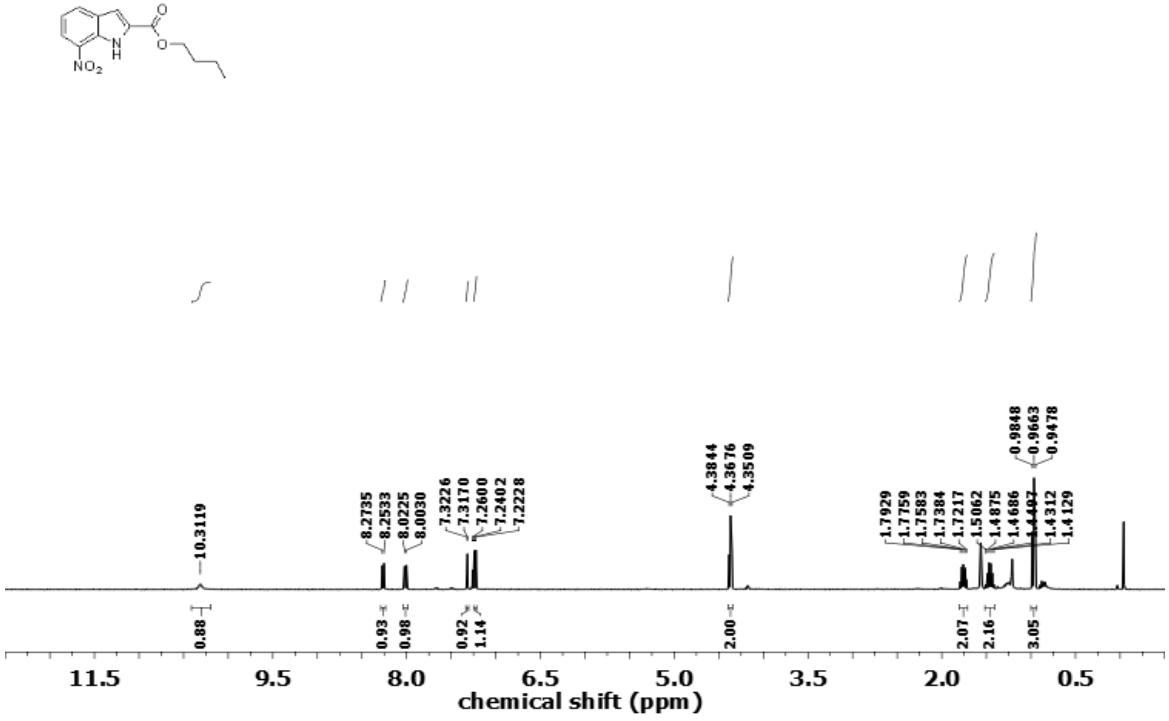

Figure 3.31 [1]H NMR spectrum of compound **3b**.

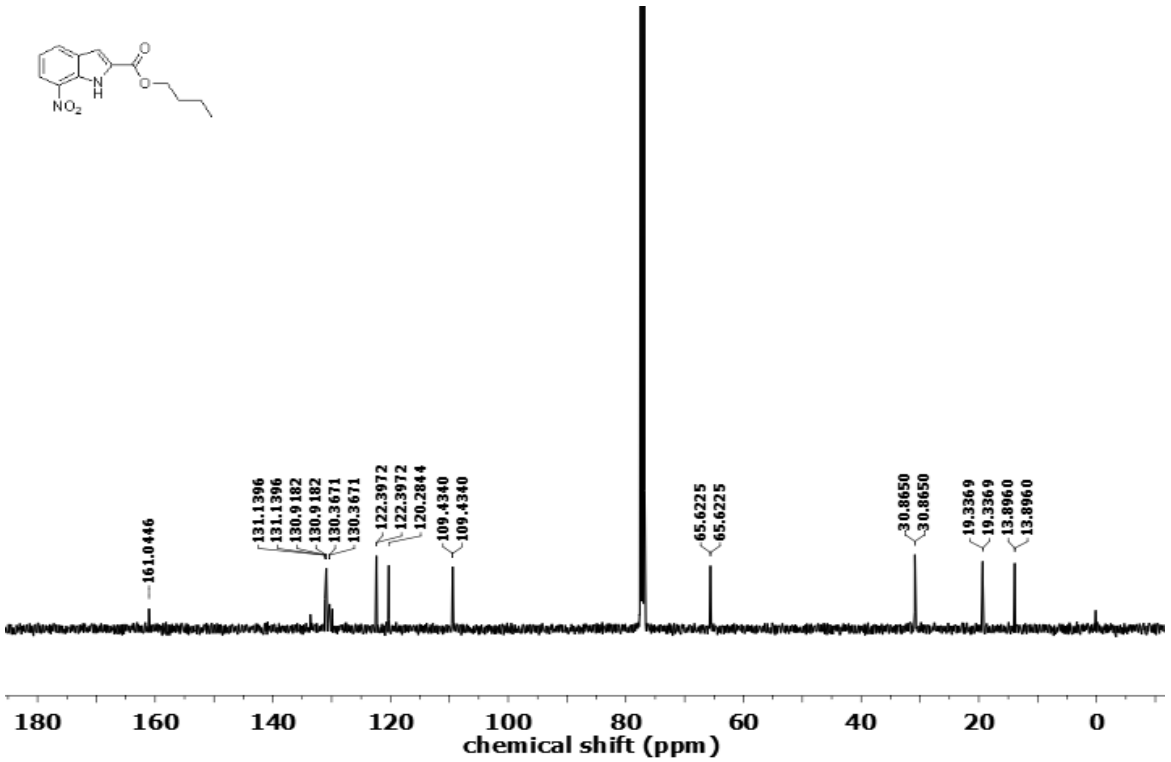

Figure 3.32 ^{13}C NMR spectrum of compound **3b**.

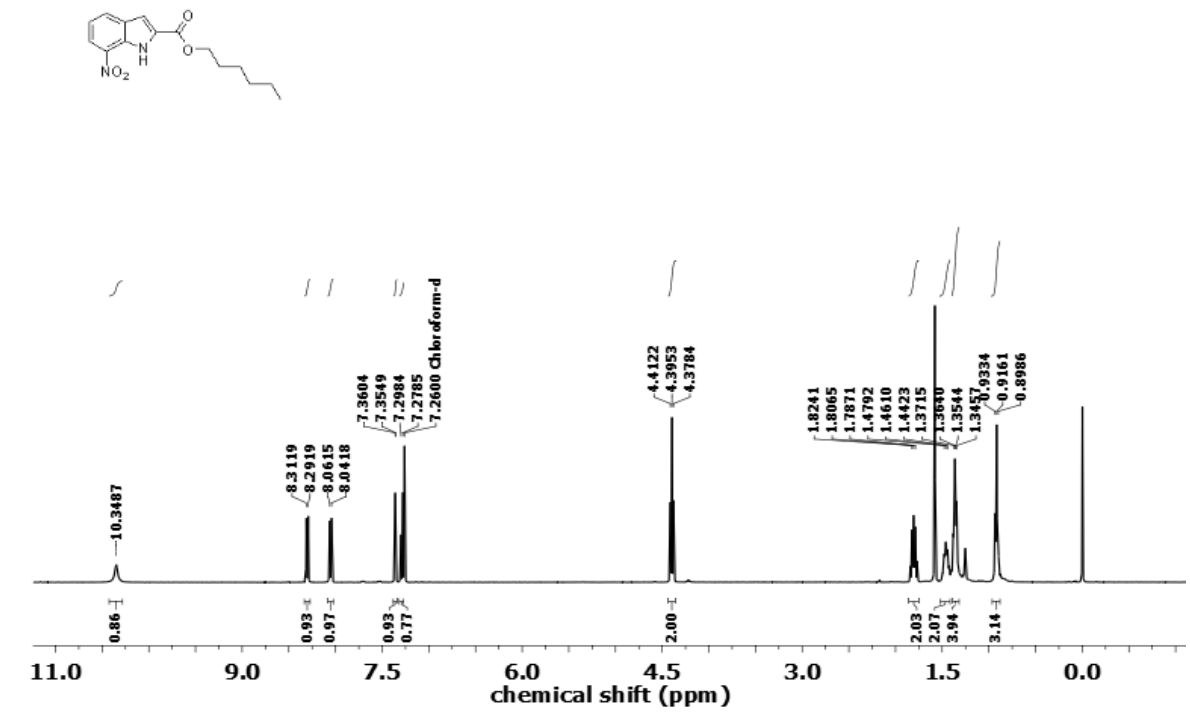

Figure 3.33 ^{1}H NMR spectrum of compound **3c**.

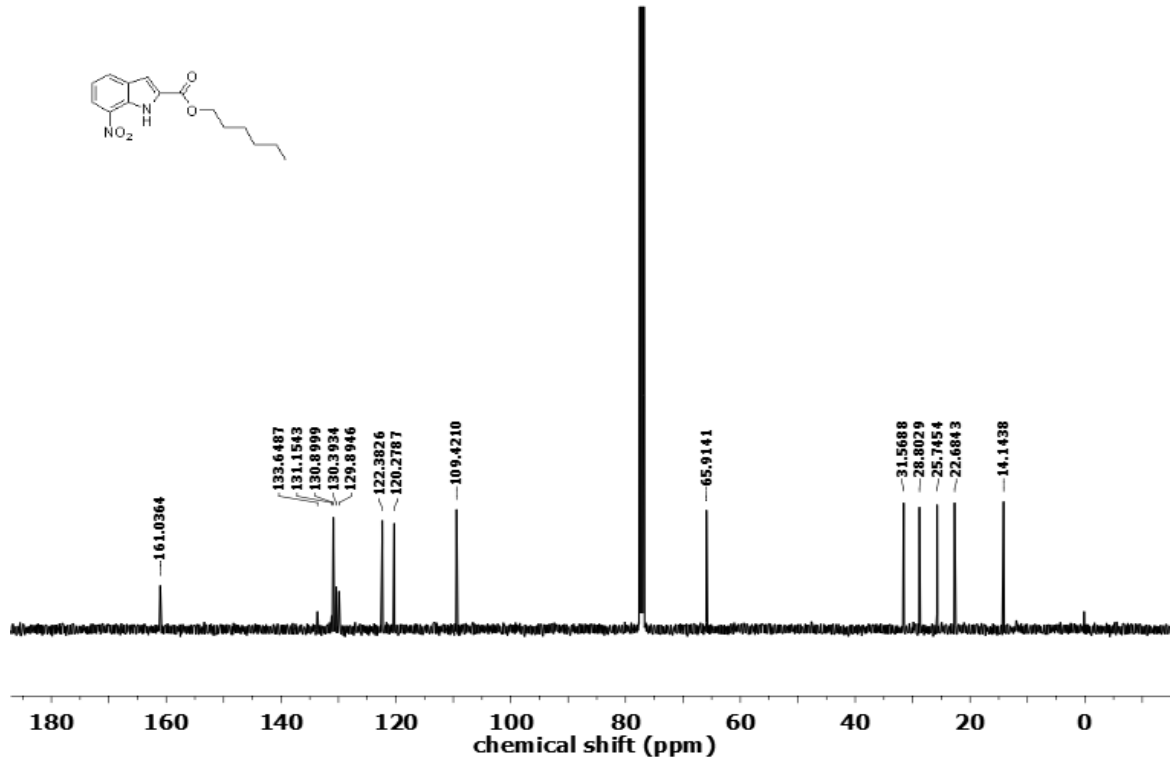

Figure 3.34 ^{13}C NMR spectrum of compound **3c**.

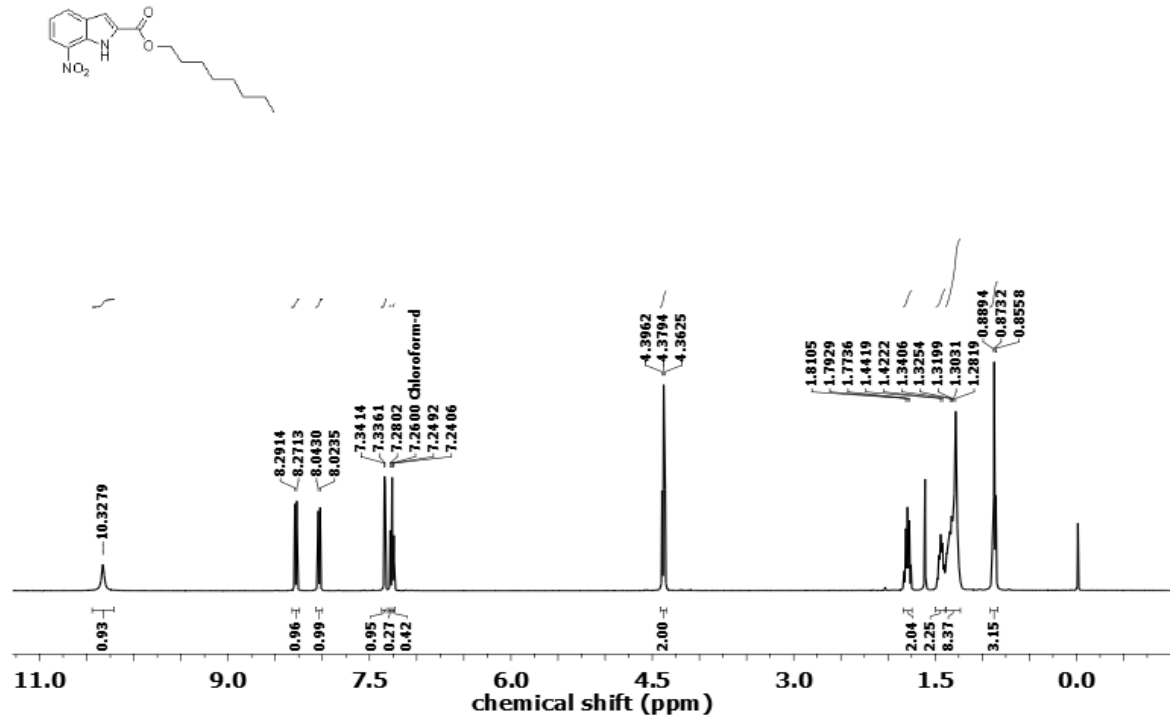

Figure 3.35 ^{1}H NMR spectrum of compound **3d**.

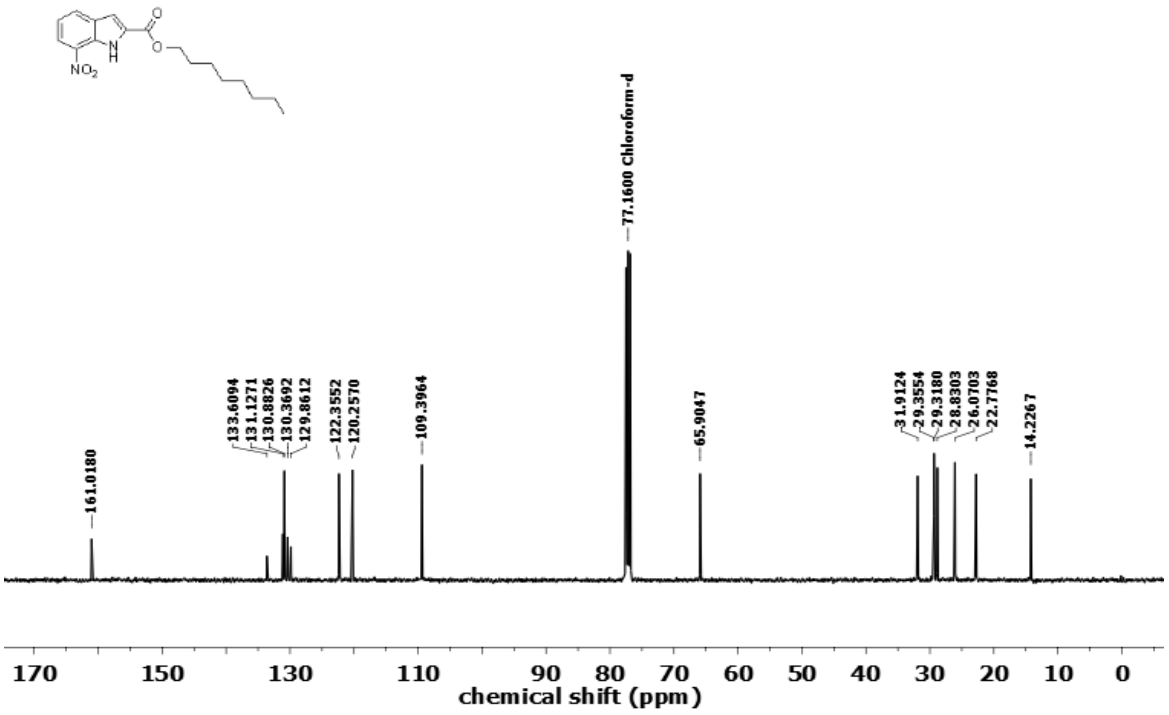

Figure 3.36 ^{13}C NMR spectrum of compound **3d**.

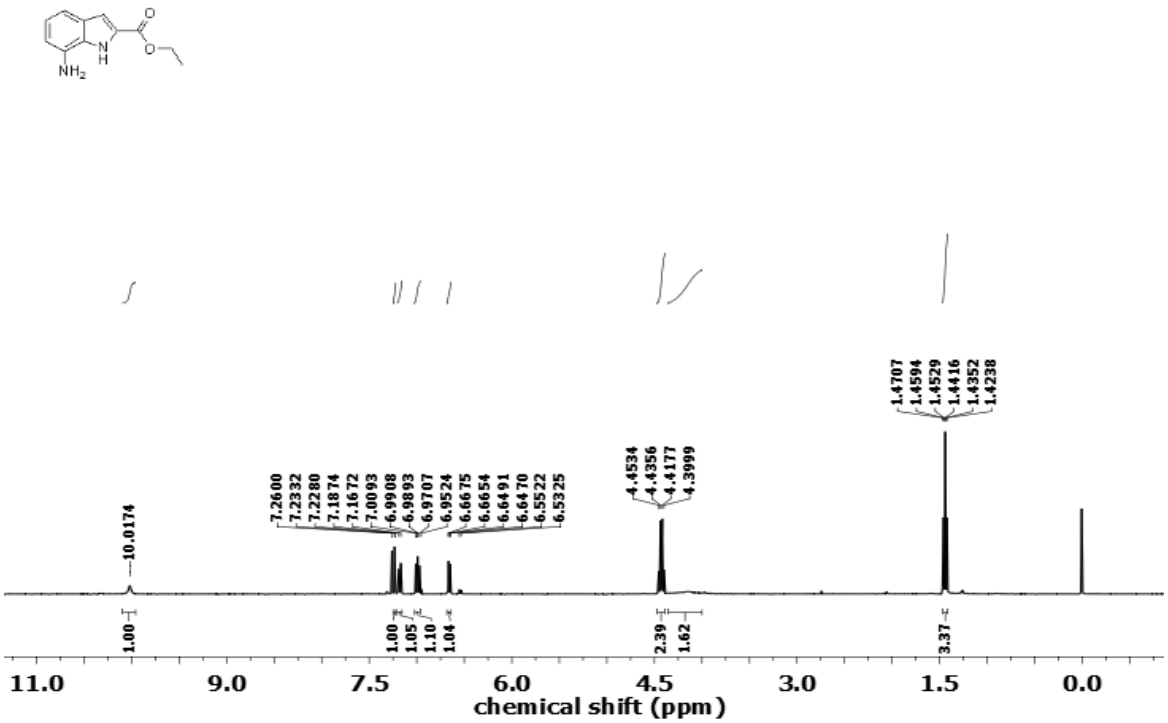

Figure 3.37 ^{1}H NMR spectrum of compound **4a**.

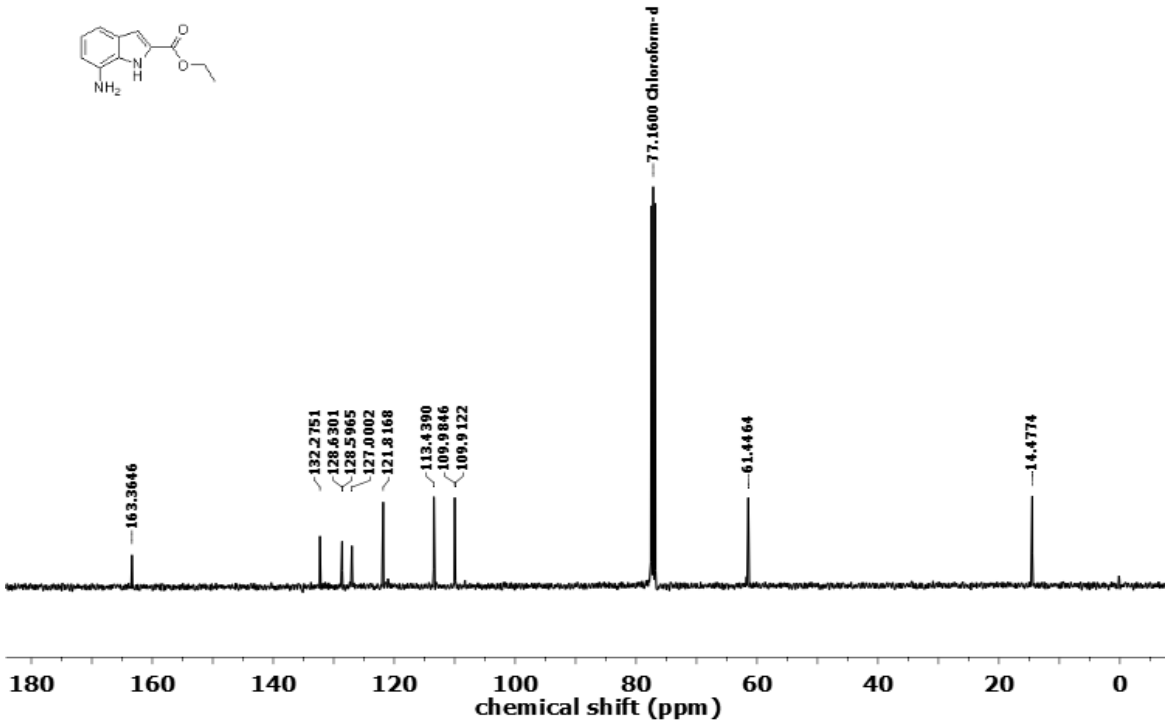

Figure 3.38 ^{13}C NMR spectrum of compound **4a**.

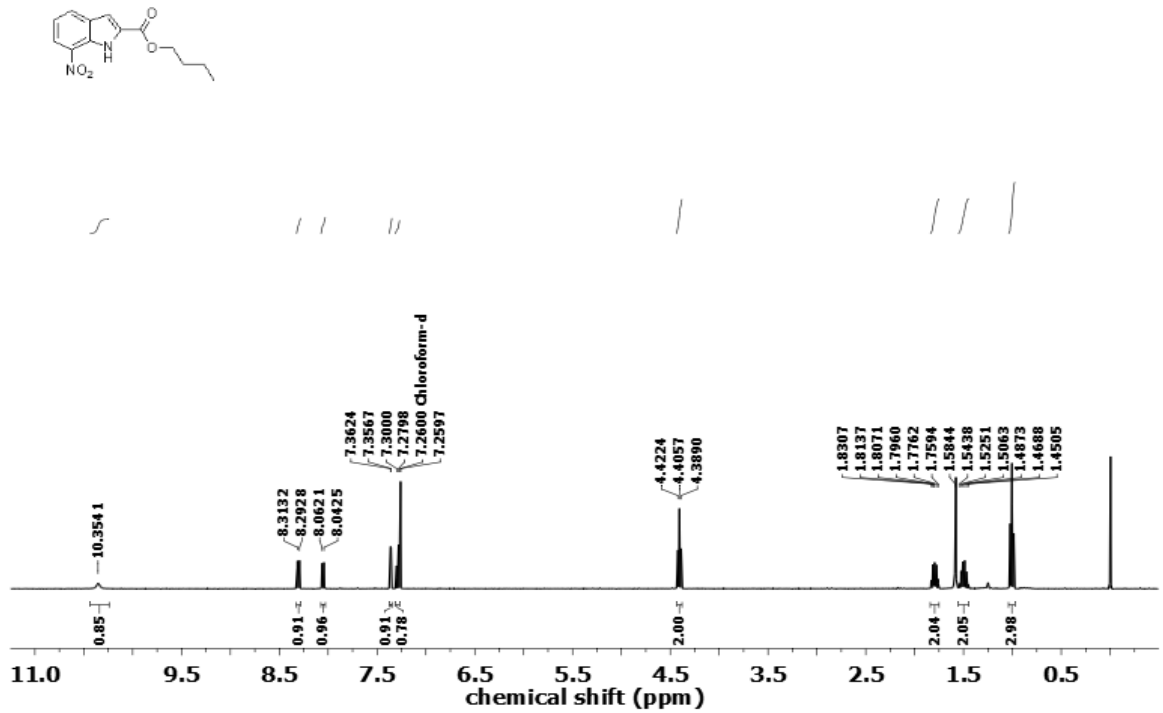

Figure 3.39 ^{1}H NMR spectrum of compound **4b**.

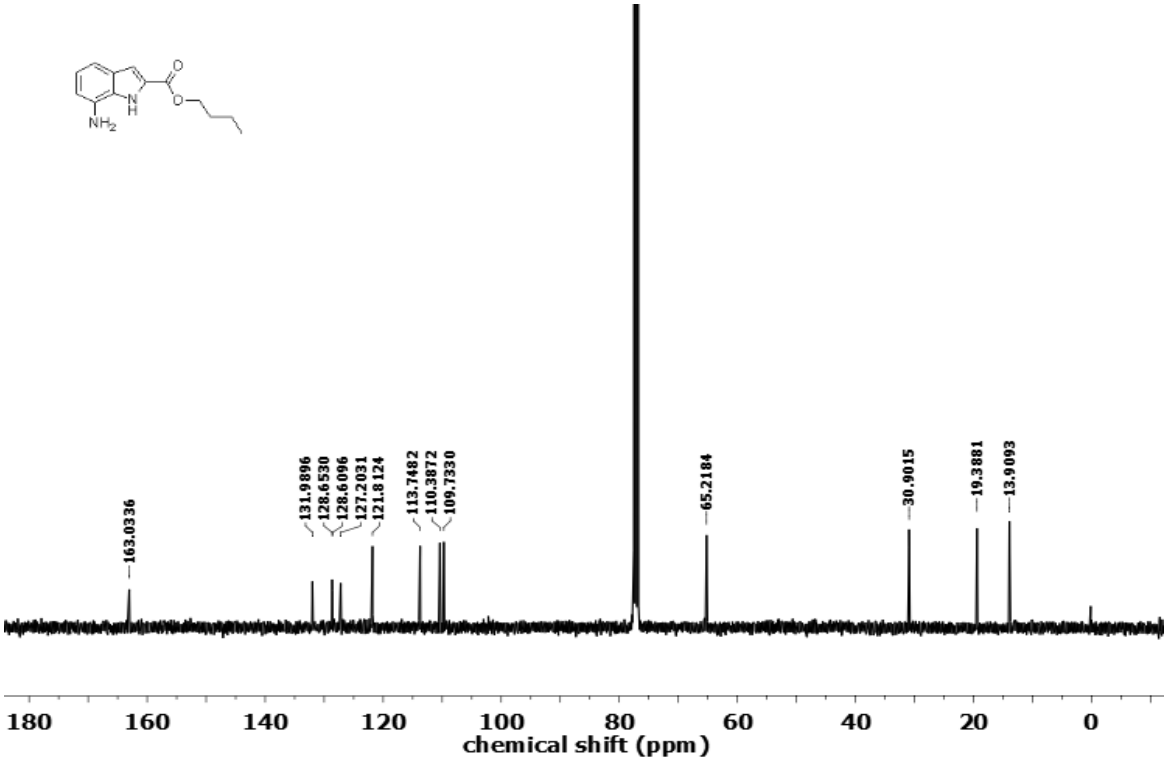

Figure 3.40 ^{13}C NMR spectrum of compound **4b**.

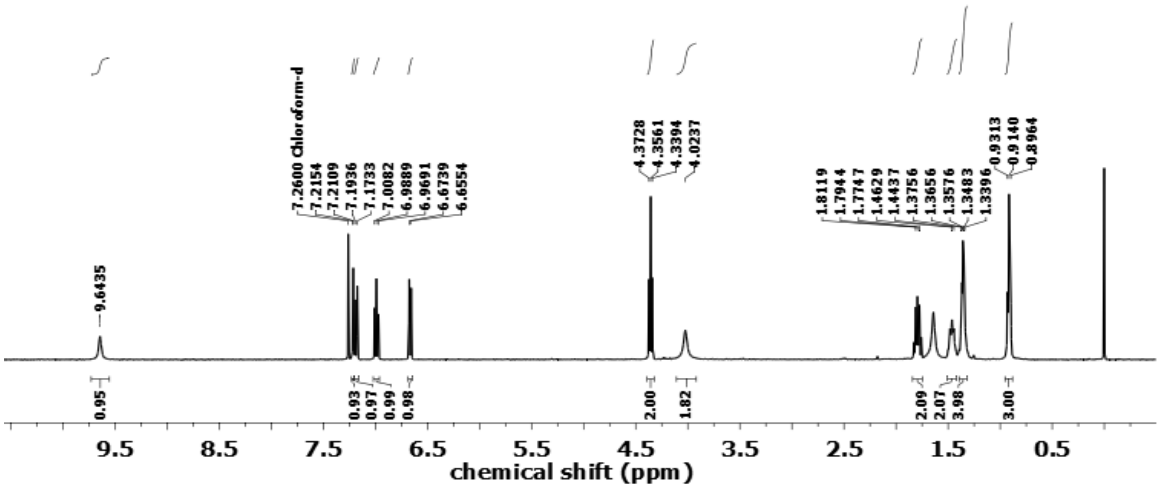

Figure 3.41 ^{1}H NMR spectrum of compound **4c**.

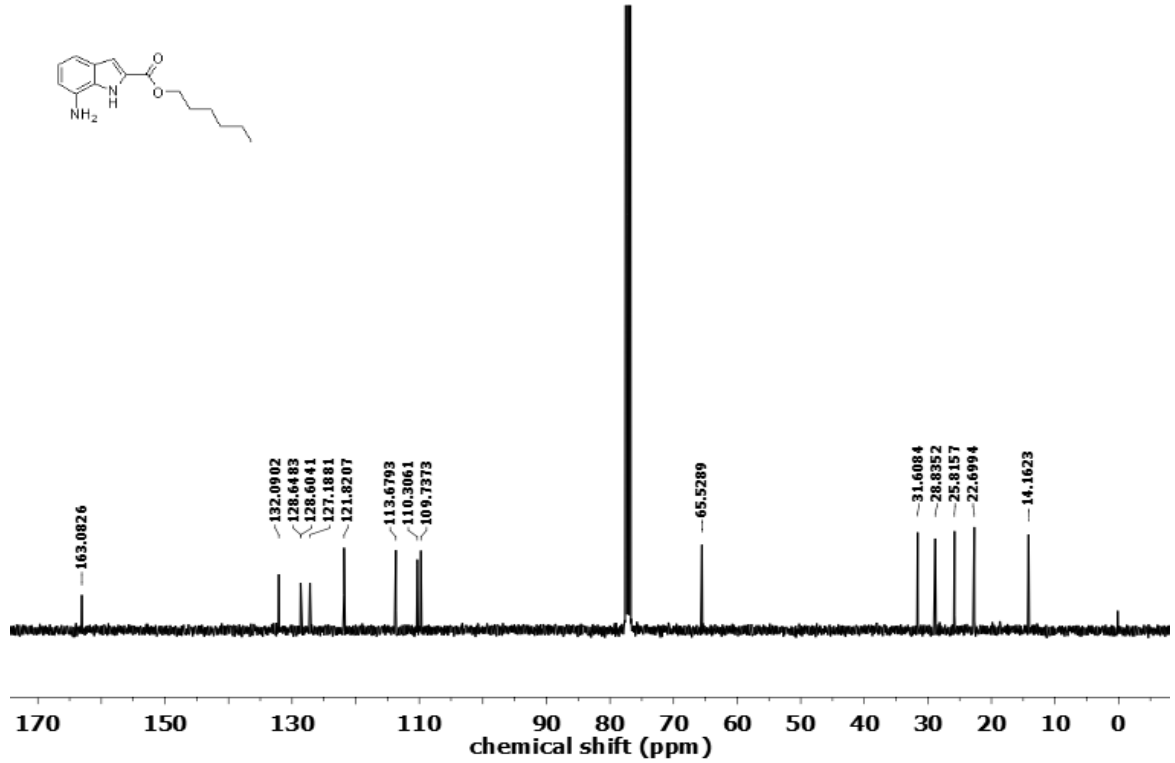

Figure 3.42 ^{13}C NMR spectrum of compound **4c**.

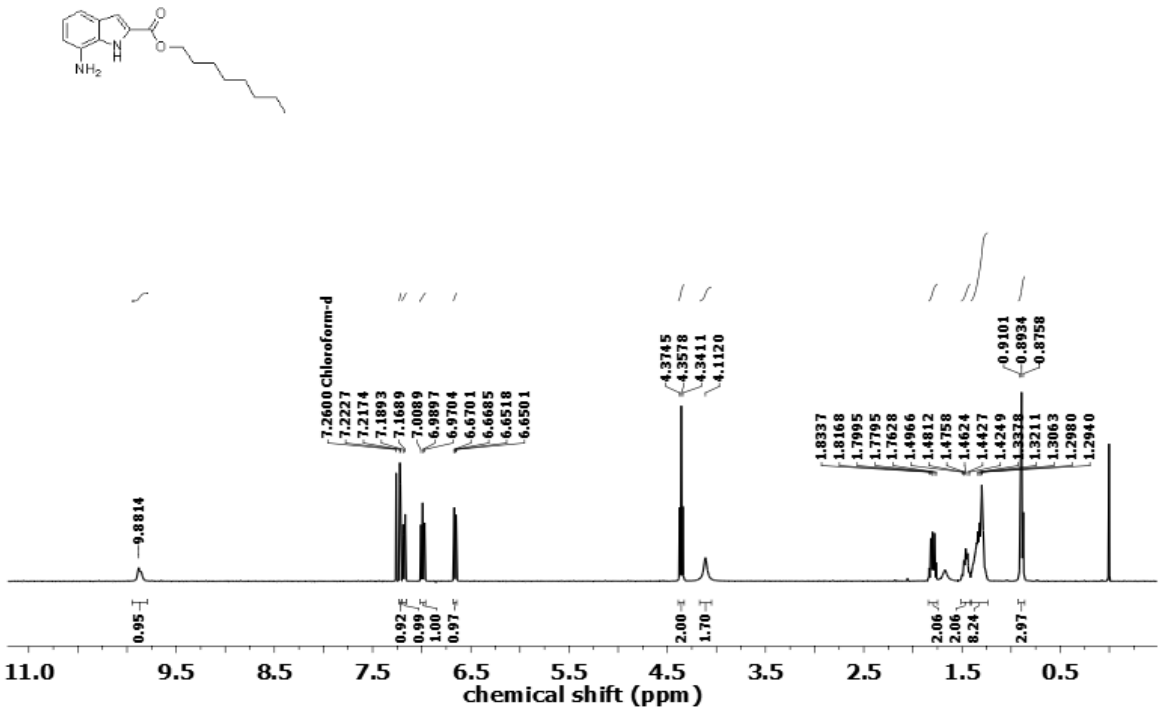

Figure 3.43 ^{1}H NMR spectrum of compound **4d**.

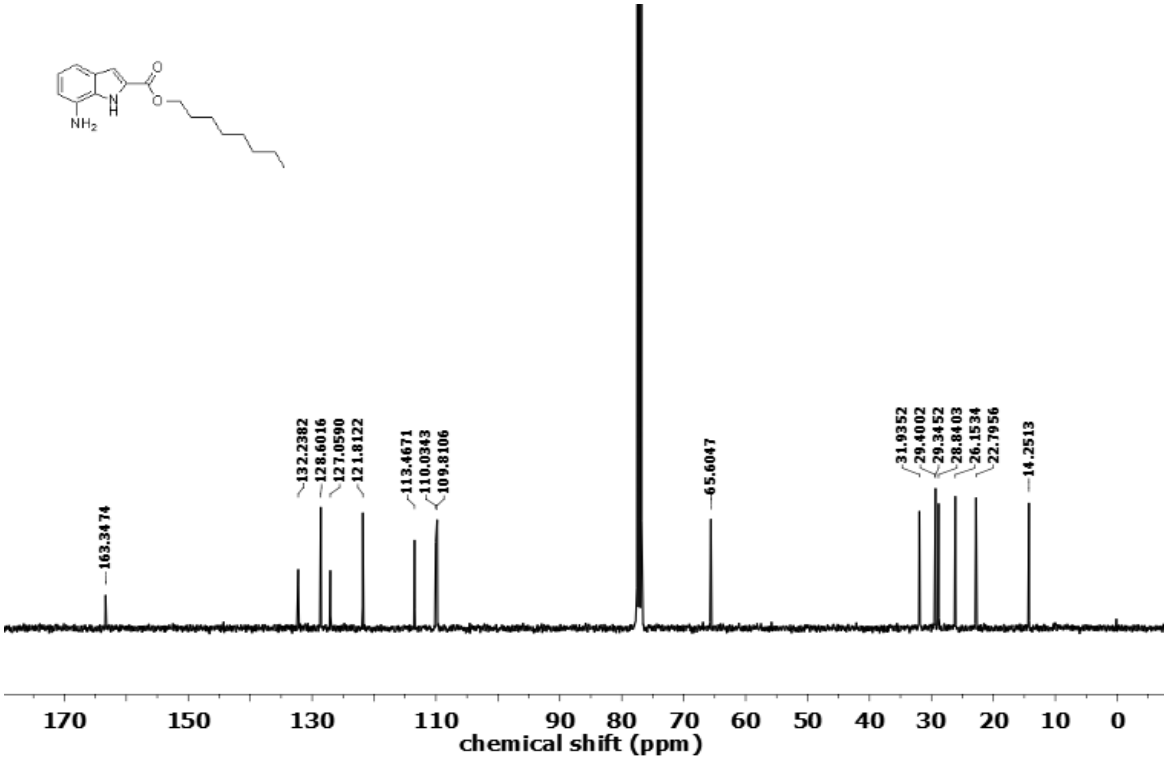

Figure 3.44 ^{13}C NMR spectrum of compound **4d**.

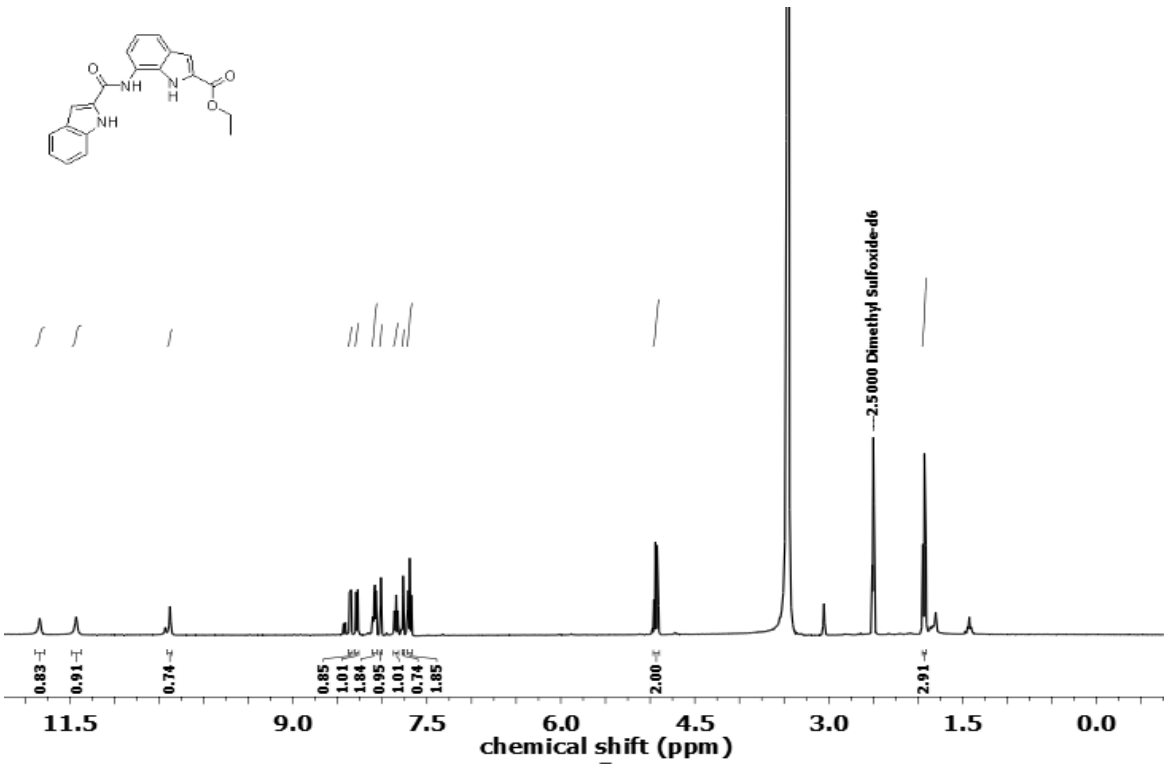

Figure 3.45 ^{1}H NMR spectrum of compound **1a**.

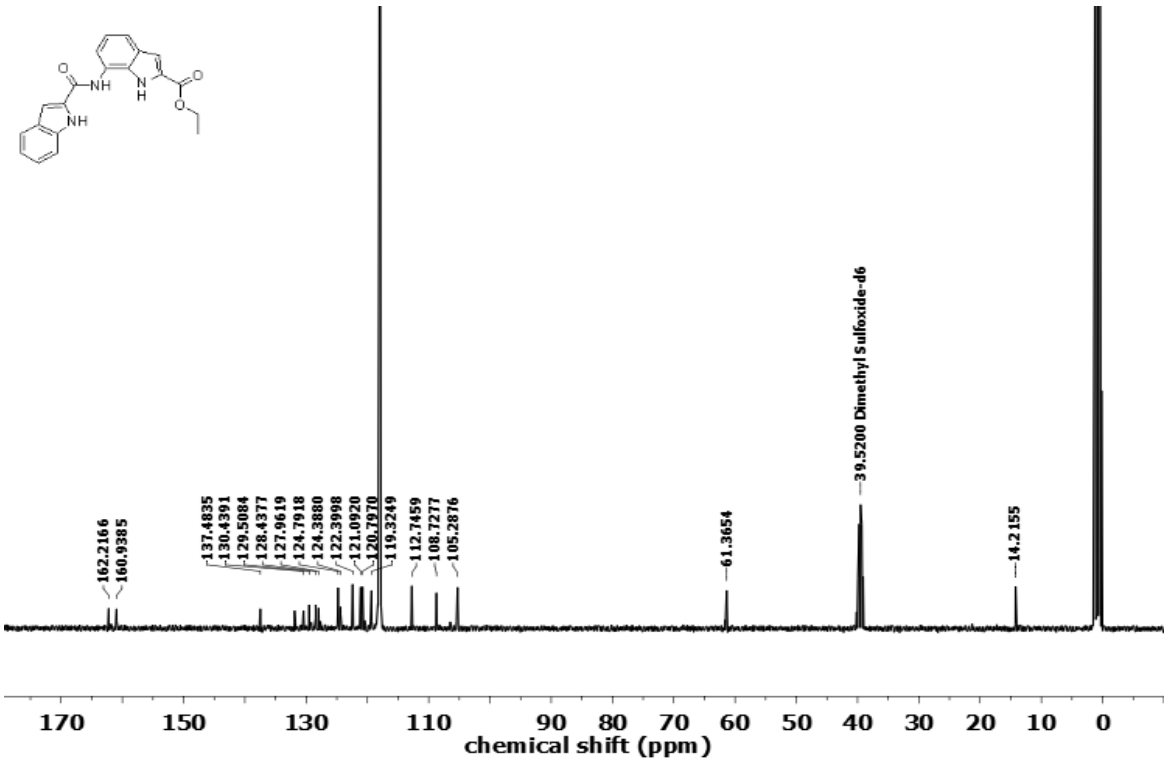

Figure 3.46 ^{13}C NMR spectrum of compound **1a**.

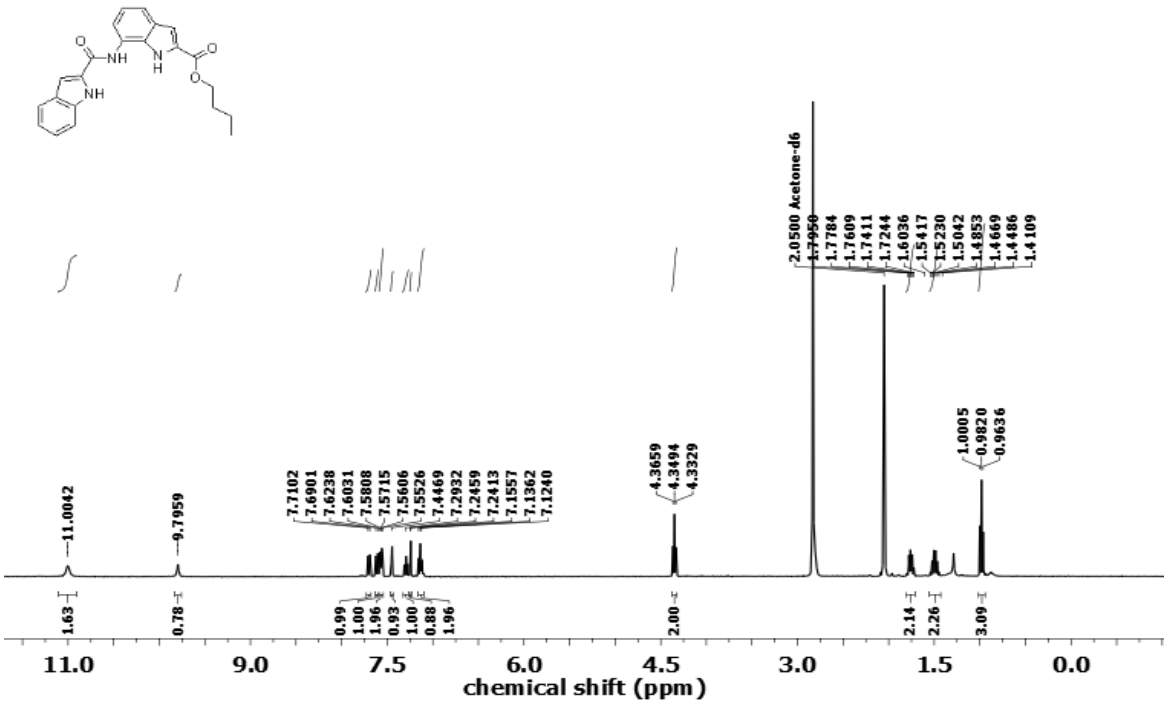

Figure 3.47 ^{1}H NMR spectrum of compound **1b**.

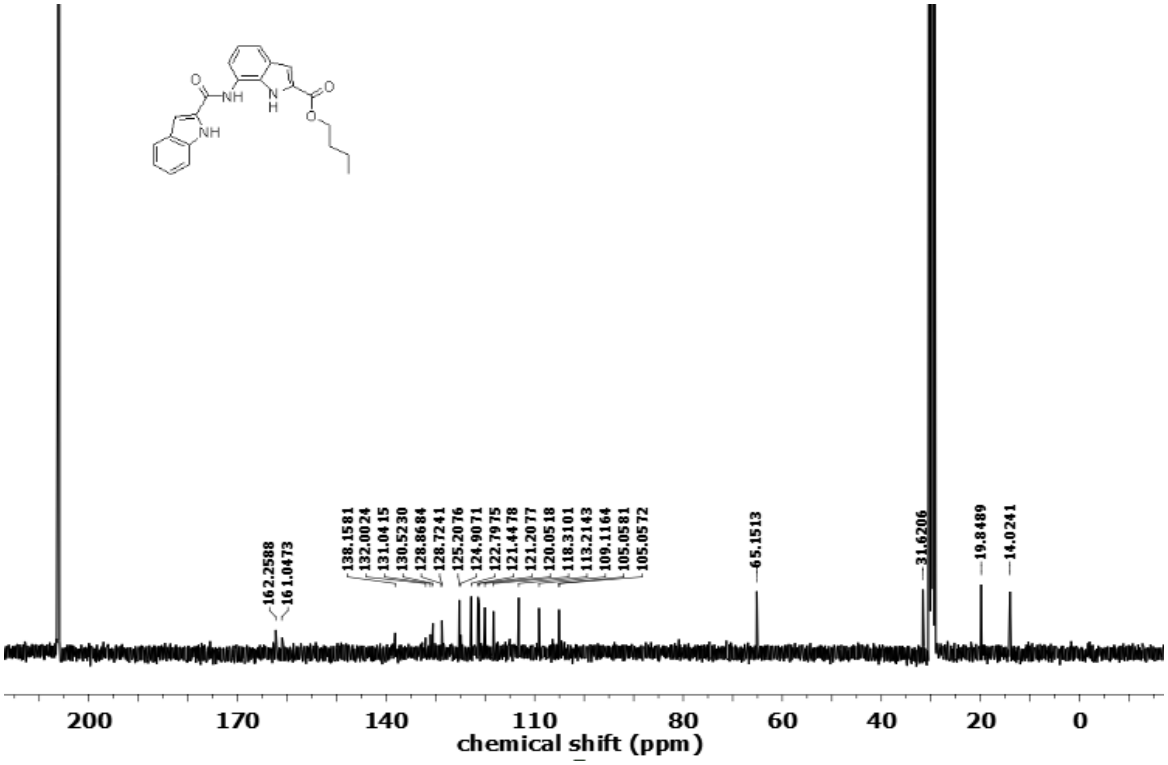

Figure 3.48 ^{13}C NMR spectrum of compound **1b**.

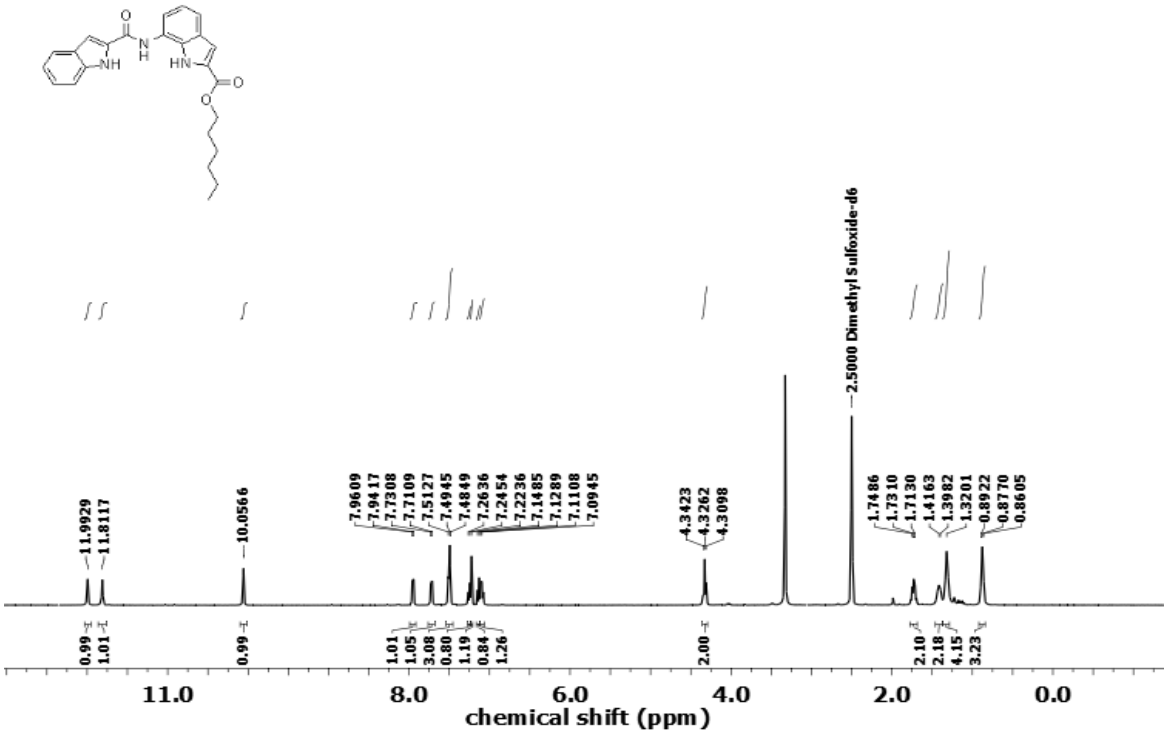

Figure 3.49 ^{1}H NMR spectrum of compound **1c**.

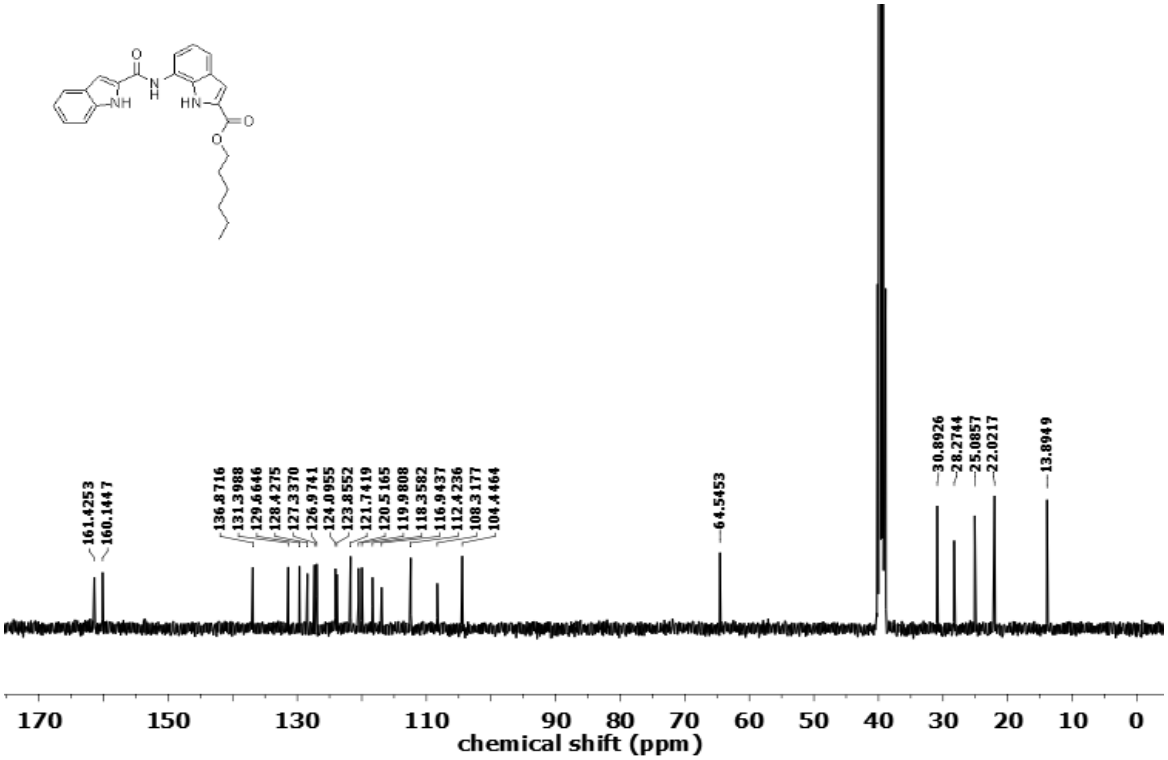

Figure 3.50 ^{13}C NMR spectrum of compound **1c**.

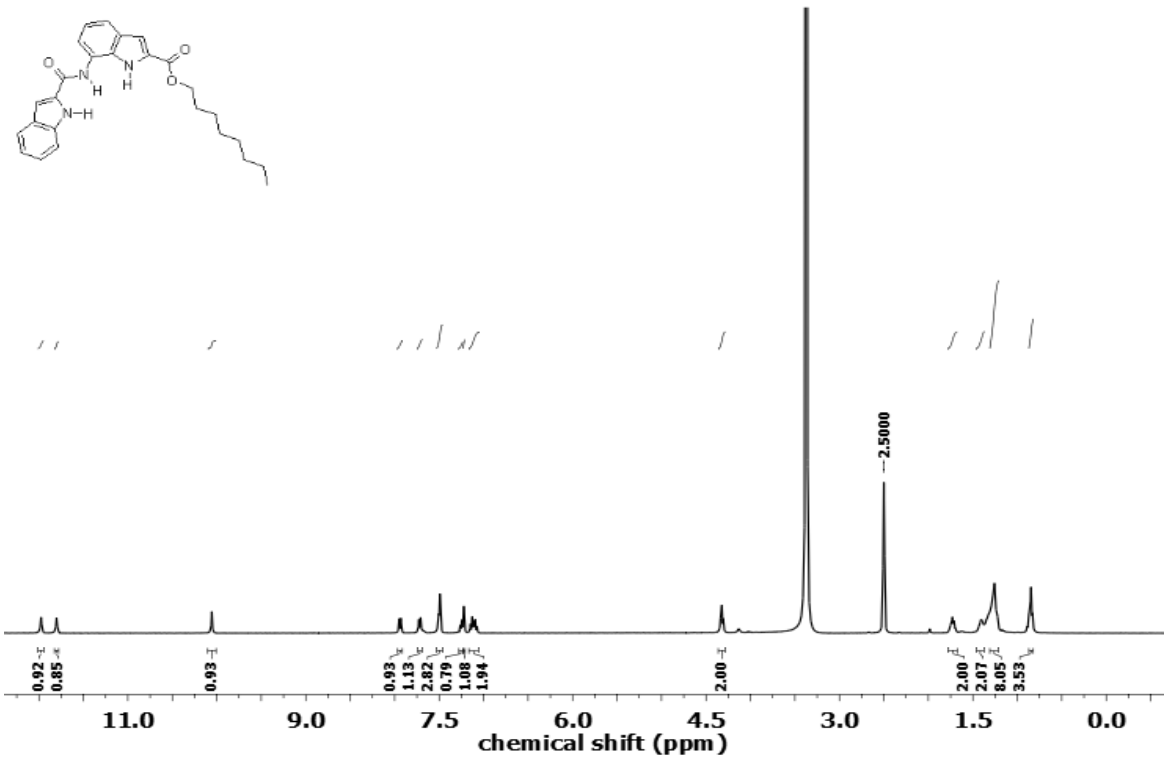

Figure 3.51 ^{1}H NMR spectrum of compound **1d**.

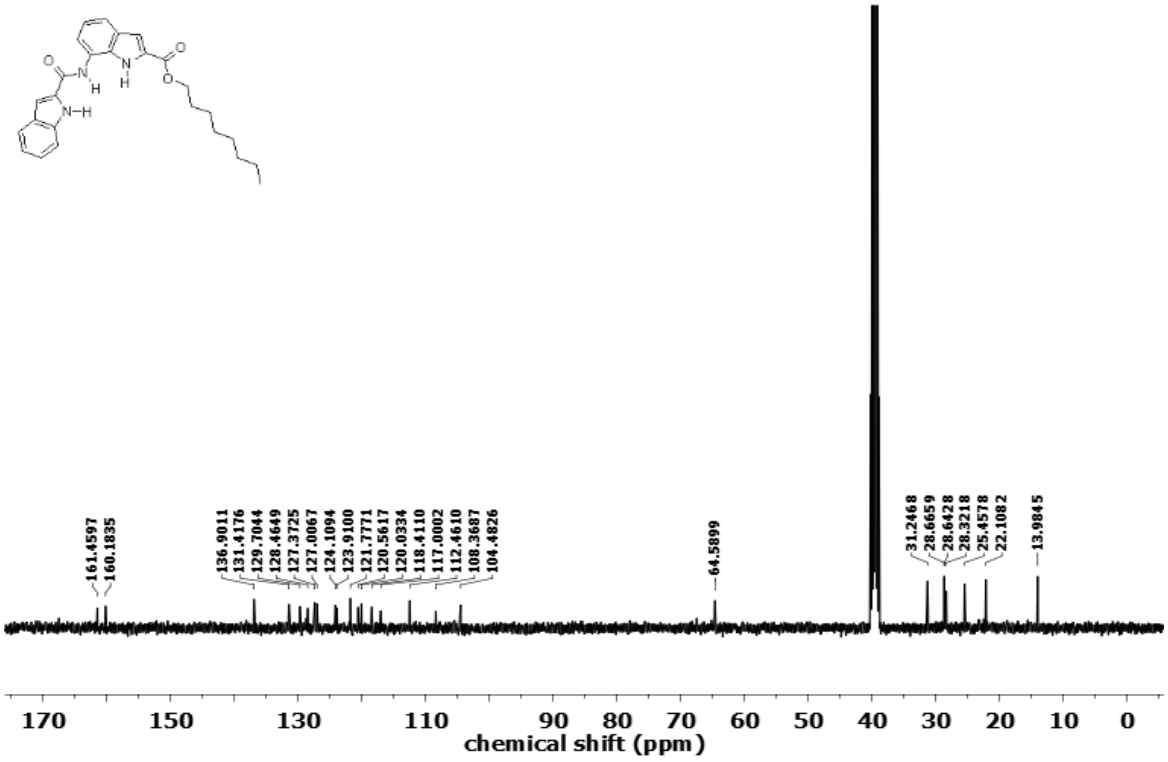

Figure 3.52 ^{13}C NMR spectrum of compound **1d**.

3.5 References

1. A. Fürstner, *Angew. Chem. Int. Ed.*, 2003, **42**, 3582-3603.
2. J. L. Seganish and J. T. Davis, *Chem. Commun.*, 2005, 5781-5783.
3. H. Konno, H. Matsuya, M. Okamoto, T. Sato, Y. Tanaka, K. Yokoyama, T. Kataoka, K. Nagai, H. H. Wasserman and S. Ohkuma, *J. Biochem.*, 1998, **124**, 547-556.
4. J. T. Davis, P. A. Gale, O. A. Okunola, P. Prados, J. C. Iglesias-Sánchez, T. Torroba and R. Quesada, *Nat. Chem.*, 2009, **1**, 138-144.
5. G. A. Islan, B. Rodenak-Kladniew, N. Noacco, N. Duran and G. R. Castro, *Bioengineered*, 2022, **13**, 14227-14258.
6. N. Darshan and H. K. Manonmani, *J. Food Sci. Technol.*, 2015, **52**, 5393-5407.
7. J. L. Sessler, L. R. Eller, W.-S. Cho, S. Nicolaou, A. Aguilar, J. T. Lee, V. M. Lynch and D. J. Magda, *Angew. Chem. Int. Ed.*, 2005, **44**, 5989-5992.
8. T. Sato, H. Konno, Y. Tanaka, T. Kataoka, K. Nagai, H. H. Wasserman and S. Ohkuma, *J. Biol. Chem.*, 1998, **273**, 21455-21462.
9. D. S. Kim and J. L. Sessler, *Chem. Soc. Rev.*, 2015, **44**, 532-546.
10. P. A. Gale, *Chem*, 2020, **6**, 2873-2875.

11. F. G. Bordwell, G. E. Drucker and H. E. Fried, *J. Org. Chem.*, 1981, **46**, 632-635.
12. N. M. Koropatkin, H. B. Pakrasi and T. J. Smith, *Proc. Natl. Acad. Sci. U.S.A.*, 2006, **103**, 9820-9825.
13. J. J. He and F. A. Quiocho, *Science (New York, N.Y.)*, 1991, **251**, 1479-1481.
14. N. M. Koropatkin, D. W. Koppenaal, H. B. Pakrasi and T. J. Smith, *J. Biol. Chem.*, 2007, **282**, 2606-2614.
15. K. H. G. Verschueren, F. Seljée, H. J. Rozeboom, K. H. Kalk and B. W. Dijkstra, *Nature*, 1993, **363**, 693-698.
16. K. J. Chang, D. Moon, M. S. Lah and K. S. Jeong, *Angew. Chem. Int. Ed.*, 2005, **44**, 7926-7929.
17. P. A. Gale, *Chem. Commun.*, 2008, 4525-4540.
18. P. A. Gale, J. R. Hiscock, C. Z. Jie, M. B. Hursthouse and M. E. Light, *Chem. Sci.*, 2010, **1**, 215-220.
19. C. Caltagirone, P. A. Gale, J. R. Hiscock, M. B. Hursthouse, M. E. Light and G. J. Tizzard, *Supramol Chem* 2009, **21**, 125-130.
20. C. Caltagirone, J. R. Hiscock, M. B. Hursthouse, M. E. Light and P. A. Gale, *Chem. Eur. J.*, 2008, **14**, 10236-10243.
21. G. W. Bates, Triyanti, M. E. Light, M. Albrecht and P. A. Gale, *J. Org. Chem.*, 2007, **72**, 8921-8927.
22. S. J. Moore, M. Wenzel, M. E. Light, R. Morley, S. J. Bradberry, P. Gómez-Iglesias, V. Soto-Cerrato, R. Pérez-Tomás and P. A. Gale, *Chem. Sci.*, 2012, **3**, 2501-2509.
23. L. A. Jowett, E. N. W. Howe, V. Soto-Cerrato, W. Van Rossom, R. Pérez-Tomás and P. A. Gale, *Sci. Rep.*, 2017, **7**, 9397.
24. , ChemAxon (https://chemaxon.com), 2012.
25. L. Xiong, X. L. Zhu, H. W. Gao, Y. Fu, S. Q. Hu, L. N. Jiang, W. C. Yang and G. F. Yang, *J. Agric. Food. Chem.*, 2016, **64**, 4830-4837.
26. T. J. Jentsch, V. Stein, F. Weinreich and A. A. Zdebik, *Physiol. Rev.* , 2002, **82**, 503-568.
27. Y. Marunaka, *J. Physiol. Sci.* , 2023, **73**, 31.
28. K. D. Legg and D. M. Hercules, *J. Phys. Chem.*, 1970, **74**, 2114-2118.
29. T. Saha, M. S. Hossain, D. Saha, M. Lahiri and P. Talukdar, *J. Am. Chem. Soc.*, 2016, **138**, 7558-7567.
30. A. Kerckhoffs and M. J. Langton, *Chem. Sci.*, 2020, **11**, 6325-6331.
31. R. L. Biltonen and D. Lichtenberg, *Chem. Phys. Lipids*, 1993, **64**, 129-142.

32. H. Goto, S. Obata, N. Nakayama and K. Ohta, CONFLEX Corporation, Tokyo, Japan, 2017.
33. H. Goto and E. Osawa, *J. Am. Chem. Soc.*, 1989, **111**, 8950-8951.
34. M. J. Frisch, G. W. Trucks, H. B. Schlegel, G. E. Scuseria, M. A. Robb, J. R. Cheeseman, G. Scalmani, V. Barone, B. Mennucci, G. A. Petersson, H. Nakatsuji, M. Caricato, X. Li, H. P. Hratchian, A. F. Izmaylov, J. Bloino, G. Zheng, J. L. Sonnenberg, M. Hada, M. Ehara, K. Toyota, R. Fukuda, J. Hasegawa, M. Ishida, T. Nakajima, Y. Honda, O. Kitao, H. Nakai, T. Vreven, J. J. A. Montgomery, J. E. Peralta, F. Ogliaro, M. Bearpark, J. J. Heyd, E. Brothers, K. N. Kudin, V. N. Staroverov, T. Keith, R. Kobayashi, J. Normand, K. Raghavachari, A. Rendell, J. C. Burant, S. S. Iyengar, J. Tomasi, M. Cossi, N. Rega, J. M. Millam, M. Klene, J. E. Knox, J. B. Cross, V. Bakken, C. Adamo, J. Jaramillo, R. Gomperts, R. E. Stratmann, O. Yazyev, A. J. Austin, R. Cammi, C. Pomelli, J. W. Ochterski, R. L. Martin, K. Morokuma, V. G. Zakrzewski, G. A. Voth, P. Salvador, J. J. Dannenberg, S. Dapprich, A. D. Daniels, O. Farkas, J. B. Foresman, J. V. Ortiz, J. Cioslowski and D. J. Fox, Gaussian, Inc., Wallingford CT, 2013.
35. A. D. Becke, *J. Chem. Phys.*, 1993, **98**, 5648-5652.
36. C. Lee, W. Yang and R. G. Parr, *Phys. Rev. B*, 1988, **37**, 785-789.
37. P. C. Hariharan and J. A. Pople, *Theoret. Chim. Acta* 1973, **28**, 213-222.
38. M. M. Francl, W. J. Pietro, W. J. Hehre, J. S. Binkley, M. S. Gordon, D. J. DeFrees and J. A. Pople, *J. Chem. Phys.* , 1982, **77**, 3654-3665.
39. S.-K. Ko, S. K. Kim, A. Share, V. M. Lynch, J. Park, W. Namkung, W. Van Rossom, N. Busschaert, P. A. Gale, J. L. Sessler and I. Shin, *Nat. Chem.*, 2014, **6**, 885-892.
40. T. Saha, M. S. Hossain, D. Saha, M. Lahiri and P. Talukdar, *J. Am. Chem. Soc.*, 2016, **138**, 7558-7567.
41. S. P. Yu, L. M. Canzoniero and D. W. Choi, *Curr Opin Cell Biol.*, 2001, **13**, 405-411.
42. M. Tsukimoto, H. Harada, A. Ikari and K. Takagi, *J. Biol. Chem.*, 2005, **280**, 2653-2658.
43. G. Picci, S. Marchesan and C. Caltagirone, *Biomedicines*, 2022, **10**.
44. J. van Meerloo, G. J. Kaspers and J. Cloos, *Methods Mol. Biol.*, 2011, **731**, 237-245.
45. V. Soto-Cerrato, P. Manuel-Manresa, E. Hernando, S. Calabuig-Fariñas, A. Martínez-Romero, V. Fernández-Dueñas, K. Sahlholm, T. Knöpfel, M. García-Valverde, A. M. Rodilla, E. Jantus-Lewintre, R. Farràs, F. Ciruela, R. Pérez-Tomás and R. Quesada, *J. Am. Chem. Soc.*, 2015, **137**, 15892-15898.

46. S. Sakamuru, M. S. Attene-Ramos and M. Xia, *Methods Mol. Biol.*, 2016, **1473**, 17-22.
47. A. Ashkenazi, *Nat. Rev. Drug Discov.*, 2008, **7**, 1001-1012.
48. D. Poncet, P. Boya, D. Métivier, N. Zamzami and G. Kroemer, *Apoptosis*, 2003, **8**, 521-530.
49. X. Liu, C. N. Kim, J. Yang, R. Jemmerson and X. Wang, *Cell*, 1996, **86**, 147-157.
50. P. Li, D. Nijhawan, I. Budihardjo, S. M. Srinivasula, M. Ahmad, E. S. Alnemri and X. Wang, *Cell*, 1997, **91**, 479-489.
51. X. Jiang and X. Wang, 2004, **73**, 87-106.
52. S. Salvioli, A. Ardizzoni, C. Franceschi and A. Cossarizza, *FEBS Lett.*, 1997, **411**, 77-82.
53. S. T. Smiley, M. Reers, C. Mottola-Hartshorn, M. Lin, A. Chen, T. W. Smith, G. D. Steele, Jr. and L. B. Chen, *Proc. Natl. Acad. Sci. U.S.A.*, 1991, **88**, 3671-3675.
54. S. S. Sabharwal and P. T. Schumacker, *Nat. Rev. Cancer*, 2014, **14**, 709-721.
55. G. Y. Liou and P. Storz, *Free Radic. Res.* , 2010, **44**, 479-496.
56. L. A. Sena and N. S. Chandel, *Mol. Cell*, 2012, **48**, 158-167.
57. J. Zielonka and B. Kalyanaraman, *Free Radic. Biol. Med.* , 2010, **48**, 983-1001.
58. P. Klán, T. Šolomek, C. G. Bochet, A. Blanc, R. Givens, M. Rubina, V. Popik, A. Kostikov and J. Wirz, *Chem. Rev.*, 2013, **113**, 119-191.
59. P. Sebej, J. Wintner, P. Müller, T. Slanina, J. Al Anshori, L. A. Antony, P. Klán and J. Wirz, *J. Org. Chem.*, 2013, **78**, 1833-1843.
60. S. Muralidharan, N. D. A. Dirda, E. J. Katz, C.-M. Tang, S. Bandyopadhyay, P. O. Kanold and J. P. Y. Kao, *PLOS ONE*, 2016, **11**, e0163937.
61. S. Blake, R. Capone, M. Mayer and J. Yang, *Bioconjug. Chem.* . 2008, **19**, 1614-1624.
62. P. Thordarson, *Chem. Soc. Rev.*, 2011, **40**, 1305-1323.
63. I. Fishov and C. L. Woldringh, *Mol. Microbiol.*, 1999, **32**, 1166-1172.
64. W. Wehrli, *Rev. Infect. Dis.*, 1983, **5**, S407-S411.
65. A. D. Becke, *J. Chem. Phys.*, 1993, **98**, 5648-5652.
66. C. Lee, W. Yang and R. G. Parr, *Phys. Rev. B*, 1988, **37**, 785.
67. P. C. Hariharan and J. A. Pople, *Theoret. Chim. Acta*, 1973, **28**, 213-222.
68. M. M. Francl, W. J. Pietro, W. J. Hehre, J. S. Binkley, M. S. Gordon, D. J. DeFrees and J. A. Pople, *J. Chem. Phys.*, 1982, **77**, 3654-3665.

Chapter 4

Phototriggered release of transmembrane chloride carrier from an o-nitrobenzyl-linked procarrier

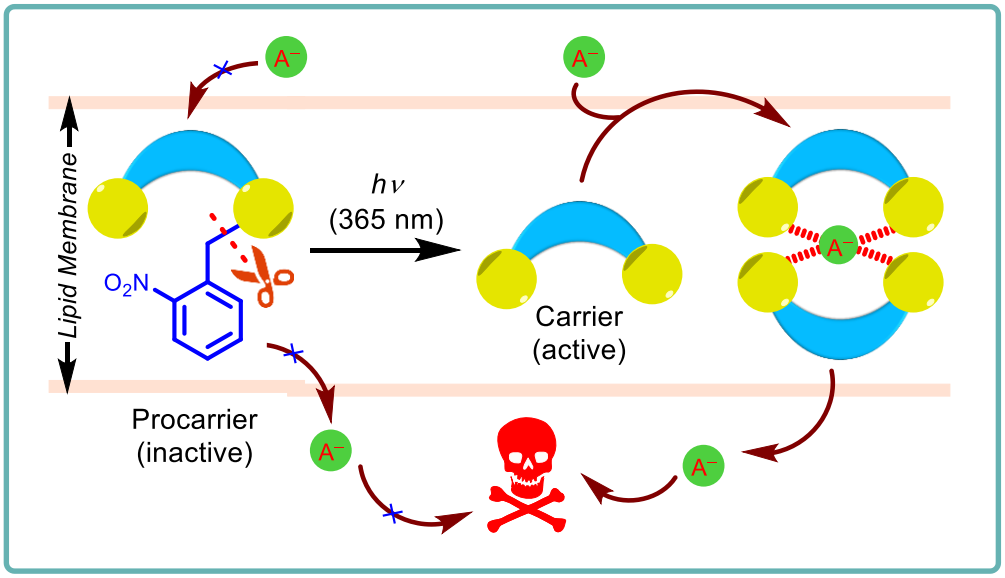

4.1 Introduction

As discussed in the previous chapter, the attachment of a photocleavable protecting group (PPG) to the amide N-H of the bisindole carrier was attempted but unsuccessful. Hence, for proof of concept, it was planned to simplify the carrier structure by using a single indole unit (i.e., 1*H*-indole-2-carboxamides) which would have the minimum required binding sites, one indole N-H and one amide N-H. The amide can be functionalized with a PPG prior to synthesis.

As detailed in Chapter 1, the ability of synthetic ion carriers to cause apoptotic cancer cell death via perturbation of intracellular chloride ion concentrations is attractive as these molecules function in the lipid membrane[1-3] and, unlike traditional anticancer drugs, require no binding targets such as specific genes or proteins/enzymes. Therefore, in principle, synthetic chloride carriers can overcome the resistance related to the mutations and over-expression of genes and proteins. The difference in levels of toxicity shown by these compounds towards normal cells when compared to tumor cells is not statistically significant due to their non-specificity and non-target mode of approach. This toxicity is considered a limitation for the practical application of ion carriers in anticancer therapy. Thus, achieving specificity and precise spatiotemporal control is a major challenge.

Therefore, there is a need to develop stimuli-responsive systems that can be applied selectively to cancer cells. In this line, pH was used primarily to activate the ion transports in specific pH ranges (Figure 4.1A).[4-7] Recently, enzymes (esterase and glycosylase) have been used for releasing the active ion carrier from a procarrier (i.e., the inactive form of the carrier molecule) (Figure 4.1B).[8] Photoisomerization of molecules, on the other hand, was used to activate or deactivate channel/carrier-mediated ion transport (Figure 4.1C).[9, 10]

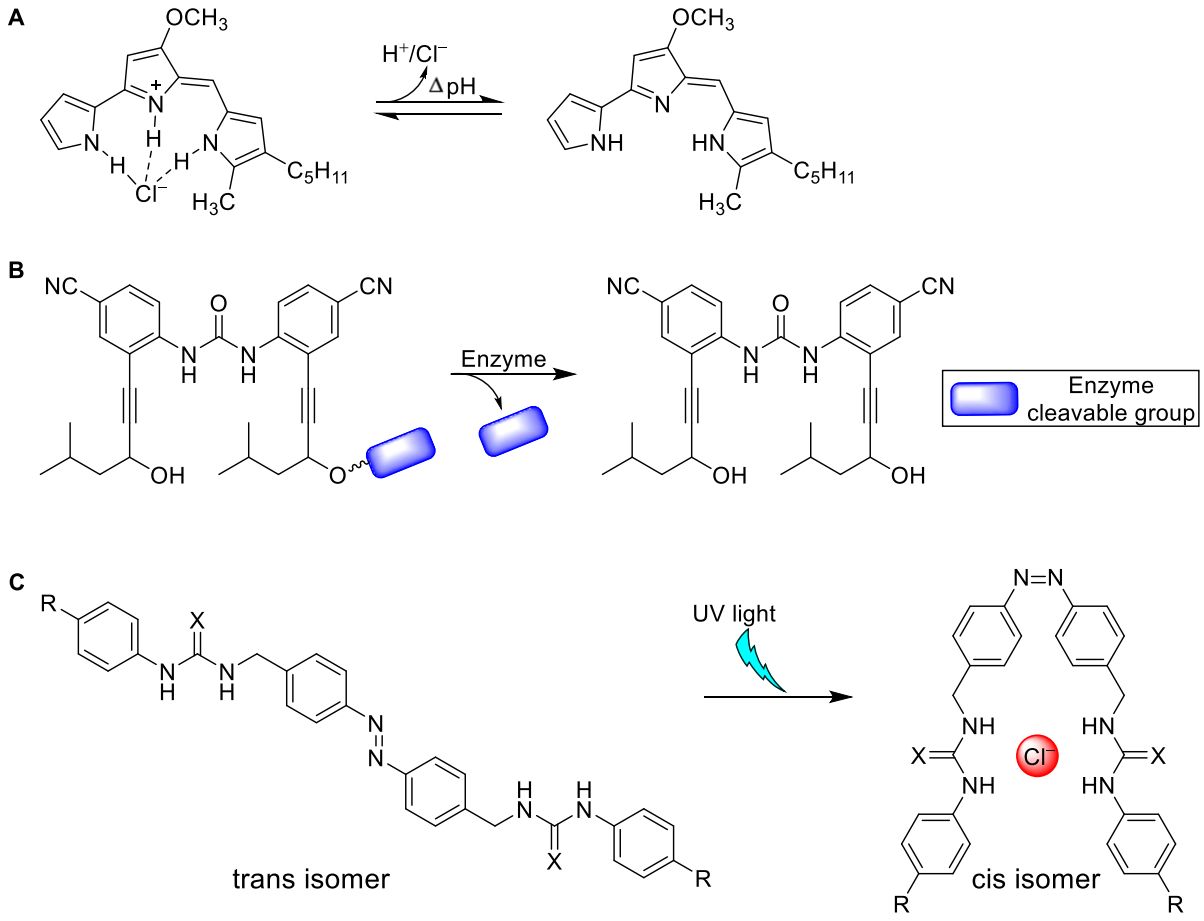

Figure 4.1 pH-regulated H^+/Cl^- cotransport by Phenylthiosemicarbazone (**A**). Enzyme-mediated activation of membrane impermeable procarrier for the transport of chloride across lipid membrane (**B**). Photoactivated trans-to-cis isomerization of azobenzene-based chloride carrier (**C**).

Recently the photoactivated approach has attracted considerable interest for the delivery of drug molecules, as light enables precise spatiotemporal control to boost the therapeutic activity of the drug for the treatment of cancer.[11, 12] The basic principle of photoactivated drug delivery entails the attachment of a photocleavable protecting group to the drug active site to create an inactive form of drug or prodrug. After irradiation with light of appropriate wavelength, the prodrug gets activated in the target area by the cleavage of the photocleavable group (Figure 4.2). Shi et al. reported light-driven photoisomerization of azobenzene moiety as a remote control for the regulated release of the anticancer drug doxorubicin from silica nanoparticles (MSNs).[13] Choi and co-workers reported the light-driven controlled release of *o*-nitrobenzyl-based methotrexate, an anticancer drug, for targeted drug delivery.[14] Lin and co-workers reported *o*-nitrobenzyl-based porphyrin anticancer prodrug to minimize side effects of the drug through the light-controlled dosage of the drug to enhance the tumor affinity of porphyrin.[15] Yi

and coworkers have illustrated the photoactivation of an anticancer prodrug to release the 5-fluorouracil (an anticancer drug to treat solid cancers, such as colon, breast, rectal, and pancreatic cancers), and induce cellular apoptosis.[16]

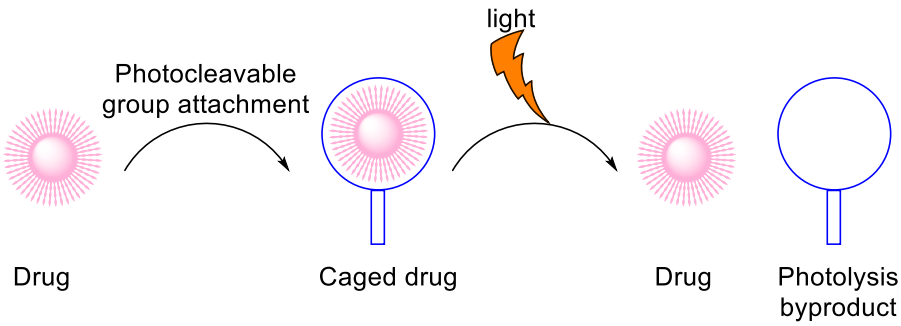

Figure 4.2 General principle of photoactivated drug delivery.

To overcome the problem associated with synthetic ion carriers for cancer treatment, we aimed to apply the photocleavable drug release strategy in synthetic ion carriers. Among diverse the photocleavable protecting groups (PPGs), the *o*-nitrobenzyl (ONB) group has received special attention for the controlled release of bioactive molecules[17-19] due to their ease of synthesis, activation ability in both solution and solid states, ability to protect a variety of functional groups, higher efficiency of photolysis and well-established photolysis mechanism (Figure 4.3).[20-22] These properties are in stark contrast to the xanthene and 6-nitrocoumarin-7-ylmethyl (ncm) PPGs mentioned in the previous chapter which were difficult to synthesize and integrate into the carrier. Therefore, the use of an *o*-nitrobenzyl photocleavable protecting group was planned for the design of a procarrier (an inactive form of carrier).

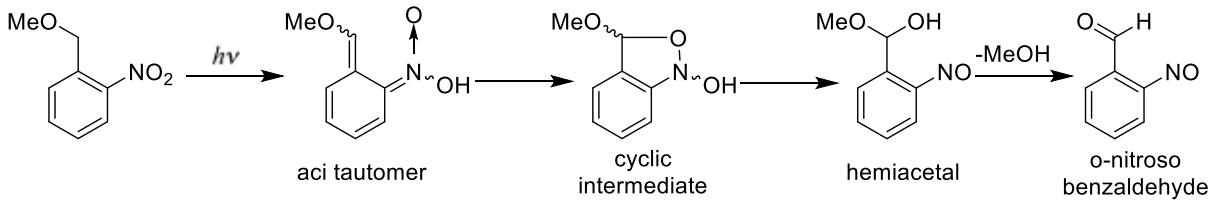

Figure 4.3 Mechanism of photolytic cleavage of *o*-nitrobenzyl group.

In this design, the *N*-phenyl-1*H*-indole-2-carboxamides **1a – 1d** were selected as the ion carrier system (Figure 4.4A). The *para*-substituent of the *N*-phenyl ring was changed among R = $–CH_3$, $–C(CH_3)_3$, –Br and $–CF_3$ to vary the acidity of $N–H_b$ proton. Theoretical estimation based

using the calculator plugins of the MarvinSketch program[23] gave pK_a = 14.31, 14.23, 13.89 and 13.86 for the N–H_b protons of **1a – 1d**, respectively (Figure 4.4B), suggesting the higher acidity of the proton when a stronger electron-withdrawing R group was used. The R groups also influenced the acidity of N-H_a protons in the same way (i.e., pK_a = 11.85, 11.85, 11.77 and 11.76 for **1a – 1d**, respectively). The program was also utilized in predicting the membrane permeability of these molecules, logP = 3.60, 4.63, 3.85 and 3.96 for **1a – 1d**, respectively. Compound **2** was designed as the procarrier form of **1d** (Figure 4.4A). Relatively higher pK_a = 11.85 for N–H_a proton and the absence of the N-H_b proton were considered as crucial limitations of **2** to be an anion carrier although, its lipophilicity (i.e., logP = 5.49) was ideal for the membrane permeation.

A

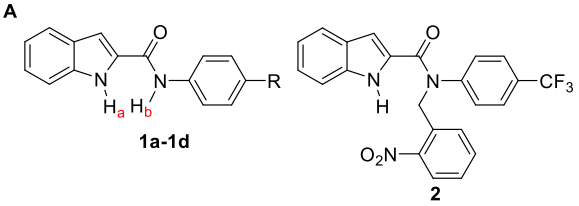

1a: R = –CH_3, **1b:** R = –$C(CH_3)_3$,**1c:** R = –Br,**1d:** R = –CF_3

B

Compound	R	logP	pK$_a$	
			NH_a	NH_b
1a	-CH_3	3.60	11.85	14.31
1b	-$C(CH_3)_3$	4.63	11.85	14.23
1c	-Br	3.85	11.77	13.89
1d	-CF_3	3.96	11.76	13.86

Figure 4.4 Structure of carriers **1a – 1d** and procarrier **2** (**A**). Log P and pK_a values of carrier **1a – 1d** calculated by MarvinSketch program (**B**).

4.2 Results and Discussion

4.2.1 Synthesis

All indole amide derivatives **1a – 1d** and procarrier **2** of the active carrier **1d** were prepared from commercially available 1H-indole-2-carboxylic acid. The compounds **1a – 1d** were synthesized by EDC·HCl-HOBt coupling reaction of 1H-indole-2-carboxylic acid with *para*-substituted aniline derivatives **4a – 4d** (Scheme 4.1). The procarrier **2** was synthesized from 1H-indole-2-carboxylic acid by treatment with $SOCl_2$, followed by coupling of **5** (Scheme 4.1) which was prepared by reductive amination of *o*-nitro benzaldehyde and **4d** (Scheme 4.1). All compounds were characterized by ^{1}H and ^{13}C NMR, IR, HRMS and Melting point.

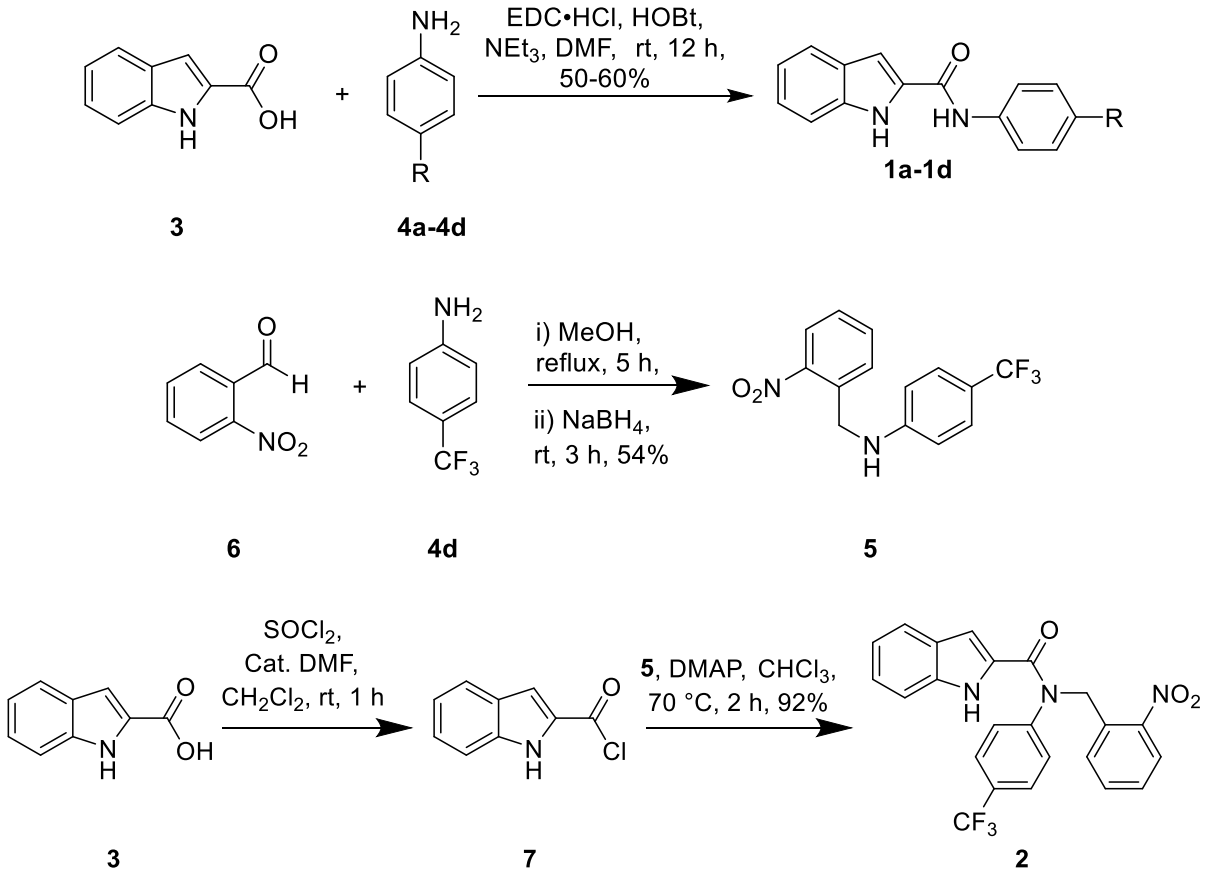

Scheme 4.1 Synthesis scheme of carriers **1a – 1d** and procarrier **2**.

4.2.2 Anion recognition studies by ^{1}H NMR titration

Initially, the Cl^- ion binding properties of **1a – 1d** were verified by ^{1}H NMR titration experiments in CD_3CN. If Cl^- is interacting with a proton of **1a – 1d**, then there would be a downfield or upfield chemical shift of interacting protons in the NMR spectrum. Upon addition of tetrabutylammonium chloride (TBACl) (0.4 M in CD_3CN) to **1a – 1d** (0.005 M in CD_3CN), downfield shifts of H_a, H_b, and H_c protons were observed indicating the interactions of these protons with the Cl^- ion (Figure 4.5A–4.8A). Job's plot analysis was performed to check the stoichiometry of ion binding. The Job's plot analysis based on the change in N-H_a proton chemical shift of **1a-1d** confirmed the 1:1 complexation of the receptor and Cl^- (Figure 4.5C–4.8C). The binding constant, K_a = 599.43 $\pm$ 12.57 M^{-1} was also calculated for **1d** using Bindfit program (Figure 4.8B).[24, 25] Cl^- ion binding constants for **1a** (K_a = 281.76 ± 3.47 M^{-1}), **1b** (K_a = 505.73 ± 15.1 M^{-1}), and **1c** (K_a = 656.14 ± 9.20 M^{-1}) were relatively poor (Figure 4.5B–4.7B). The ^{1}H NMR titration of **1d** with Br^- showed 1:1 and 1:2 binding stoichiometries

with $K_{a(1:1)}$ = 103.31 ± 2.45 M^{-1} and $K_{a(1:2)}$ = 9.83 ± 1.04 M^{-1}, respectively (Figure 4.9). The binding constant of **1d** with I^- could not be calculated precisely due to the insufficient shifts of the H_a, H_b, and H_c protons (Figure 4.10).

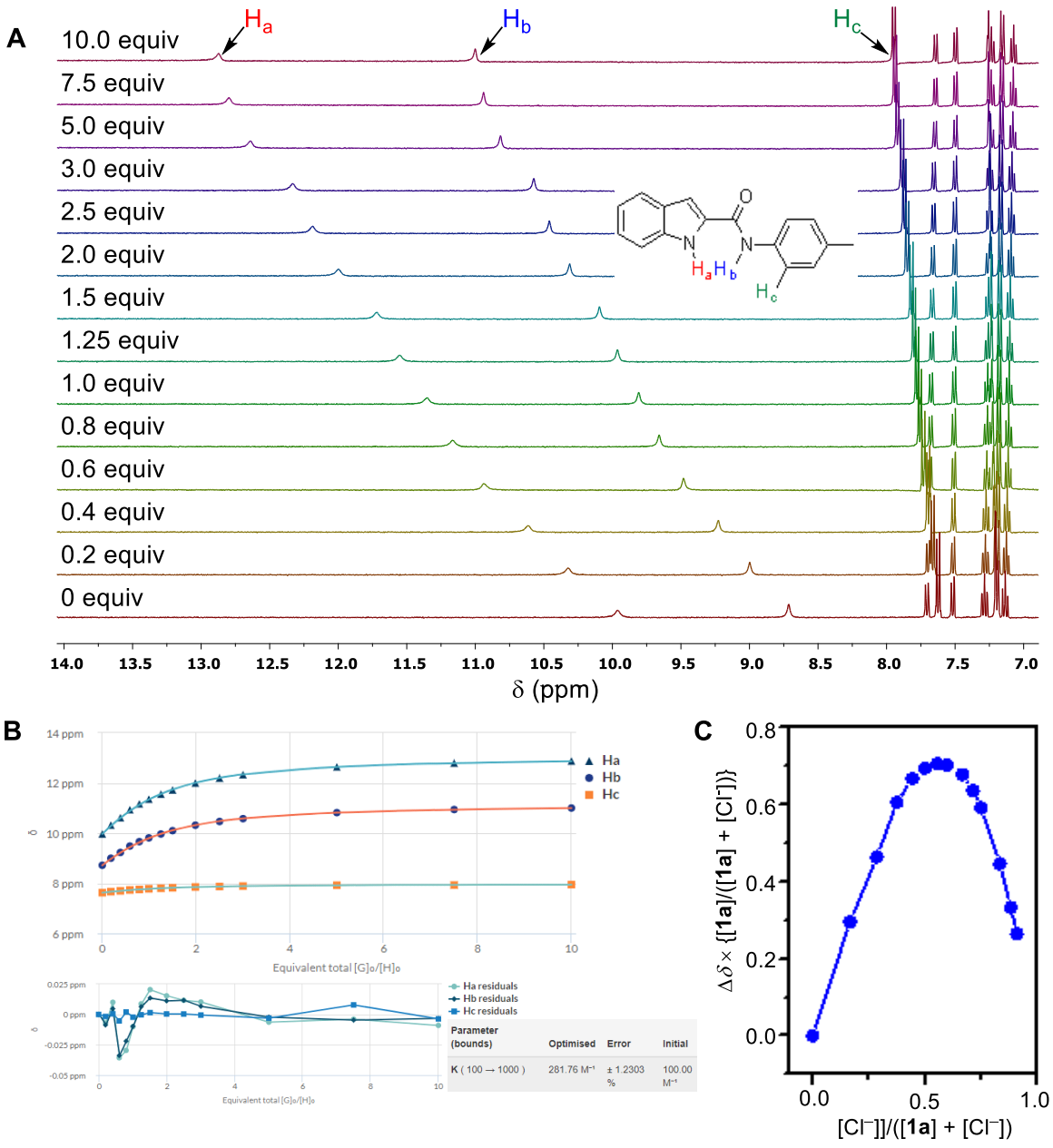

Figure 4.5 ^{1}H NMR titration spectra for **1a** (0.005 M) with stepwise addition of TBACl (0.4 M) in CD_3CN. The equivalents of added TBACl are shown on the stack spectra (**A**). The plot of chemical shift (δ) of H_a, H_b, and H_c protons *vs* concentration of TBACl added, fitted to 1:1 binding model of BindFit v0.5 (**B**). Job plot analysis for the N-H_a proton shift of **1a** upon titration with TBACl (**C**).

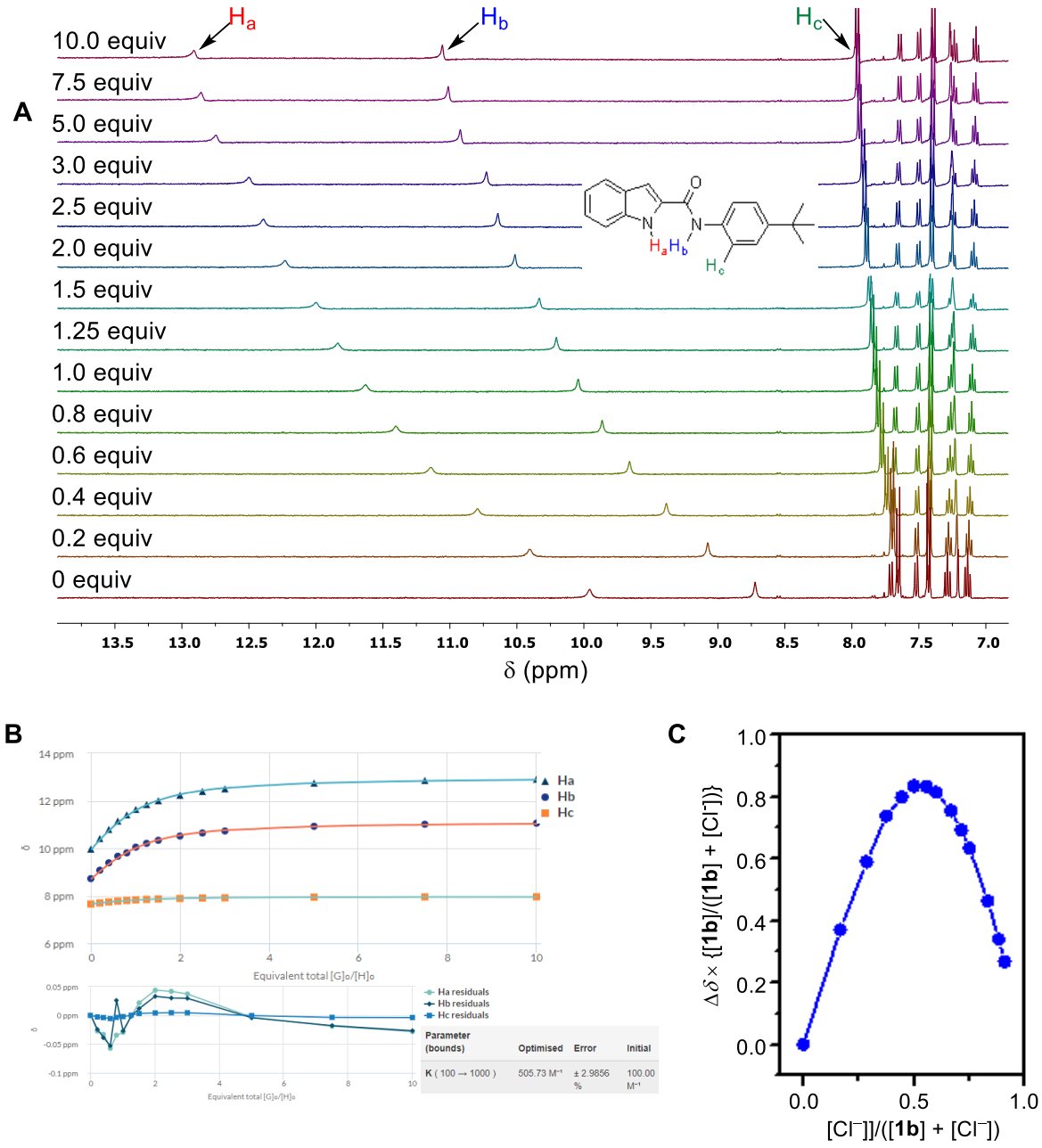

Figure 4.6 ^{1}H NMR titration spectra for **1b** (0.005 M) with stepwise addition of TBACl (0.4 M) in CD_3CN. The equivalents of added TBACl are shown on the stack spectra (**A**). The plot of chemical shift (δ) of H_a, H_b, and H_c protons *vs* concentration of TBACl added, fitted to 1:1 binding model of BindFit v0.5 (**B**). Job plot analysis for the N-H_a proton shift of **1b** upon titration with TBACl (**C**).

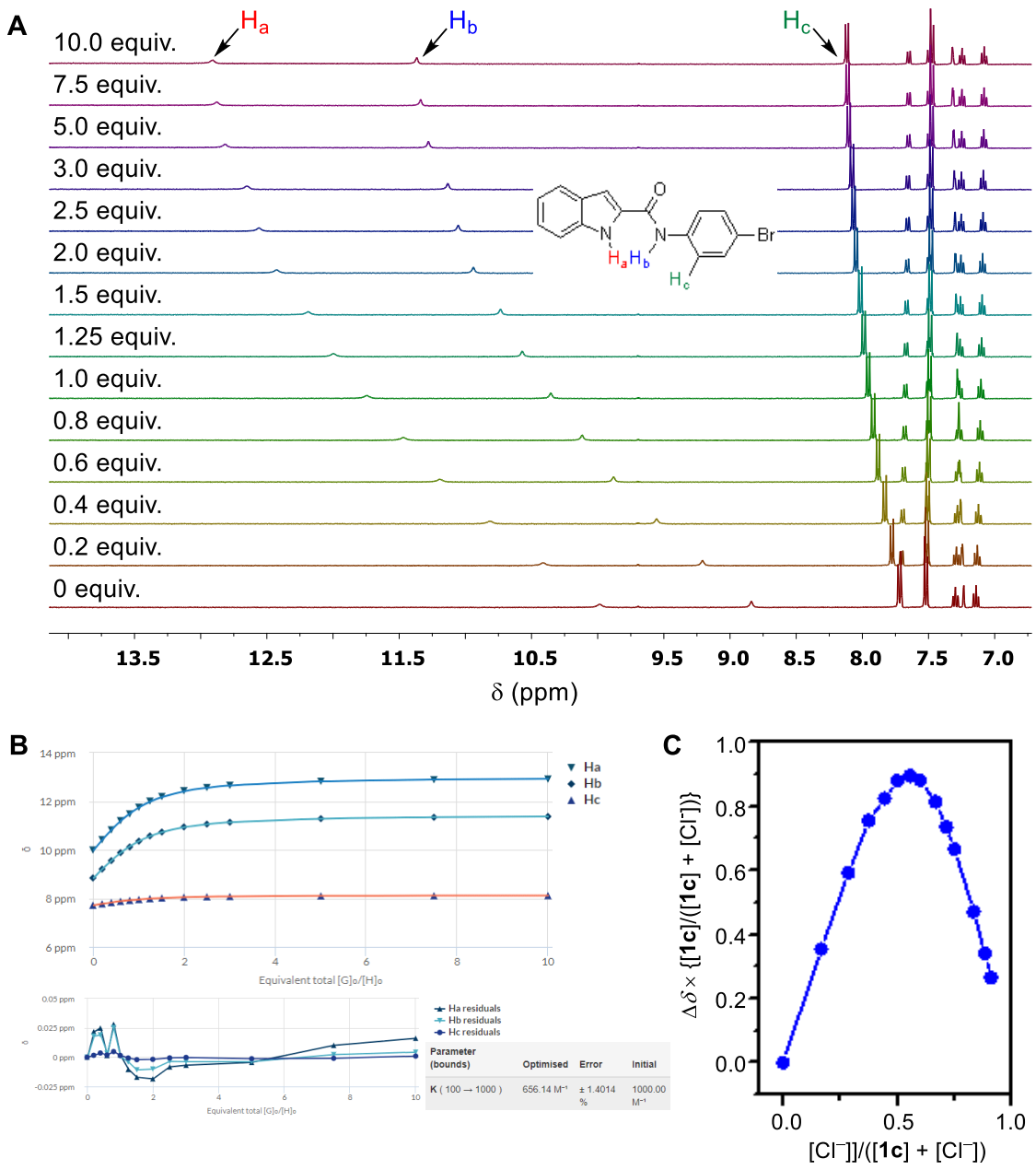

Figure 4.7 ^{1}H NMR titration spectra for **1c** (0.005 M) with stepwise addition of TBACl (0.4 M) in CD_3CN. The equivalents of added TBACl are shown on the stack spectra (**A**). The plot of chemical shift (δ) of H_a, H_b, and H_c protons *vs* concentration of TBACl added, fitted to 1:1 binding model of BindFit v0.5 (**B**). Job plot analysis for the N-H_a proton shift of **1c** upon titration with TBACl (**C**).

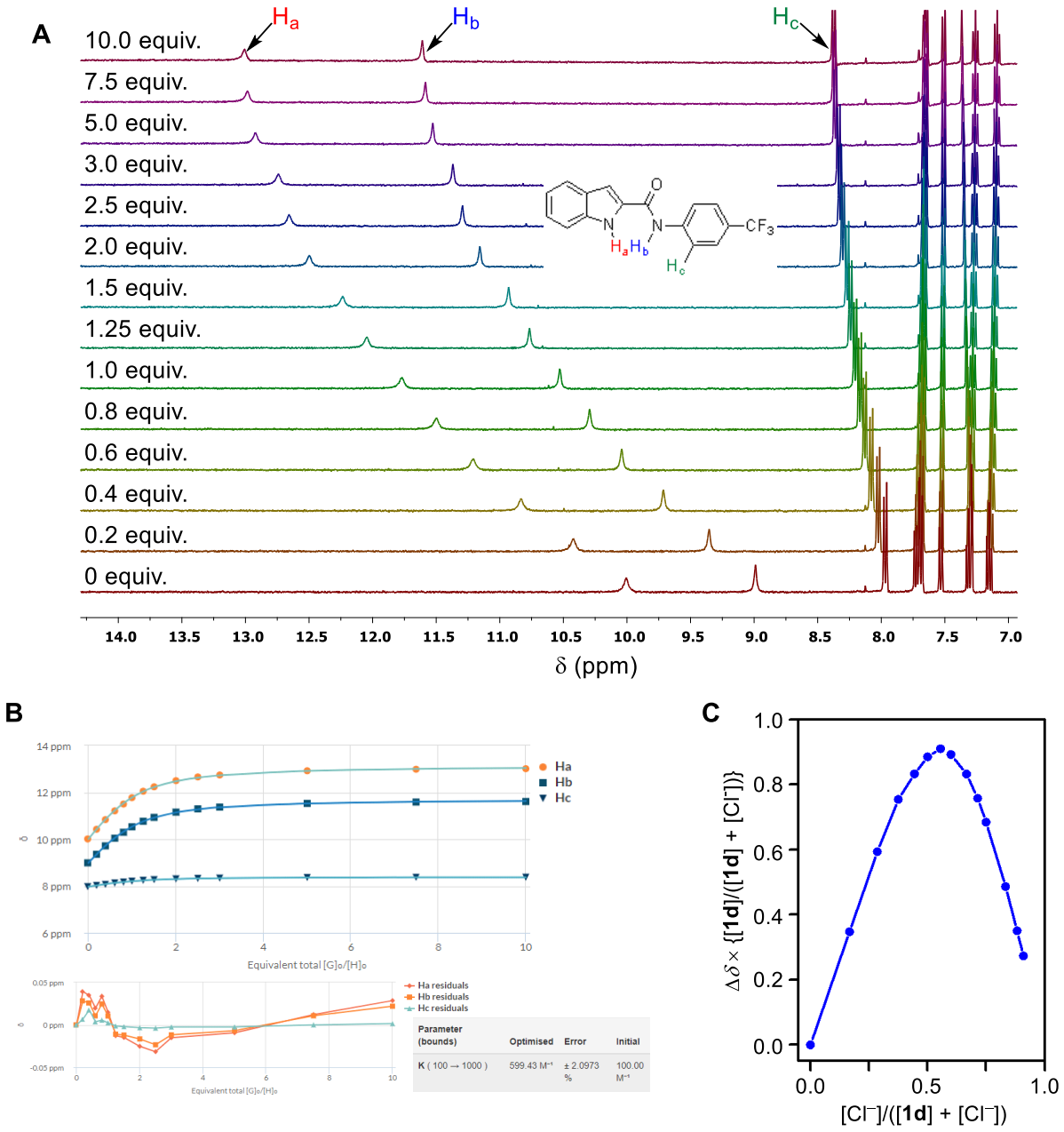

Figure 4.8 ^{1}H NMR titration spectra for **1d** (0.005 M) with stepwise addition of TBACl (0.4 M) in CD_3CN. The equivalents of added TBACl are shown on the stack spectra (**A**). The plot of chemical shift (δ) of H_a, H_b, and H_c protons *vs* concentration of TBACl added, fitted to 1:1 binding model of BindFit v0.5 (**B**). Job plot analysis for the N-H_a proton shift of **1d** upon titration with TBACl (**C**).

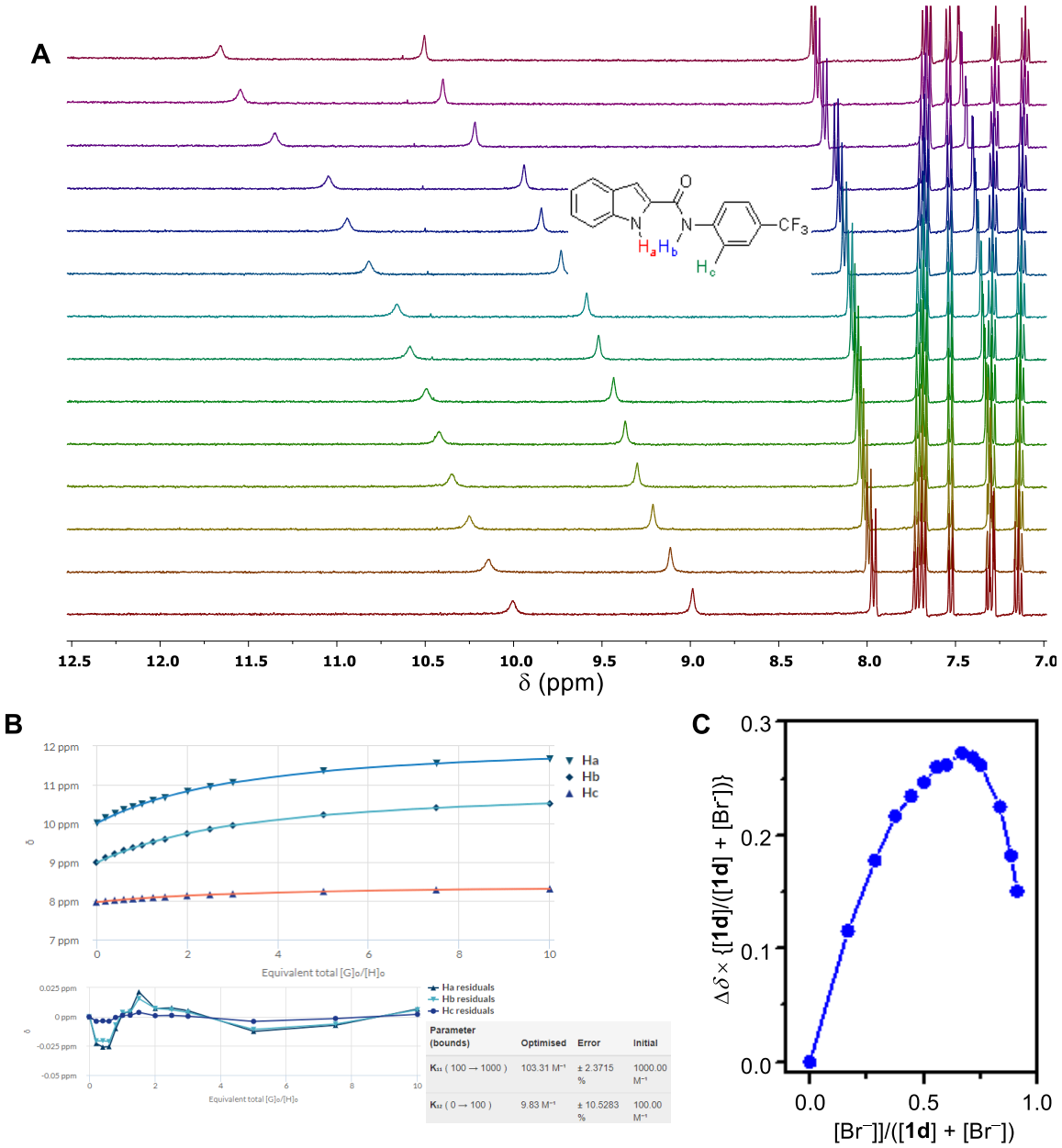

Figure 4.9 ^{1}H NMR titration spectra for **1d** (0.005 M) with stepwise addition of TBABr (0.4 M) in CD_3CN. The equivalents of added TBABr are shown on the stack spectra (**A**). The plot of chemical shift (δ) of H_a, H_b, and H_c protons *vs* concentration of TBABr added, fitted to 1:1 binding model of BindFit v0.5 (**B**). Job plot analysis for the N-H_a proton shift of **1d** upon titration with TBABr (**C**).

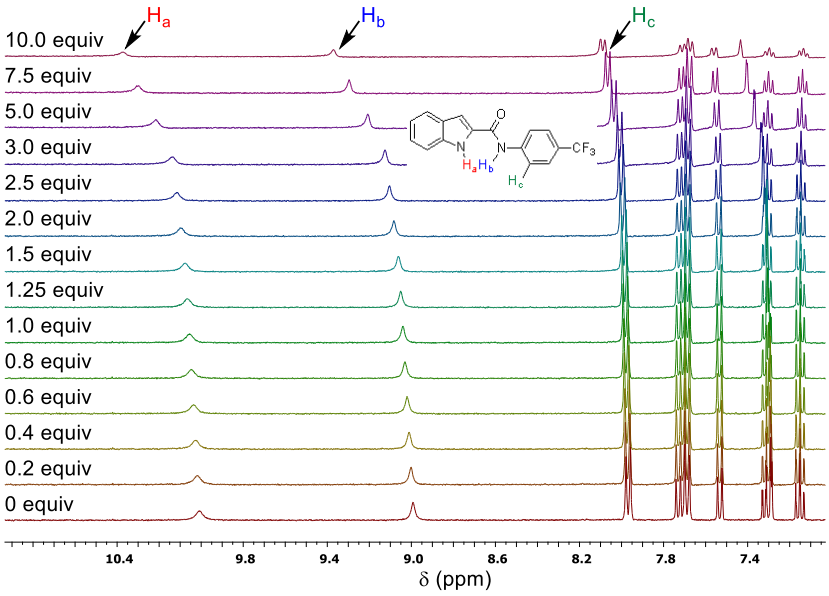

Figure 4.10 ^{1}H NMR titration spectra for **1d** (0.005 M) with stepwise addition of TBAI (0.4 M) in CD_3CN. The equivalents of added TBAI are shown on the stack spectra.

4.2.3 Ion transport studies

The ion transport properties of carriers **1a** – **1d** and **2** were examined across large unilamellar vesicles (LUVs) entrapped with HPTS (EYPC-LUVs⊃HPTS). The collapse of the applied pH gradient (pH_{in} = 7.0 and, pH_{out} = 7.8) upon the addition of each compound was monitored by measuring the change in HPTS fluorescence at λ_{em} = 510 nm (λ_{ex} = 450 nm) with time. The comparative ion transport activity of **1a** – **1d** at concentration c = 400 nM provided the sequence: **1d** >> **1c** > **1b** ~ **1a** which suggests the roles of N-H proton acidity as well as log$P$ values in the transport activity (Figure 4.13A). Compound **2** was inactive at this concentration, confirming the successful caging of carrier activity by the ONB group which acts as a barrier for efficient ion binding. The Hill analysis of the concentration profile of **1d** provided the effective concentration at 50% activity, EC_{50} = 0.219 μM (i.e., compound/lipid ratio = 0.327 mol%). The calculated Hill coefficient, n = 1.88 indicates the involvement of two molecules of **1d** in the active carrier formation (Figure 4.12). For **1c**, the EC_{50} and n values were 0.768 μM and 2.72, respectively (Figure 4.11). Hill analysis of **1a** and **1b** could not be performed due precipitation of these compounds at high concentrations.

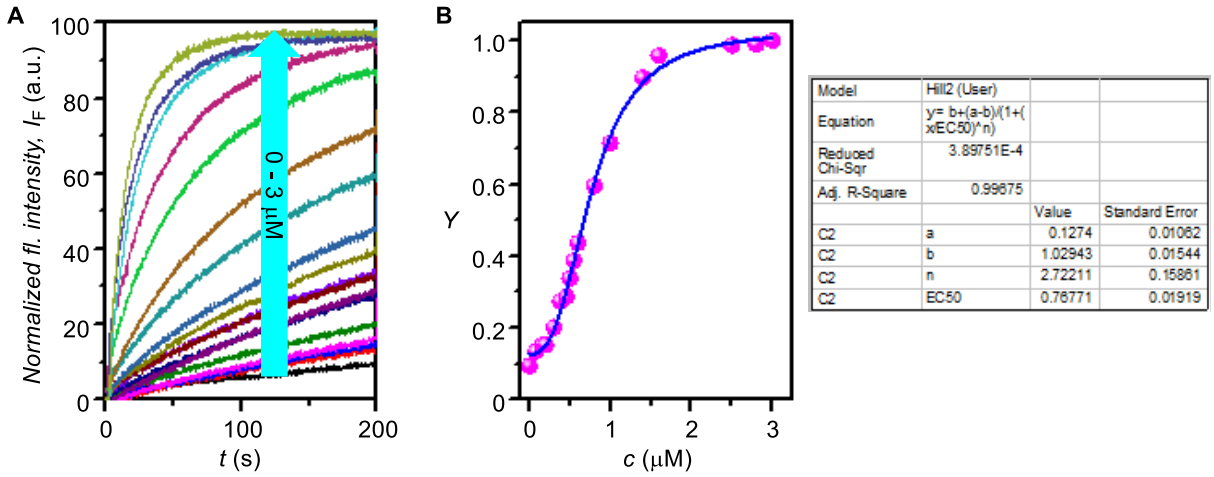

Model	Hill2 (User)		
Equation	y= b+(a-b)/(1+(x/EC50)^n)		
Reduced Chi-Sqr	3.89751E-4		
Adj. R-Square	0.99675		
		Value	Standard Error
C2	a	0.1274	0.01062
C2	b	1.02943	0.01544
C2	n	2.72211	0.15861
C2	EC50	0.76771	0.01919

Figure 4.11 Concentration-dependent activity of compound **1c** across EYPC–LUVs⊃HPTS (**A**). Hill analysis of compound **1c** at *t* = 190 s (**B**).

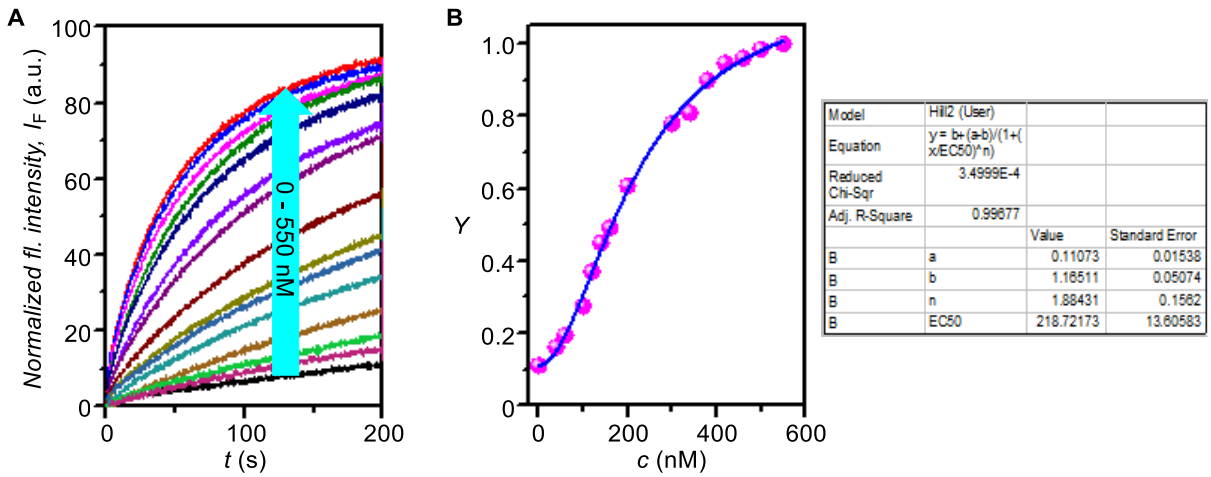

Model	Hill2 (User)		
Equation	y= b+(a-b)/(1+(x/EC50)^n)		
Reduced Chi-Sqr	3.4999E-4		
Adj. R-Square	0.99677		
		Value	Standard Error
B	a	0.11073	0.01538
B	b	1.16511	0.05074
B	n	1.88431	0.1562
B	EC50	218.72173	13.60583

Figure 4.12 Concentration-dependent activity of compound **1d** across EYPC–LUVs⊃HPTS (**A**). Hill analysis of compound **1d** at *t* = 190 s (**B**).

The most active N-aryl-1H-indole-2-carboxamide **1d** was then studied for its ion selectivity across EYPC–LUVs⊃HPTS. The ion selectivity of **1d** was performed by the variation of extravesicular cations or anions with iso-osmolar intravesicular NaCl. Variation of external cations (i.e., M^+ = Li^+, Na^+, K^+, Rb^+, and Cs^+) in the vesicles did not provide any noticeable difference in the ion transport rate after the addition of **1d** indicating no role of alkali metal cations in the transport process (Figure 4.13C). However, the change of external anions (i.e., X^- = F^-, Cl^-, Br^-, OAc^-, and NO_3^-) in the EYPC–LUVs⊃HPTS provided a significant variation

in ion transport activity (Figure 4.13B). The order of activity was $Cl^- >> Br^- \sim F^- > OAc^- > NO_3^-$. The ion selectivity data confirmed **1d** to be a chloride-selective carrier.

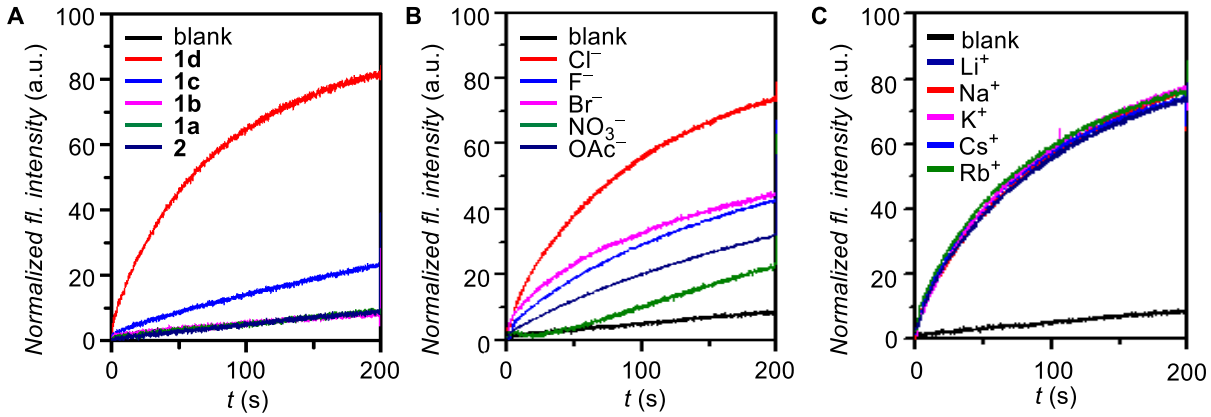

Figure **4.13** Comparison of ion transport activities of **1a – 1d** and **2** (400 nM each) across EYPC–LUVs⊃HPTS (**A**). Anion selectivity of **1d** (340 nM) was measured by varying the external anions of EYPC–LUVs⊃HPTS (**B**). Cation selectivity of **1d** (340 nM) measured by varying external cations across EYPC–LUVs⊃HPTS (**C**).

The ion selectivity data shows transport activity of **1d** is anion-dependent and cation-independent. Therefore, ion selectivity studies ruled out the symport M^+/Cl^- and antiport M^+/H^+ mechanism of ion transport. Thus, H^+/Cl^- symport or Cl^-/OH^- antiport could be the mechanism of ion transport. To determine the operative ion transport mechanism, the ion transport activity of **1d** was monitored in the presence of carbonyl cyanide-4-(trifluoromethoxy) phenylhydrazone (FCCP, a proton carrier).[26] When a pH gradient is applied across the lipid bilayer, FCCP permits H^+ efflux from the intravesicular region (pH = 7.0) to the extravesicular region (pH = 7.8). Under the applied pH gradient, the transport activity of **1d** (280 nM) was enhanced two-fold in the presence of FCCP (937.5 nM) compared to that observed in its absence, ruling out the H^+/A^- symport mechanism. The cooperative effect on transport activity of **1d** with FCCP shows a faster exchange of OH^-/X^-, thus confirming the antiport transport mechanism (Figure 4.13A). Further to confirm the antiport mechanism, the transport activity of **1d** was monitored in the presence and absence of valinomycin (a natural K^+ ion selective carrier).[27] The pulse of K^+ ion was given in extravesicular buffer (10 mM HEPES, 100 mM KCl, pH = 7.0). The transport activities of **1d** (340 nM) in the absence and presence of valinomycin (15 pM) were comparable under the applied pH gradient (pH_{in} = 7.0 and pH_{out} = 7.8) across HPTS entrapped vesicles (Figure 4.13B). Therefore, FCCP and

valinomycin coupled ion transport data corroborates the OH^-/Cl^- antiport as the main transport mechanism.[28]

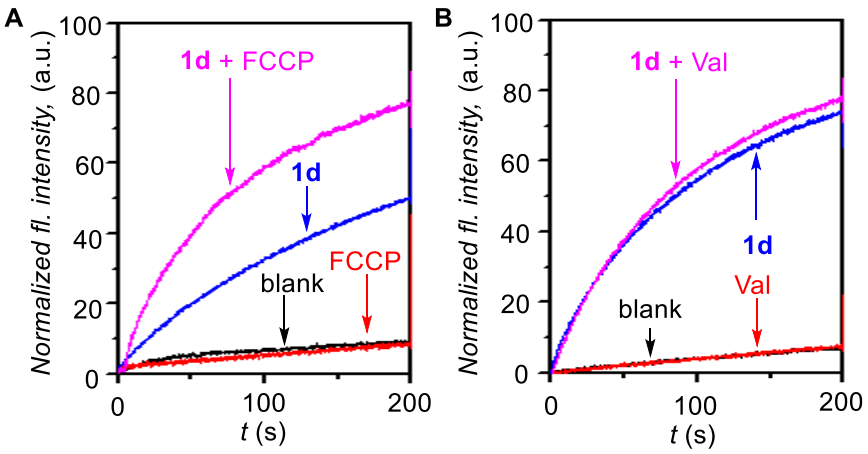

Figure 4.14 Comparison of ion transport activity of **1d** (340 nM) in the presence and absence of FCCP (937.5 nM) (**A**). Comparison of ion transport activity of **1d** (280 nM) in the presence and absence of valinomycin (15 pM) (**B**).

Subsequently, the Cl^- transport activity of **1d** and procarrier **2** across EYPC–LUVs⊃lucigenin (Cl^- selective fluorescent dye) were monitored at λ_{em} = 535 nm (λ_{ex} = 455 nm) by applying a gradient of intravesicular NO_3^- and extravesicular Cl^- upon addition of 2 M NaCl. The Cl^- influx activities of carrier **1d** (2 μM) and its procarrier **2** (2 μM) were monitored over time. Carrier **1d** exhibited efficient Cl^- transport while procarrier **2** was completely inactive at the same concentration (Figure 4.15A). This result successfully corroborates our hypothesis that the photocleavable protecting group ONB inactivates the carrier molecule by blocking one of the ion binding sites. A concentration-dependent Cl^- influx study of **1d** across EYPC–LUVs⊃lucigenin gave EC_{50} = 1.251 μM and n = 2.047 (Figure 4.16). The Hill coefficient values further confirmed the involvement of two molecules of **1d** in the active carrier formation. The involvement of cations in the ion transport process was assessed across EYPC-LUVs⊃ lucigenin by the variation of extravesicular cations. EYPC-LUVs⊃ lucigenin were suspended in different alkali metal chloride salt (MCl, M^+ = Li^+, Na^+, K^+, Rb^+, and Cs^+) solutions for the assay. The variation of external cations showed no significant difference in the rate of Cl^- influx of **1d** (1.25 μM) clearly indicating the ion transport process to be cation-independent (Figure 4.15B).

The antiport ion transport mechanism was confirmed by monitoring Cl^- transport activity across EYPC-LUVs⊃ lucigenin using valinomycin (a natural K^+ selective carrier). In this assay, KCl solution was added in the extravesicular medium keeping the intravesicular $NaNO_3$ solution. Under the applied Cl^- gradient, the rate of Cl^- influx by **1d** (1.25 μM) was investigated in the absence and presence of valinomycin (1.25 μM). The Cl^- influx activity of **1d** in the presence of valinomycin was significantly higher (Figure 4.15C), which further confirms the antiport of anions as the main transport mechanism.

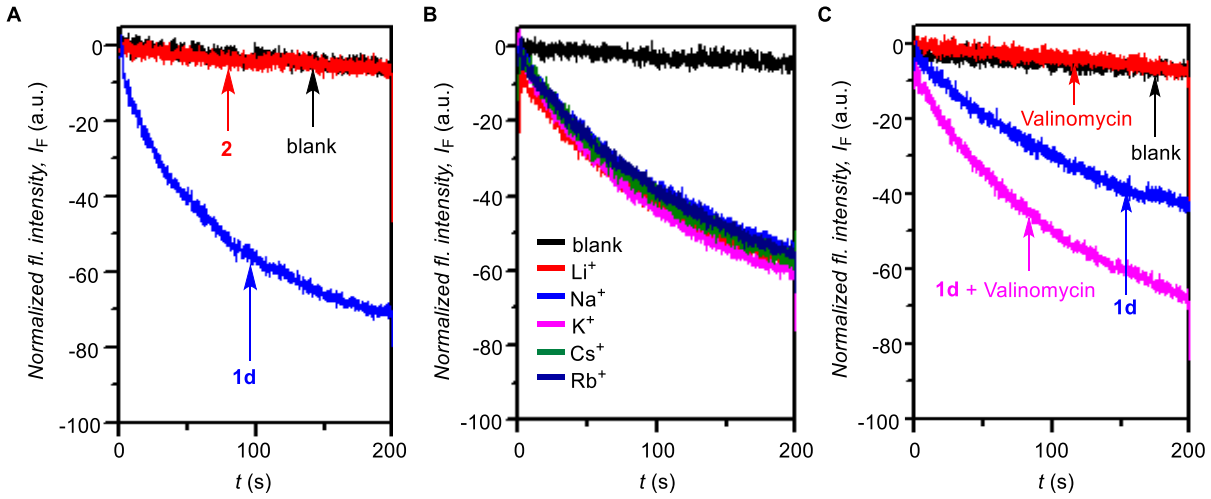

Figure 4.15 Comparison of Cl− influx activity of **1d** and **2** (2 μM each) across EYPC–LUVs⊃lucigenin (**A**). Cation selectivity of **1d** (1.25 μM) by the variation of external cations of EYPC–LUVs⊃lucigenin (**B**). Comparison of Cl^- influx activity of **1d** (1.25 μM) in the absence and the presence of valinomycin (1.25 μM) (**C**).

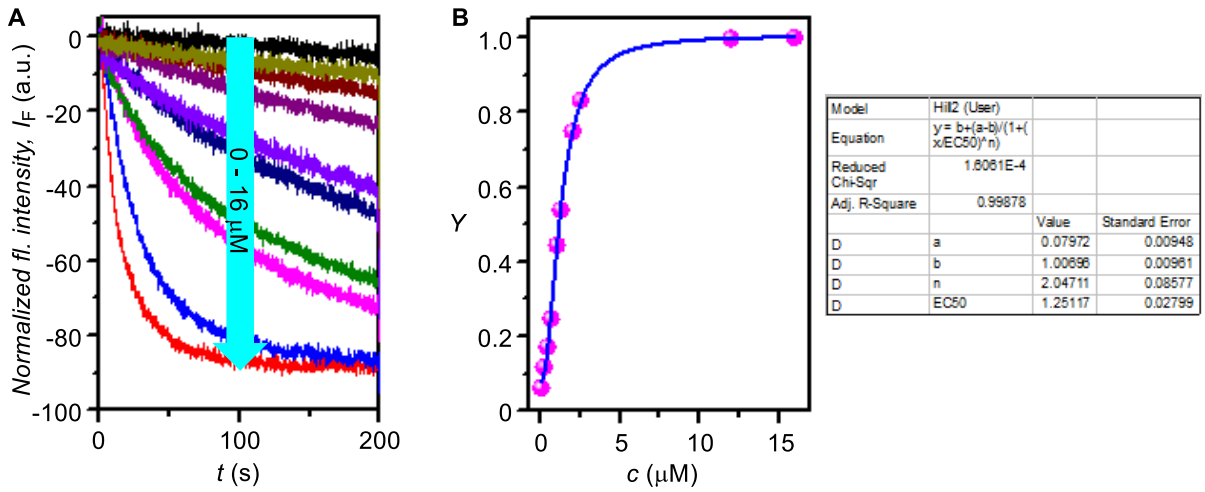

Model	Hill2 (User)		
Equation	y= b+(a-b)/(1+(x/EC50)^n)		
Reduced Chi-Sqr	1.8061E-4		
Adj. R-Square	0.99878		
		Value	Standard Error
D	a	0.07972	0.00948
D	b	1.00698	0.00961
D	n	2.04711	0.08577
D	EC50	1.25117	0.02799

Figure 4.16 Concentration-dependent activity of compound **1d** across EYPC-LUVs⊃lucigenin. (**A**). Hill plot analysis of compound **1d** at t = 290 s (**B**).

4.2.4 Geometry optimization

Based on the experimentally determined Hill coefficient value of approximately 2, the geometry-optimized structure of the [(**1d**)$_2$+Cl$^-$] complex was obtained first by generating the most probable conformation by using the CONFLEX 8 program[29, 30] (Figure 4.17A and 4.17B), and subsequently optimizing the generated conformation by using the Gaussian 09 program suite[31] with B3LYP functional[32, 33] and 6-311G(d,p) basis set.[34, 35] The geometry-optimized structure of the [(**1d**)$_2$+Cl$^-$] complex showed two receptor molecules oriented orthogonally around the central Cl$^-$ ion (Figure 4..17C). The structure confirmed that each receptor participates in anion recognition through N_{indole}–H_a···Cl$^-$ (N_{indole}···Cl$^-$ = 3.22 Å) as well as N_{amide}–Hb···Cl$^-$ (N_{amide}···Cl$^-$ = 3.38 Å) interactions (Figure 4.17C). In addition to these, the C_{ortho}···Cl$^-$ distance of 3.75 Å and the C_{ortho}–Hc···Cl$^-$ bond angle of approximately 144.8^o confirmed the presence of C_{ortho}–Hc···Cl$^-$ interaction between the receptor and the ion.

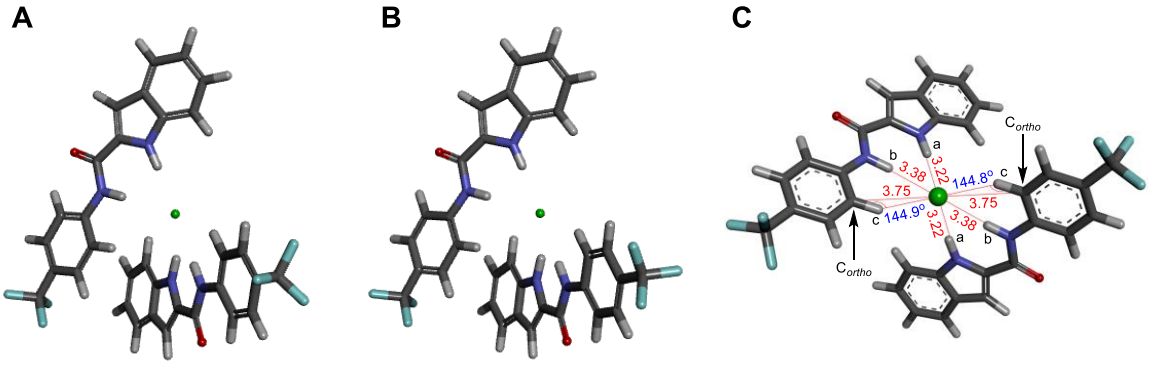

Figure 4.17 Most probable conformation of two molecules of **1d** and Cl$^-$. Conf-1 (Boltzmann population 50.0732%) (**A**). Conf-2 (Boltzmann population 49.9268%) (**B**). Geometry optimized structure of receptor (**1d**) and Cl$^-$ interaction.

4.2.5 Photolysis study

The assessment of the photolytic conversion of procarrier **2** to the active carrier **1d** was confirmed by ^{1}H NMR. The solution of procarrier **2** in deuterated dimethyl sulfoxide (DMSO-d_6) (5 mg in 0.5 mL) was irradiated by 3 LEDs of 365 nm wavelength having 1 W power each with 5 min interval of time for 45 min and the NMR spectrum was recorded at each time point. The $H_{a'}$ signal of **2** at δ = 11.78 ppm disappeared upon photoirradiation, with the appearance of a new signal at δ = 11.81 ppm that corresponds to the indole H_a, indicating the release of **1d** (Figure 4.18). Similarly, the appearance of an amide H_b signal at δ = 10.52 ppm confirmed the

cleavage of the ONB moiety from the indole-2-carboxamide. The disappearance of the $H_{c'}$ signal at δ = 5.45 ppm and the appearance of the new H_c signal at δ = 11.66 ppm confirmed the formation of o-nitrosobenzaldehyde **8** as the photocleavage product.[20]

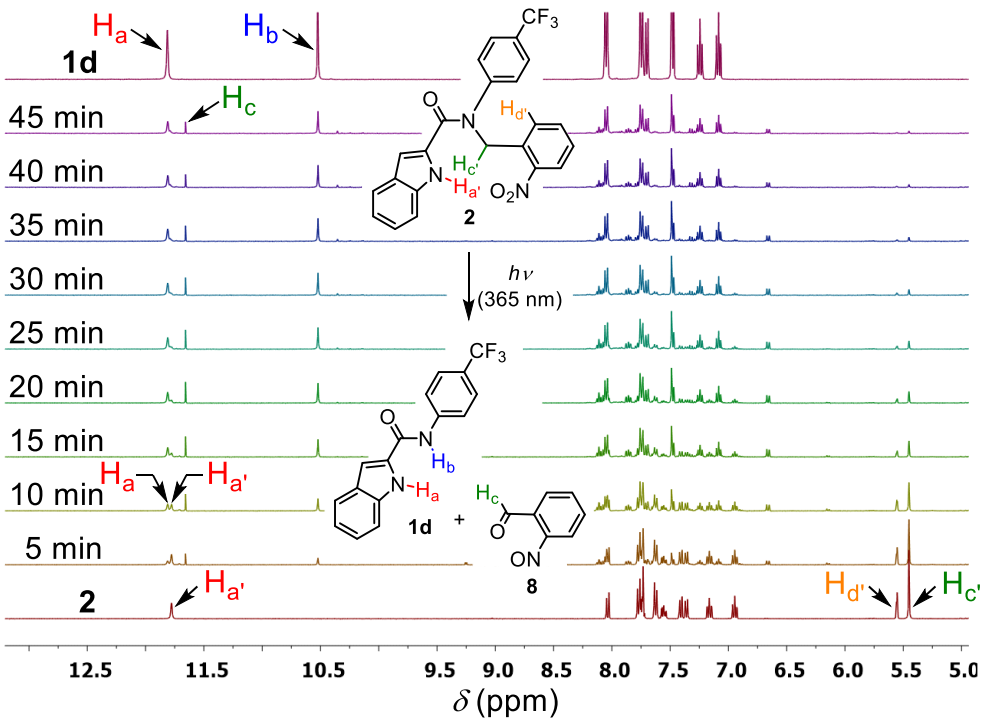

Figure 4.18 Phototriggered release of indole carboxamide **1d** from procarrier **2** monitored by ^{1}H NMR in DMSO-d_6 recorded at intervals of 5 min.

4.2.6 Photoactivation of procarrier in lipid membrane

The successful release of the indole carboxamide **1d** upon photoirradiation of corresponding ONB-protected derivative **2** prompted us to study photoactivated transmembrane ion transport by **2**. For this purpose, the ion transport activities were monitored across EYPC–LUVs⊃HPTS after photo irradiating (λ = 365 nm) samples of **2** (380 nM) for varied durations (irradiation time t_R = 0, 1, 2, 3 and 5 min) in the presence of the LUVs (Figure 4.19A). During the ion-transport experiments, the activities of these samples (i.e., relative fluorescence intensity F_R) at 190 s after NaOH addition were compared by setting the HPTS fluorescence of the blank sample to 0 and that of **1d** (380 nM) to 100. The nonirradiated sample of as-synthesized **2** was inactive (F_R = 1.7) as expected (Figure 4.19B). Upon irradiating **2** for t_R = 1 min, the percent transport efficiency F_R was recorded as 42.3. It is interesting to note that up to 90.5% transport efficiency of **2** was recovered by irradiating the sample for just 3 min. A sample of 1% DMSO,

when photoirradiated for 5 min under comparable conditions, gave only F_R = 0.1, which confirms that 365 nm light does not destroy the integrity of the lipid bilayer membrane.

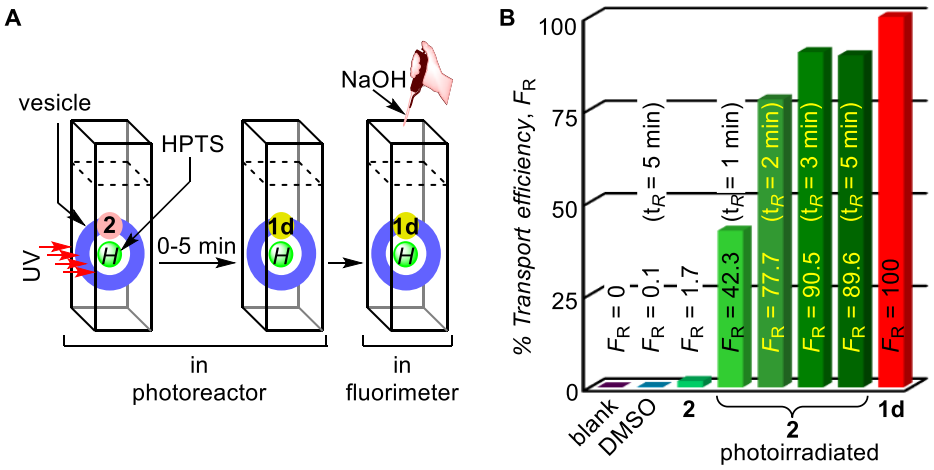

Figure 4.19 Schematic representation of experimental study of photoactivated ion transport of procarrier **2** across EYPC–LUVs⊃HPTS (**A**). Percent transport efficiencies of photoirradiated samples measured relative to the activity of **1d** (**B**).

4.2.7 Biological studies

Cl^- carriers are known to cause apoptotic cell death via disturbance of ion homeostasis. Therefore, the cytotoxic effect of the procarrier **2** and Cl^- carrier **1d** were evaluated in the MCF-7 cell line using MTT assay. When the cells were incubated with compound **2** for 24 h, no significant cytotoxicity was observed (Figure 4.20A). Surprisingly, compound **1d** also showed poor cytotoxicity. Interestingly, when the cells in the culture were analysed under a microscope, significant precipitation of **1d** (10 μM) was observed in the extracellular media (Figure 4.20D and 4.20E). Such precipitation was not observed for the compound **2**. Therefore, the poor cytotoxicity of **1d** was attributed to the low cell permeability/solubility of the compound.[36, 37] To check whether the procarrier can be subjected to photorelease within cells, the cells were incubated with compound **2** for 4 h and then irradiated with 365 nm light of 3 W energy for 5 min. The cells were then kept in the incubator for a further 20 h and monitored by standard MTT assay. The photoirradiated cells incubated with compound **2** showed pronounced cell death. However, photoirradiated control cells were completely viable (Figure 4.20A).

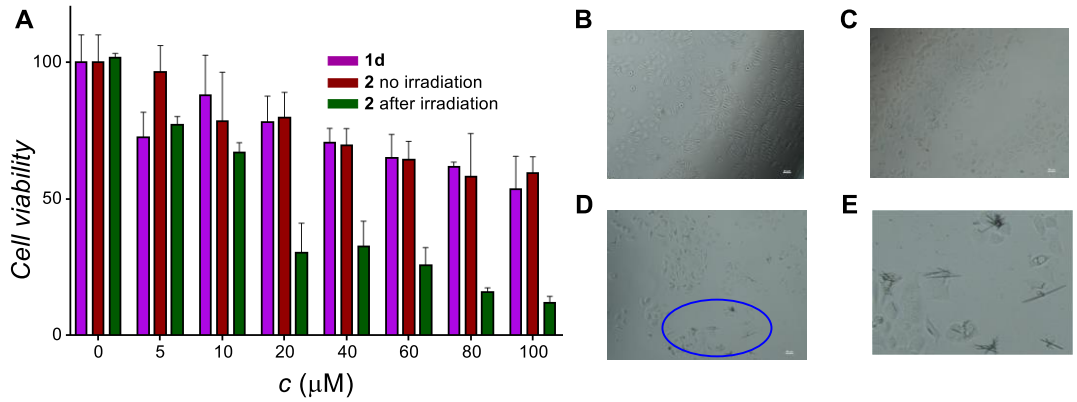

Figure 4.20 Cell viability obtained from MTT assay upon incubation of **1d** and **2** for 24 h in MCF 7 cell lines. Mean cell viability was represented from three independent experiments (**A**). Cell images were taken from 96 well plate before initiating the MTT assay with control (**B**); compound **2** (**C**) and compound **1d** (**D**) at 10 μM concentration. Zoomed part of Figure D (**E**). For figures A-C, scale bar = 50 μM.

To evaluate the cytotoxicity of the *o*-nitrosobenzaldehyde (**8**) byproduct, compound **11** was synthesised as per the reported procedure. The compound *p*-methoxyphenol (**9**) was already reported to be non-toxic to cells.[38] Therefore, compound **11** upon photoirradiation with 365 nm light would result in the formation of non-toxic compounds **9** and **8** (Figure 4.21). If toxicity is observed for the photoirradiated sample of **11**, it would be mainly due to *o*-nitrosobenzaldehyde **8**.

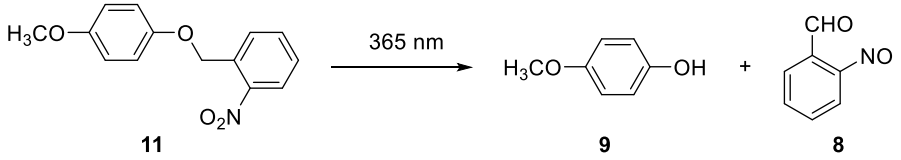

Figure 4.21 Photocleavage of compound **11** by 365 nm UV light.

At first, the formation of *p*-methoxyphenol **9** upon photoirradiation of **11** was monitored by TLC. Complete conversion of **11** to **9** was observed when solution of compound **11** in chloroform was placed in a quartz cuvette and then irradiated with 365 nm wavelength light for 10 min (Figure 4.22).

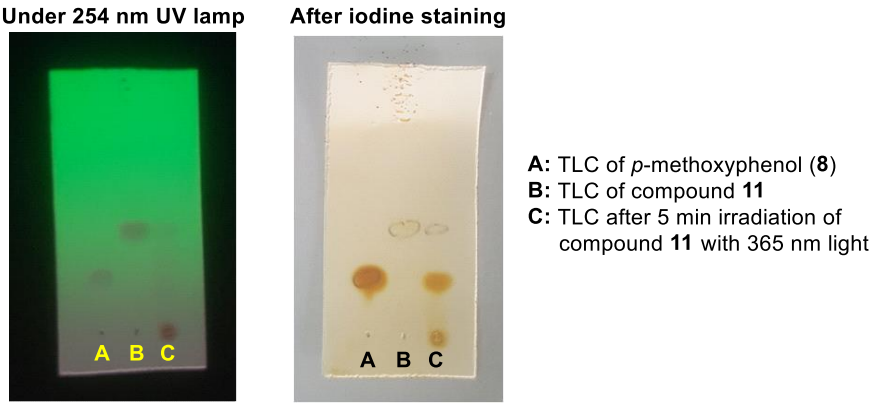

Figure 4.22 Photocleavage of compound **11** monitored by TLC method.

The cells were incubated with compound **11** for 4 h and irradiated by light of 365 nm wavelength for 5 min. The cells were incubated for another 20 h and cell viability was monitored by standard MTT assay. Compound **11** showed negligible cytotoxicity compared to the photoreleased carrier **1d** from procarrier **2** (Figure 4.23). This data successfully established our proposition of inducing cell death by photoactivating Cl^- transport in cancer cells.

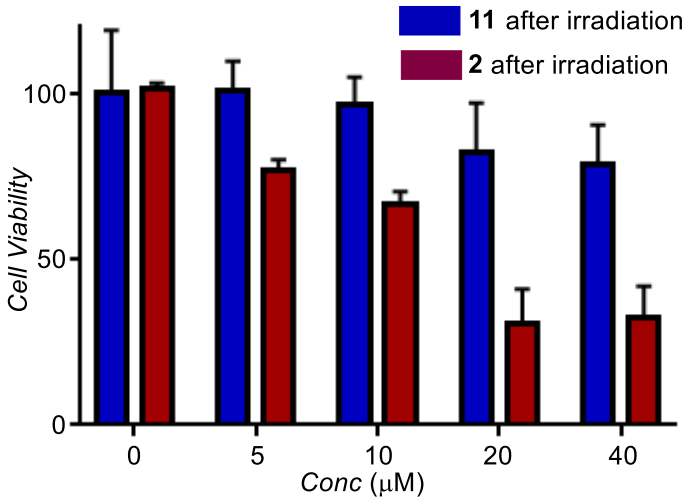

Figure 4.23 Cell viability data obtained from MTT assay upon addition of **2** and **11** for 24 h in MCF 7 cell lines. Mean cell viability was represented from three independent experiments.

4.3 Conclusion

In summary, we have designed and synthesized simple N-aryl-1H-indole-2-carboxamide carriers **1a** – **1d** and an *o*-nitrobenzyl (ONB) protected procarrier. The ^{1}H NMR titration confirmed the hydrogen bond interaction of indole N-H, amide N-H and ortho C-H of amide

N-H with anion. The ONB protected procarrier with *p*-CF_3-phenyl as the aryl group was inactive while the free carboxamide **1d** was an efficient carrier of ion giving EC_{50} = 0.219 µM and Hill coefficient, n = 1.88 when studied using EYPC–LUVs⊃HPTS. The carrier also exhibited chloride/anion antiport across lipid bilayer membranes. The geometry-optimized structure of the 2:1 carrier-Cl^- complex showed multivalent hydrogen bond interactions involved in the recognition of the anion. The mechanism of ONB photo-cleavage was also confirmed by a ^{1}H NMR study. The photocleavage of the ONB group facilitated up to 90.5% transport efficiency within 3 minutes of radiation. The photorelease of carrier **1d** from procarrier **2** within cancer cells and the resulting cell death were also confirmed by MTT assay. In conclusion, we have successfully achieved proof of the light-activated concept with the simple system. This rewarding outcome, based on our simple and innovative concept, can be extended in photodynamic therapy for surface cancer treatment and can also be adapted for deep-seated cancer therapy employing endoscopes or optical fibers.

4.4 Experimental section

4.4.1 General methods

All chemical reactions were performed under a nitrogen atmosphere. All reagents and solvents for synthesis were purchased from commercial sources (Sigma-Aldrich, Spectrochem) and used further without purification. The column chromatography was carried out using Merck silica gel (100-200/ 230-400 mesh size). The thin layer chromatography was performed on Merck silica gel 60-F254 plates. Egg yolk phosphatidylcholine (EYPC) as a solution of chloroform (25 mg / mL), mini extruder set and polycarbonate membranes of 100 nm and 200 nm were purchased from Avanti Polar Lipids. HEPES, HPTS, lucigenin, NaOH, Triton X-100, FCCP, valinomycin, Sephadex G50 and inorganic salts of molecular biology grade were obtained from Sigma Aldrich.

4.4.2 Physical measurements

All NMR spectra were recorded on Bruker Avance III HD 400 MHz and JEOL JNM-ECS 400 MHz nuclear magnetic resonance (NMR) spectrometers. The ^{1}H NMR spectra were recorded at 400 MHz whereas ^{13}C spectra were at 101 MHz. The residual solvent signals were considered as an internal reference (δ_H = 7.26 ppm for $CDCl_3$, δ_H = 2.50 for DMSO-d_6, and

δ_H = 1.94 for CD_3CN) to calibrate spectra. The chemical shifts were reported in ppm. Following abbreviations were used to indicate multiplicity patterns m: multiplet, s: singlet, d: doublet, t: triplet, q: quartet, dd: doublet of doublets, td: triplet of doublets, dt: doublet of triplets, ddd: doublet of doublets of doublets. Coupling constants were measured in Hz. Infra-red (IR) spectra were measured in cm^{-1} using a Bruker ALPHA-E FT–IR spectrophotometer. Melting points were measured in open glass capillaries on a micro melting point apparatus. High-resolution mass spectra (HRMS) were recorded on a Waters SYNAPT G2 mass spectrometer equipped with a Waters Z-Spray™ electrospray ionization (ESI) source. Fluorescence experiments were on a HORIBA Jobin Yvon Fluoromax® 4 spectrofluorometer equipped with injector port and magnetic stirrer. All buffer solutions were adjusted to the necessary pH using a Hanna Instruments pHep® (HI98107) pocket-sized pH tester. All buffer solutions were prepared from the autoclaved water. The data from fluorescence studies was processed using OriginPro 8.5 software.

4.4.3 Synthesis

General procedure for synthesizing Indole amide derivatives (1a–1d):

General Method A: In a 100 mL round bottom flask, indole-2-carboxylic acid (300 mg, 1.86 mmol), EDC·HCl (428 mg, 2.23 mmol), and HOBt (301 mg 2.23 mmol) were dissolved in DMF (3 mL). The resulting solution was stirred at room temperature for 30 min. After 30 min, *para*-substituted aniline derivative **4a – 4d** (2.80 mmol) and NEt_3 (389 µL, 2.80 mmol) were added. The reaction mixture was stirred at room temperature for an additional 12 h. After completion of the reaction, the reaction mixture was quenched by water (10 mL), extracted with ethyl acetate (3 × 10 mL), washed with brine (2 × 10 mL), the organic layer dried over Na_2SO_4 and concentrated under reduced pressure. The purification of the crude product was done by using silica gel chromatography to give pure **1a – 1d**.

***N*-(*p*-tolyl)-1*H*-indole-2-carboxamide (1a):**

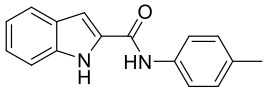

1a

Eluent for column chromatography: CH_2Cl_2; **Physical appearance:** obtained as white solid; Yield = 54%; **M.P.:** 248.0 °C; **^{1}H NMR (400 MHz, DMSO-d_6):** δ 11.71 (s, 1H), 10.13 (s, 1H), 7.72 – 7.64 (m, 3H), 7.47 (dd, *J* = 8.2, 0.8 Hz, 1H), 7.41 (dd, *J* = 2.1, 0.7 Hz, 1H), 7.22 (ddd, *J* = 8.2, 7.0, 1.1 Hz,

1H), 7.17 (d, *J* = 8.2 Hz, 2H), 7.07 (ddd, *J* = 8.0, 7.0, 1.0 Hz, 1H), 2.29 (s, 3H); **^{13}C NMR (101 MHz, DMSO-d$_6$):** δ 159.6, 136.8, 136.4, 132.5, 131.6, 129.1, 127.0, 123.7, 121.7, 120.2, 119.9, 112.4, 103.6, 20.5; **IR (ν cm^{-1}):** 3740, 3674, 3616, 3400, 3300, 1640, 1600, 1517, 1403, 1300, 1225, 810, 739, 630; **HRMS (ESI):** Calcd. for $C_{16}H_{15}N_2O$ $[M+H]^+$: 251.1184; Observed: 251.1190.

***N*-(4-(*tert*-butyl) phenyl)-1*H*-indole-2-carboxamide (1b):**

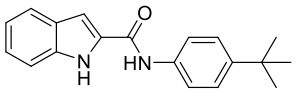

1b

Eluent for column chromatography: 6% ethyl acetate in petroleum ether; **Physical appearance:** obtained as a white solid; Yield = 50%; **M.P.:** 205.0 °C; **^{1}H NMR (400 MHz, CDCl$_3$):** δ 9.54 (s, 1H), 7.88 (s, 1H), 7.68 (d, *J* = 8.1 Hz, 1H), 7.59 (d, *J* = 8.6 Hz, 2H), 7.47 – 7.38 (m, 3H), 7.31 (t, *J* = 8.0 Hz, 1H), 7.17 (dd, *J* = 7.7, 7.2 Hz, 1H), 7.01 (d, *J* = 1.7 Hz, 1H), 1.34 (s, 9H); **^{13}C NMR (101 MHz, CDCl$_3$):** δ 159.7, 147.9, 136.7, 134.9, 131.0, 127.8, 126.2, 125.0, 122.2, 121.0, 120.2, 112.2, 102.6, 34.6, 31.5; **IR (ν cm^{-1}):** 3743, 3676, 3623, 3269, 2936, 1739, 1643, 1518, 1466, 1372, 1226, 808, 737; **HRMS (ESI):** Calcd. for $C_{19}H_{21}N_2O$ $[M+H]^+$: 293.1654; Observed: 293.1660.

***N*-(4-bromophenyl)-1*H*-indole-2-carboxamide (1c):**

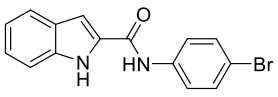

1c

Eluent for column chromatography: 5% ethyl acetate in petroleum ether; **Physical appearance:** obtained as a white solid Yield = 55%; **M.P.:** 276.0 °C; ^{1}H **NMR (400 MHz, DMSO-*d*$_6$):** δ 11.77 (s, 1H), 10.33 (s, 1H), 7.82 – 7.78 (m, 2H), 7.69 (d, *J* = 8.0 Hz, 1H), 7.59 – 7.54 (m, 2H), 7.47 (d, *J* = 8.2 Hz, 1H), 7.43 (d, *J* = 1.8 Hz, 1H), 7.23 (ddd, *J* = 8.2, 7.0, 0.9 Hz, 1H), 7.08 (dd, *J* = 10.9, 3.9 Hz, 1H); **^{13}C NMR (101 MHz, DMSO-*d*$_6$):** δ 159.8, 138.4, 136.9, 131.6, 131.2, 127.0, 124.0, 122.0, 121.8, 120.0, 115.2, 112.4, 104.2; **IR (ν cm^{-1}):** 3744, 3672, 3607, 3405, 3328, 1702, 1642, 1586, 1387, 1297, 1223, 1058, 812, 742, 623; **HRMS (ESI):** Calcd. for $C_{15}H_{12}BrN_2O$ $[M+H]^+$: 317.0113; Observed: 317.0115.

***N*-(4-(trifluoromethyl) phenyl)-1*H*-indole-2-carboxamide (1d):**

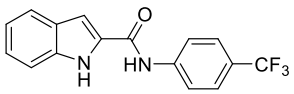

1d

Eluent for column chromatography: 4% ethyl acetate in petroleum ether; **Physical appearance:** obtained as a white solid, Yield = 60%; **M.P.:** 270.0 °C; **^{1}H NMR (400 MHz, DMSO-*d*$_6$)**: δ 11.81 (s, 1H), 10.52 (s, 1H), 8.05 (d, *J* = 8.5 Hz, 2H), 7.75 (d, *J* = 8.6 Hz, 2H), 7.70 (d, *J* = 7.9 Hz, 1H), 7.48 (dd, *J* = 7.2, 1.3 Hz, 2H), 7.24 (ddd, *J* = 8.1, 7.0, 1.1 Hz, 1H), 7.12 – 7.05 (m, 1H).; **^{13}C NMR (101 MHz, DMSO-*d*$_6$)**: δ 160.1, 142.7, 137.0, 130.9, 126.9, 126.0 (q, *J* = 3.8 Hz), 124.7 (d, *J* = 222.2 Hz), 124.1, 123.2 (d, *J* = 20.2 Hz), 121.9, 120.1, 119.8, 112.5, 104.6; **IR (ν cm^{-1}):** 3745, 3307, 1654, 1527, 1408, 1317, 1234, 1100, 829, 743; **HRMS (ESI):** Calcd. for $C_{16}H_{12}F_3N_2O$ $[M+H]^+$: 305.0901; Observed: 305.0906.

Synthesis of *N*-(2-nitrobenzyl)-4-(trifluoromethyl) aniline (5):

In a 25 mL round bottom flask, the solution of *o*-nitrobenzaldehyde **6** (500 mg, 3.31 mmol) and 4-(trifluoromethyl)aniline **4d** (533 mg, 3.31 mmol) was refluxed for 5 h. The reaction mixture was allowed to cool to room temperature. Subsequently, $NaBH_4$ (250 mg, 6.62 mmol) was added to the reaction mixture and stirred for 3 h at room temperature. The solvent was evaporated under reduced pressure. The residue was dissolved in ethyl acetate (30 mL), and water (15 mL) was added. The crude product was extracted in ethyl acetate (3 × 20 mL). The organic layer was washed with water (2 × 10 mL) and brine (2 × 10 mL), dried over Na_2SO_4 and filtered. The filtrate was concentrated under reduced pressure. The purification of the crude product was done using silica gel column chromatography (Eluent: 1% ethyl acetate in petroleum ether) to obtain **5** (yield = 55%) as a yellow liquid. **^{1}H NMR (400 MHz, CDCl$_3$)**: δ 8.11 (d, *J* = 7.8 Hz, 1H), 7.63 – 7.57 (m, 2H), 7.46 (ddd, *J* = 6.4, 5.8, 3.1 Hz, 1H), 7.38 (d, *J* = 8.8 Hz, 2H), 6.58 (t, *J* = 5.7 Hz, 2H), 4.79 (d, *J* = 6.1 Hz, 2H), 4.71 (d, *J* = 5.7 Hz, 1H); **^{13}C NMR (101 MHz, CDCl$_3$)**: δ 150.0, 148.3, 134.7, 134.0, 129.7, 128.5, 126.9 (q, *J* = 3.7 Hz), 125.6, 125.0 (q, *J* = 272 Hz), 119.7 (q, *J* = 30.3 Hz), 112.2, 45.5; **IR (ν, cm^{-1}):** 3745, 3430, 2926, 1614, 1523, 1319, 1274, 1104, 1057, 824, 730, 590; **HRMS (ESI:** Calcd. for $C_{15}H_{12}BrN_2O$ $[M+H]^+$: 295.0856; Observed: 295.0690.

Synthesis of *N*-(2-nitrobenzyl)-*N*-(4-(trifluoromethyl) phenyl)-1*H*-indole-2-carboxamide (2):

To a solution of indole-2-carboxylic acid **3** (100 mg, 0.62 mmol) in CH_2Cl_2 (2 mL), thionyl chloride (0.09 mL, 1.24 mmol) and 2 drops of DMF were added. The reaction mixture was stirred for 1 h at room temperature. Then the solvent was evaporated to dryness in *vacuo* to give indole-2-carbonyl chloride **7**. The residue was dissolved in $CHCl_3$ (3 mL). To this solution amine **5** (50 mg, 0.17 mmol) in $CHCl_3$ (3 mL) was added dropwise followed by the addition of DMAP (21 mg, 0.17 mmol). The reaction mixture was heated at 70 °C and stirred for 1 h and quenched with water. Following extraction with CH_2Cl_2 (3 × 10 mL), the organic phase was washed with water (2 × 10 mL) and brine (2 × 10 mL) and then dried over Na_2SO_4, filtered and concentrated under reduced pressure. The crude product was purified by silica gel column chromatography (Eluent: CH_2Cl_2) to give the pure compound **2** (yield = 92%) as a white solid. **M.P.:** 226.0 °C; **^{1}H NMR (400 MHz, $CDCl_3$):** δ 9.31 (s, 1H), 8.04 (dd, *J* = 8.2, 1.2 Hz, 1H), 7.70 (t, *J* = 8.8 Hz, 3H), 7.64 (td, *J* = 7.6, 1.3 Hz, 1H), 7.50 – 7.43 (m, 1H), 7.43 – 7.36 (m, 4H), 7.27 (dd, *J* = 7.1, 1.2 Hz, 1H), 7.06 (td, *J* = 8.0, 7.0, 1.0 Hz, 1H), 5.53 (s, 2H), 5.45 (dd, *J* = 2.1, 0.8 Hz, 1H); **^{13}C NMR (101 MHz, $CDCl_3$):** δ 162.6, 148.6, 146.2, 135.8, 133.9, 132.5, 130.8 (q, J = 33.5 Hz), 129.3, 128.6, 128.6, 128.5, 127.5, 127.2 (q, *J* = 3.7 Hz), 123.7 (q, *J* = 273 Hz), 125.4, 120.9, 111.80, 108.2, 52.1. **IR (ν cm^{-1}):** 3322, 2923, 2853, 1594, 1515, 1405, 1319, 1267, 1113, 1066, 848, 748; **HRMS (ESI):** Calcd. for $C_{23}H_{17}F_3N_3O_3$ $[M+H]^+$: 440.1222; Observed: 440.1217.

Synthesis of 1-((4-methoxyphenoxy)methyl)-2-nitrobenzene (11):

To a stirring solution of **9** (100 mg, 0.856 mmol) in THF (2 mL) *t*BuOK (135.59 mg, 1.208 mmol) was added at 0 °C. Then *o*-nitrobenzyl bromide (174 mg, 0.856 mmol) was added and the reaction mixture was stirred for 2 h. The reaction mixture was quenched by water (4 mL) Following the extraction with ethyl acetate (3 × 10 mL). The organic layer was washed with brine (2 × 3 mL), dried over Na_2SO_4, filtered and concentrated under reduced pressure. The crude product was purified by silica gel column chromatography (Eluent: 5% ethyl acetate in petroleum ether) to obtain **11** (yield = 60%). **^{1}H NMR (400 MHz, $CDCl_3$):** δ 8.16 (dd, *J* = 8.2, 1.2 Hz, 1H), 7.91 (dd, *J* = 7.9, 1.0 Hz, 1H), 7.68 (td, *J* = 7.7, 1.3 Hz, 1H), 7.52 – 7.44 (m, 1H), 6.927 (dt, *J* = 9.2, 2.8 Hz, 2H), 6.848 (dt, *J* = 9.2, 2.8 Hz, 2H), 5.44 (s, 2H), 3.77 (s, 3H) **^{13}C NMR (101 MHz, $CDCl_3$):** δ 154.49, 152.42, 134.41, 134.09, 133.74, 128.73, 128.35, 125.06,

116.05, 114.91, 67.68, 55.85; **HRMS (ESI):** Calcd. for $C_{13}H_{14}NO_4$ $[M+H]^+$: 260.0923; Observed: 260.0914.

4.4.4 Anion Binding Studies by ^{1}H NMR

^{1}H NMR titration was carried out at room temperature on a Bruker 400 MHz spectrometer. The residual solvent signal (CD_3CN, $\delta_H = 1.94$) was considered as an internal reference to calibrate spectra. Both the tetrabutylammonium chloride (TBACl) salt and receptor were dried in high vacuum before use. The titrations were performed by the addition of aliquots from the TBACl solution (0.4M in CD_3CN) to the solution of receptor **1d** (0.005 M in CD_3CN). The NMR spectra of each solution were recorded at room temperature on a Bruker 400 MHz instrument. All NMR data were processed using MestReNova 6.0 and collected data was fitted in a different binding mode using BindFit v0.5.[25, 39]

4.4.5 Ion Transport Studies[28, 40-42]

Ion transporting activity studies across EYPC-LUVs⊃HPTS

The ion transport studies across EYPC-LUVs⊃HPTS were performed by following the vesicle preparation protocol 1 and assay protocol 1 discussed in Chapter 2.

Ion selectivity studies across EYPC-LUVs⊃HPTS

The ion selectivity of most active carrier **1d** across EYPC-LUVs⊃HPTS was investigated by following the vesicle preparation protocol 1 and assay protocols 2 and 3 discussed in Chapter 2.

Ion transport mechanism by HPTS assay

Ion transport activity in the presence of FCCP (Assay protocol 7): Following the vesicle preparation protocol 1 procedure as stated the Chapter 2 vesicles were prepared. The fluorescence intensity of carrier **1d** was measured in the absence and presence of FCCP. In clean and dry fluorescence cuvette 1975 μL HEPES buffer solution (10 mM HEPES, 100 mM

NaCl, pH = 7.0) and 25 μL EYPC-LUVs⊃HPTS were taken, then this solution was placed in a slowly stirring condition in a fluorescence instrument equipped with magnetic stirrer. The time-dependent fluorescence intensity was measured at λ_{em} = 510 nm (λ_{ex} = 450 nm) by the addition of 20 μL 0.5 M NaOH (at t = 20 s) to create a pH gradient across the intra and extracellular system, followed by the addition of FCCP (at t = 50 s) and carrier in DMSO solution (at t = 100 s), finally, vesicles were lysed at t = 300 s using 10% Triton X-100 (25 μL) to achieve complete disturbance of pH gradient. The time axis was normalized according to Equation 1 (Chapter 2). The time-dependent collected data was normalized to percent change in intensity using Equation 2 (Chapter 2).

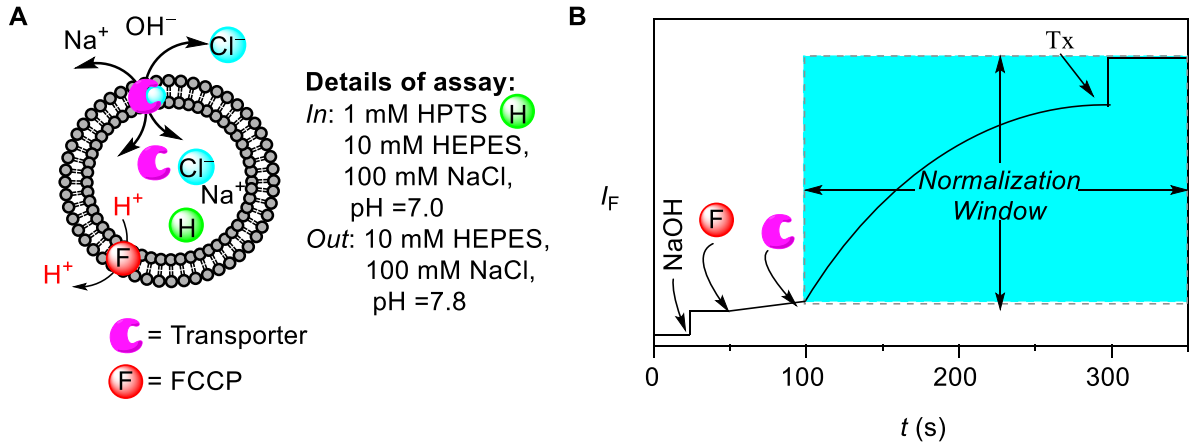

Figure 4.24 Representative fluorescence-based FCCP assay using EYPC-LUVs⊃HPTS (**A**) and representation of ion transport kinetics showing normalization window (**B**).

Ion transport activity in the presence of valinomycin (Assay protocol 8): The vesicles were prepared using the vesicle preparation protocol 1 as mentioned in Chapter 2. The fluorescence data was investigated in the absence and presence of valinomycin. In a clean and dry fluorescence cuvette, 1975 μL HEPES buffer (10 mM HEPES, 100 mM KCl, pH = 7.0) was taken, followed by the addition of 25 μL EYPC-LUVs⊃HPTS. The resulting solution was slowly stirred using a magnetic stirrer equipped with a fluorescence instrument. The time-dependent fluorescence intensity was monitored at λ_{em} = 510 nm (λ_{ex} = 450 nm). The pH gradient was created by the addition of 0.5 NaOH (20 μL) at t = 20 s, followed by the addition of valinomycin at t = 50 s, carrier in DMSO solution at t = 100 s, and finally, complete disturbance of pH gradient was achieved by lysing the vesicles with 10% Triton X-100 (25 μL)

at t = 300 s. Fluorescence intensity was normalized to percent change in intensity using Equation 2 (Chapter 2).

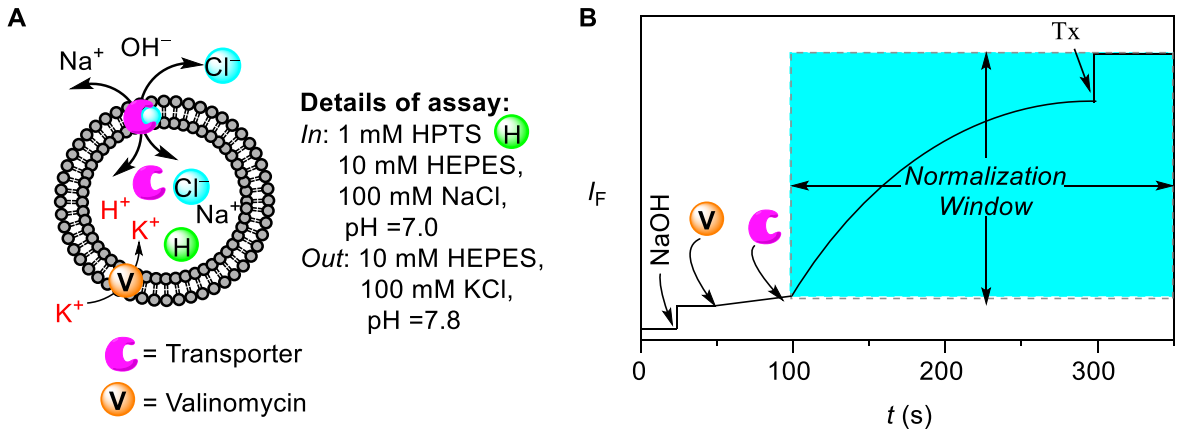

Figure 4.25 Representative fluorescence-based valinomycin assay using EYPC-LUVs⊃HPTS (**A**) and representation of ion transport kinetics showing normalization window (**B**).

Chloride transport activity studies across EYPC–LUVs⊃lucigenin: Chloride transport properties of all carriers across EYPC-LUVs⊃lucigenin were performed by following vesicle preparation protocol 2 and assay protocol 4 mentioned in Chapter 3.

Cation selectivity assay across EYPC–LUVs⊃lucigenin vesicles:

The cation selectivity study of **1d** was performed by following vesicle preparation protocol 2 and assay protocol 5 described in Chapter 3.

Ion transport activity across EYPC–LUVs⊃lucigenin in the presence of valinomycin:

The antiport mechanism of transport was confirmed by performing ion transport activity of **1d** in the presence of valinomycin by following vesicle preparation protocol 2 and assay protocol 6 described in Chapter 3.

4.4.6 Photolysis studies[20]

Assessment of photolysis of procarrier 2 using ^{1}H NMR spectroscopy: In a clean and dry NMR tube, the solution of procarrier **2** (5 mg in 0.5 mL) was taken in DMSO-d_6. The ^{1}H NMR spectrum of the sample was recorded first (t = 0 min). Then, the tube was kept in a photoreactor and irradiated with UV light (3 × 3 Watt LEDs, λ = 365 nm) for 5 min, and the ^{1}H NMR

spectrum of the irradiated sample was recorded (t = 5 min). The irradiation process was repeated at an interval of 5 min, till 45 min, and the ^{1}H NMR spectrum was recorded at the end of each irradiation. All ^{1}H NMR spectra were processed using MestReNova 6.0 by considering the residual solvent peak as an internal reference. Upon photoirradiation, the appearance and disappearance of the different proton peak signals were monitored by stacking all calibrated spectra. The photolytic conversion of procarrier **2** to carrier **1d** was confirmed by comparing the ^{1}H NMR spectra with as-synthesized **1d**.

Phototriggered activation of ion transport across EYPC-LUVs⊃HPTS

Preparation of HEPES buffer and stock solutions: The HEPES buffer of pH = 7.0 was prepared by dissolving an appropriate amount of solid HEPES (10 mM) and NaCl (100 mM) in autoclaved water. The pH was adjusted to 7.0 by the addition of aliquots from 0.5 M NaOH solution using a pH meter. The stock solutions of carrier **1d** (38 μM) and procarrier **2** (38 μM) were prepared using HPLC grade DMSO.

Preparation of EYPC-LUVs⊃HPTS: The vesicles were prepared by the following vesicle preparation protocol 1 as stated in Chapter 2.

Phototriggered activation and ion transport assay in LUVs: In clean and dry fluorescence cuvette, 1975 μL HEPES buffer (10 mM HEPES, 100 mM NaCl, pH = 7.0) and 25 μL EYPC-LUVs⊃HPTS vesicles were placed. To this suspension, either carrier **1d** (20 μL) or procarrier **2** (20 μL) was added to get a final concentration of 380 nM. For procarrier **2**, the suspension was irradiated with 365 nm wavelength UV (using three 3 W LEDs each placed at a distance of 2 cm) for time, t_R = 0, 1, 2, 3, and 5 min. Each irradiated sample was then placed in the fluorescence instrument equipped with a magnetic stirrer. The fluorescence intensity of HPTS at λ_{em} = 510 nm (λ_{ex} = 450 nm) of each sample was monitored as a course of time t. At t = 100 s, a pH gradient was created by the addition of 20 μL NaOH (0.5 M). Finally, at t = 300 s vesicles were lysed by the addition of 10% Triton X-100 (25 μL) to get the complete destruction of the applied pH gradient. Each time-dependent fluorescence data was normalized using Equation 2. A sample containing 1975 μL HEPES buffer (10 mM HEPES, 100 mM NaCl, pH = 7.0), 25 μL EYPC-LUVs⊃HPTS and 20 μL DMSO was also subjected to 5 min irradiation with the same UV LEDs. The ion transport activity of this sample was measured by adding 20 μL NaOH (0.5 M) at t = 100 s of the kinetics experiment, and this data was used as

control data. The time axis was normalized according to Equation 1. The time-dependent data were normalized to percent change in fluorescence intensity using Equation 2.

Then the normalized fluorescence intensity (i.e., activity) value at t = 190 s after NaOH addition was noted from the plot. The data was further normalized to get *% transport efficiency* F_R by setting the HPTS fluorescence of the blank sample to 0 and that of **1d** (380 nM) to 100 (Equation 5).

The time-dependent data were normalized to percent change in fluorescence intensity using Equation 5:

$$F_R = [(I_{S(t = 190)} - I_{blank(t = 190)}) / (I_{\mathbf{1d}(t = 190)} - I_{blank(t = 190)})] \times 100 \quad \text{Equation 5}$$

Where, $I_{S(t = 190)}$ is the normalized fluorescence intensity of a photoirradiated sample at 190 s, $I_{\mathbf{1d}(t = 190)}$ is the normalized fluorescence intensity of a photoirradiated sample of **1d** at 190 s, and $I_{blank(t = 190)}$ is the normalized fluorescence intensity of the blank at 190 s.

4.4.7 Biological Studies

Cell culture protocol:[42] The MCF 7 cells were grown in High Glucose Dulbecco's Modified Eagle Medium (DMEM; Invitrogen or Lonza) containing 10% fetal bovine serum (FBS; Invitrogen), 2 mM L-glutamine (Invitrogen) and 100 units/mL penicillin-streptomycin (Invitrogen). Cells were maintained in 100 mm tissue culture-treated dishes (Corning) at 37 °C in a humidified 5% CO_2 incubator (Thermo Scientific).

MTT-based cytotoxicity assay: The cells were dispersed in a 96-well flat bottom tissue culture treated plates (Corning) at a density of 10^4 cells/well (per 100 µL) and incubated at 37 ^oC in a 5% CO_2 incubator for 24 h. Compounds were added to each well in different concentrations by maintaining a maximum amount of DMSO at 2 µL and incubated for 24 h. DMEM solution containing compounds in each well were replaced with 110 µL of MTT-DMEM mixture (0.5 mg MTT/mL of DMEM) and incubated for 4 h in identical conditions. After 4 h, the MTT solution was removed and 100 µL of DMSO was added to each well to dissolve the formazan crystals. The absorbance was recorded in a microplate reader (Varioskan Flash) at the wavelength of 570 nm. All experiments were performed in triplicates, and the relative cell viability (%) was expressed as a percentage of untreated cells.

Phototriggered activation in cells: The cells were dispersed in a 96-well flat bottom tissue culture treated plates (Corning) at a density of 10^4 cells/well (per 100 µL) and incubated at 37 ^oC in a 5% CO_2 incubator for 24 h. Compound **2** was added to each well in different concentrations by maintaining a maximum amount of DMSO at 2 µL and incubated for 4 h. Then the whole cell plate covered with aluminium foil was irradiated for 5 minutes on High-Performance 2UV Transilluminator at 365 nm. The cell plate was then kept back in the incubator for another 20 h. Then normal protocol for the MTT assay was followed.

Cytotoxicity of the *o*-nitrosobenzaldehyde byproduct (8):

Cell viability: The cells were dispersed in 96-well flat bottom tissue culture treated plates (Corning) at a density of 10^4 cells/well (per 100 µL) and incubated at 37 ^oC in a 5% CO_2 incubator for 24 h. Compound **11** was added to each well in different concentrations by maintaining a maximum amount of DMSO at 1.5 µL and incubated for 4 h. Then the whole cell plate covered with aluminium foil was irradiated for 5 minutes on High-Performance 2UV Transilluminator at 365 nm. The cell plate was then kept back in the incubator for another 20 h. Then normal protocol for the MTT assay was followed. The obtained data was compared with that of compound **2**.

Live cell imaging: The cells were dispersed in 96-well flat bottom tissue culture treated plates (Corning) at a density of 10^4 cells/well (per 100 µL) and incubated at 37 ^oC in a 5% CO_2 incubator for 24 h. Compounds were added to each well in different concentrations by maintaining a maximum amount of DMSO at 2 µL and incubated for 24 h. Before initiating the MTT assay, the images were taken using a Nikon Eclipse TS 100 fluorescence microscope. The images were taken at 10 µM concentration for both compounds **1d** and **2**. The precipitation rate was seen more for compound **1d** compared to **2**.

4.4.8 Theoretical calculations

To get an idea about the conformation of [(**1d**)$_2$+Cl^-], several initial geometries of the complex were generated using the CONFLEX 8 software package using MMFF94s force field. The Boltzmann populations of two top conformations, i.e., **Conf-1** (Figure 4.26A and **Conf-2**Figure

4.26B), were 50.0732% and 49.9268%, respectively. The conformations of **Conf-1** and **Conf-2** were also almost identical (Figure 4.26C). Subsequently, **Conf-1** was optimized by the Gaussian 09 program package using B3LYP functional and 6-311G(d,p) basis set. Conformations with Boltzmann population ≤ 0.0000250432% were not considered.

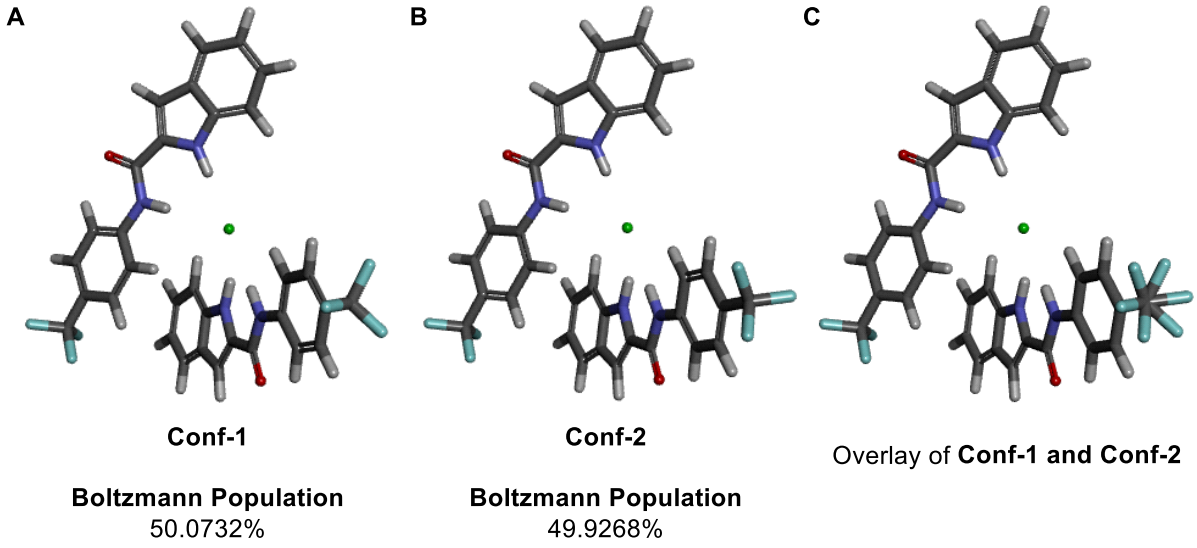

Figure 4.26 Initial geometries of **Conf-1** (**A**) and **Conf-2** (**B**) for [(**1d**)$_2$+Cl$^-$], optimized by CONFLEX 8 software using MMFF94s force field. The Boltzmann populations of conformations **Conf-1** (**A**) and **Conf-2** are also provided. The overlay image of **Conf-1** and **Conf-2** (**C**).

Table 4.1 Atomic coordinates of [(**1d**)$_2$+Cl$^-$] after geometry optimization by Gaussian 09 program using B3LYP functional and 6-311G(d,p) basis set.

Charge = –1 Multiplicity = 1

Atom #	Atom Type	X	Y	Z
1	C	0.860555	5.551988	-4.362511
2	C	1.652419	4.430082	-4.014964
3	C	1.176356	3.444431	-3.159506
4	C	-0.121273	3.599403	-2.649448
5	C	-0.937989	4.723925	-2.986916
6	C	-0.423189	5.705817	-3.858049
7	N	-0.844127	2.793926	-1.793154
8	C	-2.098274	3.374168	-1.576115

9	C	-2.176991	4.553843	-2.296093
10	C	-3.173407	2.841291	-0.724861
11	O	-4.261391	3.466412	-0.628248
12	N	-2.931551	1.653905	-0.055753
13	C	-3.803019	0.964809	0.807652
14	H	-0.497466	1.920734	-1.402094
15	C	-3.323975	-0.233919	1.379379
16	C	-4.121881	-0.973234	2.239903
17	C	-5.42108	-0.541323	2.543885
18	C	-5.896966	0.650325	1.985376
19	C	-5.106455	1.400504	1.119835
20	C	-6.247989	-1.292276	3.513
21	F	-6.058731	-0.88303	4.853817
22	F	-5.98348	-2.671912	3.514991
23	F	-7.62848	-1.154817	3.286008
24	H	1.268977	6.298281	-5.031943
25	H	2.650301	4.340208	-4.4245
26	H	1.781385	2.588528	-2.89376
27	H	-1.02305	6.566205	-4.127307
28	H	-3.036701	5.19933	-2.305385
29	H	-2.028523	1.201152	-0.179389
30	H	-2.324619	-0.570828	1.13988
31	H	-3.744736	-1.892638	2.663717
32	H	-6.897613	0.987885	2.214521
33	H	-5.473665	2.311516	0.682864
34	C	-0.821392	-5.601578	-4.326066
35	C	-1.616849	-4.476586	-3.997222
36	C	-1.151163	-3.484816	-3.143118
37	C	0.139674	-3.636749	-2.615222
38	C	0.959881	-4.764274	-2.933675
39	C	0.455652	-5.752383	-3.80396
40	N	0.852024	-2.825246	-1.755849
41	C	2.102915	-3.404521	-1.518403
42	C	2.19003	-4.589709	-2.228283
43	C	3.167306	-2.86564	-0.657444

44	O	4.252199	-3.492384	-0.538988
45	N	2.919144	-1.67073	-0.004286
46	C	3.779961	-0.974749	0.864249
47	H	0.500841	-1.949067	-1.375708
48	C	5.073435	-1.416177	1.208648
49	C	5.853734	-0.658096	2.076302
50	C	5.369226	0.535602	2.623408
51	C	4.084827	0.979532	2.277567
52	C	3.296781	0.23202	1.414771
53	C	6.238903	1.362558	3.487458
54	F	7.135618	0.602539	4.259461
55	F	5.522676	2.16505	4.390018
56	F	7.057437	2.263698	2.76675
57	H	-1.22164	-6.352593	-4.995159
58	H	-2.609229	-4.389108	-4.420437
59	H	-1.758865	-2.626456	-2.891768
60	H	1.058368	-6.6151	-4.059008
61	H	3.049357	-5.235733	-2.221643
62	H	2.019623	-1.216425	-0.146354
63	H	5.441253	-2.337137	0.793552
64	H	6.84162	-1.007383	2.34104
65	H	3.69924	1.898013	2.695491
66	H	2.302052	0.569161	1.157026
67	Cl	-0.003279	-0.008418	-0.375841

To get an idea of the Cl^- recognition ability of *o*-nitrosobenzaldehyde **8** (byproduct of the photocleavage) different conformations of [**1d**+**8**+Cl^-] species were generated by CONFLEX 8 software following the method stated above. The first ten conformations **conf 1 – conf 10** were selected based on the decreasing Boltzmann populations (Figure 4.26). In all conformations, the position of the Cl^- ion was in the anion binding pocket of **1d** as expected. No interaction between molecule **8** and the Cl^- ion was evident.

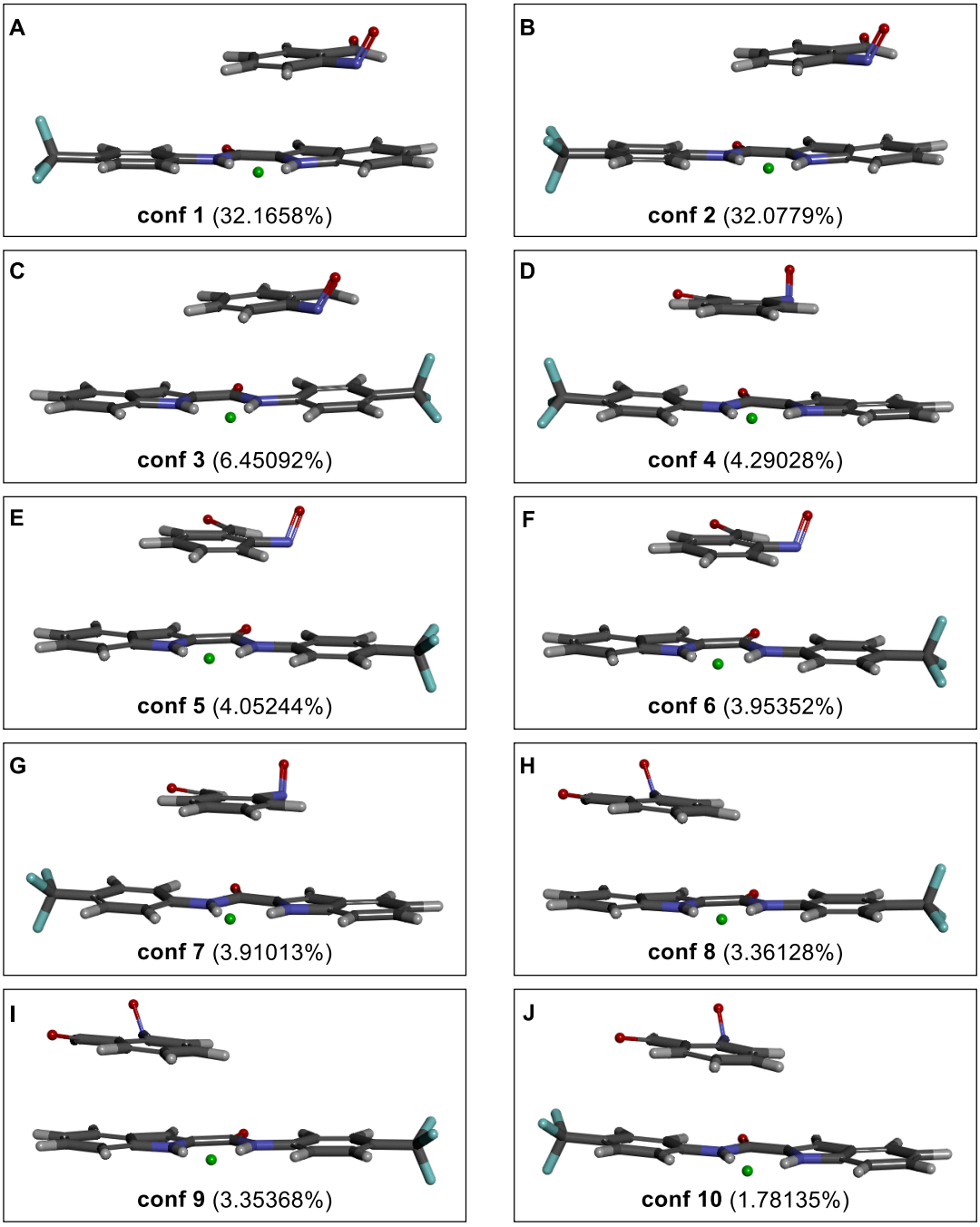

Figure 4.27 Geometry optimised top ten conformations (**conf 1 - conf 10**) of [**1d**+**8**+Cl^-], generated using CONFLEX 8 software using MMFF94s force field (**A–J**). The Boltzmann populations of conformations are provided within the brackets.

4.4.9 NMR spectra

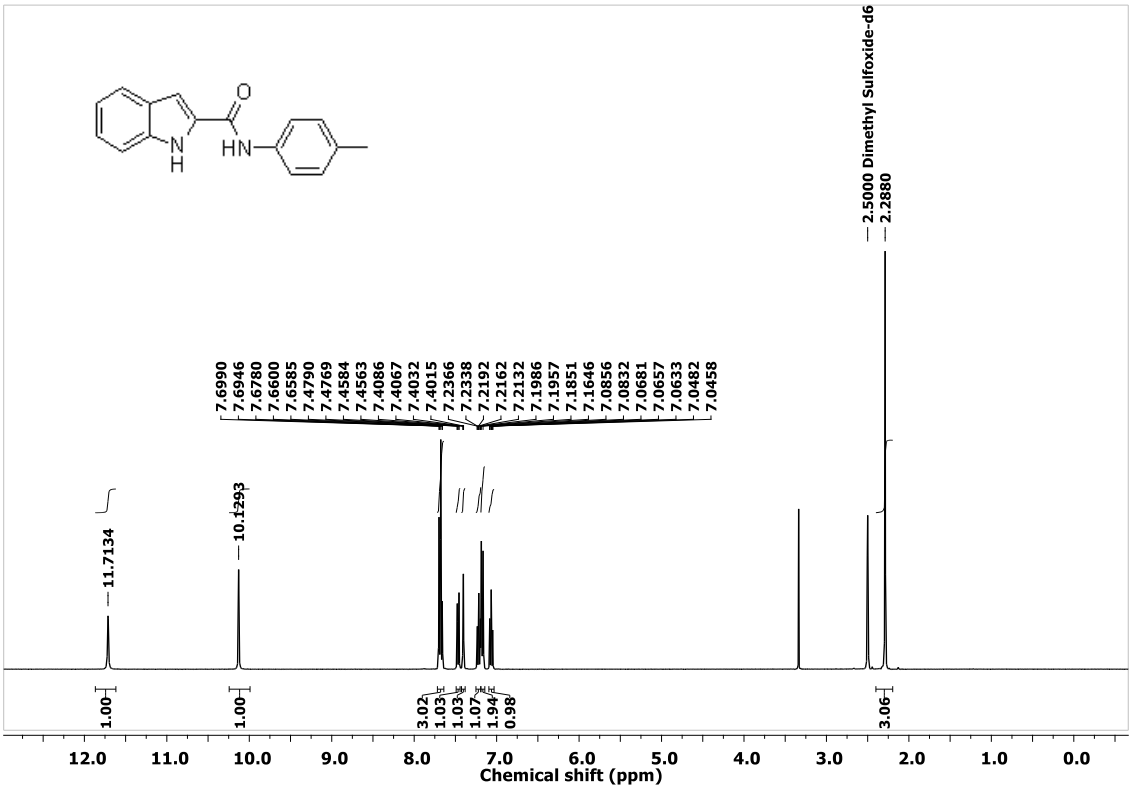

Figure 4.28 ^{1}H NMR spectrum of compound **1a**.

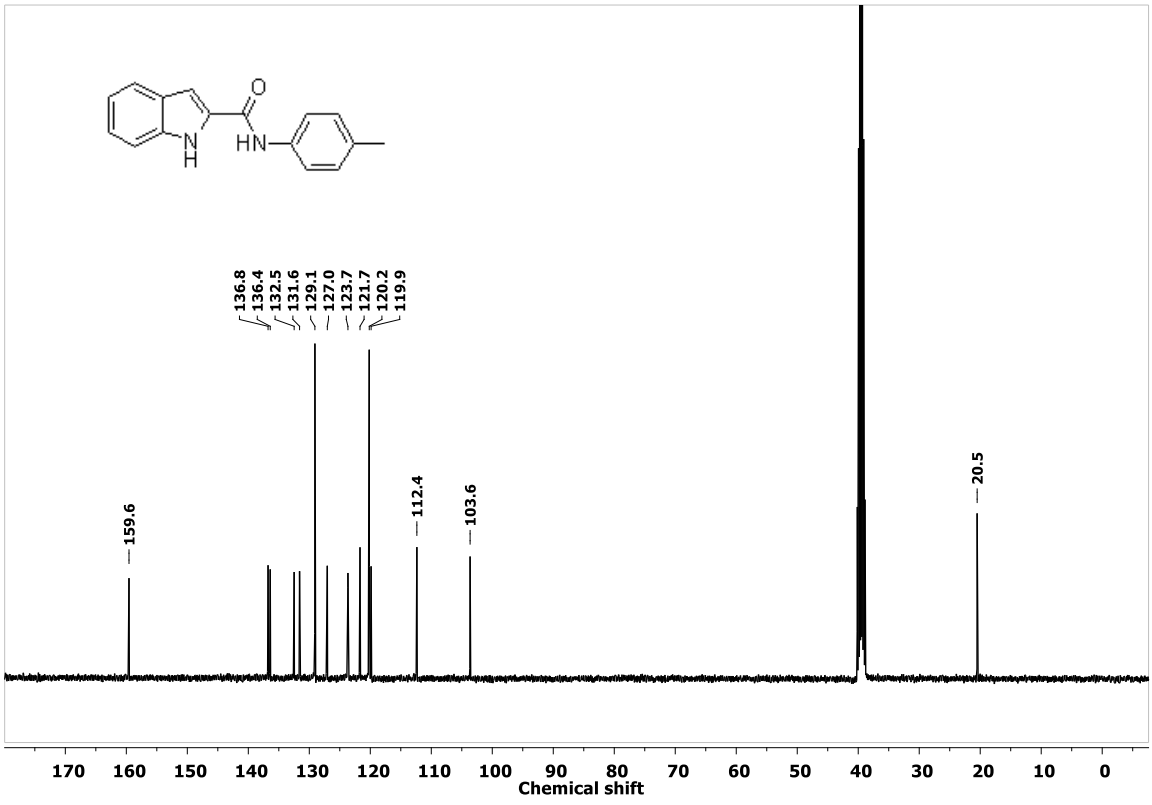

Figure 4.29 ^{13}C NMR spectrum of compound **1a**.

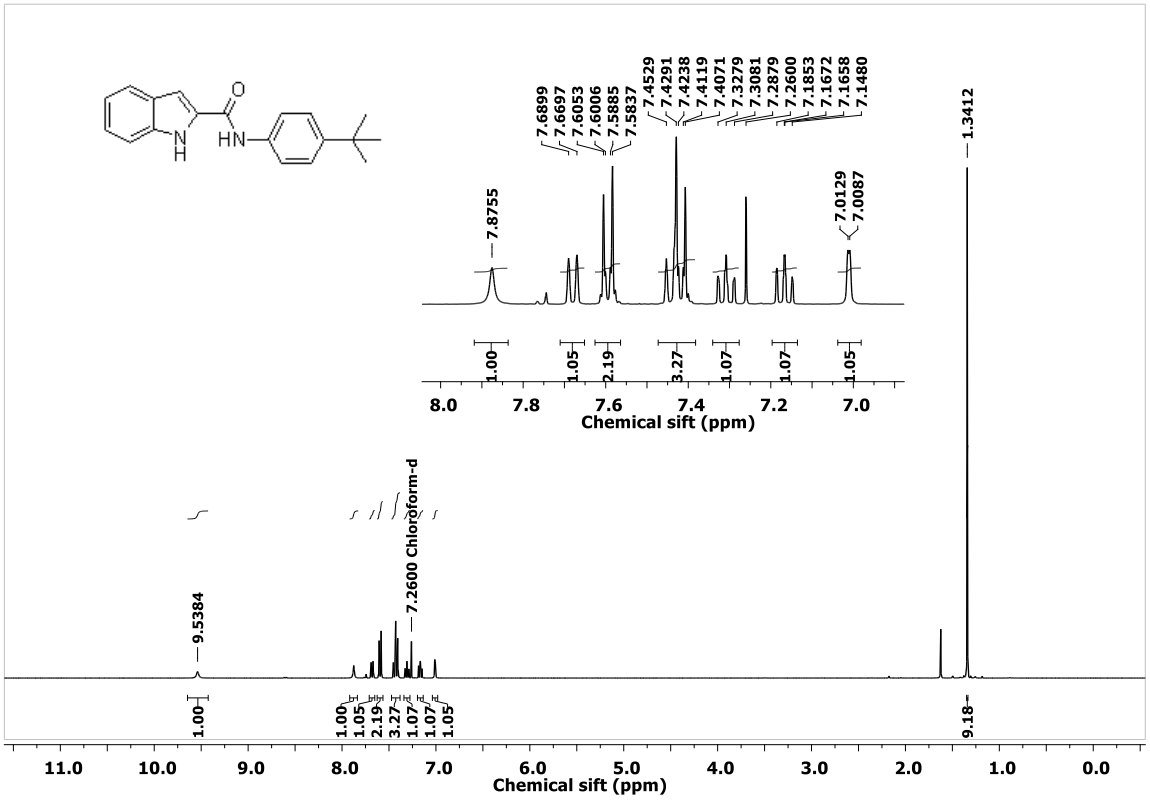

Figure 4.30 ^{1}H NMR spectrum of compound **1b**.

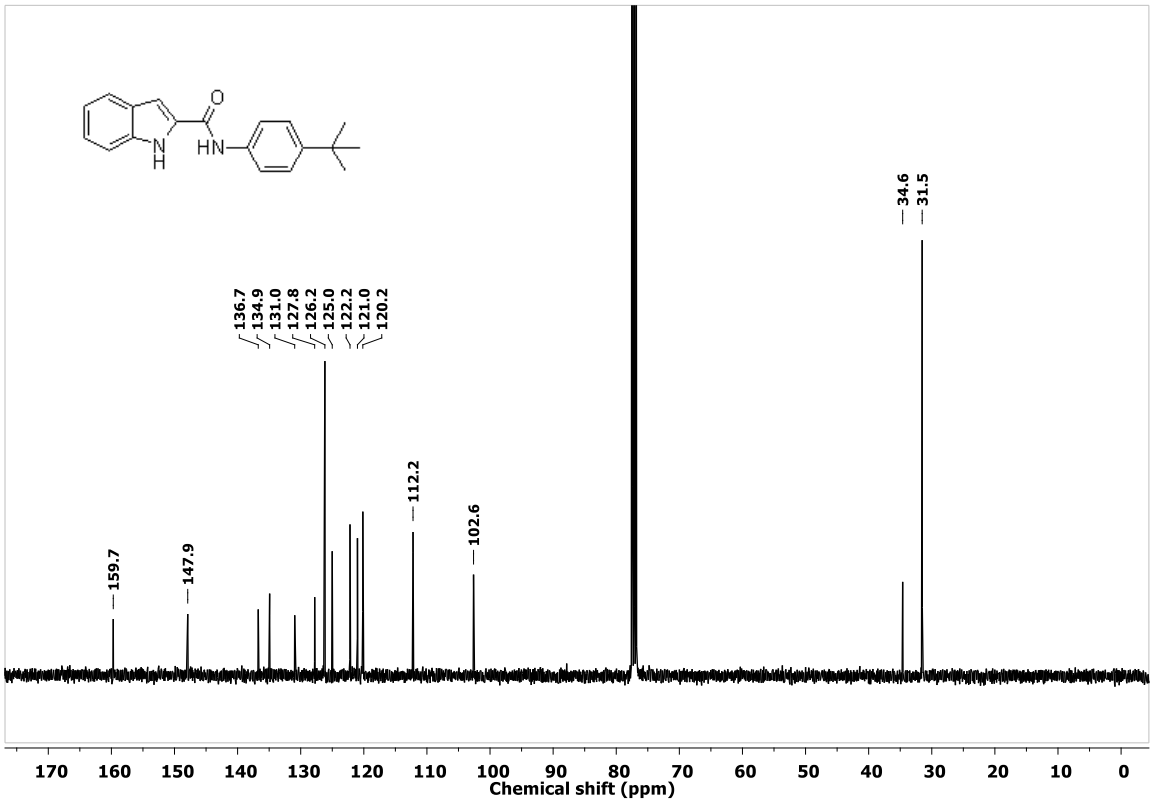

Figure 4.31 ^{13}C NMR spectrum of compound **1b**.

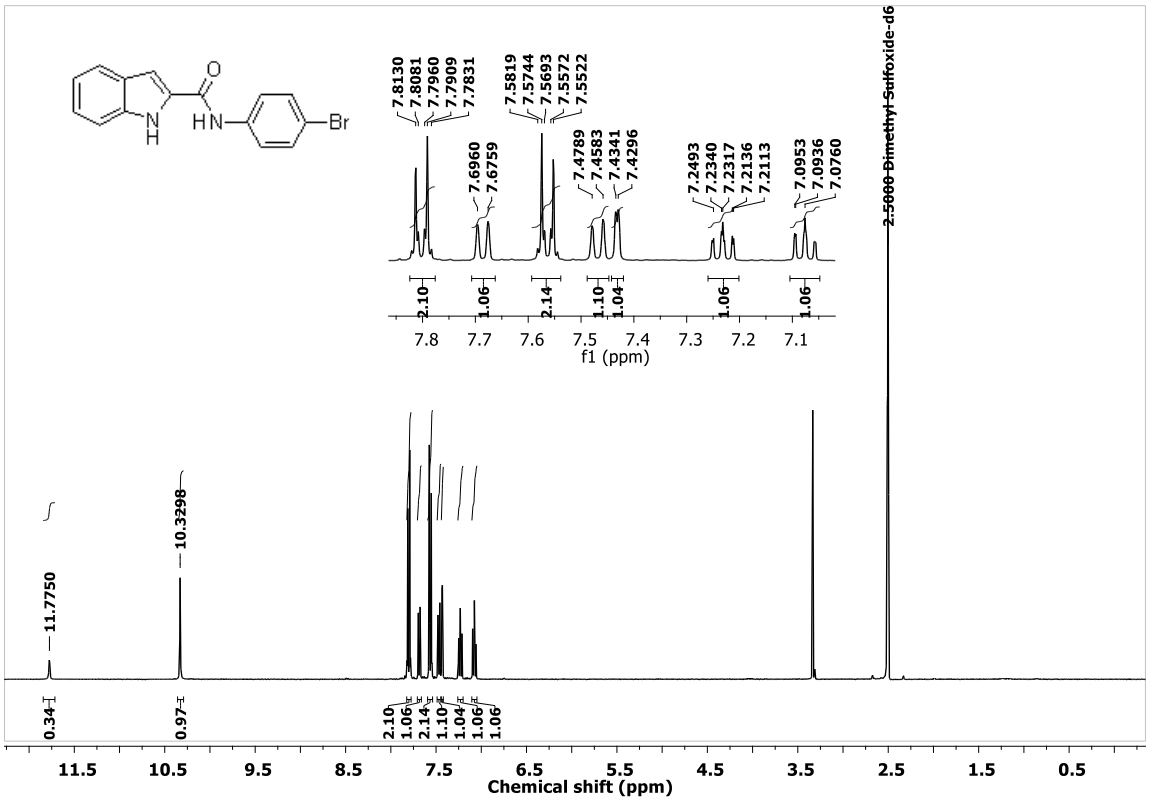

Figure 4.32 ^{1}H NMR spectra of compound **1c**.

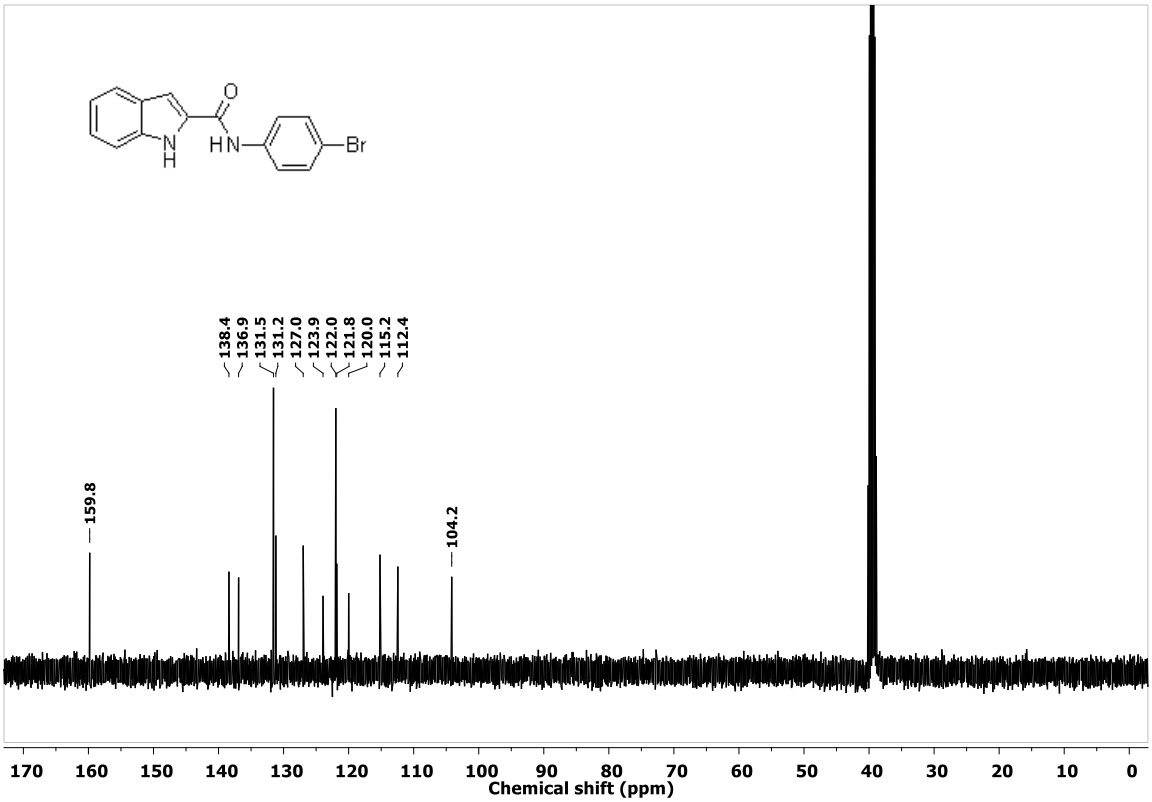

Figure 4.33 ^{13}C NMR spectrum of compound **1c**.

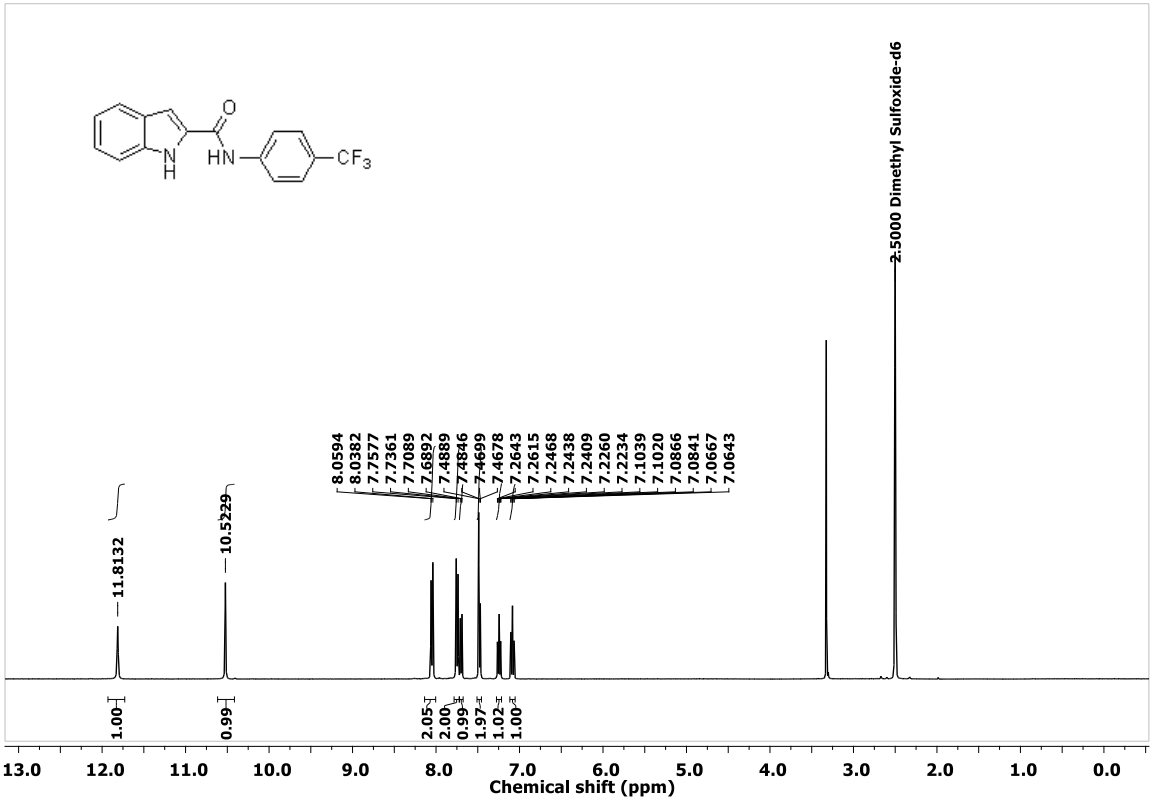

Figure 4.34 ^{1}H NMR spectrum of compound **1d**.

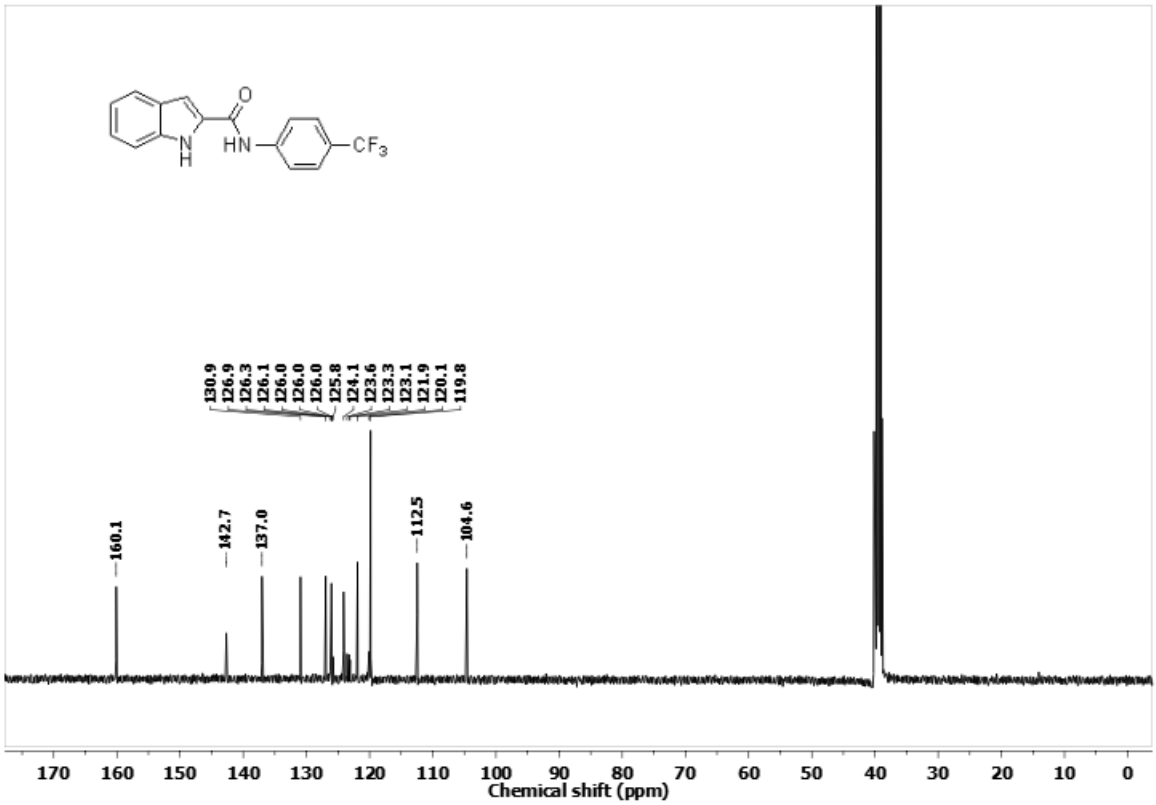

Figure 4.35 ^{13}C NMR spectrum of compound **1d**.

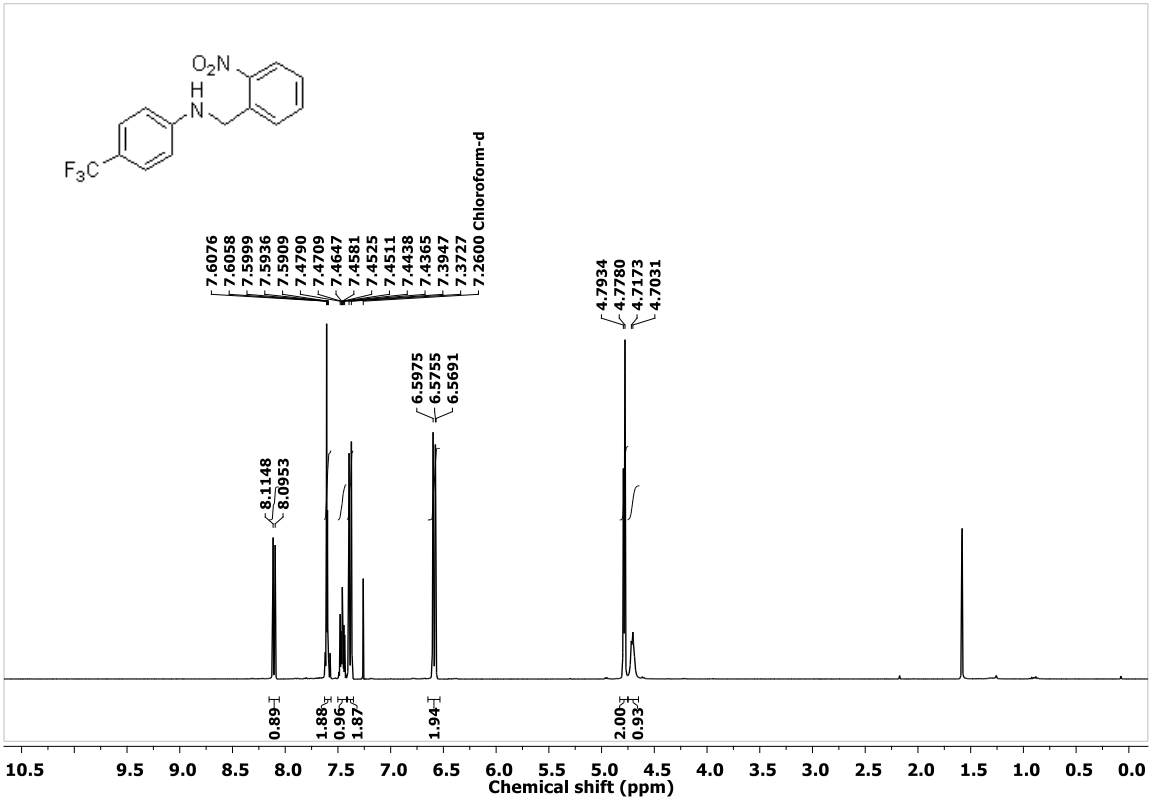

Figure 4.36 ^{1}H NMR spectrum of compound **5**.

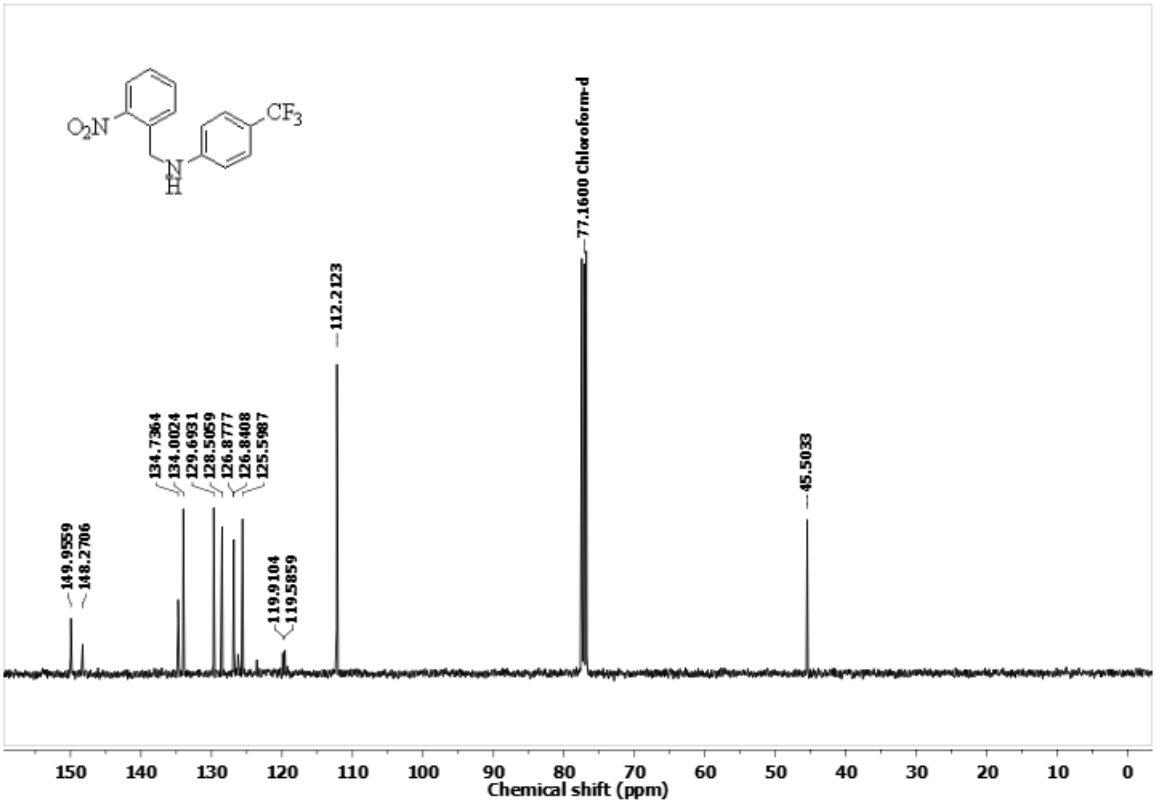

Figure 4.37 ^{13}C NMR spectrum of compound **5**.

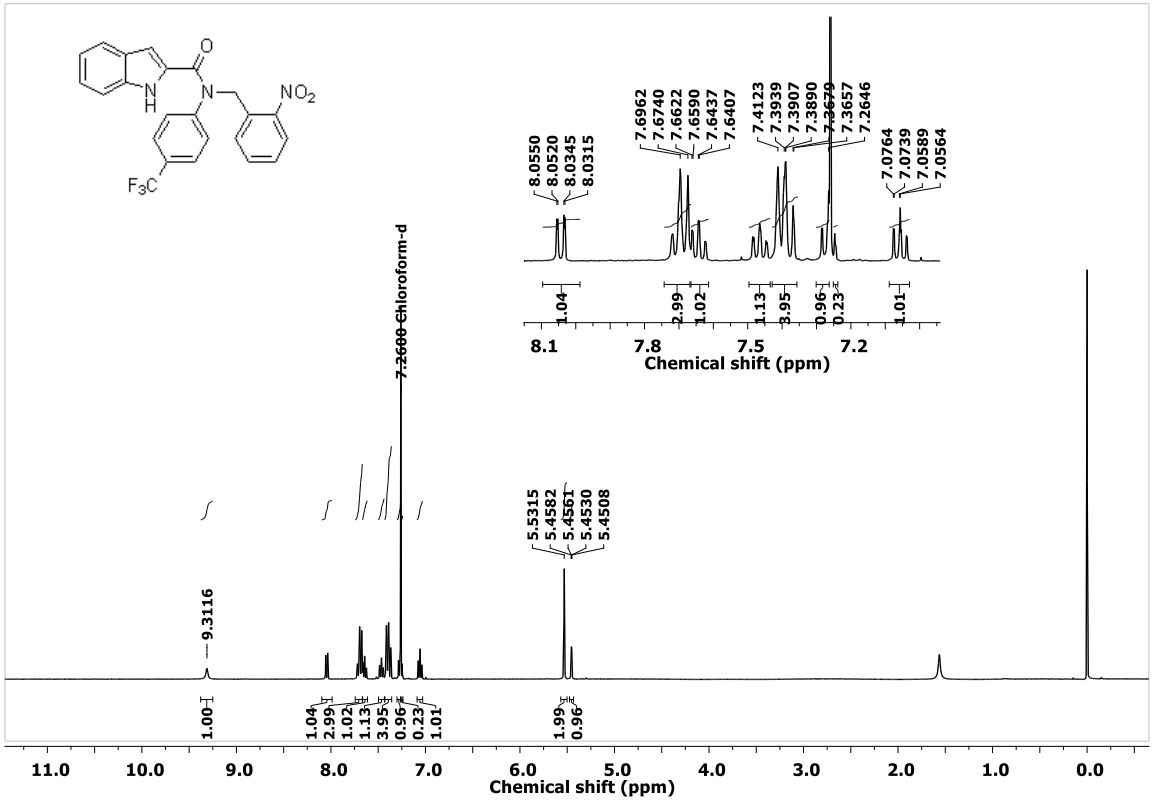

Figure 4.38 ^{1}H NMR spectrum of compound **2**.

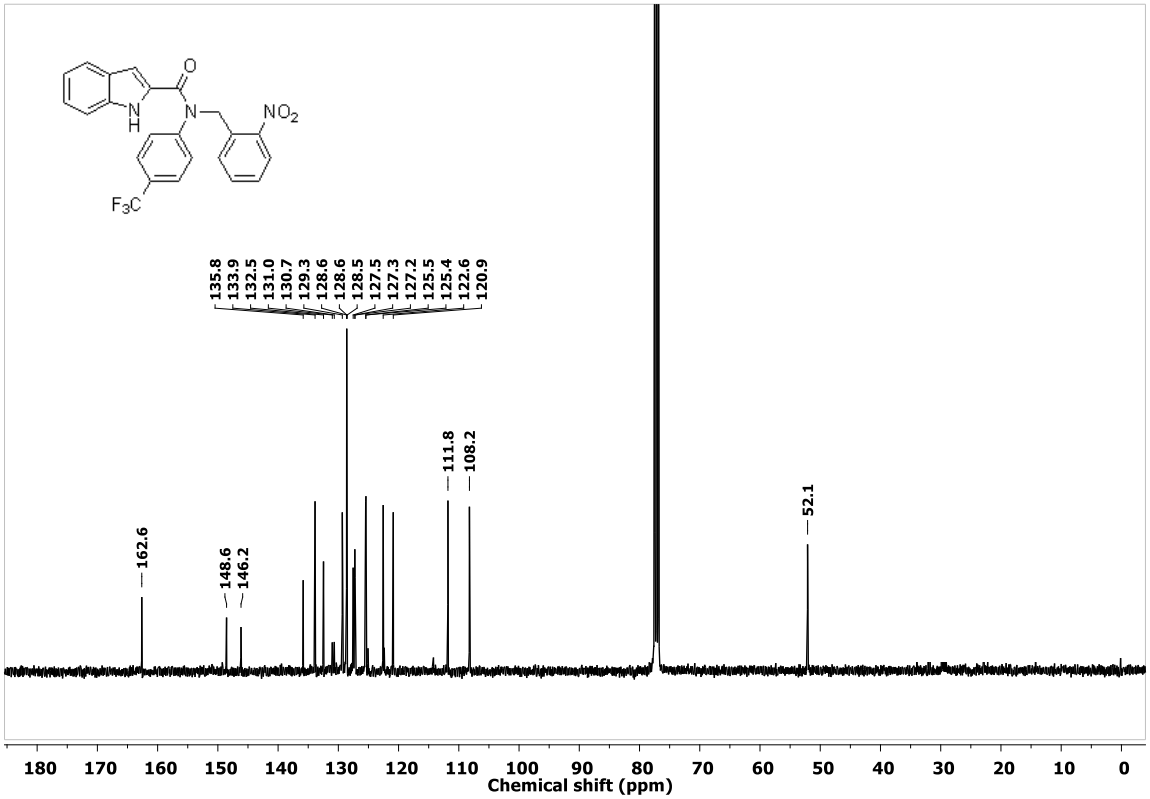

Figure 4.39 ^{13}C NMR spectrum of compound **2**.

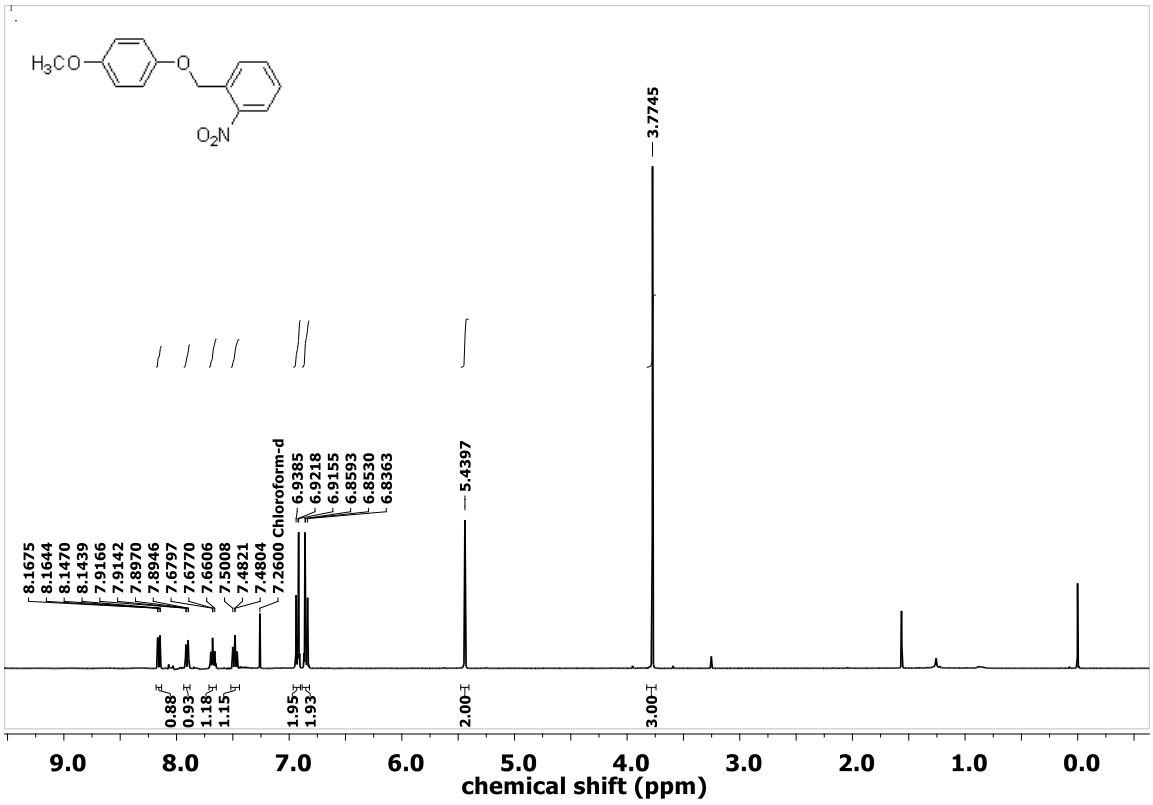

Figure 4.40 [1]H NMR spectrum of compound **11**.

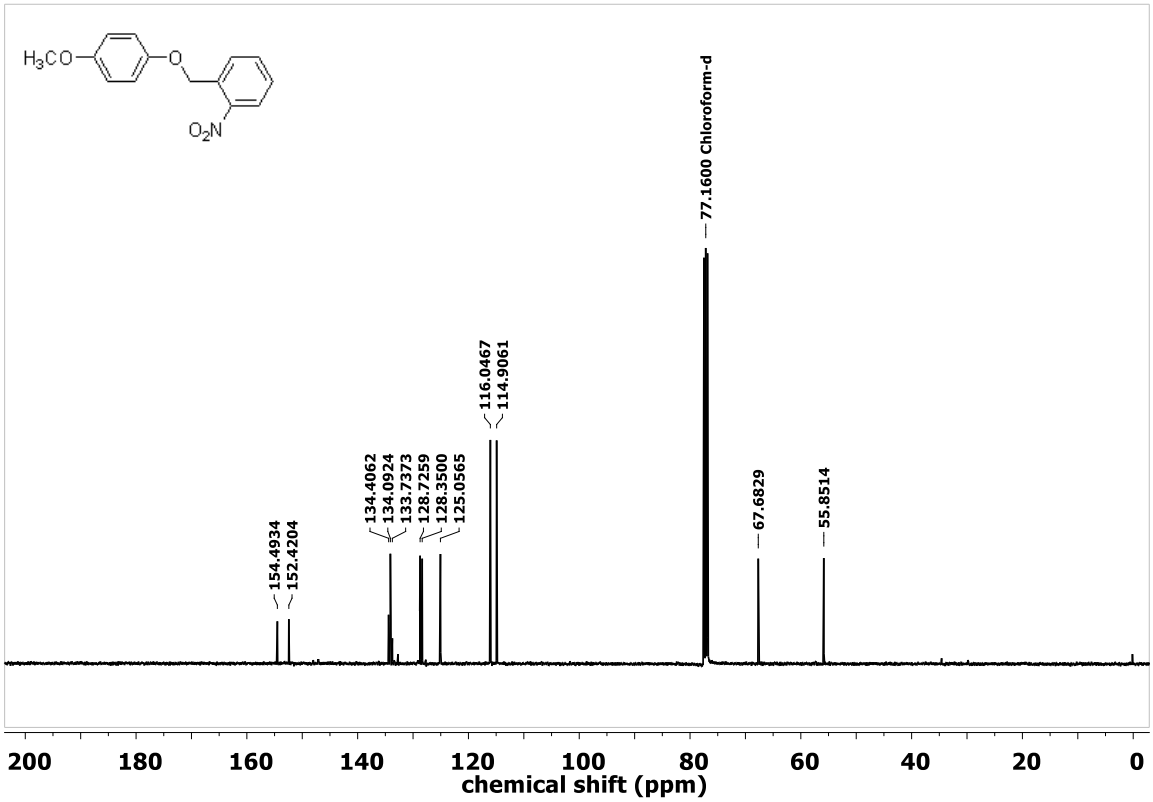

Figure 4.41 [13]C NMR spectrum of compound **11**.

4.5 References

1. S. K. Ko, S. K. Kim, A. Share, V. M. Lynch, J. Park, W. Namkung, W. Van Rossom, N. Busschaert, P. A. Gale, J. L. Sessler and I. Shin, *Nat. Chem.*, 2014, **6**, 885-892.
2. H. Valkenier, L. W. Judd, H. Li, S. Hussain, D. N. Sheppard and A. P. Davis, *J. Am. Chem. Soc.*, 2014, **136**, 12507-12512.
3. T. Saha, M. S. Hossain, D. Saha, M. Lahiri and P. Talukdar, *J. Am. Chem. Soc.*, 2016, **138**, 7558-7567.
4. E. N. W. Howe, N. Busschaert, X. Wu, S. N. Berry, J. Ho, M. E. Light, D. D. Czech, H. A. Klein, J. A. Kitchen and P. A. Gale, *J. Am. Chem. Soc.*, 2016, **138**, 8301-8308.
5. N. Busschaert, R. B. P. Elmes, D. D. Czech, X. Wu, I. L. Kirby, E. M. Peck, K. D. Hendzel, S. K. Shaw, B. Chan, B. D. Smith, K. A. Jolliffe and P. A. Gale, *Chem. Sci.*, 2014, **5**, 3617-3626.
6. A. Roy, D. Saha, P. S. Mandal, A. Mukherjee and P. Talukdar, *Chem. Eur. J.*, 2017, **23**, 1241-1247.
7. S. V. Shinde and P. Talukdar, *Angew. Chem. Int. Ed.*, 2017, **56**, 4238-4242.
8. Y. R. Choi, B. Lee, J. Park, W. Namkung and K.-S. Jeong, *J. Am. Chem. Soc.*, 2016, **138**, 15319-15322.
9. Y. R. Choi, G. C. Kim, H.-G. Jeon, J. Park, W. Namkung and K.-S. Jeong, *Chem. Commun.*, 2014, **50**, 15305-15308.
10. E. B. Park and K.-S. Jeong, *Chem. Commun.*, 2015, **51**, 9197-9200.
11. Y. Yanmei, M. Jing and X. Bengang, *Wiley Interdiscip Rev Nanomed Nanobiotechnol*, 2017, **9**, e1408.
12. N. C. Fan, F. Y. Cheng, A. Ho Ja-an and C. S. Yeh, *Angew. Chem. Int. Ed.*, 2012, **51**, 8806-8810.
13. L. Jianan, B. Wenbo, P. Limin and S. Jianlin, *Angew. Chem. Int. Ed.*, 2013, **52**, 4375-4379.
14. S. K. Choi, M. Verma, J. Silpe, R. E. Moody, K. Tang, J. J. Hanson and J. R. Baker, *Bioorg. Med. Chem.*, 2012, **20**, 1281-1290.
15. L. Weiying, P. Daiwei, W. Bin, L. Lingliang, G. Cancheng and Y. Jinbin, *Eur. J. Org. Chem.*, 2008, **2008**, 793-796.
16. S. Mo, Y. Wen, F. Xue, H. Lan, Y. Mao, G. Lv and T. Yi, *Sci. Bull.*, 2016, **61**, 459-467.

17. W. Lin, C. Albanese, R. G. Pestell and D. S. Lawrence, *Chem. Biol.*, 2002, **9**, 1347-1353.
18. R. Reinhard and B. F. Schmidt, *J. Org. Chem.*, 1998, **63**, 2434-2441.
19. M. S. Kim and S. L. Diamond, *Bioorganic Med. Chem. Lett.*, 2006, **16**, 4007-4010.
20. Y. V. Il'ichev, M. A. Schwörer and J. Wirz, *J. Am. Chem. Soc.*, 2004, **126**, 4581-4595.
21. I. R. Dunkin, J. Gebicki, M. Kiszka and D. Sanin-Leira, *J. Chem. Soc., Perkin Trans. 2*, 2001, 1414-1425.
22. X. Bai, Z. Li, S. Jockusch, N. J. Turro and J. Ju, *Proc. Natl. Acad. Sci.*, 2003, **100**, 409-413.
23. G. Mehta, P. Talukdar and N. Mohal, *Marvin 5.8.0, ChemAxon, 2012 (http://www.chemaxon.com)*, 2001, **42**, 7663-7666.
24. G. Mehta, S. Lakshminath and P. Talukdar, *BindFit v0.5. http://app.supramolecular.org/bindfit/ (accessed July 2017).* 2002, **43**, 335-338.
25. P. Thordarson, *Chem. Soc. Rev.*, 2011, **40**, 1305-1323.
26. R. Benz and S. McLaughlin, *Biophys. J.*, 1983, **41**, 381-398.
27. L. Rose and A. T. A. Jenkins, *Bioelectrochemistry*, 2007, **70**, 387-393.
28. T. Saha, S. Dasari, D. Tewari, A. Prathap, K. M. Sureshan, A. K. Bera, A. Mukherjee and P. Talukdar, *J. Am. Chem. Soc.*, 2014, **136**, 14128-14135.
29. H. Goto, S. Obata, N. Nakayama and K. Ohta, CONFLEX Corporation, Tokyo, Japan, 2017.
30. H. Goto and E. Osawa, *J. Am. Chem. Soc.*, 1989, **111**, 8950-8951.
31. M. J. Frisch, G. W. Trucks, H. B. Schlegel, G. E. Scuseria, M. A. Robb, J. R. Cheeseman, G. Scalmani, V. Barone, B. Mennucci, G. A. Petersson, H. Nakatsuji, M. Caricato, X. Li, H. P. Hratchian, A. F. Izmaylov, J. Bloino, G. Zheng, J. L. Sonnenberg, M. Hada, M. Ehara, K. Toyota, R. Fukuda, J. Hasegawa, M. Ishida, T. Nakajima, Y. Honda, O. Kitao, H. Nakai, T. Vreven, J. J. A. Montgomery, J. E. Peralta, F. Ogliaro, M. Bearpark, J. J. Heyd, E. Brothers, K. N. Kudin, V. N. Staroverov, T. Keith, R. Kobayashi, J. Normand, K. Raghavachari, A. Rendell, J. C. Burant, S. S. Iyengar, J. Tomasi, M. Cossi, N. Rega, J. M. Millam, M. Klene, J. E. Knox, J. B. Cross, V. Bakken, C. Adamo, J. Jaramillo, R. Gomperts, R. E. Stratmann, O. Yazyev, A. J. Austin, R. Cammi, C. Pomelli, J. W. Ochterski, R. L. Martin, K. Morokuma, V. G. Zakrzewski, G. A. Voth, P. Salvador, J. J. Dannenberg, S. Dapprich, A. D. Daniels, O. Farkas, J. B. Foresman, J. V. Ortiz, J. Cioslowski and D. J. Fox, Gaussian, Inc., Wallingford CT, 2013.

32. A. D. Becke, *J. Chem. Phys.*, 1993, **98**, 5648-5652.
33. C. Lee, W. Yang and R. G. Parr, *Phys. Rev. B*, 1988, **37**, 785.
34. R. Krishnan, J. S. Binkley, R. Seeger and J. A. Pople, *J. Chem. Phys.*, 2008, **72**, 650-654.
35. M. J. Frisch, J. A. Pople and J. S. Binkley, *J. Chem. Phys.*, 1984, **80**, 3265-3269.
36. D. H. Jornada, G. F. dos Santos Fernandes, D. E. Chiba, T. R. de Melo, J. L. dos Santos and M. C. Chung, *Molecules (Basel, Switzerland)*, 2015, **21**, 42.
37. S. Varghese Gupta, D. Gupta, J. Sun, A. Dahan, Y. Tsume, J. Hilfinger, K.-D. Lee and G. L. Amidon, *Mol. Pharm.*, 2011, **8**, 2358-2367.
38. K. A. Pardeshi, G. Ravikumar and H. Chakrapani, *Org. Lett.*, 2018, **20**, 4-7.
39. S. Blake, R. Capone, M. Mayer and J. Yang, *Bioconjug. Chem.* . 2008, **19**, 1614-1624.
40. P. Talukdar, G. Bollot, J. Mareda, N. Sakai and S. Matile, *J. Am. Chem. Soc.*, 2005, **127**, 6528-6529.
41. V. Gorteau, G. Bollot, J. Mareda, A. Perez-Velasco and S. Matile, *J. Am. Chem. Soc.*, 2006, **128**, 14788-14789.
42. T. Saha, A. Gautam, A. Mukherjee, M. Lahiri and P. Talukdar, *J. Am. Chem. Soc.*, 2016, **138**, 16443-16451.

Overall conclusion

In conclusion, I have accomplished the basic objective of my doctoral research study by the introduction of photoactivation in the field of synthetic transmembrane ion transport systems. The thesis focused on the design and synthesis of novel synthetic ion carriers and the application of a photocleavable protecting group to control the transport activity of the ion carrier. The main content of the thesis investigated the relation of lipophilicity and pK_a with ion transport activity, ion selectivity, mechanism of ion transport across lipid membrane and selective activation in the cancer cells for their biomedical application. In chapter 2, I have introduced the application of carbohydrate-based systems in the ion transport process. In chapter 3, I have shown the bisindole system as efficient anion carriers and achieved some amount of selective cytotoxicity in cancerous cells over non-cancerous cell. In chapter 4, was able to establish the proof of light responsive ion transport concept with a simple indole moiety *in vitro*. The photocontrolled induction of apoptotic cancer cell death via transmembrane chloride transport-mediated disturbance of cellular ion homeostasis using ion transport systems could find a place among the next generation tools for cancer treatment.

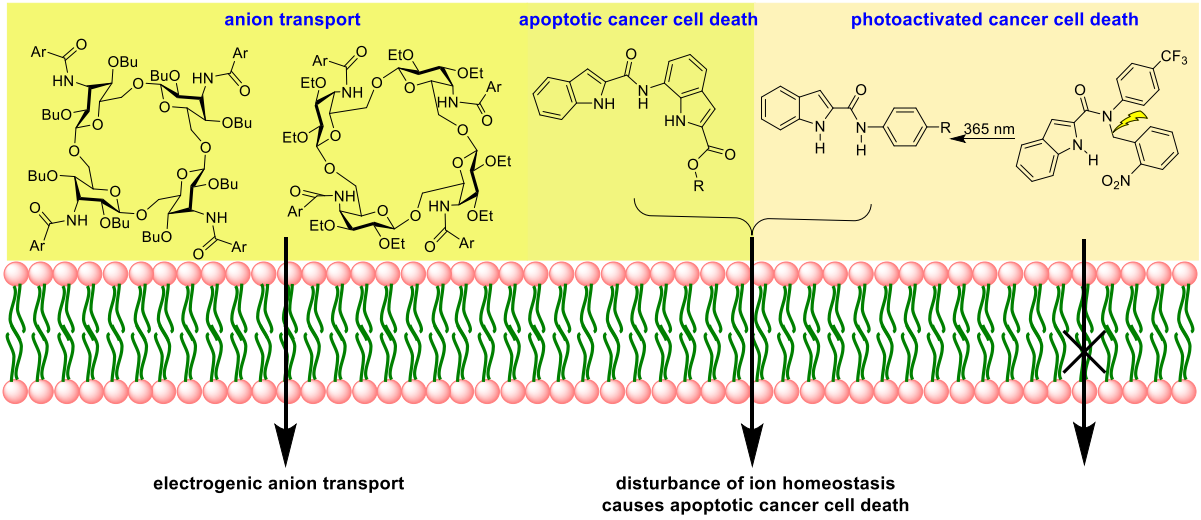

Future direction

Through smart optimization of the carrier structure, PPGs could be coupled with more complex and efficient ion carriers. This concept can be reattempted with the bisindole system. Light is an ideal stimulus for the biomedical application due to its benign nature, spatiotemporal control easy to use and does not cause any contamination. Photoactivated procarrier are superior compare to other stimuli responsive carriers as it is easy to tune different wavelength that can be usable for different applications. This simple and innovative concept of photoactivation, can be extended to photodynamic therapy for surface cancer treatment and can also be adapted for deep-seated cancer therapy employing endoscopes or optical fibers. Thus, further development of these systems is required for incorporating more potent ion carriers caged with PPGs active in the far red to near IR region, which is the most compatible for biomedical use.

Publication list

1. S. B. Salunke, J. A. Malla, P. Talukdar. 'Phototriggered activation of transmembrane chloride transport from o-nitrobenzyl based procarrier'. *Angew.Chem. Int. Ed.* 2019, **58**, 5354-5358.
2. S. B. Salunke, S. N. Save, N. J. Roy, R. Naorem, S. Sharma, and P. Talukdar. 'Bisindole based small molecules as transmembrane anion transporters and potential anticancer agents. *Org. Biomol. Chem.* 2024, **22**, 4987-4992
3. S. B. Salunke, N. J. Roy, M. Ahmad, R. Sharma, P. Talukdar, Y. Tsvetkov and co-workers. 'Cyclic oligosaccharide-based anion carriers'. (*Manuscript under preparation*).

End of thesis